Characterization of the fiber-matrix interface fracture properties in long fiber composites

Hugo Girard

N° d'ordre NNT : 2024ISAL0072

**THESE de DOCTORAT DE L'INSA LYON,
membre de l'Université de Lyon**

Ecole Doctorale N° EDA 034
Matériaux de Lyon

Spécialité/ discipline de doctorat : Matériaux

Soutenue publiquement le 10/09/2024, par :

Hugo Girard

Characterization of the fiber-matrix interface fracture properties in long fiber composites

---

Devant le jury composé de :

Carrère	Nicolas	Professeur	IRDL	Président
Estevez	Rafael	Professeur	SIMaP	Rapporteur
Laurin	Frédéric	Directeur de recherche	ONERA	Rapporteur
Drapier	Sylvain	Professeur	EMSE	Examinateur
Long	Didier	Directeur de recherche	MatéIS	Examinateur
Muñoz-Reja	Mar	Maître de conférences	Université de Séville	Examinatrice
Godin	Nathalie	Maître de conférences	MatéIS	Directrice de thèse
Doitrand	Aurélien	Maître de conférences	MatéIS	Co-directeur de thèse
Rinaldi	Renaud	Maître de conférences	MatéIS	Invité
Bikard	Jérôme	Encadrant industriel	Syensqo	Invité

Département FEDORA – INSA Lyon - Ecoles Doctorales

SIGLE	ECOLE DOCTORALE	NOM ET COORDONNEES DU RESPONSABLE
ED 206 CHIMIE	**CHIMIE DE LYON** **https ://www.edchimie-lyon.fr** Sec. : Renée EL MELHEM Bât. Blaise PASCAL, 3e étage **secretariat@edchimie-lyon.fr**	**M. Stéphane DANIELE** C2P2-CPE LYON-UMR 5265 Bâtiment F308, BP 2077 43 Boulevard du 11 novembre 1918 69616 Villeurbanne **directeur@edchimie-lyon.fr**
ED 341 E2M2	**ÉVOLUTION, ÉCOSYSTÈME, MICROBIOLOGIE, MODÉLISATION** **http ://e2m2.universite-lyon.fr** Sec. : Bénédicte LANZA Bât. Atrium, UCB Lyon 1 Tél : 04.72.44.83.62 **secretariat.e2m2@univ-lyon1.fr**	**Mme Sandrine CHARLES** Université Claude Bernard Lyon 1 UFR Biosciences Bâtiment Mendel 43, boulevard du 11 Novembre 1918 69622 Villeurbanne CEDEX **e2m2.codir@listes.univ-lyon1.fr**
ED 205 EDISS	**INTERDISCIPLINAIRE SCIENCES-SANTÉ** **http ://ediss.universite-lyon.fr** Sec. : Bénédicte LANZA Bât. Atrium, UCB Lyon 1 Tél : 04.72.44.83.62 **secretariat.ediss@univ-lyon1.fr**	**Mme Sylvie RICARD-BLUM** Laboratoire ICBMS - UMR 5246 CNRS - Université Lyon 1 Bâtiment Raulin - 2ème étage Nord 43 Boulevard du 11 novembre 1918 69622 Villeurbanne Cedex Tél : +33(0)4 72 44 82 32 **sylvie.ricard-blum@univ-lyon1.fr**
ED 34 EDML	**MATÉRIAUX DE LYON** **http ://ed34.universite-lyon.fr** Sec. : Yann DE ORDENANA Tél : 04.72.18.62.44 **yann.de-ordenana@ec-lyon.fr**	**M. Stéphane BENAYOUN** Ecole Centrale de Lyon Laboratoire LTDS 36 avenue Guy de Collongue 69134 Ecully CEDEX Tél : 04.72.18.64.37 **stephane.benayoun@ec-lyon.fr**
ED 160 EEA	**ÉLECTRONIQUE, ÉLECTROTECHNIQUE, AUTOMATIQUE** **https ://edeea.universite-lyon.fr** Sec. : Philomène TRECOURT Bâtiment Direction INSA Lyon Tél : 04.72.43.71.70 **secretariat.edeea@insa-lyon.fr**	**M. Philippe DELACHARTRE** INSA LYON Laboratoire CREATIS Bâtiment Blaise Pascal, 7 avenue Jean Capelle 69621 Villeurbanne CEDEX Tél : 04.72.43.88.63 **philippe.delachartre@insa-lyon.fr**
ED 512 INFOMATHS	**INFORMATIQUE ET MATHÉMATIQUES** **http ://edinfomaths.universite-lyon.fr** Sec. : Renée EL MELHEM Bât. Blaise PASCAL, 3e étage Tél : 04.72.43.80.46 **infomaths@univ-lyon1.fr**	**M. Hamamache KHEDDOUCI** Université Claude Bernard Lyon 1 Bât. Nautibus 43, Boulevard du 11 novembre 1918 69 622 Villeurbanne Cedex France Tél : 04.72.44.83.69 **direction.infomaths@listes.univ-lyon1.fr**
ED 162 MEGA	**MÉCANIQUE, ÉNERGÉTIQUE, GÉNIE CIVIL, ACOUSTIQUE** **http ://edmega.universite-lyon.fr** Sec. : Philomène TRECOURT Tél : 04.72.43.71.70 Bâtiment Direction INSA Lyon **mega@insa-lyon.fr**	**M. Etienne PARIZET** INSA Lyon Laboratoire LVA Bâtiment St. Exupéry 25 bis av. Jean Capelle 69621 Villeurbanne CEDEX **etienne.parizet@insa-lyon.fr**
ED 483 ScSo	**ScSo**[1] **https ://edsciencessociales.universite-lyon.fr** Sec. : Mélina FAVETON Tél : 04.78.69.77.79 **melina.faveton@univ-lyon2.fr**	**M. Bruno MILLY** (INSA : J.Y. TOUSSAINT) Univ. Lyon 2 Campus Berges du Rhône 18, quai Claude Bernard 69365 LYON CEDEX 07 Bureau BEL 319 **bruno.milly@univ-lyon2.fr**

1. ScSo : Histoire, Géographie, Aménagement, Urbanisme, Archéologie, Science politique, Sociologie, Anthropologie

Et ça continue (encore et encore!)
C'est que le début (d'accord, d'accord!)
Francis Cabrel

Remerciements

L'écriture des remerciements rime avec la fin de la thèse, déjà trois années, passées si rapidement que l'on viendrait à se demander si les principes de la relativité tiennent toujours lors de cet exercice.

Tout d'abord je souhaiterais remercier tous les membres de mon Jury de thèse, particulièrement les rapporteurs, Rafael Estevez et Frédéric Laurin pour leur analyse fine et pertinente du manuscrit de thèse. J'ai aussi beaucoup apprécié les longs échanges motivants et instructifs lors de la soutenance avec les autres membres du Jury : Nicolas Carrère, Sylvain Drapier, Mar Muñoz-Reja et Didier Long.

Place maintenant aux trois piliers de ce projet de thèse : le laboratoire MatéIS, l'entreprise Syensqo (anciennement Solvay) et l'Université de Rowan (USA), sans lesquels rien n'aurait été possible (voir Figure non numérotée ci-dessous).

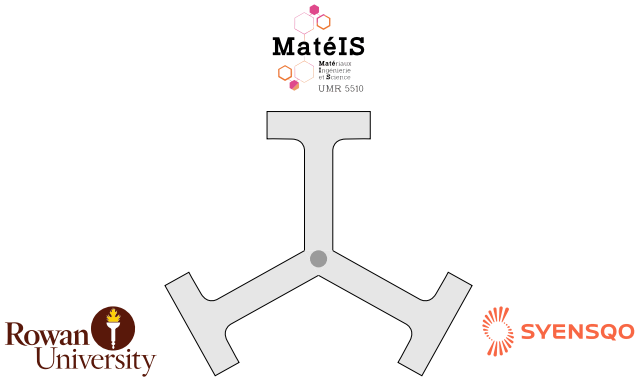

MatéIS : je tiens à remercier tous les membres du laboratoire pour ces trois dernières années, je me suis senti comme une fibre dans de la résine et cela grâce à vous. Je garde de supers souvenirs des parties de pétanque, des soirées au 100H, des séminaires et j'en passe. Une ambiance de ouf pour une équipe de ouf. Merci aux doctorants et post-docs, je ne peux pas tous vous citer car on m'a reproché un manuscrit un peu trop long, mais vous aurez toujours une place dans ma "heart's bibliography".

Syensqo : un grand merci à Jérôme Bikard, Lise Trouillet-Fonti et Didier Long pour votre aide et suivi tout au long du projet. Merci d'avoir pris le temps de m'aguiller lors de nos discussions.

Rowan University : a huge thank you to Behrad Koohbor, whose experiments were at the heart of this thesis. I have never regretted contacting you at the start of my thesis, as our collaboration has been so fruitful. I am very happy that you welcomed me for a few weeks in your laboratory at Rowan to carry out some very nice experiments. I would also like to thank Kazi and Nicholas for their help :)

Lumière s'il vous plaît, laissez maintenant la place à l'équipe de choc, la dream team, dénommée les "Nice Super-visors". Ils sont trois et ont tout déchiré (voire fissuré) durant ces trois années (voir cette deuxième Figure non numérotée, elle ne sert à rien, cela me fait très plaisir).

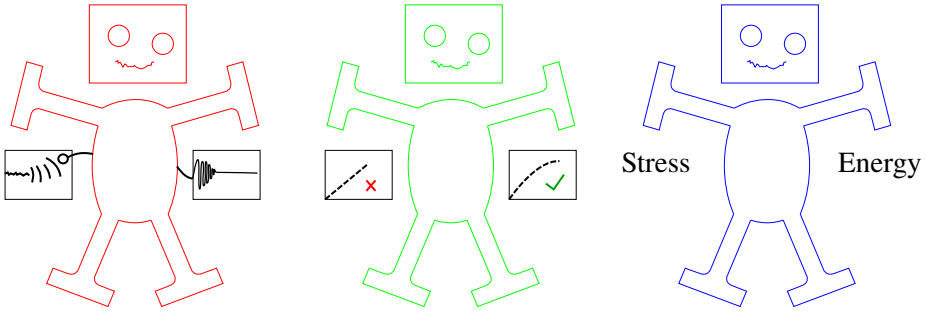

Nathalie Godin | Renaud Rinaldi | Aurélien Doitrand

Je souhaiterais premièrement vous remercier tous les trois pour vos discours lors de la soutenance, ils m'ont beaucoup touchés. Merci Nathalie (à gauche en rouge) d'avoir dirigé ma thèse, tu as apporté ton regard critique sur mon travail ainsi que ta rigueur et ton expérience scientifique. Tu as toujours relu mes documents, pas toujours très accessibles, avec motivations et tu as suivi mon travail lors des nombreuses réunions. Je garde de très bons souvenirs de notre conférence ECCM21 à Nantes. Renaud (au milieu en vert), tout d'abord je suis désolé de ne pas avoir évolué au-delà du rond dans un carré et du linéaire élastique, je sais que cela t'a beaucoup pesé (ne t'empêchant cependant pas de pouvoir monter à la Croix-Rousse). Merci pour ton humour et enthousiasme lors de nos nombreuses discussions. J'ai grandement apprécié tous nos moments passés ensemble, au labo et en dehors, particulièrement la séance nettoyage de la salle du Synchrotron Soleil, mazette quel kiff ! Enfin, last but not least, Aurélien Doitrand (à droite en bleu), merci de m'avoir guidé durant ces trois ans. J'ai tellement appris à tes côtés. Ta réactivité, motivation et pertinence ont permis à ces travaux de recherche d'aller tellement plus loin. Je t'en suis très reconnaissant. J'ai rencontré plus qu'un Super-visor mais un ami. Nos activités extra-labo,

toujours placées sous le signe de la bonne humeur ont grandement contribuées à la réussite de cette thèse. J'espère sincèrement que cela continuera « encore et encore ». A tous les trois, merci du fond du cœur et continuez comme ça !!

Mes co-bureaux, pas facile de me supporter tous les jours, mais ils ont triomphé, "veni, vidi, vici". Benjamin, j'espère que tu arriveras un jour à viser la poubelle en la plaçant à plus d'un mètre. Milena, merci pour ton aide lors des différents essais, on a passé trois super années dans nos différents bureaux. Je voudrais aussi remercier Thomas Duminy, qui pourrait prétendre sans vergogne à rejoindre la dream team. Tu m'as beaucoup apporté, tant sur le plan scientifique que personnel, tu as aussi largement contribué au bon déroulement de ma thèse. J'espère que nos chemins se recroiseront un jour dans un labo quelque part.

Enfin, sans qui tout cela n'aurait jamais eu lieu, ma famille. Je tiens à la remercier tout particulièrement pour m'avoir supporté tout au long de ma vie, votre soutien a été sans faille. Se retrouver tous ensemble à la soutenance m'a beaucoup touché. Loupyx merci beaucoup de m'avoir soutenu durant cet exercice. Trois magnifiques années à tes côtés (1-2 .. 3-4 .. 5-saucisses). Mon petit cerveau, parfois 1000% préoccupé par la thèse, n'a pas du être simple à supporter, chapeau bas. La réussite de cette thèse réside en grande partie dans ta présence, merci mille fois.

Allez encore une petite Figure non numérotée mais avec échelle svp, trop souvent utilisée lors de la soutenance mais jamais présentée dans le manuscrit, enjoy! (merci Jérôme, désolé d'avoir cassé le tomographe au passage mais la photo en jette).

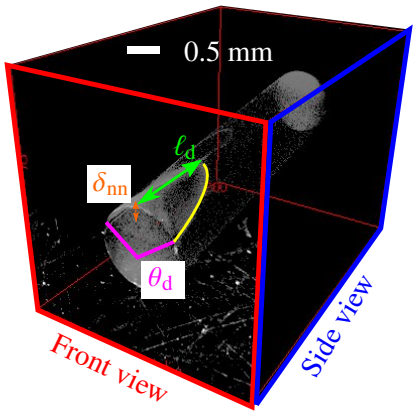

Contents

Abbreviations	Definitions
AE	Acoustic emission
CA	Coupling Agent
CC	Coupled Criterion
CF	Carbon Fiber
CFRP	Carbon Fiber Reinforced Polymer
CZM	Cohesive Zone model
DGEBA	Diglycidyl Ether Bisphenol A
DIC	Digital Image Correlation
DMA	Dynamic Mechanical Analysis
DoF	Degrees of Freedom
ERR	Energy Release Rate
FE	Finite Element
FRP	Fiber Reinforced Polymer
GF	Glass Fiber
GFRP	Glass Fiber Reinforced Polymer
IERR	Incremental Energy Release Rate
IFSS	Interfacial Shear Strength
IFS	Interfacial Friction Stress
ILSS	Interlaminar Shear Strength
LEFM	Linear Elastic Fracture Mechanics
MA	Matched Asymptotic
NOCA	No Coupling Agent
NPDGE	Neopentanediol Diglycidylether Glycidylethers
PE	Plain Strain
PF	Phase-Field approach for fracture
PS	Plain Stress
RVE	Representative Volume Element
SEM	Scanning Electron Microscope

Table 1 – Abbreviations used in the manuscript with their corresponding definitions.

Table 2 – Variables used in the manuscript with their corresponding definitions.

Variables	Definitions
A	Function depending on specimen geometry and material behavior
α	Inter-center angle
α_{Dun}, β_{Dun}	Dundurs's parameters
C_{f}	Coefficient of friction
d	Inter-center distance
d_{f}	Fiber diameter
d_{i}	Inclusion size
δ_{nn}	Debonding opening
$\delta_{\text{nn}}^{\text{plateau}}$	Debonding opening at the plateau - minimizing the energy condition
$\delta_{\text{nn}}^{\text{arrest}}$	Arrest debonding opening
δ	CZM separation
δ_{c}	CZM critical separation
δ_0^{τ}	CZM damage initiation tangential separation
δ_0^{σ}	CZM damage initiation normal separation
δ_{n}	CZM normal separation
δ_{t}	CZM tangential separation
δ_{eq}	CZM dimensionless effective relative separation
δ_{nc}	CZM critical normal separation
δ_{tc}	CZM critical tangential separation
$\delta_{\text{eq}}^{\text{soft}}$	CZM dimensionless effective relative damage initiation separation
$\delta_{\text{nc}}^{\text{soft}}$	CZM normal damage initiation separation
E^*	Harmonic mean of the effective elastic moduli of the two constituents
E	Young's modulus
E_{l}	Longitudinal elastic modulus
E_{t}	Transverse elastic modulus

Continued on next page

Table 2 – Variables used in the manuscript with their corresponding definitions. (Continued)

Variables	Definitions
f	Stress criteria
$\mathcal{F}_1$	Experimental-numerical results difference
$\mathcal{F}_2$	Equivalent-normal stress isocontours difference
$\mathcal{F}_3$	Difference with the converged solution
F_r	Experimental reaction force
F_i	Force at the fiber-matrix debonding initiation
F_max	Force at the complete interface failure
F_f	Friction force after failure
γ	Interface brittleness number
γ_SV	Surface energies of solid-vapor
γ_SL	Surface energies of solid-liquid
γ_LV	Surface energies of liquid-vapor
Γ_c	Crack path at initiation
Γ	Crack path - debonding path
G	Energy release rate (ERR)
G_c	Critical energy release rate
G_inc	Incremental energy release rate (IERR)
$\overline{G_\mathrm{c}}$	Global interface critical ERR
G_IC	Critical energy release rate in mode I
G_IIC	Critical energy release rate in mode II
G_IIIC	Critical energy release rate in mode III
G_I	Energy release rate in mode I
G_II	Energy release rate in mode II
G_III	Energy release rate in mode III
h	Numerical model thickness
h_0	Sample thickness
k	Function depending on specimen geometry and material behavior

Continued on next page

Table 2 – Variables used in the manuscript with their corresponding definitions. (Continued)

Variables	**Definitions**
K_c	Critical stress intensify factor
κ_k	Kolosov's constant
L	Numerical model width
L_f	Fiber length
L_0	Sample width
ℓ	Crack or debonding length
ℓ_d	Debonding length
ℓ_{trans}	Critical transfer length
ℓ_c	Crack length at initiation
L_{emb}	Embedded fiber length
ℓ_{mat}	Material characteristic length
λ	G_{IIC} to G_{IC} ratio
μ	Shear to tensile strength ratio
μ_k	Shear modulus
n	Power-law exponent
N	Number of recorded AE events
ν	Poisson's ratio
P_i	Interfacial pressure
ψ	Mode mixity
r	Fiber radius
RF_x, RF_y	Nodal reaction force
S_{node}	Node-surrounding weight surface
S	Crack surface - debonding surface
S_c	Crack surface at initiation
σ	Stress - traction
σ_{nn}	Normal stress component
σ_{nt}	In-plane shear stress component

Continued on next page

Table 2 – Variables used in the manuscript with their corresponding definitions. (Continued)

Variables	Definitions
σ_{nz}	Out-of-plane shear stress component
σ_{eq}	Equivalent stress
σ_c	Interfacial tensile strength
σ^{∞}	Remote tensile stress - remote loading
σ_f^c	Tensile strength of the fiber for ℓ_{trans}
σ_f	Fiber tensile loading
σ_{req}^{∞}	Remote loading required to fulfill the condition
σ_G^{∞}	Remote loading required to fulfill the energy condition
σ_{σ}^{∞}	Remote loading required to fulfill the stress condition
T_g	Glass transition temperature
τ_{bond}	Bond strength
τ_i	Interfacial shear stress
τ_c	Interfacial shear strength (IFSS)
τ_{fr}	Interfacial friction stress
θ	Debonding path
θ_{arrest}	Debonding angle after unstable growth
θ_d	Debonding angle
$\theta_d^{plateau}$	Debonding angle at the plateau - minimizing the energy condition
θ_f	Fiber angular location
θ_{final}	Debonding angle just before sample failure
θ_{ini}	Debonding angle at initiation
θ_l	Debonding angle after unstable growth - lower bound
θ_T	Angle between the main coordinate system and the interfacial coordinate system
θ_u	Debonding angle after unstable growth - upper bound
θ_i	Angular location maximizing stress or elastic strain energy variation

Continued on next page

Table 2 – Variables used in the manuscript with their corresponding definitions. (Continued)

Variables	**Definitions**
θ_c	Contact angle
$\Delta\theta$, $\Delta\theta^+$, $\Delta\theta^-$	Increment of debonding angle
$\Delta\theta^+_{TC}$	Increment of debonding angle of the tension/compression transition
U	Imposed displacement
U_c	Displacement at crack initiation
U_σ	Displacement required to fulfill the stress condition
U_G	Displacement required to fulfill the energy condition
V_f	Fiber volume fraction
V_m	Matrix volume fraction
W_A	Work of adhesion
W_M	Work associated with other mechanisms
W_k	Kinetic energy
W_d	Dissipated energy
W_{el}, W	Elastic strain energy
W_{ext}	External work forces

Résumé de la thèse

Les problèmes d'interface entre différents matériaux sont rencontrés dans de nombreux secteurs industriels car ils apparaissent régulièrement dans des pièces assemblées ou des matériaux hétérogènes. Les structures constituées de ces éléments sont aujourd'hui de plus en plus utilisées, en particulier pour des applications aéronautiques et aérospatiales, où les assemblages collés et les matériaux composites sont principalement utilisés pour réduire la masse des structures et éviter les opérations d'assemblage, *e.g.*, boulonnage, rivetage. La mécanique de ces problèmes d'interface s'étend intrinsèquement sur différentes échelles de taille, de l'échelle macroscopique pour les grandes pièces collées à l'échelle microscopique pour les interfaces dans les matériaux hétérogènes, tels que les interfaces fibre-matrice dans les composites à fibres longues. Pour ces derniers, l'interface fibre-matrice est un aspect primordial des propriétés mécaniques globales puisqu'elle détermine bien souvent l'amorçage des premiers endommagements ainsi que le transfert de charge entre la matrice et les fibres [PSL06; JHJ12]. En effet, la décohésion à l'interface fibre-matrice est généralement le premier type d'endommagement qui se produit dans les composites à fibres longues. Une fois amorcée, la décohésion fibre-matrice se propage puis dévie éventuellement dans la matrice. Ce phénomène conduit à la coalescence des décohésions et de leurs microfissures matricielles respectives, pouvant conduire à la fissuration du pli [ST12]. D'autres phénomènes d'endommagement en découlent comme le délaminage entre les plis, la rupture de fibres ou, dans les cas les plus critiques, la défaillance complète de la pièce composite. L'interface fibre-matrice a donc une influence prédominante sur le processus d'endommagement des composites, de sorte qu'il est crucial de caractériser l'interface fibre-matrice afin de prévenir ou de contrôler l'endommagement dans ces derniers.

En réalité, la définition de l'interface fibre-matrice n'est pas simple d'un point de vue expérimental puisqu'elle dépend de l'échelle d'observation par rapport à la dimension de la fibre. L'interface peut être conceptualisée soit comme une surface d'épaisseur nulle reliant la fibre et la matrice, soit comme une région de transition d'épaisseur finie lorsque sa dimension est non négligeable par rapport aux autres dimensions caractéristiques du matériau. Quelques observations expérimentales ont

validé l'existence d'une région avec une constitution différente près de l'interface fibre-matrice [Wil+90; Dow+00; Bog+99; KSW01]. Cette région est communément appelée *interphase*. Dans le manuscrit, la région *interphase* sera considérée comme une interface car les fibres étudiées ont un diamètre allant de 1 à 2 mm, très supérieur à l'épaisseur de l'interphase qui est généralement de l'ordre de $\simeq 1$ µm [KSW01].

Il existe de nombreuses techniques expérimentales pour mesurer les propriétés à rupture des interfaces fibre-matrice. Parmi les différentes méthodes, la plupart se concentrent sur la détermination des propriétés de cisaillement telles que l'essai de pull-out [YT10] ou l'essai de fragmentation [NOT08]. Herrera-Franco et Drzal [HD92] et Zhandarov et Mäder [ZM05] ont passé en revue la plupart des méthodes existantes. Cependant, il y a un manque de techniques expérimentales pour déterminer les propriétés en traction, malgré les méthodes proposées dans [KMM98]. Il convient de noter que les propriétés en traction sont aussi importantes que celles de cisaillement, en particulier lorsque le composite est soumis à une sollicitation transverse à la direction des fibres. De plus, l'un des principaux inconvénients de ces techniques, souligné dans la littérature, est le manque de normalisation, où des écarts importants peuvent être observés entre les essais, et surtout entre les opérateurs. Par exemple, Pitkethly *et al.* [Pit+93] ont réalisé une campagne de tests sur des microcomposites similaires dans 12 laboratoires différents à travers le monde. L'objectif de ce travail était d'évaluer la dépendance des propriétés déterminées par rapport au type d'essai et à la procédure expérimentale. Des variations importantes ont été observées entre les techniques, en particulier, les tests de pull-out et de fragmentation ont donné des résultats allant jusqu'à 250 % de différence relative pour une même configuration fibre/matrice. Par conséquent, une modélisation précise du problème, combinée à une observation plus approfondie du dispositif expérimental, pourrait contribuer à réduire les écarts et à déterminer plus précisément les propriétés à rupture. Par ailleurs, le développement de techniques expérimentales impliquant la sollicitation de l'interface fibre-matrice en traction est aussi nécessaire. Pour ces raisons, l'utilisation d'un microcomposite mono-fibre soumis à une traction transverse semble pertinente puisque la décohésion passe d'un mode d'ouverture à un mode de cisaillement. Cette technique permet donc de déterminer les propriétés à rupture à la fois de traction et de cisaillement. Des échantillons microcomposites mono-fibre sollicités en traction sont donc étudiés dans ce travail de thèse, schématiquement représentés dans la Figure 1a. Certains de ces échantillons ont été obtenus en collaboration avec le professeur Behrad Koohbor de l'université de Rowan. La caractérisation expérimentale de la décohésion, qui doit encore être développée, est au cœur des travaux.

La Figure 1b montre les paramètres géométriques de la décohésion. La décohésion peut donc être décrite par son angle θ_{d} au bord libre, déterminé par l'angle entre les deux pointes de fissure. La quantité δ_{nn} correspond à l'ouverture normale maximale de la décohésion située au pôle au bord libre de la fibre par rapport à la direction

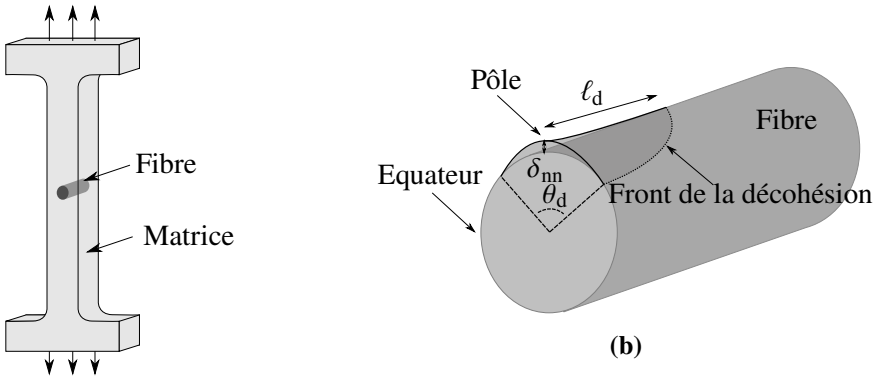

Figure 1 – (a) Exemple d'échantillon microcomposite mono-fibre utilisé dans ces travaux de thèse. (b) Différents paramètres géométriques introduits pour décrire la géométrie de la décohésion.

de sollicitation. L'ouverture de la décohésion correspond à la distance séparant les deux lèvres de la fissure. La longueur de décohésion selon l'épaisseur est décrite par ℓ_d, qui correspond à la longueur de décohésion dans la direction de l'épaisseur au pôle de la fibre. La caractérisation est effectuée à l'aide d'une ou deux caméras positionnées perpendiculairement l'une vis-à-vis de l'autre. La caméra frontale fournit des champs de déplacement en utilisant de la Corrélation d'Images Numériques (CIN) mais ne permet pas d'observer la décohésion qui s'amorce sur la face opposée. L'utilisation de la seconde caméra permet donc de capturer la propagation de la décohésion dans l'épaisseur, quel que soit l'endroit où la décohésion s'amorce. L'ouverture de la décohésion δ_{nn} est évaluée par CIN sur la surface frontale à l'aide des logiciels VIC 2D et Ufreckles, qui fournissent tous deux des résultats similaires. L'ouverture fournit donc le chargement au moment de l'amorçage et l'ouverture tout au long du processus de décohésion. La longueur de la décohésion ℓ_d est déterminée visuellement en contrôlant le changement d'intensité du niveau de gris. L'angle de la décohésion θ_d est déterminé soit visuellement, soit *via* le résidu de CIN, important dans la zone de décohésion. La variation de ces paramètres géométriques donnent des chargements à l'amorçage de la décohésion similaires. Un exemple d'évolution d'angle de décohésion en fonction de la contrainte globale est présenté en Figure 2, pour deux échantillons.

L'observation visuelle et par résidu de CIN donnent des résultats similaires en termes d'angle de décohésion, quantifiant ainsi l'incertitude de la mesure (zone hachurée sur la Figure 2). Cependant, cette méthode n'est pas en mesure de fournir un angle de décohésion cohérent pour les petites fibres, *i.e.*, lorsque l'ouverture de la décohé-

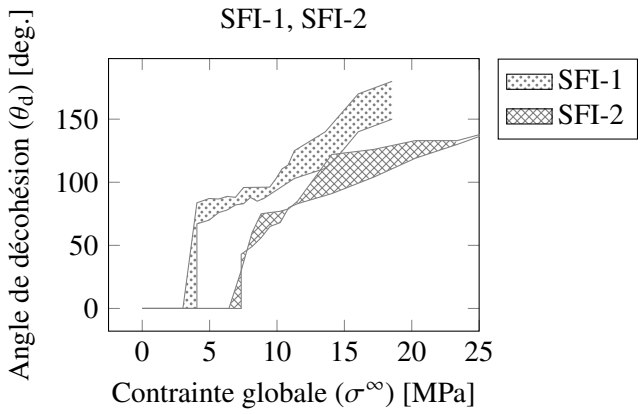

Figure 2 – Variation de l'angle de décohésion en fonction de la contrainte globale pour deux échantillons référencés SFI-1 et SFI-2.

soion reste inférieure à la résolution de la caméra. Dans l'ensemble, les différents échantillons fournissent des résultats expérimentaux pertinents pour une modélisation numérique plus poussée afin d'identifier précisément les propriétés à rupture de l'interface fibre-matrice.

La modélisation de la décohésion fibre-matrice a évolué, passant de modèles analytiques à des modèles éléments finis couplés à des approches de rupture spécifiques. Les modèles analytiques sont avantageux car ils sont très efficaces lorsque la configuration est simple. Cependant, ils ne prennent pas en compte certaines des conditions expérimentales réelles potentiellement observées pour les essais microcomposite [Pit+93]. Les exemples incluent le désalignement des fibres, une configuration de chargement imparfaite, un défaut dans la fabrication de l'échantillon. Ceux-ci peuvent être intégrés grâce à des simulations éléments finis et l'utilisation de modèle de prévision d'amorçage et de propagation de fissures. Parmi les modèles utilisés, le Critère Couplé (CC) [Man09; GMG15] et les Modèles de Zone Cohésive (MZC) [Koy+09; Kus+11] semblent être pertinents pour étudier numériquement la décohésion fibre-matrice. Le CC est efficace dans le cas des petites déformations et dans le cadre de l'élasticité linéaire, ce qui est considéré avec la matrice époxy utilisée dans ces travaux de thèse. Quelques études ont utilisé le CC pour prédire la décohésion à l'interface fibre-matrice [Man09; GMG15; Muñ+16a]. Cependant, aucune de ces études n'a utilisé le CC en conjonction avec des observations expérimentales pour identifier les propriétés à rupture de l'interface fibre-matrice. Le CC est donc appliqué dans ce travail de thèse à la prédiction de la décohésion fibre-matrice et à l'identification des propriétés à rupture en utilisant des observations expérimentales

de la décohésion. L'amorçage unstable de la décohésion pour un certain angle observé expérimentalement peut être reproduit par le CC. L'amorçage est suivi d'une propagation stable de la décohésion, cette seconde phase est aussi prédite par le CC en fonction des propriétés à rupture de l'interface. En limitant les angles de décohésion obtenus *via* le CC à la plage mesurée expérimentalement, il est possible de déterminer une gamme de taux de restitution d'énergie critiques et de résistances critiques admissibles. Les propriétés à rupture identifiées sont du même ordre de grandeur que celles déterminées dans d'autres travaux pour une configuration similaire.

Les prédictions du CC et MZC ont été principalement comparées sur la base du chargement à l'amorçage uniquement [GPM14; Gen+19]. Les MZC sont donc aussi appliqués à la décohésion fibre-matrice à la fois sur l'amorçage et la propagation et comparés aux observations expérimentales ainsi qu'aux prédictions du CC. Les MZC sont capables de reproduire le processus de décohésion détaillé précédemment. Les propriétés à rupture identifiées à l'aide des MZC fournissent une variation de l'angle de décohésion proche de celle obtenue expérimentalement et *via* le CC, voir Figure 3. De même, les propriétés identifiées par le CC ou les MZC sont proches, à l'exception du taux de restitution d'énergie critique en cisaillement. Cependant, l'approche d'identification inverse n'est pas aussi efficace que celle du CC, car les MZC impliquent des non-linéarités dans la résolution des calculs éléments finis. A contrario, le CC ne décrit pas la présence d'une possible zone d'élaboration en amont de la décohésion.

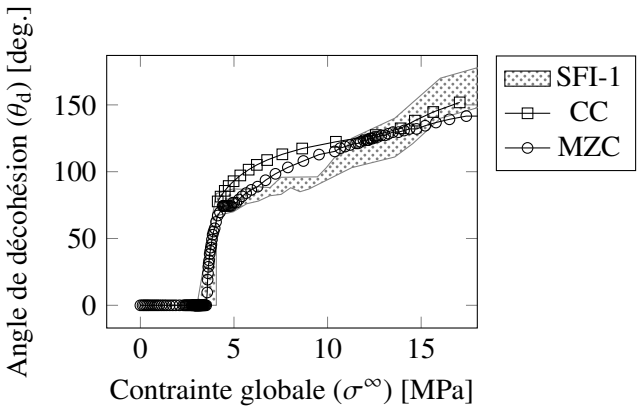

Figure 3 – Variation de l'angle de décohésion en fonction de la contrainte globale appliquée. Comparaison entre les mesures expérimentales (échantillon référencé SFI-1) et les résultats obtenus par le CC et MZC.

Contrairement aux MZC, la plupart des applications du CC sont néanmoins lim-

itées à une fissure unique avec un chemin de fissure connu. La principale difficulté réside dans la détermination du chemin de la fissure, qui peut être théoriquement décrit par une infinité de configurations. La plupart des études actuelles basent le chemin de la fissure sur des formes géométriques paramétrées [Gar+16] ou sur des isovaleurs de contrainte [Leg14], qui ne prennent pas forcément en compte l'aspect énergétique inhérent au CC. Une approche est donc proposée en 2D pour évaluer la solution du CC basée sur des formes de décohésion obtenues *via* les isovaleurs de contrainte et sur la condition en énergie dans une configuration à deux fibres où le chemin de la fissure n'est plus symétrique par rapport à la direction de sollicitation. En fonction des propriétés à rupture de l'interface, *i.e.*, l'indice de fragilité de l'interface γ, trois configurations différentes peuvent être rencontrées :

- $\gamma < 1$: la prédiction des formes de décohésion basée sur les isovaleurs en contrainte fournit une approximation correcte des formes possibles de décohésion à l'amorçage ;
- $1 < \gamma < 1.4$: les formes de décohésion à l'amorçage possibles se situent entre les prédictions de décohésion basées sur les isovaleurs en contrainte et celles basées sur l'énergie ;
- $\gamma > 1.4$: la prédiction de la décohésion basée sur l'énergie fournit une bonne approximation, car la solution tend à être contrôlée par la condition en énergie.

La Figure 4 montre la configuration d'angles à l'amorçage obtenue *via* les différentes approches et illustre les différentes configurations mentionnées ci-dessus.

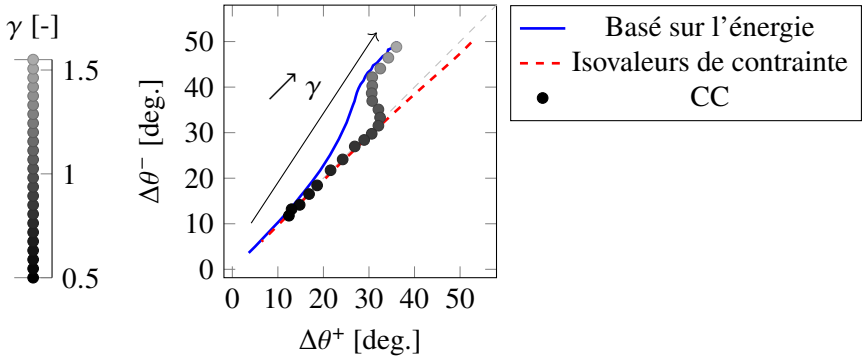

Figure 4 – Variation de la solution du CC (marqueurs en niveau de gris), vis-à-vis des solutions proposées par les formes de décohésion basées sur les isovaleurs de contrainte et sur l'énergie.

Les modèles 2D utilisés jusqu'à présent tendent à représenter les phénomènes au centre de l'échantillon, mais les observations expérimentales sont effectuées sur les bords libres, où des singularités de contrainte peuvent être présentes. Un modèle 3D permet de prendre en compte ces singularités. De plus, le CC n'a pas encore été appliqué à la décohésion fibre-matrice en 3D. Cependant, la mise en œuvre du CC en 3D est plus compliquée car sa résolution nécessite de connaître le chemin de la fissure. La détermination de formes de décohésion basées sur les isovaleurs de contrainte normale est numériquement efficace puisqu'elle peut être menée indépendamment des propriétés à rupture de l'interface. La gamme de taux de restitution d'énergie critique en mode I identifiée à l'aide du modèle 2D (CC et MZC) est proche de celle du modèle 3D. Le modèle 2D sous-estime légèrement la résistance à la traction car il ne considère pas la singularité. La modélisation 2D est donc pertinente à des fins d'efficacité pour l'identification des propriétés à rupture de l'interface. Cependant, les formes de décohésion basées sur les isovaleurs de contrainte ne font pas intervenir de cisaillement sur le chemin de la décohésion en 3D, de ce fait, aucune identification des propriétés à rupture en cisaillement n'est possible.

Par conséquent, les formes de décohésion basées sur les isovaleurs de contrainte, mais aussi sur l'énergie, sont comparées en 3D pour évaluer la forme optimale de la décohésion à l'amorçage. Les formes basées sur l'énergie sont plus difficiles à déterminer car elles nécessitent la comparaison de toutes les formes du front de fissure possibles. Sur la base des observations expérimentales, des hypothèses sont formulées concernant le lieu d'amorçage et la description de la forme du front de fissure. Les solutions du CC obtenues *via* les deux approches sont comparées dans la Figure 5 pour une gamme de propriétés à rupture, *i.e.*, d'indices de fragilité γ.

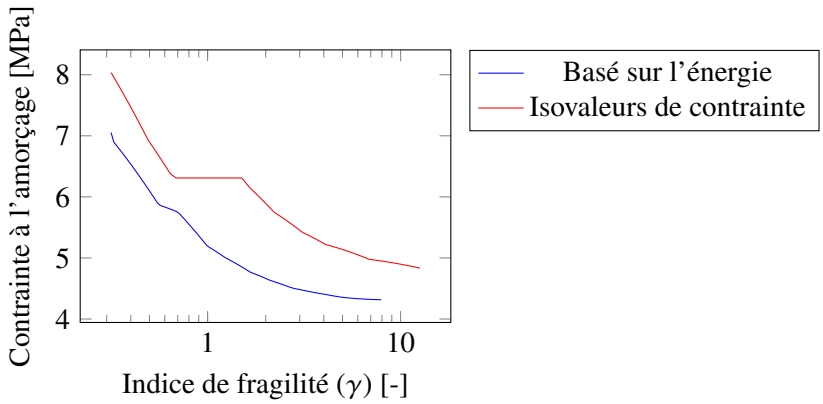

Figure 5 – Solutions du CC obtenues *via* les formes 3D de decohésion basées sur les isovaleurs de contrainte ou l'énergie, pour une gamme d'indice de fragilité.

Contrairement au modèle 2D, les formes basées sur l'énergie fournissent la solution optimale quel que soit l'indice de fragilité γ. Les formes basées sur les isovaleurs de contrainte surestiment de 15% maximum la solution optimale pour des indices de fragilité petits ($\gamma < 1$) ou grands ($\gamma > 6$). Des différences plus importantes, allant jusqu'à 30 %, sont observées pour des indices de fragilité intermédiaires ($1 < \gamma < 6$). L'identification inverse des propriétés à rupture de l'interface est effectuée sur la base des formes de décohésion basées sur les isovaleurs de contrainte et sur l'énergie, *i.e.*, optimales. Seules les propriétés à rupture d'ouverture sont identifiées, car les propriétés de cisaillement influencent légèrement la solution du CC pour les petites surfaces de décohésion telles que celles observées expérimentalement. Les deux approches donnent des propriétés à rupture similaires en termes de résistance à la traction, la différence devient plus prononcée en termes de taux de restitution d'énergie critique pour des indices de fragilité intermédiaires. Les formes optimales de décohésion fournissent une topologie cohérente avec celles observées expérimentalement, fournissant des valeurs appropriées de la longueur, l'angle et l'ouverture de la décohésion. Les formes basées sur les isovaleurs de contrainte sont différentes de celles observées expérimentalement.

En conclusion, ce travail de thèse a permis de caractériser expérimentalement la décohésion fibre-matrice à l'aide de résultats d'essais microcomposites à fibre unique sollicités transversalement. Cet essai, couplé à un modèle éléments finis, permet d'identifier les propriétés à rupture d'ouverture et de cisaillement de l'interface fibre-matrice. Le CC et les MZC ont été utilisés pour modéliser la décohésion de l'interface fibre-matrice. Les deux approches sont capables de reproduire le processus de décohésion observé expérimentalement. L'utilisation d'un modèle 2D permet de déterminer les propriétés à rupture de cisaillement de l'interface, contrairement au modèle 3D. Le modèle 2D ne tient pas compte de la singularité au bord libre et sous-estime donc la résistance à la traction par rapport au modèle 3D. Dans un cas général, des formes de décohésion basées sur les isovaleurs de contrainte donne une solution du CC proche de l'optimum lors de l'utilisation d'un modèle 2D. En revanche, l'écart se creuse lors de l'utilisation d'un modèle 3D où l'hypothèse des isovaleurs de contrainte entraîne une différence sur le chargement à l'amorçage allant jusqu'à 30% avec la solution optimale.

General introduction

This thesis is part of a collaboration between the MatéIS laboratory and Solvay (now Syensqo). Most of the work was carried out at MatéIS, at the INSA engineering school in Lyon. The aim of the project is to develop new techniques for characterizing the fiber-matrix interface in long fiber composites from experimental and numerical points of view. During the project, a collaboration with Professor Behrad Koohbor at Rowan University was established, some of the experiments being carried out by members of this institution and used in this thesis work.

How can the fracture properties of the fiber-matrix interface in long fiber composites be characterized? This is the question that this thesis aimed to answer. It is introduced in Chapter I that well-controlled interface properties enable control over the overall failure process of the composite part. In-depth characterization of composites failure mechanisms is crucial since structures made from these materials are nowadays increasingly employed, especially in aeronautic and aerospace applications, wherein composite materials are used primarily for weight reduction. Those familiar with composite materials sciences can skip the first Chapter and start reading afterwards. Chapter I details how important interfaces are in composites, with a theoretical explanation backed up by experimental results. Particularly, Chapter I further highlights the need of developing accurate methods for characterizing fiber-matrix interfaces fracture properties in order to improve and optimize the durability of composite components. Such accurate characterization methods may involve the use of numerical models to take into account the finer details of the experimental configuration and thus deduce the most accurate possible interface fracture properties. Particularly, this thesis work focuses on the characterization of glass fiber/epoxy matrix interface through an experimental-numerical dialogue.

Following the first chapter, the thesis is divided into six further chapters, detailed as follows:

- Chapter II: A twofold state of the art is presented, the first part being devoted to the experimental aspects of fiber-matrix interface fracture characterization. In particular, a review of how interface fracture properties can be measured is

proposed, providing some key aspects on the motivation for this thesis work. Existing experimental approaches are summarized, along with their main limitations. The second part reviews various models for assessing fiber and matrix debonding. A chronological presentation is adopted, focusing on the current approach. Alongside the presentation of the models, their main limitations and questions are also reviewed.

- Chapter III: A comprehensive description of the experimental campaign is given in this chapter, focusing on the characterization of the fiber-matrix debonding process. The sample configurations, ranging from single- to double-fiber composites, are presented, together with the manufacturing procedure. Overall, experimental set-up and methods are developed to monitor the debonding initiation and propagation at the fiber-matrix interface using both front and side observations. The debonding characteristics are measured and debonding shapes can then be derived as a function of the remote loading. These results will serve as a basis for further numerical studies.

- Chapter IV: Numerical simulations of the fiber-matrix debonding are assessed in order to predict debonding initiation and propagation. This is used to set-up a method for the inverse identification of fiber-matrix fracture properties. 2D and 3D modelings are considered so as to evaluate the influence of the free surface singularity at the fiber-matrix interface. Two modeling approaches, namely the Coupled Criterion (CC) and Cohesize Zone Models (CZM) are implemented and compared.

- Chapter V: The influence of a neighboring fiber on fiber-matrix debonding initiation and propagation is assessed numerically. A method for optimal initiation crack shape determination is proposed to implement the CC in case of asymmetric stress and energy fields. Debonding initiation in two-fiber specimen obtained by means of the CC or CZM is compared to experiments.

- Chapter VI: A focus on 3D modeling of debonding initiation using the CC is made with an emphasize on 3D optimal crack shape determination. Optimal shape determination is achieved by minimizing the crack initiation loading. These optimal shapes are compared with those determined experimentally and to stress isocontours-based 3D crack shapes. Interface fracture properties are identified on the basis of the stress-isocontours-based and optimal shapes.

- Chapter VII: The last chapter naturally draws the conclusions and perspectives to this thesis work.

CHAPTER I

The role of the fiber-matrix interface

Content

I.1 History of composites

Composite materials, commonly known as *composites*, are commonly defined as the fourth category of materials after the classic metals, ceramics and polymers. Several definitions exist to describe this category of materials. One generally accepted definition is that a composite is an assembly of two or more immiscible constituents that results in larger *performance* than the constituents themselves [Ber12]. The term *performance* can be, for instance, understood as an improvement in stiffness or strength, as well as a reduction in density or resistivity. The properties of composite materials therefore depend on: i) the properties of the constituents and ii) their relative content, iii) the structure, which depends on the scale, and iv) the interface between the constituents.

Despite human's major influence in the development of composites, nature has been making use of these materials for millions of years. For instance, wood is an astonishing creation of nature. Trees in general are capable of withstanding great stress without being damaged. Because of its heterogeneous structure, made up mostly of cellulose, hemicellulose and lignin [NR12], wood has high mechanical properties in relation to its mass, *i.e.*, high specific stiffness [Arr+23; Ash16]. All the constituents form cells aligned in the direction of the tree's growth, resulting in highly anisotropic mechanical properties [Din75]. As a consequence, the mechanical properties in the longitudinal direction of the cells are around ten times greater than those in the perpendicular, transverse directions. Additionally, the overall strength of wood is improved because its damage processes involve several mechanisms such as crack deflection, crack arrest and cellulose fiber breakage. All of the above mechanisms result in greater energy consumption during fracture, which translates into greater overall strength.

Another question might be: how can we obtain a material that is both strong and tough? Ceramic materials are known for their brittleness and sudden breakage. Nature has come up with nacre, a lamellar composite structure composed of aragonite platelets and several layers of biomolecules [Cur77]. Nacre therefore offers increased toughness compared to aragonite itself, but the overall stiffness remains equivalent [Bar+06]. The increased toughness results from several damage mechanisms such as crack deflection, crack branching and surface friction, as the layers are relatively soft, allowing greater energy dissipation at fracture. In this regard, attempts have been made to reproduce this type of composite using alumina platelets within a glass phase [Bou+14].

Modern composites are more commonly known as bi-component materials made up of a matrix, *i.e.*, a soft component, and a reinforcement, *i.e.*, a stiff component. This new definition of composites emerged recently, in the 20^{th} century, with the advent of Glass Fiber Reinforced Polymers (GFRP) and the long fiber composites. However, composite materials have been used by human for thousands of years.

The concept of relative importance, introduced by Mike F. Ashby in 1987 [Ash87] and represented schematically in Figure I.1, translates the importance of one category of materials relative to others for mechanical and civil engineering applications over the years. The chronology emphasizes the early appearance of the composite application 3000 BC with the mud brick reinforced with straw. The Mesopotamian civilization was the first to use composite materials for construction [Hna20]. At that time, mud bricks were mainly used for building construction because of their availability. The mud was first shaped and dried in the sun before being used. However, this material was very vulnerable to cracking, particularly during drying due to shrinkage effects. The mud bricks were therefore reinforced with randomly distributed straws to improve their resistance to crack appearance. The addition of straw improved the

overall properties of the bricks, and composite materials were born.

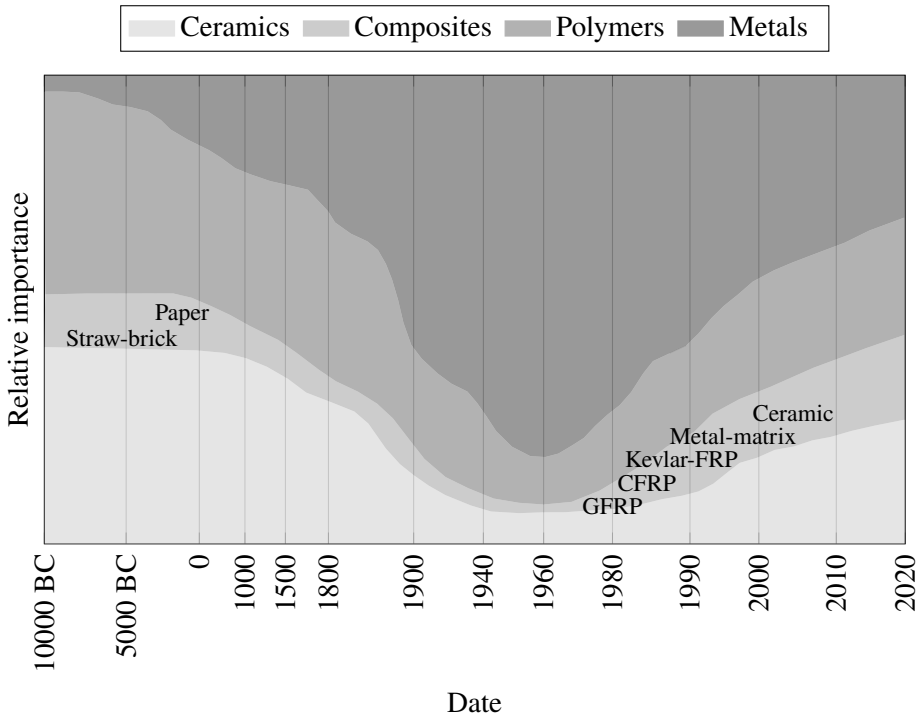

Figure I.1 – Evolution of the *relative importance* of the four main categories of materials as introduced by Mike Ashby in his book entitled "*Technology of the 1990s: advanced materials and predictive design*" [Ash87].

Papyrus is another early composite. Both a plant species and a writing material, papyrus was first used by the Egyptian civilization because of its availability in the Nile delta to produce writing materials. Papyrus was harvested for its stalk, from which the central pith was extracted and cut into thin layers. The layers were then pressed together in two different directions to remove the water, and dried to produce a smooth, fine writing surface [Bau+22]. The action of the water causes the cellular structure to transform into a paste that bonds the layers together [All96].

Going back to Figure I.1, the relative importance of composite materials then declined in relation to metal and other material categories from the year 0 until the industrial revolution. In the 1930s, the discovery of new polymers, such as polyester and epoxies, with improved mechanical properties [JK73], opened up new possibilities as uncured to cured materials for embedding discontinuous reinforcements. Games Slayter, an American engineer, developed Glass Fiber (GF), which marked the beginning of the modern era of composites. The use of very thin, aligned glass

fibers, combined with a newly developed polymer, made it possible to obtain interesting mechanical properties for composites. Thirty years later, Carbon Fiber (CF) brought high mechanical properties to composites, enabling new high-performance applications such as aeronautics. The development of new technologies has enabled the creation of metallic and ceramic composites offering relevant properties in terms of thermal resistance for engine application for instance. Over the years, the overall cost of composites has fallen as applications have increased. Professor Mike Ashby stated in 1980 that: *We are just now in the middle of another revolution, a transition from the steel age to one dependent on other, more advanced, materials* underlining the essential aspect of composites in the overall development of industry and, more generally, of the mankind.

I.2 Modern composite materials

According to the previous definition of composite materials, many common materials can be considered as such, *e.g.*, paper, reinforced rubber, concrete. All the materials mentioned above contain a discontinuous phase within a continuous phase, which differentiates them from hybrid materials, which generally combine two continuous phases. To define a composite material precisely, other characteristics than constituent nature need to be taken into account. Especially, the reinforcement is one of the main characteristic to describe a composite. It can be characterized by its shape and size, usually described by an aspect ratio for elongated regular objects, but also by its orientation and concentration. Concentration is generally referred to as volume or mass fraction. For example, a volume fraction of 1 corresponds to a fully reinforced material and *vice versa*. On the basis of the above statements, modern composite materials can be classified according to: i) the shape of the reinforcement, ii) the nature of the constituents, iii) their spatial arrangement and iv) the phase content.

On the one hand, reinforcement shapes are often either particles or fibers. Particle-reinforced composites are increasingly employed in many industrial applications as they offer improved properties compared to pure matrices, such as increased stiffness, toughness, or reduced shrinkage effects. However, in most applications, particles are employed to reduce costs without inducing any loss of properties [Ber12]. Fiber Reinforced Polymers (FRP) can be divided into two categories: continuous (long) and discontinuous (short) fibers. In either case, fiber orientation drives the composite properties, leading to different degrees of anisotropy. Such *on-demand* materials are useful for industrial applications since the material behavior can be adapted to meet specific requirements. Among all the types of fiber available, glass and carbon fibers are the most common, not to forget the emerging natural ones.

On the other hand, composite materials can be described by the nature of the ma-

trix. There are three main categories of matrices employed nowadays: organic, metallic, and ceramic. So far, organic matrices are the most commonly used because their manufacturing is simpler and less expensive. However, ceramic and metallic matrices are capable of withstanding high-temperature conditions (> 200°C), unlike organic matrices. Among organic matrices, thermoset matrices remain the most widely used because they are easier to manufacture than the emerging thermoplastic matrices.

When dealing with weight reduction in industrial design, it is certain that composites will be one of the potential solutions to the problem. Furthermore, the global mass market for composite materials primarily uses long fiber composites with organic matrices due to their overall great properties. Thus, these composites require thorough characterization for the optimization of their properties. These properties are highly dependent on the scale studied and can be divided into either elastic properties or fracture properties. Elastic properties refer to the overall stiffness of the composite, while fracture properties refer to the stress state at which damages are likely to occur and the energy per unit surface dissipated due to fracture. Composite elastic moduli in both longitudinal and transverse directions of a unidirectional composite can be approximated using Voigt [Voi89] and Reuss [Reu29] bounds, respectively. The Voigt bound considers the composite elastic behavior as two parallel springs replicating the matrix and fiber responses. Strain is uniform within the composite constituents, while the stress varies. The longitudinal, *i.e.*, fiber direction, elastic modulus E_l can be evaluated using Equation (I.1), where the latter varies linearly with the fiber volume fraction V_f (see Figure I.2) and is mainly controlled by the fiber elastic modulus E_f.

$$E_\mathrm{l} = V_\mathrm{f} E_\mathrm{f} + V_\mathrm{m} E_\mathrm{m} \qquad \text{(I.1)}$$

$$\frac{1}{E_\mathrm{t}} = \frac{V_\mathrm{f}}{E_\mathrm{f}} + \frac{V_\mathrm{m}}{E_\mathrm{m}} \qquad \text{(I.2)}$$

$$V_\mathrm{f} + V_\mathrm{m} = 1 \qquad \text{(I.3)}$$

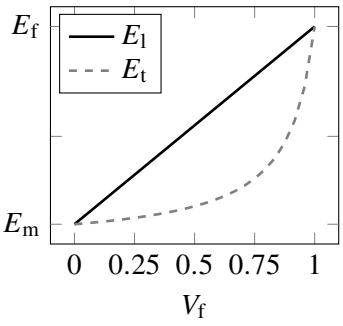

Figure I.2 – Reuss (E_t) and Voigt (E_l) elastic moduli as a function of the fiber volume fraction.

On the other hand, the Reuss bound describes the transverse elastic behavior of the composite, where springs in series are considered. The stress is, therefore, uni-

form, contrary to the strain. The transverse elastic modulus E_t can be described by the relationship in Equation (I.2), where matrix elastic modulus E_m has a major influence, and the inverse of the transverse modulus varies linearly with the matrix volume fraction V_m.

While the elastic properties of composites are crucial to the design of relevant industrial parts, the fracture properties are as important. The following section outlines the importance of fracture properties in composites, in particular the key role of the fiber-matrix interface.

I.3 Scale of the study and corresponding damage mechanisms

Composite material damages are challenging to predict since their heterogeneous structure involves several length scales. Figure I.3 shows the different scales commonly used to describe composite structure.

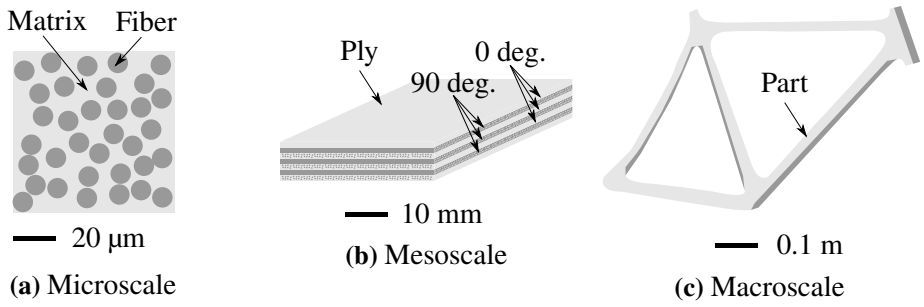

(a) Microscale **(b)** Mesoscale **(c)** Macroscale

Figure I.3 – Different scales involved in long fiber composite material from the micrometer to meter.

Figure I.3a shows the microscopic scale at which the fiber and matrix can be distinguished, with the typical unit of measurement being the micrometer (µm). This scale usually implies homogeneous and isotropic properties for both the fibers and matrix. It is worth noting that some fibers, such as carbon fiber, exhibit anisotropic properties [SNN20]. The mesoscale (Figure I.3b) considers the clustering of multiple fibers within the matrix that make up the composite ply. Therefore, at the mesoscale, properties remain homogeneous within the same ply, but the orientation of the fibers generates anisotropic properties. Therefore, each ply exhibits the same anisotropic properties in its local orientation, while the overall properties of the composite depend on the orientation of each ply with respect to the composite global coordinate system. Finally, the macroscale (Figure I.3c) is characterized by the dimensions of the actual

structure, where the composite material can be considered homogeneous, potentially exhibiting anisotropic properties.

It is worth mentioning that the damage mechanisms occurring at each scale are correlated with one another. The damage process in composite materials is commonly considered as follows, according to several authors [ST12; JPL13]: i) fiber-matrix interface debonding, ii) propagation of fiber-matrix debonding, potentially kinking into the adjacent matrix and creating microcracks, iii) coalescence of such microcracks within the ply, potentially resulting in larger damages, such as iv) fiber breakage and ply delamination, and finally, v) the global composite failure. The fiber-matrix interface is, therefore, crucial for the overall fracture properties of the composite, as this phenomenon drives damage initiation and load transfer. Each type of damage occurs at a specific scale; for instance, fiber-matrix debonding, microcracks, and fiber breakage are characteristic of the microscale, while delamination typically occurs at the mesoscale finally. Composite failure is a macroscopic event.

Figure I.4 shows a Scanning Electron Microscopy (SEM) observation of a damaged composite microstructure (glass fiber/epoxy) loaded transversely, illustrating the microscale damage process where debonding and microcracks can be observed.

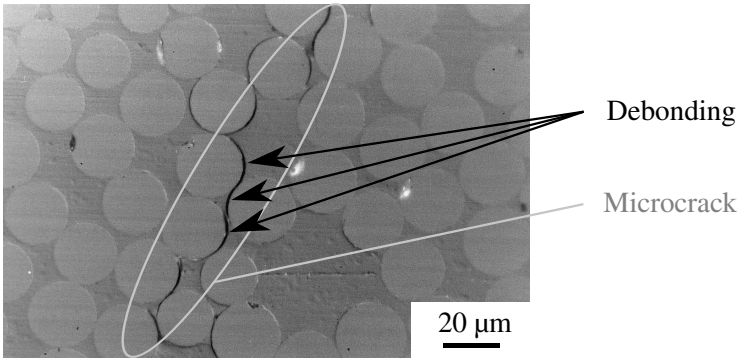

Figure I.4 – SEM observation of the debondings and associated microcracks coalescence leading to larger transversal cracking within the ply extracted from [GS99].

Since the fiber-matrix interface is observed as a preferential site for damage initiation, further investigations are conducted in the sequel.

I.4 The role of fiber-matrix interface properties in the overall response

Based on the aforementioned experimental observations, optimizing and controlling the interface is crucial when designing a composite part to meet specific demands.

So far, the damage process can lead to either a progressive failure, as previously described, or a more sudden one. The work of fracture resulting from a progressive damage process, weak fiber-matrix interface, allows the composite to undergo further damage after its initiation, possibly permitting detection before complete failure. Conversely, a strong fiber-matrix interface enables the composite part to withstand greater loads before being damaged. Nevertheless, such damage may be catastrophic and could result in a sudden and complete failure of the entire composite part. Such differences in the damage process can be attributed to the fiber-matrix interfacial fracture properties.

For instance, when a blunted crack occurs within an unidirectional composite loaded longitudinally (see Figure I.5a), it is potentially caused by porosity or a previous debonding, resulting in a stress intensification, *i.e.*, a singularity, at the crack tip (as seen in the variation of σ_{yy} at the blunted crack tip vicinity in Figure I.5b). The singularity facilitates the propagation of the blunted crack in the opening mode, perpendicularly to the loading direction. Such configuration implies a second singularity that acts ahead of the crack tip in the direction of crack propagation, as emphasized by the variation in σ_{xx} in Figure I.5b. As the blunted crack approaches a potential fiber, it and its associated second singularity will generate local tension loading at the fiber-matrix interface. This could potentially lead to the initiation of early debonding before the main crack reaches the fiber-matrix interface, as shown in Figure I.5c. This phenomenon is known as the Cook and Gordon effect [CG64].

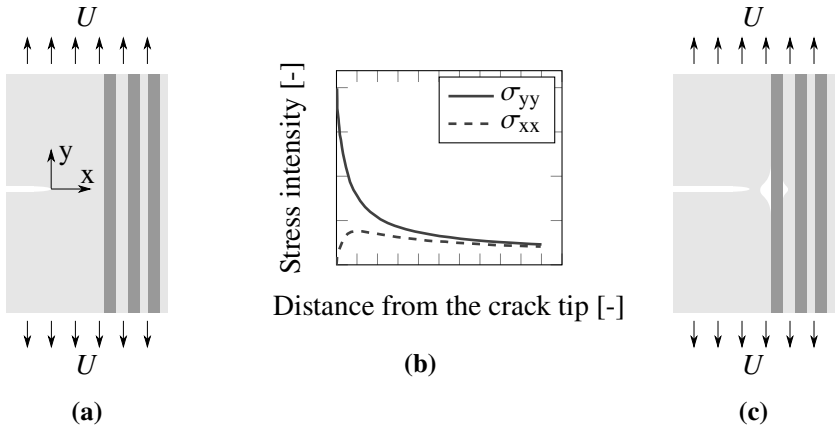

Figure I.5 – (a) Cook and Gordon effect schematic representation with a weak fiber (dark gray) -matrix (light gray) interface ahead of an elliptic crack tip solicited under mode I. (b) Variation of both longitudinal and traversal stresses ahead of the crack tip, from [CG64]. (c) Debonding initiation at the fiber-matrix interface located ahead of the main crack due to local tension stress.

Based on the Cook and Gordon effect, two distinct fracture processes can be encountered. On one hand, the fiber-matrix interface possesses relatively strong fracture properties compared to the fiber. In this configuration, the tensile stress induced by the crack is not sufficient to initiate debonding at the interface. Therefore, the more favorable scenario for the crack is to propagate and penetrate the fiber, as shown in Figure I.6a. This configuration may lead to sudden failure since the crack will no longer be arrested by any obstacle. On the other hand, when the interface is relatively weak compared to the fiber, debonding may be initiated due to either tensile or shear stresses, or both, depending on the opening and shear properties. The crack is consequently trapped at the interface because the most favorable scenario is to propagate along the interface. This scenario results in a larger work of fracture, as additional surfaces are released compared to the first scenario and frictional effects occur at the interface, as shown in Figure I.6b.

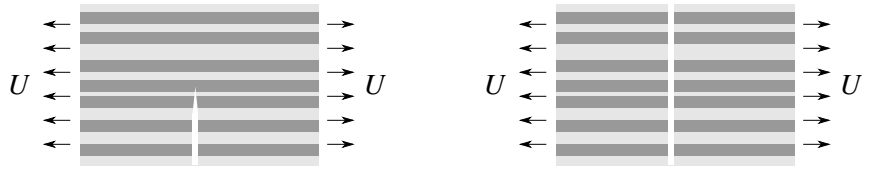

(a) Strong interface

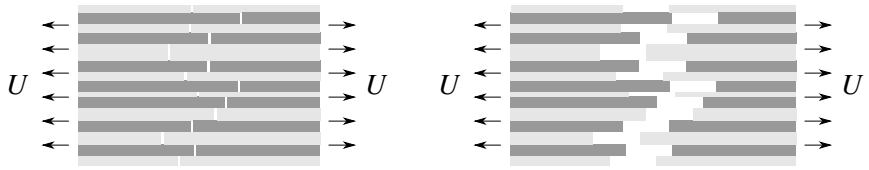

(b) Weak interface

Figure I.6 – Schematic representation of both damage processes of crack growth through long fibers (dark gray) and matrix (light gray) under longitudinal remote imposed displacement (U). (a) Straight crack propagation trough the composite caused by strong interface fracture properties. (b) Deviated crack propagation caused by the weak interface fracture properties.

Despite the key role of the interface in longitudinally loaded composites, damage initiation in transversely loaded composites, as shown in Figure I.4, is even more triggered by the strengths of the fiber and matrix and associated interface [MD91]. In such a configuration, interfaces are further loaded since the fiber, matrix and fiber-matrix interface carry equal load. Additionally, the latter loading is enhanced because stress concentrations appear at the interface due to the mismatch in elastic properties between the fiber and matrix. The stress fields acting at a spherical inclusion interface within an infinite medium can be addressed using the solution presented in [Goo33;

Man09]. The stress intensification is particularly pronounced at the specimen center and even more so at the free surfaces, where stress theoretically tends toward an infinite value. Moreover, neighboring fibers play a major role in intensifying the stress fields close to the interface, creating areas of highly localized stress concentration [LK22], which lead to preferential sites for debonding and microcracks. The overall transversal strength of the composite will, therefore, be even more controlled by the interface strength compared to the longitudinal strength.

Figure I.7 illustrates two different damage scenarios of transversely loaded composite damage, whether a weak or strong interface is considered. When the fiber-matrix interface is relatively strong (Figure I.7a), an existing crack emanating from a potential pre-existing defect or porosity will not be deflected by the fiber-matrix interface, resulting in a straight crack path. Both the matrix and the fiber are penetrated, inducing a relatively small work of fracture, as presented in longitudinally loaded composites. On the contrary, a weak interface (Figure I.7b) provokes the crack to deviate from its pure opening mode propagation. Such a scenario induces a larger work of fracture and a less sudden failure of the composite but at a smaller loading intensity. Moreover, the crack transitions from debonding to matrix cracking.

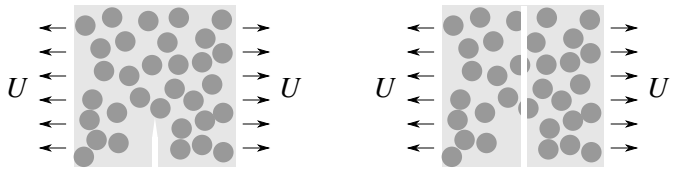

(a) Strong interface

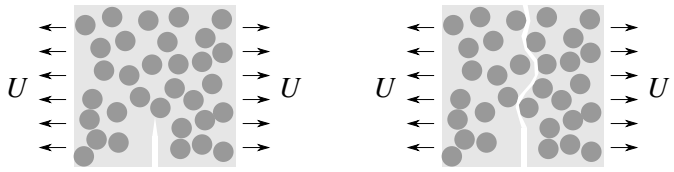

(b) Weak interface

Figure I.7 – Schematic representation of two damage processes of transversely loaded composite. (a) Straight crack propagation trough the composite caused by strong interface fracture properties. (b) Deviated crack propagation caused by transition from debonding to matrix microcracking.

The strengths of the fiber, matrix, and fiber-matrix interface are, therefore, key parameters in initiating the damage process within the associated loading range. These previous hypotheses can be corroborated by different experimental observations presented in the sequel.

I.5 Experimental evidence of the role of fiber-matrix interface properties

I.5.1 Influence on the damage mechanism

Hogg has studied the influence of both stress and an acidic environment on the failure of GFRP [Hog90], particularly on the damage mechanisms involved. No degradation of the composite behavior occurs when it is subjected solely to an acidic environment. However, several catastrophic industrial failures of GFRP under acidic environments were observed, marked by particularly sharp and sudden failures. Stress corrosion crack growth is characterized by the straightness and sharpness of the crack and the flat, stepped nature of the fracture surface, which differs from the fracture surface observed in an air environment.

Figure I.8 shows two different fracture surfaces of a unidirectional glass fiber composite tested under long-term exposure to acid and in air.

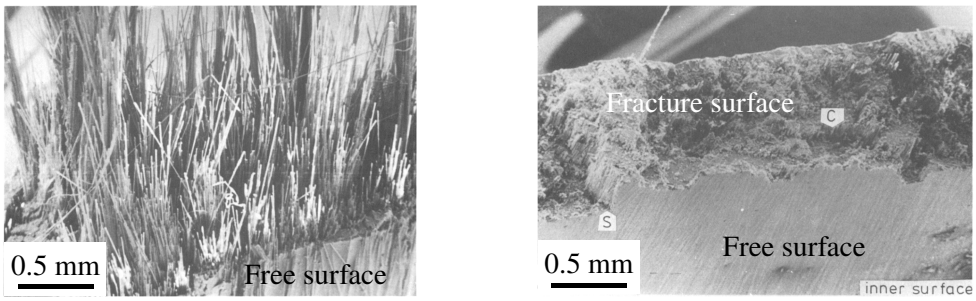

(a) Air environment **(b)** Acidic environment

Figure I.8 – SEM observations of fracture surfaces of unidirectional glass fiber composite tested (a) in air under monotonic loading and (b) under long-term exposure to acid under constant loading, both extracted from [Hog90].

It was shown in [SM66] that acid has a strong negative effect on the glass fiber strength in the vicinity of flaws under stress. As explained by the Cook and Gordon effect (see Section I.4), a pre-existing crack in a unidirectional composite loaded in the fiber direction can propagate either by penetrating the fiber or by initiating debonding at the interface. Thus, there is a competition between these two phenomena, depending on both interface and fiber strengths. In an air environment (Figure I.8a), larger loadings are required to propagate a crack. Since the interface strength is relatively weak compared to the strength of the fibers, this induces debonding and pull-out, which explains the *hairy* fracture surface. In an acid environment (Figure I.8b), cracks propagate at lower loads. Since the fiber strength is much smaller in such an environ-

ment, the stress concentration at the crack tip is sufficient to break the fiber but not to induce debonding. As a consequence, a straight crack surface is observed with no cracks deviation. Similar fiber or interface properties influence on the fracture surface were observed in [BBB73], [MD91], [Jan92].

While most of the configurations mentioned earlier primarily involve tensile loading, it is important to note that interface properties also significantly influence the damage process in composite specimens subjected to compression. Madhukar and Drzal [MD92] conducted a study examining the influence of fiber-matrix interface strength in longitudinally compressed graphite/epoxy composites. They tested three types of fibers: one untreated and two with different treatments, which resulted in varying levels of Interfacial Shear Strength (IFSS). Figure I.9 shows the different fracture surfaces and the corresponding schematic failure process associated with these different samples.

SEM observation of the fracture surface of the low IFSS sample is shown in Figure I.9a, where delamination coupled with fiber buckling are observed, evident from the presence of bent fibers. The notable separation of fibers from the matrix can be attributed to the low interfacial properties. In essence, the fibers and matrix easily separate, leading to significant fiber bending and consequent buckling. Increasing the IFSS results in a different type of fracture, as shown in Figure I.9b, where localized microbuckling becomes apparent. In contrast to the random localization of microbucklings on the low IFSS fracture surface, these bucklings now cluster in broken fibers of uniform length, indicating that fracture occurs in the region of maximum shear. Despite interfacial debonding, groups of fibers in this configuration remain united within the cluster, suggesting a stronger interfacial adhesion. With a high IFSS, the material fails along a single plane where the compressive strength of the fibers is reached. Weak zones in the matrix or interface cause slight deviations in the cracks, resulting in the stepped surface observed in Figure I.9c. Notably, most of the fibers remain together in this scenario, emphasizing the relatively good strength of the interface, as the crack remains within the transverse plane.

In general, most experimental studies have noted the transition from an interface-induced fracture process to a matrix/fiber-induced one as interfacial strength increases. The primary change in the failure process and surface characteristics observed is either the absence of residual matrix at the fiber-matrix interface (in cases of low properties) or microcracking and failure of the matrix/fiber, organized in a relatively straight plane (in cases of strong properties), as demonstrated in the research conducted by [Igl+02; DM93], for example.

These experimental observations highlight the significant influence of interface properties on the fracture process of composite materials. Consequently, interfacial properties play a crucial role in controlling the mechanical properties and strengths of composites.

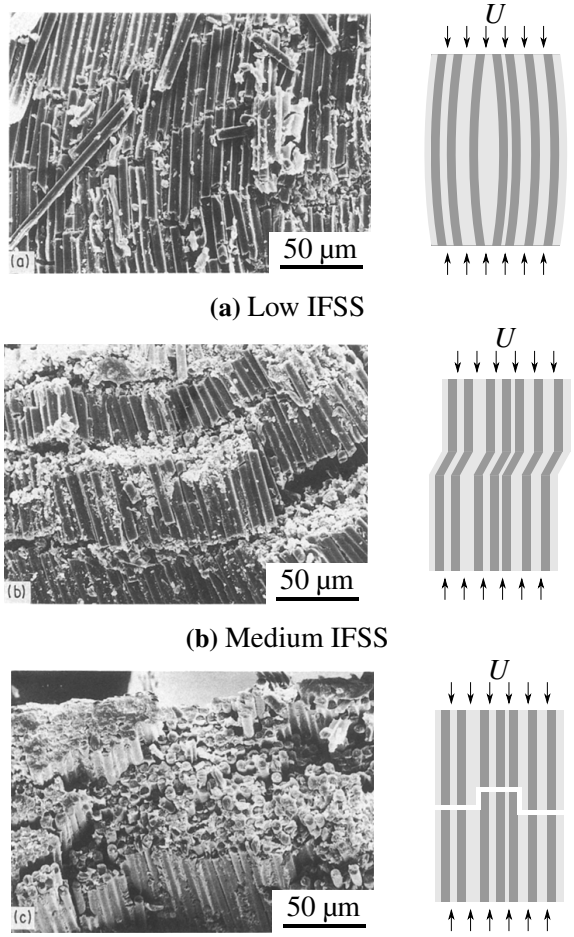

Figure I.9 – SEM observation of fracture surfaces of compressed composite samples (left) with associated schematic of the failure mechanism (right) for fiber-matrix interface with (a) low IFSS exhibiting delamination, (b) medium IFSS exhibiting fiber microbuckling and (c) high IFSS exhibiting compressive failure in several planes, reproduced from [DM93].

I.5.2 Influence on the overall composite strength

Some studies aimed at understanding the influence of interfacial properties on both the mechanical properties and specifically the strength of unidirectional composites. One might think that the elastic moduli of the composite depend only on the fiber and matrix, which can be computed using a rule of mixture, see Equation (I.1) and

Equation (I.2). Additionally, the transverse direction is known to be significantly influenced by the interfacial properties, while the longitudinal properties will remain unaffected. With this hypothesis in mind, Drzal and Madhukar [DM93] proposed a very detailed review of the role of interfacial properties in both longitudinal and transverse directions of carbon fiber/epoxy samples. The authors conducted tensile tests in both directions to evaluate elastic moduli and ultimate strengths. Specifically, they analyzed variations in the longitudinal tangent modulus of the samples at different strain levels, highlighting distinct behaviors related to the crack process. Figure I.10 shows three distinct behaviors.

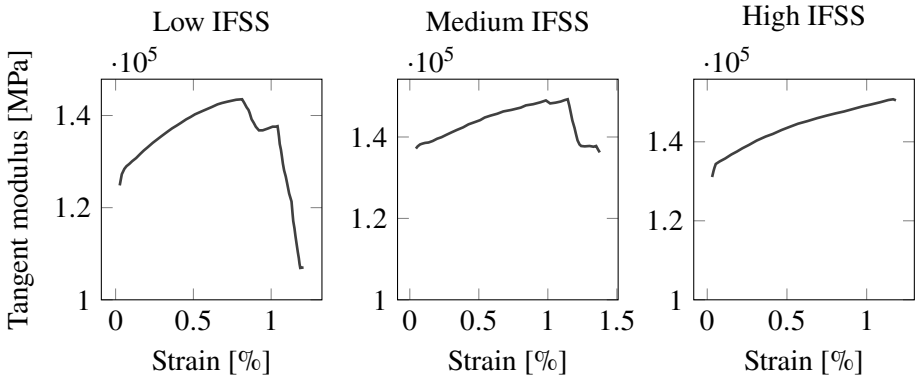

Figure I.10 – Influence of the interface properties on the variation of the longitudinal tangent modulus of unidirectional composites as a function of the strain, reproduced from [DM93].

The low IFSS sample exhibits a gradual failure accompanied by a reduction in the modulus (Figure I.10 left graph). This phenomenon can be attributed to a larger occurrence of localized damages, primarily due to weaker interface properties. In the case of the medium IFSS, there is a less noticeable decrease in the modulus, as different failure mechanisms come into play, with interfacial failure playing a less essential role (Figure I.10 center graph). Conversely, the high IFSS specimen demonstrates a steady increase in modulus until failure, showing no signs of degradation beforehand. This behavior might be linked to a sudden and relatively *damage-free* failure of the specimen (Figure I.10 right graph). It is worth noting that all these behaviors show almost linear variations in the modulus with strain, which could be explained by the alignment of the sample with respect to the loading direction.

When examining the influence of interface properties on elastic properties, only slight variations are observed. The moduli show little sensitivity to interfacial properties, remaining within the same order of magnitude considering measurement uncertainties. Conversely, strengths are more sensitive to interfacial properties, exhibit-

ing larger variations. Figure I.11 illustrates the changes in unidirectional composite strength under longitudinal and transverse loadings.

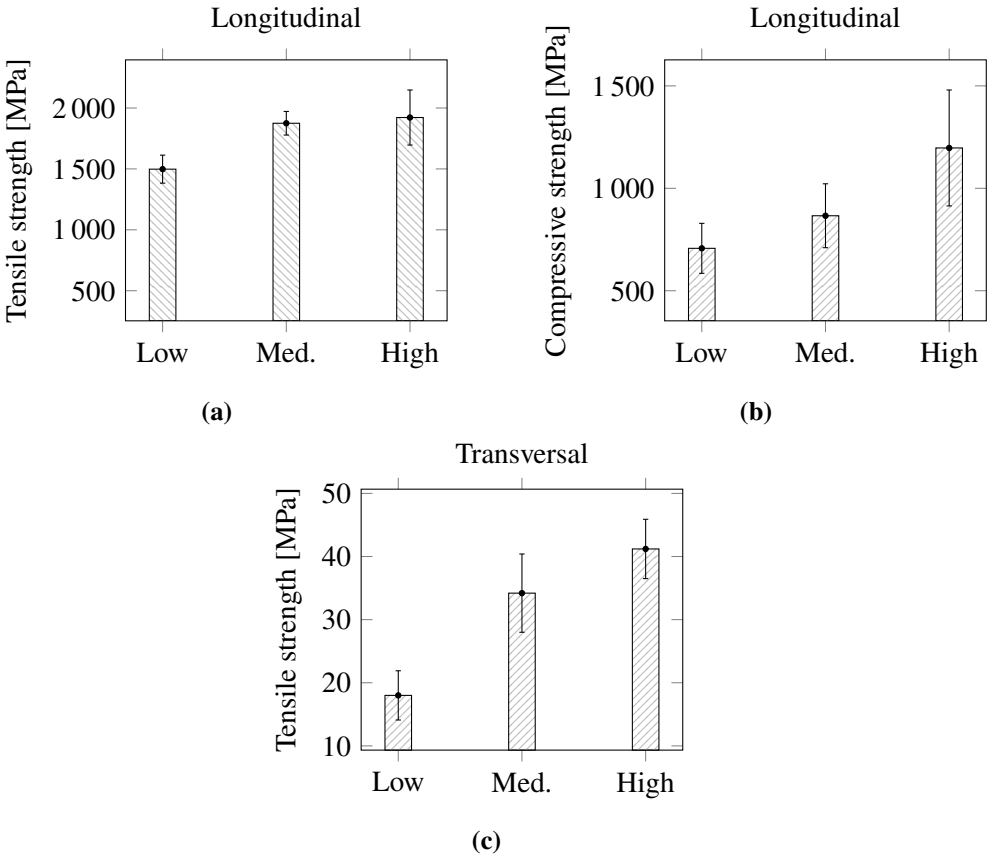

Figure I.11 – Comparison of the strengths obtained from the different interface properties, where low, med. (medium) and high refer to the IFSS, under (a) tensile - longitudinal loading, (b) compressive - longitudinal loading and (c) tensile - transversal loading, extracted from [DM93].

Longitudinal tensile strength shows a slight increase ($\simeq 25\%$) from low to medium IFSS (Figure I.11a), primarily due to a transition from interface-induced to matrix-induced damage. No significant strength change occurs at medium or high IFSS, suggesting a similar matrix cracking failure process. Increasing the IFSS does not lead to additional strength improvement in such loading configuration. Thus, interfacial properties seem to play a negligible role in longitudinal tensile strength. In contrast, transverse strength appears much more influenced by interfacial properties (Figure I.11c), with a nearly twofold increase from low to high IFSS. The primary

failure mode in transverse failure is debonding. A transition from debonding to matrix cracking also occurs, explaining the smaller difference between medium and high IFSS samples. Compressive strength similarly depends on interfacial properties and increases with larger IFSS (Figure I.11b). Different failure processes account for the variation in compressive strength, as discussed in Section I.4, ranging from delamination to stepped crack. It is worth mentioning that intralaminar shear properties are also of interest, where increasing IFSS implies greater shear strength. The same tendencies are observed in interlaminar failure, where fracture properties are enhanced, particularly the critical Energy Release Rate (ERR) in both mode I and II, denoted as G_{IC} and G_{IIC}, respectively.

Similar dependency on interfacial properties has been reported in [DY99] and [Jan92]. Specifically, Deng and Ye [DY99] varied both interfacial properties and fiber volume fraction. As expected, an increase in strength with a treated interface was noted, depending on the volume fraction. The strength was either damped or enhanced, with improved strength resulting from a larger volume fraction. This behavior was expected since a larger fiber volume fraction implied a larger area of contact between the fiber and matrix, making the composite more sensitive to the interfacial properties.

In summary, the fiber-matrix interface fracture properties have a significant influence on the fracture properties of the overall composite. Consequently, they require proper characterization in order to achieve specific fracture properties according to requirements. The following chapters are therefore devoted to the experimental characterization and modeling of the fiber matrix debonding process. In particular, Chapter II reviews existing experimental characterization approaches and their associated limitations. Existing modeling approaches are also detailed and several directions for improvement are reported and further addressed in the remaining chapters.

CHAPTER II

Characterization and modeling of the fiber-matrix interface

Content

The following state of the art chapter aims to define more precisely the fiber-matrix interface in composite material, as well as related aspects, such as experimental characterization or numerical modeling.

II.1 Definition of the interface and associated fracture properties

II.1.1 General definition

Defining the fiber-matrix interface is not straightforward from an experimental point of view, it depends on the observation scale in relation to the fiber dimension. The interface can be conceptualized either as a zero-thickness surface linking the fiber and the matrix or as a finite-thickness transition region. Few experimental observations have validated the existence of a region with a different structure near the fiber-matrix interface [Wil+90; Dow+00; Bog+99; KSW01]. This region is commonly referred to as the *interphase*, which can be described as an extension of the classical interface surface over a finite dimension where chemical, physical and mechanical properties differ from those of the bulk fiber and matrix [HD92].

Herrera-Franco and Drzal [HD92] schematically illustrated the interphase concept involving several characteristics such as potential sizing, fiber topology, or chemistry, see Figure II.1. The interface, thus, not only includes a distinct region of different properties but rather a transition region where constituents structure is locally modified resulting in a gradient of properties. In the following discussion, the *interphase* region will be referred to as the interface.

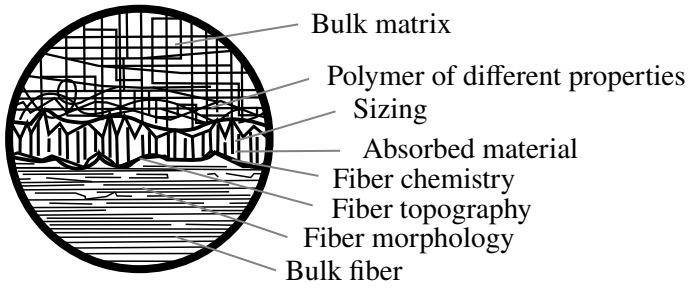

Figure II.1 – Different characteristics of the fiber-matrix interphase according to Herrera-Franco and Drzal [HD92].

II.1.2 Nature of the fiber-matrix adhesion

So far, the interface region properties are strongly governed by the chemical/morphological nature and the physical/thermodynamic compatibility between the fiber and the matrix according to Kim and May [KMM98]. Among the requirements for good adhesion, good wetting is one of the most important factors. Most commonly used composites require the impregnation of fibers by a liquid-phase matrix. Therefore,

dealing with liquid matrix processing requires optimal wetting of the fiber surfaces to achieve the optimum interface properties. The Young's relation [You05], as shown in Equation (II.1), describes the relationship between the surface energy at the contact point of three phases, *i.e.*, liquid, solid, and vapor. This relation ideally characterizes a composite impregnation process.

$$\gamma_{SV} = \gamma_{SL} + \gamma_{LV} \cos\theta_c \quad \text{(II.1)}$$

$$W_A = \gamma_{LV} (1 + \cos\theta_c) \quad \text{(II.2)}$$

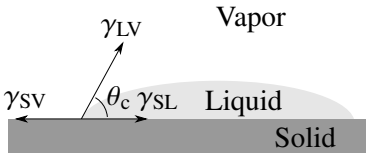

Figure II.2 – Example of liquid drop on a solid surface with the contact angle depending on the different surface energies.

The contact angle θ_c developed at the three-phase contact, as shown in Figure II.2, depends on the surface energies of solid-vapor γ_{SV}, solid-liquid γ_{SL}, and liquid-vapor γ_{LV}. Wetting or bad wetting is indicated by a contact angle θ_c smaller or larger than 90 degrees, respectively. Consequently, for proper wetting, the surface energy of the fiber γ_{SV} has to be larger than that of the matrix γ_{LV}. This leads to the Young-Dupré's relation, as shown in Equation (II.2), which relates the work of adhesion to the liquid surface energy and the contact angle. In fact, the adhesion work W_A reflects the energy gained by replacing the two free surfaces. As a result, the larger the wetting, the greater the work of adhesion formed by the physical bonds resulting from localized intermolecular forces, such as hydrogen bonds and van der Waals forces. This results in stronger fiber-matrix adhesion.

Contact angle measurement is an effective approach to determine the surface energy of a solid, and most of the method concept are reviewed by Neumann and Good in [NG79]. While determining the contact angle can be relatively straightforward on a flat surface, it becomes challenging on a cylindrical surface such as a fiber with a diameter of a few microns. Indeed, the surface energy of the fiber depends not only on intermolecular forces but also on the fiber surface topology, as explained by Good [Goo52]. Consequently, measuring the contact angle on the fiber surface provides the most accurate measurement of its free energy. One common method, as used in [KDM74; HD80; Gar+21], consists of immersing and removing one or a few fibers in a liquid of known surface tension γ_{LV}. Then, using the Wilhelmy relationship (Equation (II.3)), the contact angle can be calculated using the force F_r measured during the process and the fiber diameter d_f. Finally, the contact angle can be related to the fiber surface energy using the Owens and Wendt's [OW69] method and the Young-Laplace's equilibrium [You05].

$$F_r = \gamma_{LV} \pi d_f \cos\theta_c \tag{II.3}$$

It is noteworthy that other approaches are also employed to measure the fiber surface energy. For instance, some authors have proposed depositing a small drop of liquid on a fiber and, by observing the drop formed on the fiber surface, measuring the angle. Since most of the present thesis deals with the epoxy matrix and E-glass fiber, the surface energies for both constituents are summarized in Table II.1 and Table II.2.

Type	γ_{LV} [mJ/m^2]	Ref.
DGEBA	36.3	[PBM01]
TGMDA	41.4	[PBM01]
NPDGE	36.3	[LSB88]
DGEBA	38.8-42.0	[AH88]
DGEBA	40.0-46.0	[Foi84]

Table II.1 – Different uncured epoxy system surface energy from literature.

Type	γ_{SV} [mJ/m^2]	Ref.
untreated	33.5	[PJL00]
silane	38.8	[PJL00]

Table II.2 – E-glass fiber surface energy from literature.

Based on the previous relation regarding wetting, the surface energy of the glass fiber has to be larger than that of the uncured epoxy. However, previous authors have reported relatively similar surface energies between epoxy and glass fiber, where untreated glass fiber might not be wetted by the epoxy matrix. Surface treatment or topology improvement are therefore employed to increase surface energy. The untreated to treated glass fiber surface energies presented in Table II.2 confirm the relevance of such approaches. Although surface energy plays a strong role in achieving good adhesion, capillarity forces are not negligible in the case of few-micron fibers. Indeed, the impregnation of fiber tows requires good capillarity, which translates into having a small contact angle.

The rather small work of adhesion emanating from the physical bond formed at the interface is not the main actor in the final interface fracture properties since the resin still have to cure, despite it is generally correlated to the final properties (see Section II.1.3). Few other mechanisms and theories come into play after curing at the interface which are usually described as follow: i) mechanical interlocking, ii) electronic theories, iii) interphase, iv) adsorption , v) diffusion theory and vi) chemical bonding [SN03].

Mechanical interlocking involves the penetration of the matrix into fiber cavities, pores, and asperities to develop mechanical locking during curing or cooling, as observed in [MJ99], for instance. These mechanisms can be enhanced by controlling the fiber topology by creating asperities, or using surface treatments such as oxida-

tion [WJT20] or plasma treatment [Bag+16]. It is noteworthy that treated surfaces usually exhibit improved fracture properties.

Electronic theory explains the exchange of electrons at the interface vicinity between two media, forming a double electrical layer at the interface. The adhesive force can be described by the electrostatic force across the electrical double layer (see [DS67; Uem+23]). The final interface properties may not primarily result from this type of adhesion since the forces involved are relatively weak. However, these physical forces can enhance the wettability of the fiber surface, as observed in Wen *et al.* [Wen+22], achieved by spraying negative charges onto the fiber surface.

The adsorption mechanism encompasses all the mechanisms related to the aforementioned wetting, surface energies, and work of adhesion theories that take place at the interface between solid, liquid, and gas.

The diffusion process describes the interdiffusion of atoms and molecules across the interface. The interface strength depends on the molecular entanglement, strength between molecule and molecule length [KMM98]. Interface properties are, therefore, mainly related to the interpenetrating network formed at the interface. For instance, some authors have reported the influence of silane treated glass-fiber and the formation of a diffuse interface that couples both chemical bond and interpenetrating network. It has been shown that the transition region has different physical and mechanical properties [Dow+00; Bog+99], confirming the interphase theories where the interface is not an abrupt transition between two media. In particular, elastic properties were measured by nanoindentation in Williams *et al.* [Wil+90] and Kim *et al.* [KSW01]. Kim *et al.* demonstrated the existence of an interphase in the composite sample composed of glass fibers and vynilester matrix using nanoindentation and nanoscratch tests. Figure II.3a shows the indentation path used in [KSW01] to assess the interphase apparent stiffness and thickness, where several indentations were made every 400 nm from the matrix to the fiber. The apparent modulus is presented as a function of position in Figure II.3b and shows a transition zone between the matrix and the fiber, where the stiffness is intermediate between those of the other two components. In addition, the thickness of the interphase can be derived from the position of the indentations, where the thickness of the transition zone appears to be approximately 1.2 µm, corresponding to 13% of the nominal diameter of the fiber.

Some authors have observed that the actual stiffness of the interphase is less than that of the matrix and that the stiffness measured by microindentation is affected by the larger stiffness of the fibers, making it larger than it actually is. Williams *et al.* [Wil+90] used a shear lag approach which states that the displacement of the surface relative to the fiber surface should be linear as a function of distance from the fiber if the matrix has a constant modulus, and therefore deduced an appropriate interphase stiffness that best matched the experimental displacement. The interphase modulus obtained was about a quarter of that of the matrix used. The interphase thickness was

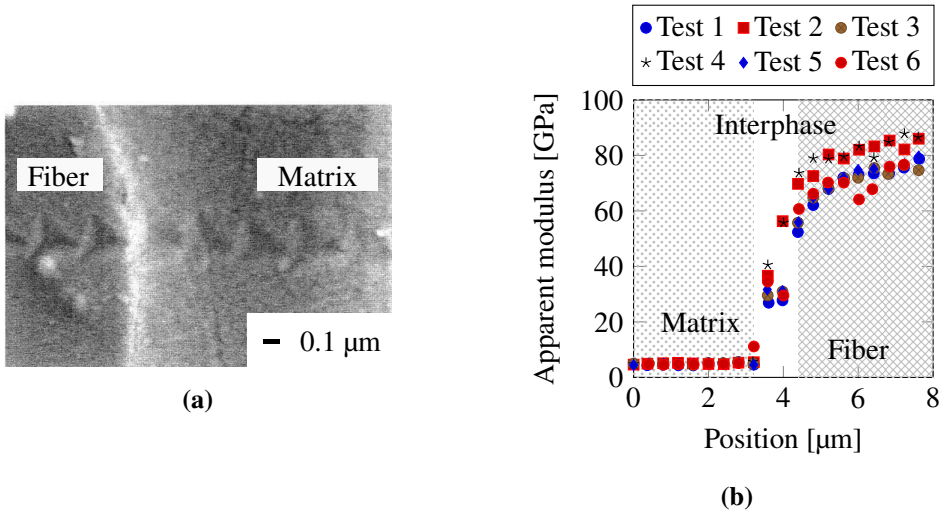

Figure II.3 – (a) SEM photography of the indent position used to assess the variation of the modulus across the interface and (b) corresponding apparent modulus value for several trials and a specific silane treatment referenced as M0.01 in [KSW01]. The different sets of markers correspond to the 6 independent tests.

also calculated using the same model and the thickness obtained was similar to that obtained by microindentation.

Finally, contrary to the adsorption theories and the physical bonds involved, chemical bonding theories are based on primary bonds, such as covalent bonds, which possess larger bonding energy. The typical bond energy of a covalent bond, for example, is on the order of 100 to 1000 kJ/mol, whereas those of van der Waals interactions and hydrogen bonds do not exceed 50 kJ/mol [SN03]. In such a mechanism of adhesion, primary bonds are formed between two compatible chemical groups located at either the fiber or matrix interface. Scola [Sco74] reported the chemical composition of both the bulk and the surface of E-glass and carbon fibers, which is detailed in Table II.3.

Fiber	Composition	Surface analysis	Probable functional group
E-glass	Si, O, Al, Ca, Mg, B, F, Fe, Na	S, O, Al	-Si-OH, -Si-O-Si
Carbon	C, O, N, H, metal impurities	C, O, H	-COOH, C-OH, C=O

Table II.3 – Chemical composition of E-glass and carbon fiber, after [Sco74].

Matrices are likely to form chemical bonds with groups of atoms located at the fiber surface. Pisanova et Mäder [PM00] explained the glass fiber-epoxy matrix adhesion by the opening of the epoxy rings to form chemical covalent bonds with the fiber. The influence of surface treatment on carbon fiber showed an increase in functional oxygen groups present at the fiber interface, where increasing exposure time results in a larger percentage of these groups, see [DSH96]. The authors stated that these oxygen groups can be both carboxylic acid and phenolic types, both of which can react with components of the epoxy matrix, forming chemical bonds. Similarly, Horie *et al.* [HHM76] demonstrated that the reaction between oxidized carbon fiber and epoxy could be attributed to strong covalent bonds resulting from either ether or ester bonds. The latter can be formed by the reaction between hydroxyl and carboxyl groups present at the fiber surface and the epoxy group of the resin.

II.1.3 Fiber-matrix interface fracture properties

The fracture properties of the fiber-matrix interface involve several of the adhesion mechanisms mentioned above. The fracture properties of the interface can no longer be associated with the work of adhesion W_A resulting from the separation of the two surfaces. In fact, it is difficult to quantify the work of adhesion because the loading required to separate the interface can cause the two components to deform. Therefore, the force required depends on the properties of the interface, its topology and the two materials involved. It is worth mentioning that failure can be adhesive, cohesive, within the interphase, or a combination of the three. Interface fracture can thus be regarded as the result of all these mechanisms. The work of fracture can therefore be determined by propagating an interface crack on the real configuration so that all the mechanisms can be taken into account. A critical stress intensify factor K_c [Irw57] or a critical energy release rate G_c [Gri21] can be derived from the loading applied for the crack to propagate.

The work of fracture therefore corresponds to the energy per unit surface released by the propagation of the crack. This work must be larger than the work of adhesion, but also sufficiently large to overcome the mechanisms involved by the interface and the mechanical loading, such as, *e.g.*, local plasticity, friction between the two lips of the crack, the vicinity of other cracks [Bra12]. The critical energy release rate (G_c) is then equivalent to the sum of the work of adhesion (W_A) and the work associated with other mechanisms (W_M), see Equation (II.4).

$$G_c = W_A + W_M \tag{II.4}$$

Interestingly, when comparing the work of adhesion with the critical energy release rate found in the literature, there is an order of magnitude difference, suggesting

that the work of adhesion plays a minor role in the final bond, whereas it is necessary to achieve adequate wetting. However, the values in Table II.1 correspond to uncured matrices system where W_A can vary with curing. For example, Koyanagi *et al.* [Koy+09] found G_c to be about 5.5 J/m^2, Varna *et al.* [VBE97] reported a value of around 2 J/m^2, both authors having studied glass fiber epoxy matrix configurations.

The properties of the fiber matrix interface have also been described in terms of critical strengths. This generally involves determining the stress state of the interface at debonding initiation. Such interface stress state can be either derived from numerical modeling or using analytical formula. For instance, Totten *et al.* [TKC16] coupled Finite Element (FE) calculation with experimental SEM observations to estimate local stress fields and deduce interfacial strengths. Ageorges *et al.* [Age+99], calculated the fiber-matrix interface strengths using an analytical formula for a single fiber sample subjected to compression. In a similar way, force balance provides the shear stress acting at the interface of an embedded fiber fragment loaded under longitudinal tension, which enables determining the IFSS τ_c or the Interfacial Friction Stress (IFS) τ_{fr}. The IFSS indicates the shear stress at debonding initiation, where the IFS describes the interface shear stress as the fiber slides through the matrix. Tensile strength σ_c can also be determined similarly by determining the tensile stress state at debonding initiation.

Similarly, some authors have found a relationship between fiber surface energy and the final fracture properties of the composite, where an increase in fiber surface energy led to enhanced Interlaminar Shear Strength (ILSS), see [Dil+95], or larger IFSS, see [Dai+11], both for carbon fiber/epoxy matrix. Gilbert *et al.* [GGM90] studied the influence of surface treatment on the surface energy of carbon fibers and the corresponding composite ILSS. The surface energies were calculated from the angle formed by a single droplet placed on the fiber, and the ILSS was determined using short beam shear tests. Figure II.4 shows the variation of the surface energy as a function of ILSS, indicating that an increase in surface energy corresponds to an increase in ILSS.

II.1.4 Dependence of fracture properties on the mode mixity

Assuming the intrinsic properties of the interface remain constant along a potential crack path, the critical ERR depends on whether the crack propagates in an opening or shear mode. Figure II.5 illustrates the different modes a crack can undergo. Mode I (Figure II.5a) corresponds to the tensile opening mode where the crack is loaded perpendicular to the crack propagation direction. Modes II (Figure II.5b) and III (Figure II.5c) correspond to respectively in-plane and out-of-plane shear. Critical ERR can therefore be divided into opening G_{IC} and shear G_{IIC} and G_{IIIC} critical ERR.

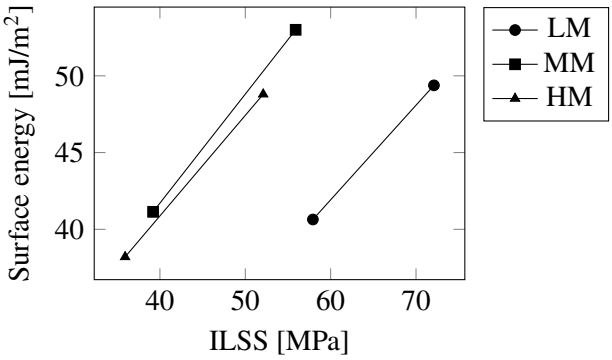

Figure II.4 – Surface energy as a function of composite ILSS for untreated and electrochemically treated fibers where LM, MM and HM refer to low, medium and high fiber modulus, respectively, see [GGM90].

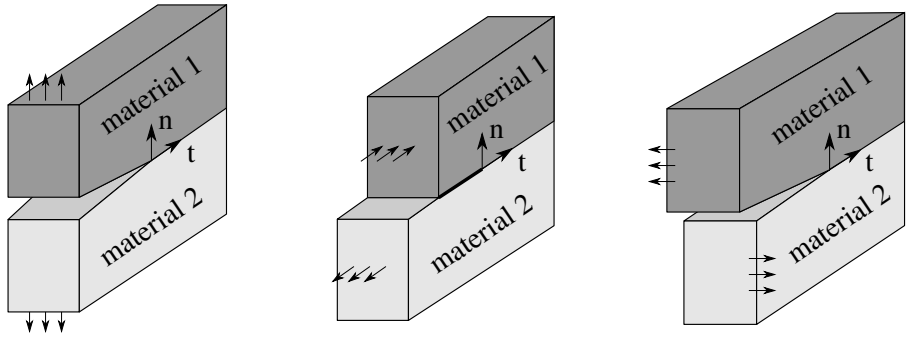

(a) Mode I **(b)** Mode II **(c)** Mode III

Figure II.5 – Different modes of fracture that a crack can undergo.

Indeed, in a homogeneous material, even under shear loading cracks are likely to propagate so that they retrieve a mode I-dominated loading, as the crack can orient itself to maximize the ERR. On the contrary, an interface crack usually propagates along the interface path, given that the fracture properties of the interface are smaller than those of the two materials involved. Another scenario is crack kinking out-of-the interface, which will not be herein studied. The crack is, therefore, trapped within the interface and no longer undergoes pure mode I propagation but rather a combination of two or more modes, characterized by the mode mixity angle ψ.

$$\psi = \arctan\left(\frac{|\sigma_{\mathrm{nt}}|}{\sigma_{\mathrm{nn}}}\right) \tag{II.5}$$

The mode mixity can be defined as the angle varying between 0 for pure mode I and $\pi/2$ for pure mode II loading when considering a 2D configuration. It can be calculated using Equation (II.5). The stress normal to the interface is denoted as σ_{nn}, while the shear component is denoted as σ_{nt}. Figure II.6a shows the variation of the critical ERR as a function of the mode mixity, where the latter varies between G_{IC} and G_{IIC}.

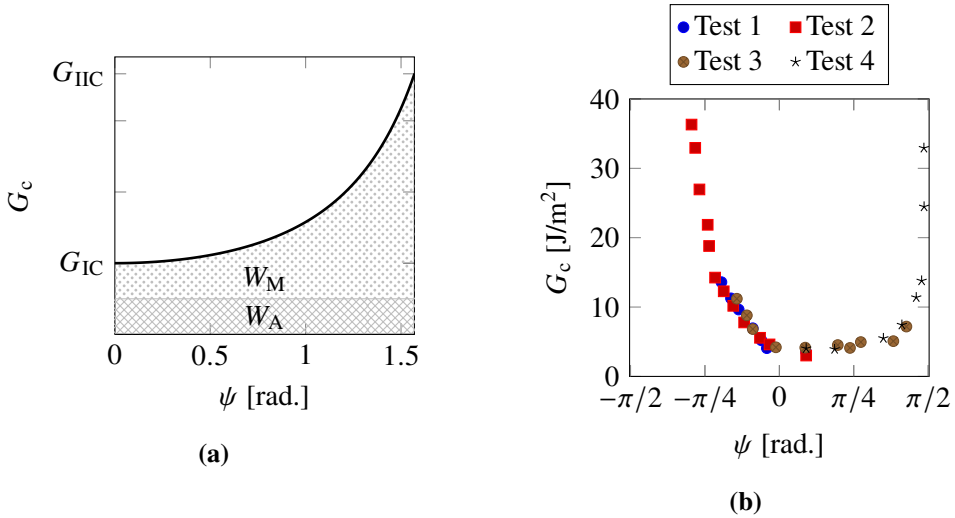

Figure II.6 – (a) Evolution of the critical ERR (G_c) as a function of the mode mixity (ψ) with decomposition of adhesion and other mechanisms, after [Bra12]. (b) Variation of the critical ERR as a function of the mode mixity for 4 different tests [LC92].

The critical ERR increases with mode mixity since the shear mode involves a larger influence of fracture mechanisms, such as friction between the two crack lips [Bra12]. The work of adhesion remains constant, while other fracture mechanisms are influenced by the mode mixity. It is commonly observed that G_{IIC} is larger than G_{IC} [LC92; Ara+22]. Such a phenomenon was observed experimentally by loading a similar interface configuration under different modes. Liechti and Chai [LC92] studied a single-edge crack on a bi-material sample, *i.e.*, a glass/epoxy sample, where several loading configurations were applied to vary the mode mixity at the interface. The authors were able to extract the loading imposed at the first interface crack propagation and therefore computed the critical ERR, as a function of the mode mixity. Figure II.6b shows the critical ERR as a function of the mode mixity, closely resembling what was proposed by Braccini [Bra12], where critical ERR increases with mode mixity. For $0 < \psi < \pi/4$, the critical ERR remains relatively independent of mode mixity, whereas for $-\pi/4 < \psi < 0$ and $\pi/4 < \psi < \pi/2$, the latter appears

to be strongly influenced by ψ. It should be noted that compression loading tends to enhance friction at the interface, resulting in a larger critical ERR for a similar ψ.

Similar experimental observations of the mode mixity influence were reported in [SLL02]. Also, Wang and Suo [WS90] found that an increase in mode mixity sometimes leads to crack branching out of the interface, even when it is not energetically favorable. This observation suggests that both the energy released by the crack and the local ERR must be considered simultaneously to study interface crack propagation. Such a statement is corroborated by the previous observation, whether a strong or weak fiber-matrix interface is considered, and by the competition between penetration and deviation when approaching the fiber-matrix interface. Martin [Mar12] proposes several explanations, introducing a deviation criteria by considering the critical ERR of the different constituents.

Similarly to a critical ERR that depends on the mode mixity, an equivalent stress can also be considered when the interface undergoes combined tensile and shear stresses. The equivalent stress σ_{eq}, coupling both tensile σ_{c} and shear strengths τ_{c}, can be described by a quadratic relationship as proposed in Martin *et al.* [Mar+20] to study debonding initiation at a spherical inclusion interface, see Equation (II.6). This formulation couples both tensile and shear stresses, where $\mu = \tau_{\text{c}}/\sigma_{\text{c}}$ denotes the corresponding strengths ratio.

$$\sigma_{\text{eq}} = \sqrt{\sigma_{\text{nn}}^2 + \frac{1}{\mu^2}\sigma_{\text{nt}}^2} \geq \sigma_{\text{c}} \tag{II.6}$$

For sufficiently large μ, the equivalent stress reverts to a pure tensile stress criterion. Similar equivalent stress was also employed by Muñoz-Reja *et al.* [Muñ+16a] to account for mode mixity. Slight variation of the latter equivalent stress was employed in Koyanagi *et al.* [Koy+09] with an additional condition when the interface undergoes compression, where coupled shear and frictional stresses are considered. Shear stress is enhanced by the increase in compressive stress. Figure II.7 shows the strength surface proposed in [Koy+09].

Despite the proposed equivalent stresses, no proper experimental formulation identification has been achieved to assess debonding at the fiber-matrix interface in the different numerical studies. To this end, Tandon *et al.* [TKB02] varied the degrees of shear and tensile stress at the interface using appropriate sample geometries. A micro-composite consisting of a SiC fiber in an epoxy matrix was studied. The authors were then able to assess interfacial shear and tensile stresses at debonding initiation and thus determine an experimental-based strength surface, which formulation is given in Equation (II.7).

$$c_2 = \sigma_{\text{nn}}^2 + c_1\sigma_{\text{nt}}^2 \tag{II.7}$$

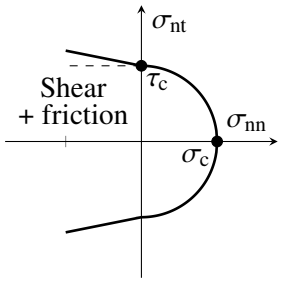

Figure II.7 – Strength surface used by Koyanagi *et al.* [Koy+09] to assess debonding at fiber-matrix interface using cohesive zone model.

The constant c_1 was identified as 1.5 by the authors based on the experimental results with a constant c_2 being equal to 1785 MPa^2.

II.1.5 Debonded or not debonded?

A binary vision of the damage state of a crack is not always suitable to describe the real configuration of damages present at the vicinity of the crack tip. Particularly, some authors found the presence of a transition zone from a partially to a totally damaged crack [EF84; HW92], *i.e.*, the plastic zone for the metal. This transition zone is usually called the *fracture process zone* for the interface. The fracture process zone is responsible for the increasing crack growth resistance [KMM98]. Although the evidence that a process zone develops at the fiber-matrix interface is not yet established, the microstructure of the composite involves several damage mechanisms, resulting in a larger-scale process zone (see Section I.3). Particularly, there is a partially damaged zone ahead of the crack tip, where debonding, matrix cracking and delamination occur. The crack, and its process zone, are in this case largely dependent on the composite microstructure parameters such as the fiber volume fraction, fiber aspect ratio, type of constituents, interface properties, layup sequence and angles, ply thickness, and loading configuration [KMM98]. For instance, several authors [TA12; SZG17; Kha19] observed fiber bridging during crack propagation tests on composites, where the mechanical properties gradually decrease, and the crack tip remains undefined. As a consequence, the stiffness in the crack vicinity can no longer be considered either identical to the bulk or non-existent, but rather as a decreasing one correlated to the damage state. The resulting stress state acting at the end of the damaged zone is, therefore, less than that of a crack without a process zone. Figure II.8 illustrates this typical fracture process on carbon fiber/epoxy sample, observed by Tamuzs *et al.* [TTV01], highlighting the different fracture processes involved and the corresponding characteristics. The authors performed a double cantilever beam test on a composite

to assess intralaminar crack propagation and associated G_{IC}. The authors described the stress variation along the crack path as a function of location and damage state, with the abscissa of the stress variation corresponding to the location of the crack path.

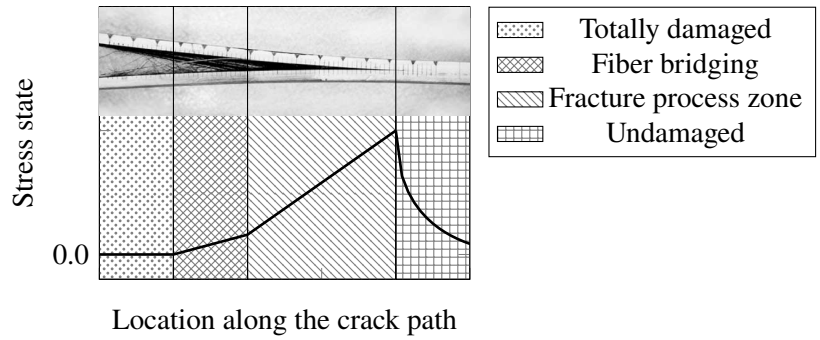

Figure II.8 – Illustration of fiber bridging and process zone during double cantilever beam test on composite sample and corresponding stress state along the crack path, from [TTV01].

To summarize, the fiber-matrix interface is a transition region between two components, and the resulting fracture properties depend on the bonding mechanisms formed between them. It is therefore difficult to distinguish the mechanisms responsible for failure, and the overall properties measured bring them all together. Various experimental approaches exist for their characterization and are further described in the sequel, along with the associated challenges and limitations.

II.2 Experimental characterization of fiber-matrix interface properties

Several experimental techniques exist to study the fiber-matrix interface and measure the intralaminar fracture properties. These techniques involve two different scales. Microcomposite characterization method employs a single fiber, usually embedded in a matrix, where fracture phenomena likely occur at the microscale. Interlaminar fracture properties are determined at the mesoscale when dealing with layup composites. For the sake of simplicity, and in line with the subject of the thesis, the following section will focus on the microcomposite tests only. However, more details about intralaminar characterization techniques can be found in [KZM95].

II.2.1 Experimental characterization of the interface properties

Microcomposite tests are the most widely used to characterize the properties of the fiber-matrix interface because they can be adapted to any types of fiber and matrix. These tests involve a variety of geometries. Herrera-Franco and Drzal [HD92] and Zhandarov and Mäder [ZM05] reviewed most of the microcomposite methods for measuring the fiber-matrix interface strengths, such as, *e.g.*, the tensile and shear strengths, σ_c and τ_c, respectively. Among the most common techniques are the multi-fragmentation test, the pull-out test and the fiber push test. Depending on the test, fracture properties can be characterized in terms of critical ERR G_c, IFSS τ_c or IFS τ_{fr}. In particular, existing methods can characterize either shear or tensile properties, with shear properties being the most widely used. The appropriate test can therefore be chosen according to a specific application.

It should be noted that these techniques are often used to compare the interfacial properties between different constituents and surface treatments. Indeed, because of the wide variation between laboratories, the measured properties cannot be taken as an absolute value of the fracture properties. Further details on scattering and the measurement solution are discussed at the end of this section.

II.2.2 Tensile characterization

Single fiber compression test

The single fiber compression test method involves subjecting a single embedded fiber to a longitudinal compressive loading where debonding is caused by the elastic mismatch between the fiber and the matrix. One of the first application of single fiber compression tests can be found in [Bro66]. Two different specimen geometries can be used, one leading to shear failure and the other to tensile failure. The two geometries are shown schematically in Figure II.9. The first geometry has a curved neck in the middle (Figure II.9a) and the second a long rectangular shape (Figure II.9b) with a uniform cross-section. When the sample is loaded, the elastic mismatch causes shear at both ends of the fiber. In contrast, the curved shape induces tensile loading, due to transverse expansion, at the interface which can cause the initiation of debonding. For both geometries, Broutman [Bro69] derived the local stress state at debonding initiation so that the interfacial tensile and shear strengths could be measured. Nowadays, FE inverse calculations are more appropriate for assessing such quantities.

Ageorges *et al.* [Age+99] used the curved geometry to determine an interfacial tensile strength σ_c, around 14 MPa for glass fiber/epoxy matrix configuration. The authors reported that, as a function of interfacial strength, there was competition between debonding, for a weak interface, and fiber compression failure, for a strong interface. Other authors [KMM98] have pointed out problems associated with this

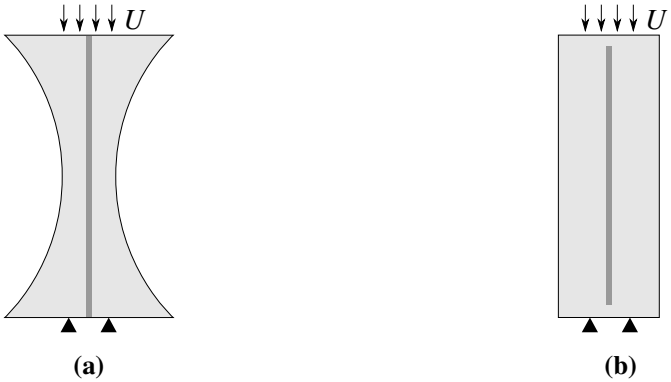

Figure II.9 – Sample geometries commonly used to perform single fiber compression test, one with curved side surfaces (a) and another with straight side surfaces (b).

characterization technique, such as the need for a transparent matrix and the requirement for perfect fiber alignment, which is difficult to achieve.

Single fiber tensile test

The single-fiber tensile test involves the transverse loading of a single embedded fiber. Due to the applied transverse loading, debonding is likely to occur in an opening mode which allows the interfacial tensile strength to be determined. Figure II.10 shows the two sample geometries commonly used.

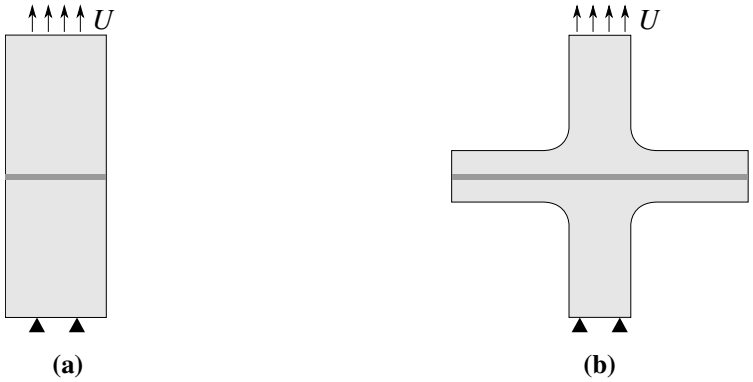

Figure II.10 – Sample geometries commonly used to perform single fiber tensile test, (a) the straight shape and (b) the cruciform shape.

The first geometry consists of a long rectangular shape with straight edges (see Figure II.10a), where debonding is likely to occur at the free surfaces due to elastic

mismatch. To overcome this free surface effect, some authors have proposed a cruciform geometry to remove the influence of the singularity and ensure that debonding occurs at the center of the sample (see Figure II.10b). Ogihara *et al.* [OSK09] compared glass fiber and epoxy matrix straight and cruciform samples to reveal the singularity at the free surface. Using a transparent matrix, the authors were able to extract the debonding length as a function of the remote stress. Figure II.11 shows the variation in debonding length for the two sample geometries, where debonding initiation occurs at a lower level of remote stress in the straight sample (σ^{∞} = 10 MPa, see round marker in Figure II.11) than in the cruciform sample (σ^{∞} = 30 MPa, see square marker in Figure II.11). Using the remote stress, the authors calculated that the tensile strength of the glass fiber/epoxy interface was around 31 MPa.

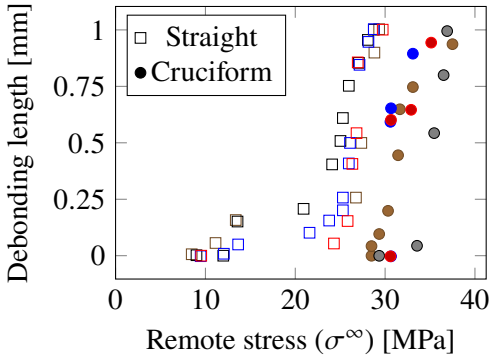

Figure II.11 – Debonding length as a function of the remote stress for both straight and cruciform samples of glass fiber and epoxy matrix, from [OSK09]. The different colors correspond to the different tests.

As with the above experiments, Tandon *et al.* [TKB00] studied the initiation and propagation of debonding on the SiC-epoxy composite samples using a cruciform shape to eliminate the effect of free surfaces. Debonding was successfully observed at the center of the samples. The length of the debonding was monitored using crack tip photoelastic fringes and the initiation stress level was derived from FE calculation. Notably, in [TKB02], the authors varied the cruciform angle to deliberately induce varying degrees of shear at the interface, thereby deriving both the tensile and shear strengths of the interface. Figure II.12 shows the variation in critical tensile and shear stresses at which debonding initiated for the various cruciform angles. When approaching a cruciform angle of 0 deg., *i.e.*, aligned with the loading direction, the shear critical stress tends toward the shear strength. The latter is determined by fitting the different configurations by a criterion. The tensile and shear strengths were determined as respectively 42.3 MPa and 34.5 MPa using the criterion given in Equa-

tion (II.7). Similar configuration has also been studied by the same authors in [BT02] to study the debonding propagation.

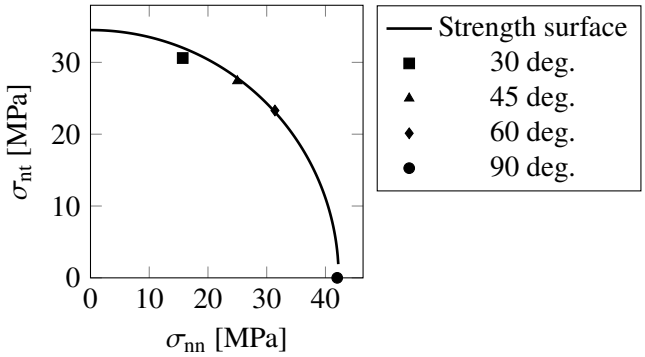

Figure II.12 – Strength surface determined by Tandon *et al.* [TKB02] experimentally using cruciform samples with varying angles which respective critical stresses are denoted by the markers.

Similar experiments have also been used to measure both the interfacial tensile and shear strengths and the critical opening and shear ERR in [Koy+09]. Glass fiber samples with epoxy matrix were investigated. The authors monitored the debonding length on straight specimens and, in combination with FE calculations, derived a set of interface properties: tensile strength σ_c in the range of 18 - 25 MPa, shear strength τ_c in the range of 18 - 22 MPa, mode I critical energy release rate G_{IC} of 5.5 J/m^2, and mode II critical energy release rate G_{IIC} of 11 J/m^2.

Meurs *et al.* [Meu+98] used straight-edged specimens to assess the tensile strength of carbon fiber/epoxy matrix interface. The authors confirmed that the singularity was responsible for the debonding initiation at the free surface. They obtained the local tensile stress at the interface using FE calculations with the experimental displacement fields used as the boundary condition. Obtained interfacial tensile stress was approximately 240 MPa, a value relatively larger than results reported by other researchers.

Similarly, Totten *et al.* [TKC16] observed the initiation of debonding inside a SEM at the free surface of a straight-edged sample. Experimental observation coupled with FE calculations was used to determine the tensile strength of the glass fiber/epoxy interface. The authors reported a tensile strength of approximately 37 MPa, slightly larger than the value measured in [OSK09].

Zhang *et al.* [Zha+97] used a pre-debonded sample to study the propagation of debonding with various glass fiber treatments (epoxy matrix). Straight-edged samples were observed under an optical microscope to assess the length of debonding. The weak interface exhibited a larger debonded surface compared to the strong interface

under a similar loading. The analytical model employed by the authors in [VBE97] enabled the calculation of critical ERR from the previous experimental observations, yielding values of $G_{IC} = 2$ J/m^2 and $G_{IIC} = 6$ J/m^2.

This specific test was conducted within a synchrotron facility by Martyniuk *et al.* [Mar+13]. The authors had the capability to monitor the progressive evolution of debonding at various loading stages. Employing a straight-edged sample consisting of glass fiber/epoxy matrix, they ensured that debonding initiation occurred at the free surface and subsequently propagated in the form of a tunnel along the fiber pole. Figure II.13 shows 3D reconstructed volumes of the developed debonding shapes corresponding to different loading levels.

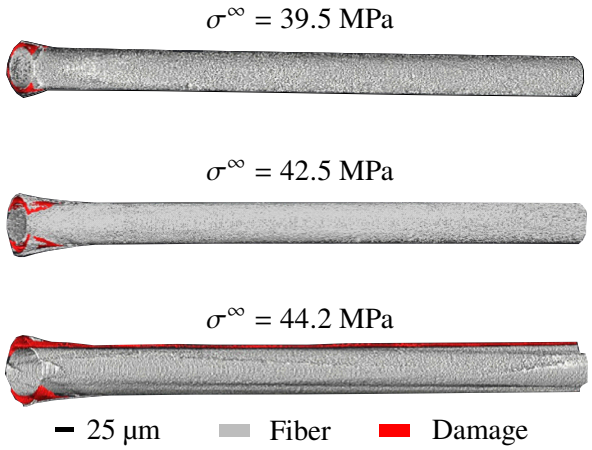

Figure II.13 – X-ray visualizations of fiber-matrix debonding formed at three different loading levels σ^∞, from [Mar+13], initiation at the free (left) fiber end.

As with compression tests on a single fiber, transparent matrices are often required for relevant experimental measurements. However, new techniques have emerged, such as free surface observation or the use of X-rays to monitor debonding propagation.

II.2.3 Shear characterization

Fiber fragmentation test

The fiber fragmentation test is one of the most common microcomposites test for estimating the properties of the fiber-matrix interface. It consists of a single fiber generally embedded in the middle of a dog bone tensile sample and aligned with the sample main axis, see Figure II.14a.

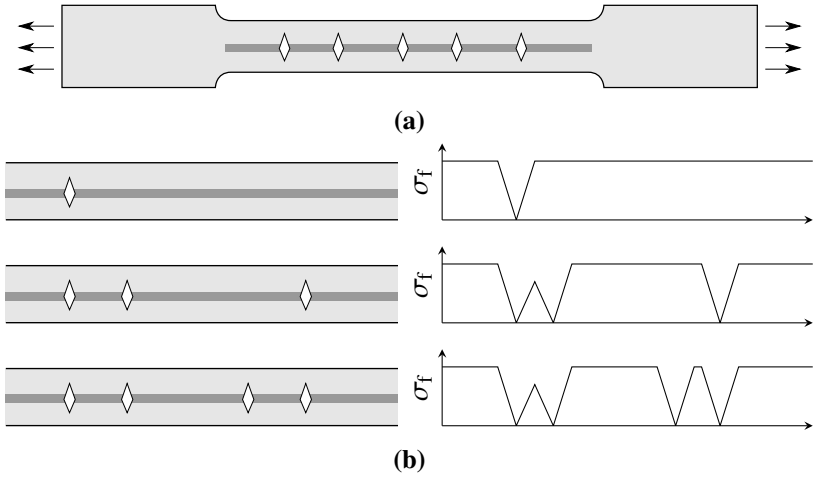

Figure II.14 – (a) Typical dog bone specimen used for fragmentation test. (b) Fiber fragments location (left) and corresponding variation of the fiber tensile stress for increasing remote loading (right).

It is imperative that the failure strain of the matrix is three times larger than that of the fiber for the test to yield accurate results. When a tensile loading is applied to the sample, the fiber gradually fractures into distinct segments at various locations. This phenomenon is attributed to larger stretching of the matrix, inducing shear stress at the fiber-matrix interface. This causes the fibers to reach their failure strength [ZLG97]. This process continues as the applied loading increases until the length of the fiber segments becomes too small to transfer adequate stress for achieving fiber strength, see Figure II.14b. The minimum length of these segments, referred to as the critical transfer length ℓ_{trans}, is subsequently reached. It is necessary to reach saturation of the fiber breakage indicated by the disappearance of events considered as fiber breakage before the failure of the complete sample, otherwise the critical transfer length ℓ_{trans} obtained is not accurate.

Several approaches can be used to measure the final length of the fiber segments required to determine the shear fracture properties. Transparent matrices allow relatively simple optical observation combined with a suitable light source [VJB96]. The photoelastic technique combined with the polarized optical microscope allows the stress distribution in the vicinity of the fiber fragment to be assessed [RCA09]. Although optical observation is relevant with transparent matrices, most thermoplastic, yet semi-crystalline, matrices do not allow this process. Acoustic Emission (AE) is therefore another useful technique for monitoring the number of fiber breaks during testing [Net+89; Ham+19; Ham+21]. The average length of the fiber segments

can be determined by the total length of the fiber divided by the number of acoustic events. Another approach is to locate the acoustic event using two sensors that measure the position of the events from the speed of the wave in the matrix. This enables to locate the fiber breakage locations and deduce the length of the segments. Acoustic emission has been used successfully to measure fiber strength parameters in fragmentation tests, with results comparable to those obtained by optical microscopy [CM96]. In addition, acoustic emission is more efficient because fragment size can be obtained without sample observation. Lutz *et al.* [Lut+18] used acoustic emission to determine critical transfer length for carbon fiber and epoxy matrix sample with different fiber treatment surfaces. Acoustic events were located using two sensors, revealing homogeneous distribution over the entire gauge length and enabling the determination of the critical transfer length. Other acoustic events due to matrix microcracks and fiber-matrix debonding were also recorded but not located. Figure II.15 shows the cumulative number of recorded AE events N superimposed on the remote stress σ^∞ as a function of the sample strain, for two different fiber surface treatments.

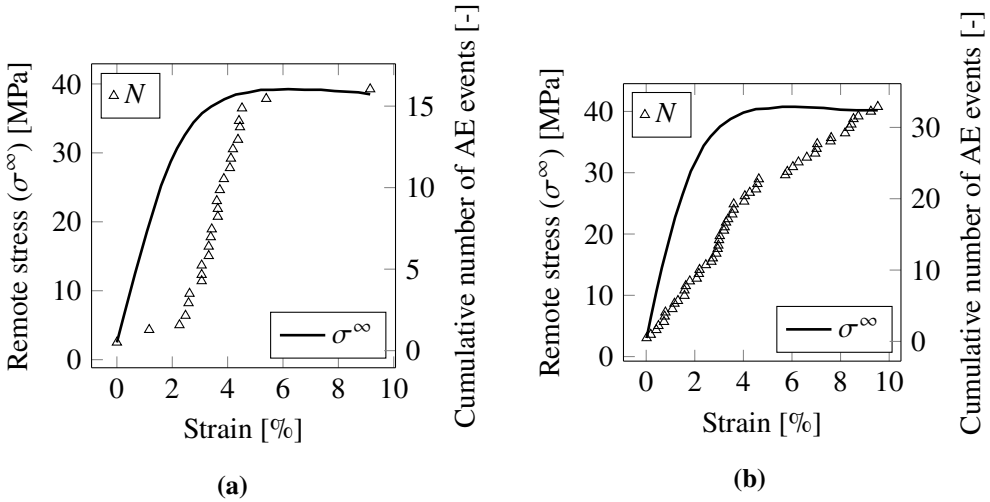

Figure II.15 – Variation of the remote stress and cumulative number of AE events as a function of the remote strain for (a) oxidized carbon fiber (TCF) and (b) commercial epoxy-sized carbon fiber (SCF) with an epoxy matrix, from [Lut+18].

On the one hand, Figure II.15a shows the fiber breaks saturation before the complete failure of the sample, indicated by the last AE event. This enables the critical transfer length to be determined. On the other hand, no saturation is reached before complete sample failure in Figure II.15b, suggesting strong interface fracture properties. This is also reflected in large amplitude AE events. However, no critical transfer

length can be deduced from this sample.

Once the fiber breakage saturation is reached, the critical transfer length can be determined, Kelly and Tyson [KT65] proposed using a force balance to calculate the shear strength of the interface, see Equation (II.8).

$$\tau_c = \frac{d_f \, \sigma_f^c(\ell_{trans})}{2\ell_{trans}} \tag{II.8}$$

The consideration of a balance of forces takes into account both friction for the debonded interface at the ends of the fiber fragment as well as shear stress for the bonded zone of the interface. The diameter of the fiber is denoted d_f and σ_f^c corresponds to the tensile strength of the fiber for the critical transfer length, since the length of the fiber increases the probability of defects and early failure. Ohsawa *et al.* [Ohs+78] proposed a different formulation for calculating the critical segment length. This can be considered to be between $\ell_{trans}/2$ and ℓ_{trans}. The average critical length can therefore be considered as an average intermediate length, as proposed in Equation (II.9).

$$\overline{\ell_{trans}} = \frac{1}{2}\left(\frac{\ell_{trans}}{2} + \ell_{trans}\right) = \frac{3}{4}\ell_{trans} \tag{II.9}$$

The final critical length is calculated as $4/3\,\overline{\ell_{trans}}$ where the latter corresponds to the averaged critical length measured experimentally. Cox [Cox52] proposed a different analytical model to describe the stress fields at the fiber-matrix interface where the shear is not constant and rather located at the end of the fiber. This formulation considers an undamaged fiber-matrix interface without permanent deformation within the matrix.

However, this test is not yet fully understood because it involves several complex mechanisms that are difficult to distinguish. Firstly, the results of fiber fragmentation really depend on the behavior of the matrix, whether it is ductile or brittle. A ductile matrix will undergo local permanent deformation in the vicinity of the fibers, whereas a brittle matrix will rather crack. Consequently, the interface may or may not be debonded [TJ97; TJ98]. As a result, Kelly and Tyson [KT65] model is only suitable in certain configuration, particularly when there is located debonding or matrix permanent deformation. Secondly, the computational formulation proposed previously assumes that the shear stress is constant along the interface, whereas some experimental observations have shown the opposite [KN02]. In particular, the stress distribution has been shown to be particularly dependent on the surface treatment and, consequently, on the state of damage of the interface [Gal93]. To this end, some authors have proposed improved models to describe the shear stress profile at the interface and actual phenomena. For example, Nair and Liu [NL97] proposed a complex

analytical model to account for the imperfect interface. In addition, matrix plasticity was taken into account in [TCJ96] and the influence of interphase in [JHJ09].

Fiber pull-out test

Alongside the fragmentation test, the single fiber pull-out test and the microbonding test are also used to assess the shear fracture properties of the fiber matrix interface. These tests involve the partial embedding of a fiber in a rather large block of matrix. The matrix is then clamped and a displacement is applied to the fiber (see Figure II.16a).

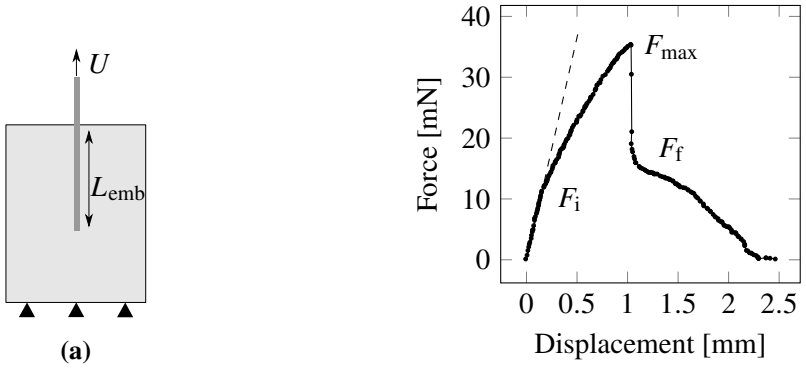

(a) **(b)**

Figure II.16 – (a) Pull-out test geometry where L_{emb} denotes the embedded fiber length and U the applied pulling displacement of the fiber. (b) Typical pull-out force-displacement curve from [Wan97].

Wang [Wan97] reported a typical force-displacement curve obtained during the pull-out test (PTFE fiber/polypropylene matrix) from which the shear strength can be derived, see Figure II.16b. Below F_i, *i.e.*, the force at debonding initiation, the interface remains undamaged, whereas above this force level the interface begins to slightly debond at the meniscus, so that the slope of the force-displacement curve begins to decrease progressively until the maximum force F_{max}. The force then suddenly drops to F_f due to abrupt interface failure and friction continues until the fiber is completely pulled out. Several authors have proposed different analytical models to determine the shear strength (τ_c), the critical ERR (G_c) and the coefficient of friction C_f. A commonly used formulation for the determination of the bond strength τ_{bond} is presented in Equation (II.10) [PD90], which consists of a classical force equilibrium.

$$\tau_{bond} = \frac{F_{max}}{2r\pi L_{emb}} \tag{II.10}$$

The calculated shear is then dependent on the embedded length L_{emb} and the fiber radius r. Difrancia *et al.* [DWC96] evaluated the critical shear strength τ_c as the slope of the maximum pull-out force as a function of crack length, see Equation (II.11). The calculated critical strength becomes independent of the embedded length L_{emb}. This can be done for a sufficiently small embedded length, otherwise fiber breakage will occur before debonding. By calculating the actual pressure developed at the interface P_i, the shear strength can be plotted as a function of pressure. A linear relationship with the slope being the coefficient of static friction C_f is often reported, Equation (II.12). This pressure at the interface is caused by shrinkage and thermal mismatch between the fiber and matrix during the sample curing [DWC96].

$$\tau_c = \frac{dF}{dL_{emb}} \frac{1}{2r\pi} \qquad \text{(II.11)} \qquad\qquad \tau_c = C_f P_i \qquad \text{(II.12)}$$

In this context, Parry *et al.* [PWL87] proposed to extract a single steel fastener from a drilled glass/epoxy composite with variable external pressure. Figure II.17a shows the force required to extract the fastener from the sample as a function of embedded length and external pressure.

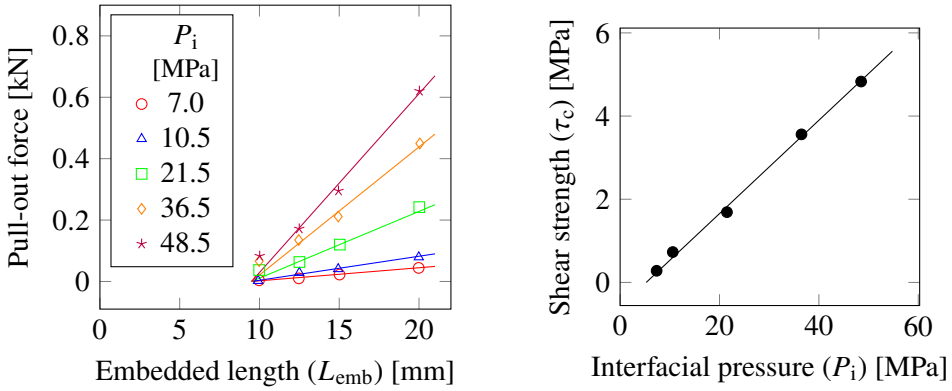

Figure II.17 – (a) Variation of the pull-out force as a function of the steel fastener embedded length for different interfacial pressures P_i. (b) Variation of the shear strength as a function of interfacial pressure where the slope of the interpolation gives the coefficient of static friction C_f, from [PWL87].

The larger the length and pressure, the larger the force required to extract the fastener. The slope of each curve gives access to the shear strength as a function of external pressure, as shown in Figure II.17b. The coefficient of static friction can

therefore be deduced from the slope of this curve, as explained previously, which was found to be approximately 0.1.

Some authors proposed to determine the interfacial sliding shear stress by taking the slope of the force-displacement curve when the fiber is sliding after the complete debonding [DWC96]. Further more complex models were developed to compute the critical ERR and derive stress distribution such as for instance the Piggott's model [Pig87] which considers both elastic properties of the constituents as well as geometry.

The pull-out test is widely used to assess the shear properties of the interface. However, this test remains very sensitive to the experimental configuration and scale. Indeed, the embedded length must be small, which complicates sample preparation, in particular for strong interface and small fiber diameter. For example, some carbon-epoxy systems have been found to have an embedded length of less than 1 mm [PD90; KBM92]. Another drawback of this approach is the development of a meniscus when the fiber and matrix come into contact with the air due to physical forces. This meniscus therefore induces perturbations in the calculated stress fields, which can make the shear strength calculation inaccurate because they are not representative of the real geometry. This meniscus is often neglected by the analytical model developed to assess the stress field, thus leading to inaccurate comparison.

The microdroplet test has been proposed to overcome the above-mentioned drawbacks. [MMR87; PTZ88]. In details, a single microdroplet of matrix is deposited onto a fiber. This approach can be used for a wide range of matrices, whether they need to be cured or melted, and fibers. For thermoplastic matrices, one approach to forming the microdroplet is to cut a thin strip of polymer film and place it over the fiber before bringing both to the melting temperature of the matrix. The fiber is then pulled with the droplet clamped, and the force required to pull the fiber can be related to the fiber-matrix shear strength. Some limitations of this technique have been reported by Herrera-Franco and Drzal [HD92]. For example, the stress state is difficult to describe analytically because the geometry of the microdroplet is generally not perfect and asymmetrical. In addition, the meniscus formed at both ends of the microdroplet makes it difficult to measure the length of the microdroplet, which has a more pronounced influence on the calculated properties of the interface compared with the pull-off test.

Other techniques for the fiber-matrix interface characterization

Other techniques have been developed to assess interfacial properties, many of which focus on shear properties. For this reason, only a brief description of these techniques will be given in the following. The pull-out test has been improved to take into account the influence of neighboring fibers by incorporating several fibers into the matrix block. In this way, the technique tends to resemble the actual microstructure of the

composites, with a larger volume fraction of fibers. This approach was used by Qiu and Schwartz [QS91] and Sastry *et al.* [SPS93].

In contrast to the pull-out test, another approach involves pushing the fiber out of a matrix block [MCM80]. Its main advantage is that the sample can be extracted from a real composite. Microindenters are commonly used to perform this test, which is similar to the microhardness test normally used to measure the hardness of materials. The force required to extract the fiber is recorded, enabling the interfacial shear properties to be deduced. However, this approach also has some disadvantages, such as the interpretation of the experimental data, the breaking of the fiber by the sharp indenter during the test [DV93] or radial matrix crack emanating from the interface [Kal+92].

II.2.4 Major discrepancies resulting from these approaches

From the articles mentioned above, there is a lack of standardization on what is actually measured with the techniques. Furthermore, depending on the fiber-matrix configuration, the phenomena are different, and a case-by-case study is therefore necessary. Herrera-Franco and Drzal [HD92] have pointed out most of the limitations associated with all the current techniques for measuring interfacial resistance.

Pitkethly *et al.* [Pit+93] carried out a round robin test on similar microcomposites in 12 different laboratories around the world. The aim of this work was to evaluate the dependence of the properties determined on the type of test and the experimental procedure. Four different techniques were compared, namely the pull-out test, the microdroplet test, the fragmentation test and the microindentation test. Samples containing two different carbon fibers were tested, one with a treated surface and the other untreated. The epoxy matrix was used for this comparison and the curing process was similar in all the laboratories. Several tests were carried out for each technique to ensure the reproducibility of the results. Figure II.18 shows the IFSS measured for untreated (Figure II.18a) and treated (Figure II.18b) fiber surfaces. Significant variations were observed between the techniques, in particular, pull-out and fragmentation test yield of up to 250% relative difference for the treated fiber. For a similar technique, larger differences were observed for the pull-out and microdroplet tests between the different laboratories, for the treated fiber.

Among the various sources of divergence, some have been reported in [Pit+93; KMM98] and are summarized below:

pull-out test: measurement of the embedded length, loading rate, alignment of the fiber with the loading axis, accuracy of measurements of fiber diameter;

microdroplet test: size and shape of the droplet, shape of the meniscus, variation in the concentration of hardener within the droplet, shape and size of the specimen

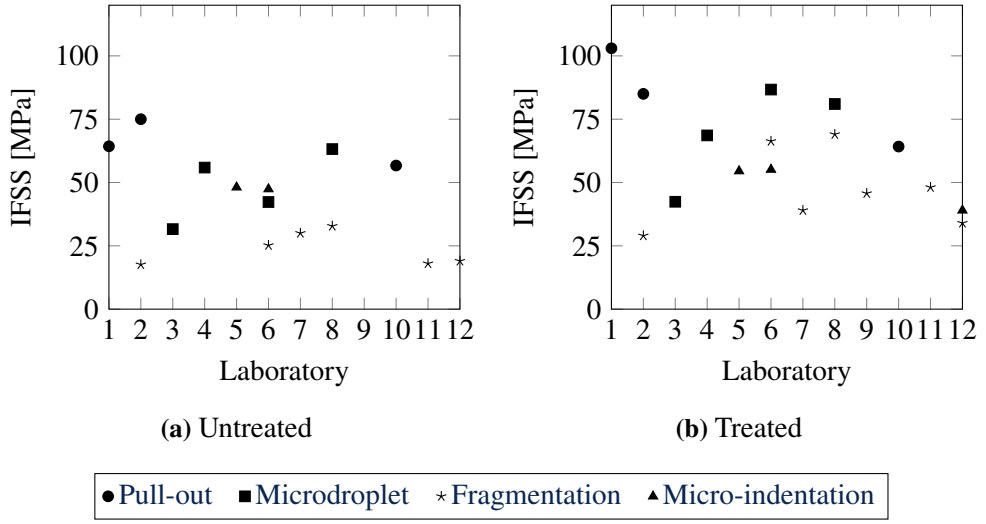

Figure II.18 – Interfacial shear strength measured using the different techniques and laboratories for (a) untreated and (b) treated carbon fibers, adapted from [Pit+93].

holder;

fragmentation test: level of preload applied to the fiber during the curing process, loading method, loading rate, method of detection of the fiber breakage;

micro-indentation test: specimen preparation, size and shape of the indenter, method for detecting the debonding, fiber splitting.

One solution to overcome these drawbacks could be to couple experimental observation with numerical simulation in order to accurately account for the actual damage process. However, this requires a thorough characterization of the debonding process. To this end, dedicated experimental set-ups have been developed to detect and monitor the debonding process and are presented in the sequel.

II.3 Crack detection and monitoring

Detection of crack initiation and propagation is crucial for determining the fracture properties of the fiber-matrix interface. Some microcomposite tests use the drop in reaction force to detect crack initiation, for example the pull-out test [Wan97]. Crack detection for multi-fragmentation tests depends on whether the matrix is transparent or not. AE is interesting because crack detection can be achieved with non-transparent matrices, but it requires localization to consider only events due to fiber breakage

[Lut+18]. Once saturation of the fiber breakage is reached, the critical transfer length can also be obtained using micro-tomography, although this is a challenging task since the resolution obtained is close to that of the fiber. In the case of a transparent matrix, the intensified stress fields near the ends of the fiber fragments can be observed using cross-polarized light. In particular, the stress fields result in birefringence colors near the fiber fragments and the interface, as observed by Kim and Nair [KN02] for carbon fiber and epoxy matrix and shown in Figure II.19.

(a) Without fragmentation **(b)** With fragmentation

Figure II.19 – Observation of the fiber during a fragmentation test, (a) before and (b) after fiber fragmentation, from [KN02].

The shape of the birefringence colors near the fiber fragments can also indicate whether there is debonding or not at the ends of the fiber fragments, see Figure II.19b. Fragmentation with debonding results in a small convex shape, whereas the absence of debonding results in a larger triangular area [KN02].

A similar technique has been adapted to single-fiber microcomposites subjected to transverse loading. Ogihara *et al.* [OSK09] monitored the debonding length as a function of remote applied loading using the change in reflective index caused by interfacial cracking, *i.e.*, the presence of air. This method enables the debonding to be observed optically on small-diameter fibers, 13 µm glass fibers in an epoxy matrix in this configuration. However, it is not possible to measure all the other debonding geometric characteristics. Koyanagi *et al.* [Koy+09] used larger diameter glass fiber (200 µm) to optically evaluate the debonding process. The authors were able to derive the debonding length and angle as a function of the remote loading from experimental observations since transparent epoxy matrix was used, see Figure II.20.

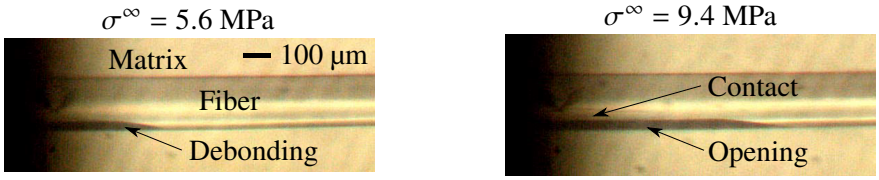

(a) **(b)**

Figure II.20 – Optical observations of the fiber-matrix debonding for two different remote loadings σ^∞, from [Koy+09].

The authors reported that the extraction technique was accurate when the debonding was mainly located at the pole of the fiber and therefore mainly subject to the opening mode, see Figure II.20a. However, as the debonding propagated, difficulties in identifying the debonding front arose due to the compressive loading acting on the fiber equator, see Figure II.20b. No crack opening was observed in this area, but a slight change in the reflective index did occur, making the debonding angle more challenging to determine. However, the above techniques are limited to transparent matrices, which is why other observation techniques have been employed, such as the observation at free surfaces or the use of X-rays. For example, Martinyuk *et al.* [Mar+13] combined SEM and X-ray observations of a single glass fiber embedded in an epoxy sample. The fiber had a 50 µm diameter. Using these techniques, the authors measured the debonding angle, opening, length and shape as a function of remote loading. Figure II.13 shows an X-ray description of debonding shapes corresponding to different loading levels. SEM observation allows the debonding process located at the sample free surface to be characterized, so that the debonding angle and opening can be determined, as shown in Figure II.21.

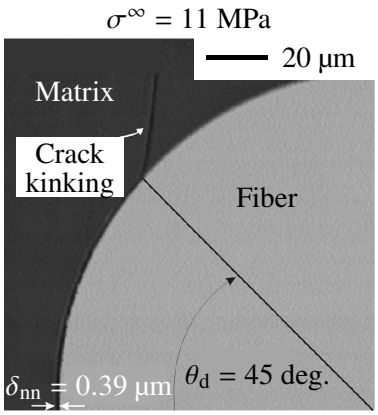

Figure II.21 – SEM observation of the fiber-matrix debonding and kinking observed at the sample free surface by Martyniuk *et al.* [Mar+13].

Digital Image Correlation (DIC) was performed on the free surface of a single glass fiber epoxy sample in Montgomery *et al.* [MKS19]. The fiber had a 23 µm diameter. A specific speckle pattern was developed to allow accurate DIC at the fiber scale. Strain fields produced a high localized band at the debonding vicinity. Displacement fields were used to extract the debonding opening at the fiber pole. The debonding was monitored until it kinked into the adjacent matrix. A similar DIC/SEM method was used by Naylor *et al.* [Nay+19] to estimate the strain fields in a woven carbon fiber/epoxy matrix composite at the fiber scale. The authors succeeded in obtaining an error in the displacement field of around 10 nm by coupling FE to DIC.

The method developed enabled the fiber and matrix debonding to be detected using the DIC residue.

The experimental method described above enables accurate characterization of the debonding process, which can then be implemented in suitable numerical models. Several numerical methods have been developed to model interface failure, from which interface properties can be deduced using an inverse identification approach. Further details regarding existing numerical models are presented in the sequel.

II.4 Modeling of fiber-matrix debonding

Recently, Martin [Mar22] summarized the different models that have been used to model fiber-matrix debonding. Table II.4 shows a timeline of these models.

1970	1980	1990	2000
Shear Lag analytical models			
		Improved analytical models	
			FE models

Table II.4 – Evolution of the fiber-matrix interface models over time, from [Mar22].

Most of the analytical models were briefly presented in the previous section but will be recalled later. Although these models have been predominant, numerical models have emerged such as the Cohesive Zone Model (CZM) [Koy+09; Kus+11], Phase-Field approach for fracture (PF) [Vod23] or the Coupled Criterion (CC) [Man09; GMG15].

II.4.1 Previous approaches

Analytical models

Many early analytical models focused on describing the stress transfer across the interface of an embedded fiber fragment. This approach proved particularly suitable for analyzing fragmentation tests. In 1952, Cox [Cox52] proposed a shear lag model to investigate the micromechanism of stress transfer across the interface. The model assumed both the fiber and matrix to be linear elastic with perfect bonding. Both constituents were subjected to tensile loading in the fiber direction, resulting in a differential displacement near the interface. This displacement can be correlated with the shear stress (τ_i) at the interface and the fiber tensile loading (σ_f). Nair [NL97] introduced an improved model specifically designed for unidirectional composites, eliminating the initially proposed matrix radius dependence in the calculation. The

calculation now depends on the composite microstructure, demonstrating better correspondence with FE results. Figure II.22a illustrates the shear stress distribution across the interface and the tensile stress within the fiber of length L_f according to the shear lag model.

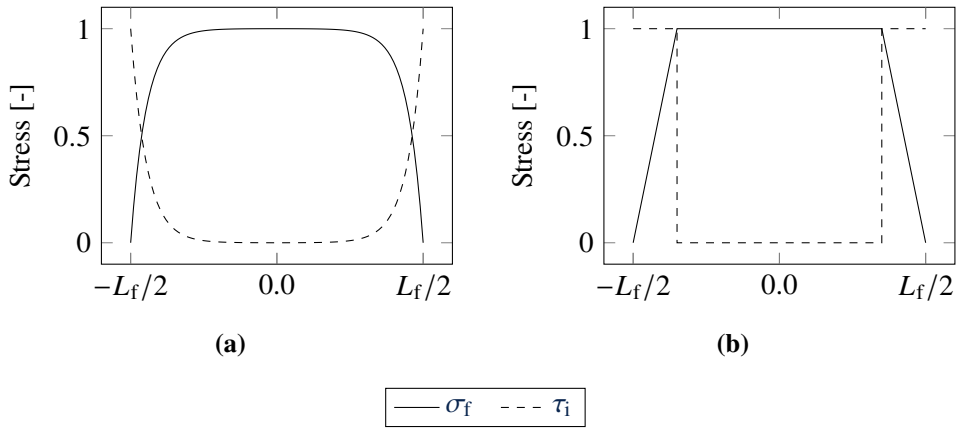

Figure II.22 – Stress variation across the interface and within the fiber for (a) the Cox model [Cox52] and (b) the Kelly and Tyson model [KT65].

In this model, the tensile stress is the highest at the fiber center, while the interfacial shear stress reaches its maximum at the fiber ends and decreases to zero at the center. In contrast to the shear lag model, which assumes a progressive decrease in shear stress from the fiber ends, the Kelly and Tyson model [KT65] assumes a constant shear at the fiber ends (see Figure II.22b) due to local debonding or matrix permanent deformation. The fiber tensile stress exhibits a linear variation within the fiber, while the shear lag model exhibits a non-linear variation. As a consequence, the Kelly and Tyson model provides a more qualitative description of the stress fields, but it is easier to implement.

Later on, numerous advanced analytical models were introduced to address scenarios involving pre-existing damage to the interface, debonding propagation, frictional behavior, and other factors. An example is the McCartney model [McC89], which provides an analytical description of stress variation in a configuration similar to the shear lag model. In this work, the author examined configurations related to matrix cracks and broken fibers with perfect bonding, and debonded interfaces, taking into consideration frictional slip controlled by Coulomb friction law. The developed model demonstrated agreement with FE results [PMQ95].

Meanwhile, Hutchinson and Jensen [HJ90] introduced a cylindrical model that assesses the energy release rate variation as a function of the debonding length. The model considered mode II propagation of pre-existing debonding, incorporating two

distinct friction mechanisms.

Although most analytical models focus on longitudinally loaded single fiber composites, the transversely loaded single fiber has also been studied. In this context, the Dundurs's parameters [Dun69] are very useful and allow the analytical solution of several elasticity problems involving a bi-material such as the single embedded fiber (Equations (II.13)-(II.14)). The parameters μ_k and κ_k represent respectively the shear modulus and the Kolosov's constant of the two constituents $k = 1, 2$.

$$\alpha_{\text{Dun}} = \frac{\mu_1(\kappa_2 + 1) - \mu_2(\kappa_1 + 1)}{\mu_1(\kappa_2 + 1) + \mu_2(\kappa_1 + 1)} \tag{II.13}$$

$$\beta_{\text{Dun}} = \frac{\mu_1(\kappa_2 - 1) - \mu_2(\kappa_1 - 1)}{\mu_1(\kappa_2 + 1) + \mu_2(\kappa_1 + 1)} \tag{II.14}$$

Notably, the stress fields at the inclusion interface can be derived from these parameters using Goodier's solution [Goo33]. The tensile and shear stresses acting at the interface are consequently dependent on the elastic properties of the constituents, their variations are shown in Figure II.23a. More precisely, stresses are represented as a function of the angle from the inclusion pole for glass fiber/epoxy configuration under plane strain assumption. The tensile stress exhibits a monotonic increase from the equator (90 deg.) to the pole of the fiber (0 deg.), while the shear stress peaks between the two. There exists a specific interface location where positive tensile stress transitions to compression, particularly as the location approaches the equator. This transition also depends on the Dundurs's parameters.

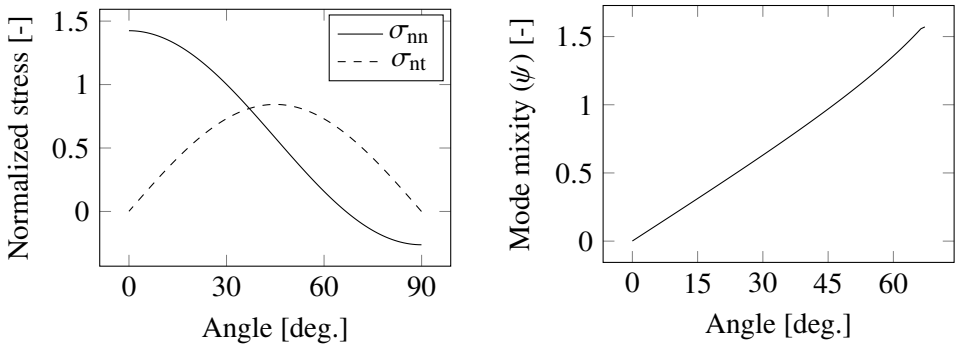

Figure II.23 – (a) Tensile and shear stresses variation at the inclusion interface under plane strain assumption and (b) corresponding mode mixity variation.

As interface debonding simultaneously involves traction and shear, the mode mixity varies accordingly, see Equation (II.5) for its calculation. Figure II.23b shows the

variation in mode mixity increasing from pole to equator. Above 60 degrees, the fiber-matrix interface undergoes compression, so that the mode mixity begins to decrease. However, conditions are often applied to the mode mixity in this configuration so that only shear is considered [PCM06]. Therefore, prediction of interface debonding requires a model that takes into account of mode mixity.

Models to account for mode mixity

The energy release rate of a debonding propagating symmetrically with respect to the loading direction on a single fiber sample was determined in 2D by Toya [Toy74] and reformulated in terms of Dundurs parameters by Mantič [Man09]. The ERR attains its maximum value for a large debonding angle.

To assess debonding propagation, it is essential to compare the energy release rate with the critical ERR G_c. As highlighted earlier (Section II.1.4), the propagation of interface cracks involves mode mixity, which significantly influences the critical ERR. As a consequence, the critical ERR depends on the mode mixity parameter ψ. Pioneering work by Hutchinson and Suo [HS91] introduced various formulations linking the critical ERR and mode mixity (Equations (II.15)-(II.16)).

$$G_c(\psi) = G_{IC}\left[1 + \tan^2\left[(1-\lambda)\,\psi\right]\right] \tag{II.15}$$

$$G_c(\psi) = G_{IC}\left[1 + (1-\lambda)\tan^2(\psi)\right] \tag{II.16}$$

Figure II.24 shows the variation of the normalized critical energy release rate for both formulations. The critical ERR increases with increasing mode mixity, noting that $\psi = 0$ and $\psi = \pi/2$ denote pure modes I and II, respectively. Another influential factor in determining the critical ERR is the parameter λ, which is related to the G_{IC} to G_{IIC} ratio. Notably, a smaller value of λ results in a larger critical ERR for a given mode mixity. The first formulation leads to a more rapid increase in G_c to a finite G_{IIC} value as the mode mixity increases, whereas the second formulation shifts the overall curve with respect to ψ and tends towards an infinite G_{IIC} value.

The λ parameter thus becomes a material property, and its accurate determination is crucial. Without proper identification of λ, the critical ERR can exhibit significant variation, as evidenced in Figure II.24 for similar mode mixity condition. As an example, Hutchinson and Suo proposed a method to assess λ based on the work of Wang and Suo concerning Brazilian disk experiments [WS90]. In their study, the authors induced and observed cracks at a PMMA-epoxy interface, varying the mode mixity from pure mode I to pure mode II. They identified λ as the value that minimized the difference with experimental observations.

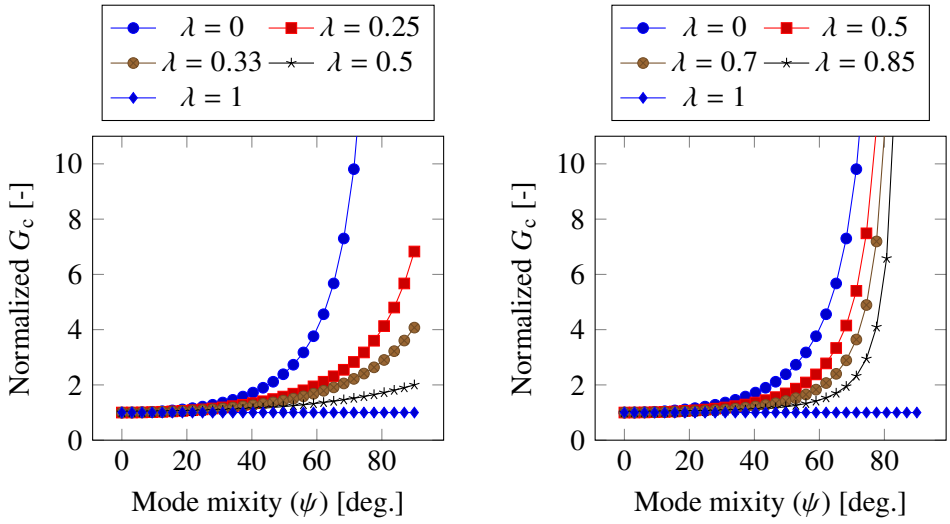

Figure II.24 – Normalized critical ERR as a function of the mode mixity for (a) Equation (II.15) formulation and (b) Equation (II.16) formulation, from [HS91].

Among other formulations of the critical ERR calculation, Muñoz-Reja *et al.* [Muñ+16a] used a quadratic formulation. The quadratic criterion provided overall agreement with the Hutchinson and Suo criterion, except for mode mixity close to $\pi/2$ where the interface transitions from tension to compression, the quadratic criterion yields a plateau. Carrère *et al.* [CML15] has also proposed a power-law criterion of G_c that relates the critical ERR in modes I and II. The latter requires a mode mixity calculation depending on the incremental energy release rate which differs from that proposed by Hutchinson and Suo, developed in the sequel.

The mode mixity is a crucial information that needs to be determined. Some authors have proposed to base the calculation of mode mixity on either stress or energy considerations. For example, Mantič [Man09] and García and Leguillon [GL12] have used a stress-based condition such as Equation (II.17), in which x indicates the location of the mode mixity calculation.

$$\psi(x) = \arctan\left(\frac{|\sigma_{nt}(x)|}{\sigma_{nn}(x)}\right) \tag{II.17}$$

Carrère *et al.* [CML15] and París *et al.* [PCM06], for instance, have based the mode mixity determination on energy considerations such as Equation (II.18), where an incremental energy release rate G_{inc} is used.

$$\psi(x) = \frac{G^{\mathrm{I}}_{\mathrm{inc}}(x)}{G_{\mathrm{inc}}(x)} \tag{II.18}$$

It is worth noting that all the calculation methods result in a comparison between the shear and opening quantities. It should also be remembered that there is an intrinsic relationship between the mode mixity calculation and the critical ERR one.

Nowadays, most fiber and matrix debonding models, and more generally interface crack models, have moved from analytical tools to numerical ones, mainly using finite element methods which allow considering the geometrical ingredients. The aim of these dedicated numerical tools is to predict crack initiation and propagation, whereas analytical models focus mainly on describing stress and energy fields.

II.4.2 Current approaches for interface crack modeling

Numerical models have subsequently been developed to assess interfacial cracking, mainly using finite element. It should be remembered that modeling interfacial cracking is not straightforward, as this mechanism involves several physical phenomena. It is therefore modeled as two surface lips between the two materials, without consideration of stiffness. Despite this major assumption, the current numerical models often manage to reproduce the experimental observations reported in the sequel.

Among these models, one could find in complement to the Linear Elastic Fracture Mechanics (LEFM) [VCP20; SCP16], the boundary element methods, employing contact to model the interface [PCV96; Táv+11], or cohesive zone models which consist in defining a traction-separation behavior of the interface [Kus+11; Koy+09]. More recently, the coupled criterion was used to assess debonding initiation in the framework of finite fracture mechanics [Man09].

The following sections are devoted to the cohesive zone model and the coupled criterion, the latter being studied in more detail as it will be primarily employed in this thesis. In addition, transverse modeling of the single-fiber composite will be of great interest in line with the main work of the thesis.

Cohesive zone model

Cohesive zone models enable the determination of both crack initiation and propagation. This concept was introduced in the early sixties by Dugdale [Dug60] for ductile materials and Barenblatt [Bar59] for brittle materials. In contrast to the binary vision of a crack where the material is either cracked or pristine, the CZM proposes an intermediate state called the process zone. The process zone represents a state where the material is neither pristine, nor fully cracked. It can be seen as a damaged state to make the transition between the two above-mentioned states. The CZM overcomes

the problem of crack initiation inherent to Griffith's theory. Moreover, CZM allow studying material behavior exhibiting plasticity in the crack tip vicinity.

The cohesive zone model is described by a traction-separation behavior, of which a triangular profile is shown in Figure II.25. When the cohesive zone is loaded, the separation δ between the two surfaces increases along with the traction σ until a critical value σ_c. This corresponds to the initiation of damage within the process zone. Once the critical stress is reached, the separation increases with progressive stiffness degradation until the critical separation δ_c, beyond which there is no longer any traction between the two surfaces. At this state, the interface can be locally considered as fully damaged, *i.e.*, cracked.

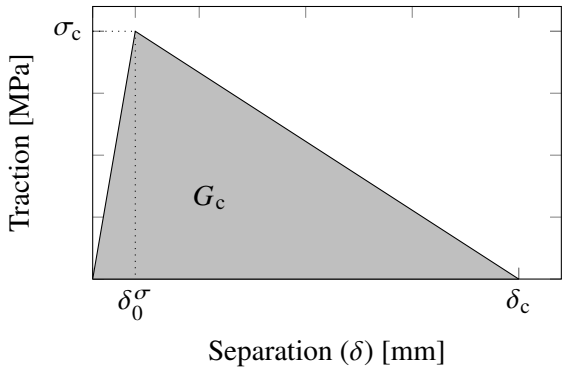

Figure II.25 – Example of traction-separation profile used in cohesive zone model.

The CZM constitutive law therefore requires two material properties as inputs in addition to the traction separation profile: the critical strength σ_c and the critical ERR G_c. The critical ERR is given by the integral of the traction-separation profile (Equation (II.19)):

$$G_c = \int_0^{\delta_c} \sigma(\delta)\, \mathrm{d}\delta \tag{II.19}$$

In the case of a triangular profile, illustrated in Figure II.25, the relationship for calculating the critical ERR reverts to Equation (II.20).

$$G_c = \frac{1}{2}\delta_c \sigma_c \tag{II.20}$$

In addition to the two required fracture parameters, the constitutive profile can be modified to account for specific fracture behavior. Various profiles have been developed for this purpose, such as, *e.g.*, bi-linear, exponential, trapezoidal, cubic polynomial. A comprehensive review of these constitutive profiles can be found in

[PP11]. For instance, Hillerborg *et al.* [HMP76] developed a linear softening model for concrete, incorporating the material tensile strength and critical ERR. To enhance computational stability, this constitutive profile was slightly modified to include an artificial stiffness. Such artificial stiffness becomes necessary due to potential infinite traction values between $\delta = 0$ and $\delta = \delta_0^\sigma$, leading to similar zero separation scenarios. Another proposed model is the tri-linear profile, characterized by a double linear softening with two different slopes. This profile has found application in analyzing concrete failure [BB02], particularly considering size effects in conjunction with two distinct critical ERR representing initial failure energy and total failure energy. Needleman introduced more complex softening profiles, including a cubic polynomial [Nee87] and exponential softening [Nee90]. These profiles have been employed to assess interfacial crack.

It should be noted that all of the above constitutive profiles can be applied to mode I crack initiation and propagation. However, they can be extended to take into account for both mode II and III loadings. For this purpose, existing mixed-mode CZM can be divided into coupled or uncoupled categories, depending on whether normal separation depends on tangential separation or *vice versa* [Dim+15]. Thus, a mixed-mode failure criterion may or not be considered. Consequently, when the criterion is reached at one point, both local traction and shear are affected since the modes are considered simultaneously [Li+06]. On the contrary, the uncoupled model allows failure to occur when the ERR in either mode I or II reaches its critical values [TSV01]. Uncoupled CZM are easier to implement and particularly useful when the configuration is likely to withstand a single mode. However, several applications of CZM are subject to mixed modes [Koy+09; Kus+11].

Coupled models can be classified into different categories whether they are derived from a potential or not. The constitutive profile is different, they take into account a coupling parameter [PP11; Dim+15]. For models not based on a potential, traction-separation profiles and their coupling are directly proposed, but they are not necessarily thermodynamically consistent [MS11]. However, they allow different critical ERR for each of the mode mixities. In contrast, potential-based CZM are derived from a potential, the latter represents the fracture energy distribution in conjunction with separation of fracture surface [PP11]. The first derivative of the potential provides the traction of the fractured surface and the second derivative provides the constitutive relationship.

For example, Tvergaard [Tve90] used a power-law to derive a dimensionless effective relative displacement δ_{eq} described in Equation (II.21), in order to extend Needleman's initial model [Nee87]. The dimensionless effective relative displacement therefore simultaneously takes into account the normal δ_{n} and tangential δ_{t} separation, with δ_{nc} and δ_{tc} their critical values, respectively.

$$\delta_{\text{eq}} = \sqrt{\left(\frac{\delta_{\text{n}}}{\delta_{\text{nc}}}\right)^2 + \left(\frac{\delta_{\text{t}}}{\delta_{\text{tc}}}\right)^2} \tag{II.21}$$

Such a formulation facilitates the definition of complex mixed mode constitutive profile, derived from a potential. For instance, the traction can be obtained from the dimensionless effective relative separation using Equation (II.22), for $0 \leqslant \delta_{\text{eq}} \leqslant 1$.

$$\sigma = \sigma_{\text{c}} \frac{\delta_{\text{n}}}{\delta_{\text{nc}}} \frac{27}{4} \left(1 - \delta_{\text{eq}}\right)^2 \tag{II.22}$$

Figure II.26a shows the Tvergaard's CZM normalized traction as a function of both normalized tensile and tangential separations. The prescribed function follows Needleman's cubic polynomial profile while considering a dimensionless effective relative separation proposed by Tvergaard.

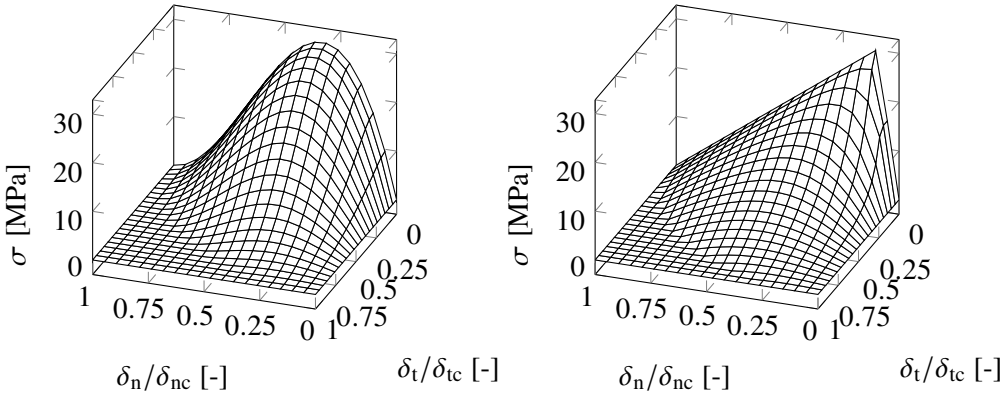

Figure II.26 – (a) Traction as a function of both tensile and tangential separations following a cubic polynomial constitutive profile [Tve90]. (b) Traction as a function of both tensile and tangential separations following a triangular constitutive profile [Hög06].

In addition, Figure II.26b shows a triangular profile coupled to a mixed mode proposed by Högberg [Hög06] and Camanho *et al.* [CDD03], which is not derived from a potential. Like Tvergaard's profile, the triangular profile uses dimensionless effective relative separation where softening is activated for a specific relative separation $\delta_{\text{eq}}^{\text{soft}}$, controlled by a specified softening separation $\delta_{\text{nc}}^{\text{soft}}$. Equation (II.23) describes the profile as a function of the both tensile and tangential softening separations. The critical ERR in both modes can be evaluated using Equation (II.20).

$$\begin{cases} \sigma = \sigma_c \left(\frac{\delta_n}{\delta_{nc}} \frac{1}{\delta_{nc}^{soft}} \right), \text{ if } 0 < \delta_{eq} \leq \delta_{eq}^{soft}, \\ \sigma = \sigma_c \left(\frac{\delta_n}{\delta_{nc}} \frac{1-\delta_{eq}}{\delta_{eq}\left(1-\delta_{eq}^{soft}\right)} \right), \text{ if } \delta_{eq}^{soft} < \delta_{eq} \leq 1. \end{cases} \tag{II.23}$$

CZM is therefore a relevant approach for assessing the initiation and propagation of fiber-matrix debonding since the process involves mixed modes. Among the various applications, one can for instance mention the pull-out test [TPW05], the push-in/out test [Esq+16].

With regard to the transverse study of the single fiber test, several studies can be reported. Most of the numerical studies investigate perfectly cylindrical or spherical inclusions in a soft medium which could describe a single fiber composite subjected to transverse loading. For instance, Needleman [Nee87] employed his CZM profile on an embedded spherical inclusion within a soft matrix. A mixed mode was taken into account, and the inclusion size was varied to observe the brittle to ductile transition. The authors found that, depending on the size of the inclusion, the interface exhibits more ductile behaviour when the inclusion size is large, and *vice versa*. As a consequence, large size inclusion induced a more sudden drop in the remote stress at the debonding initiation. Similarly, Carpinteri *et al.* [CPZ05] observed a strong influence of the inclusion size both on the remote stress at initiation and on the type of fracture, while keeping the volume fraction constant. Figure II.27a shows the tensile stress-strain curves obtained for different inclusion sizes d_i.

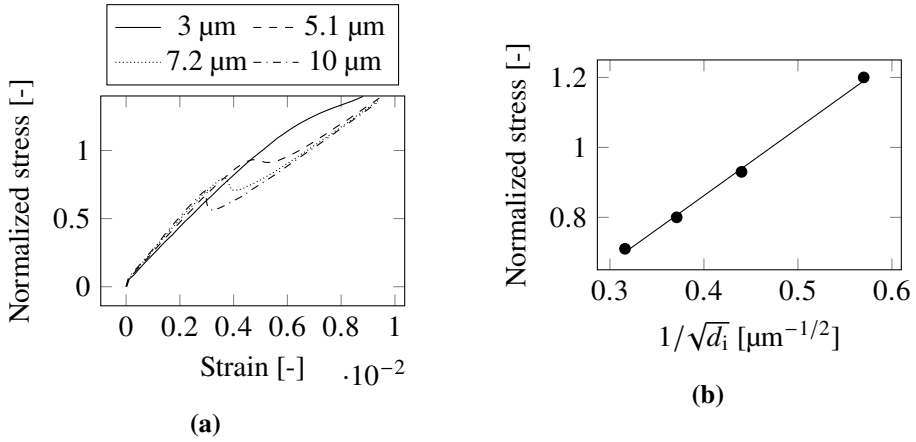

Figure II.27 – (a) Normalized stress as a function of the macroscopic strain for different inclusion sizes (d_i). (b) Normalized peak stress as a function of the inverse square root of the inclusion size, from [CPZ05].

A large inclusion leads to debonding at a lower stress and induces a more brittle fracture, resulting in a larger drop in remote stress. The authors indicated that such failure could induce snap-back instability. The small inclusion shows a more ductile fracture where the stress begins to decrease progressively, at a larger stress level. The overall strength of the interface was shown to depend on the inverse of the square root of the inclusion size (see Figure II.27b).

Other studies have implemented the CZM method to evaluate the debonding process in a more realistic composite microstructure using a Representative Volume Element (RVE). This approach allows the large-scale fracture behavior to be derived from the micro-scale configuration. For example, Cid Alfaro *et al.* [Cid+10] studied matrix microcracking in composite RVE using CZM. In particular, the authors studied the influence of the pre-damaged interface in the overall damage process, the damaged interface being the nucleation site for further damage. Similarly, Bouhala *et al.* [Bou+13] used the extended finite element method coupled with CZM to assess fiber-matrix debonding for single fiber, two-fiber and multi-fiber samples. The authors then investigated the influence of neighboring fibers, promoting or not the debonding initiation. Kushch *et al.* [Kus+11] proposed a similar study, first investigating fiber and matrix debonding in a single fiber sample. The authors found symmetrical initiation of debonding at both fiber poles, with further propagation as the remote stress increased. Comparison with previous experimental results [Zha+97] showed agreement for two different surface treatments in terms of debonding angle as a function of the remote loading (see Figure II.28).

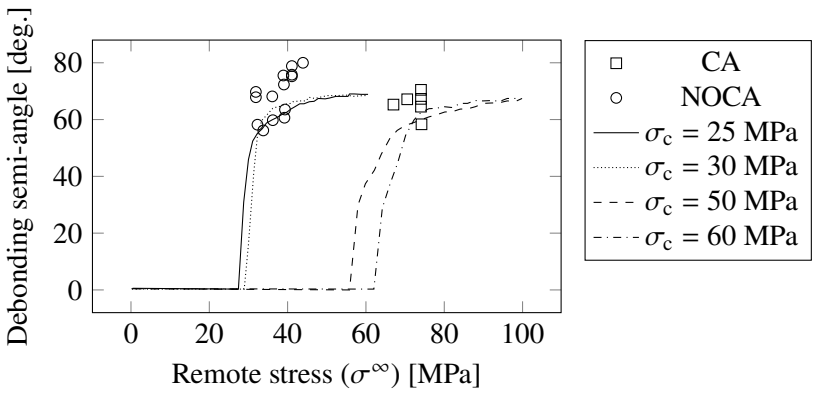

Figure II.28 – Variation of the debonding semi-angle as a function of the remote stress, comparison with experimental observations from [Zha+97] and the numerical results obtained by Kushch *et al.* [Kus+11] for different interface tensile strengths. Two fiber surfaces are considered, one with coupling agent (CA) and another without (NOCA).

Similar debonding semi-angles were reported with initiation stress levels being in same order of magnitude for both surfaces, namely with 0.5% solution of coupling agent (CA) and without coupling agent (NOCA). The authors implemented the CZM profile as a function of the interface fracture properties identified in Varna *et al.* [VBE97]. Interaction with neighboring fibers was also studied in a two-fiber sample. The angle between the two fibers varied from 0 to 90 degrees with respect to the loading direction. Such configurations lead to asymmetric debonding initiation at a different remote stress level than that of a single fiber. Finally, the authors studied multi-fiber composites, where the proximity of the fibers led to early debonding initiation. These mechanisms involve a stress redistribution on the adjacent fibers and early debonding initiation, forming a zone with concentrated debonded fibers.

All the numerical results obtained on RVE resemble to what has been already reported in Section I.3. This makes CZM particularly suitable for modeling fiber and matrix debonding. However, most of the studies mentioned above focus on 2D modeling whereas most of the experimental observations took place on the free surfaces of the sample where non-negligible effects occur such as stress singularity due to mismatch of elastic properties. Taking into account a 3D model could therefore prove to be a relevant solution, and will be studied as part of this thesis work. For instance, Koyanagi *et al.* [Koy+09] employed 3D CZM modeling that enables capturing the free surface debonding initiation location for single glass fiber/epoxy sample. Instead of basing the experimental-numerical dialogue on the debonding angle, the authors monitored the debonding length as a function of the remote stress. As a result, a range of interface properties were derived as the one minimizing the discrepancies with the experimental observations. A coupled mixed-mode CZM was therefore used where the authors primarily varied both tensile and shear strengths. Figure II.29 shows the obtained experimental debonding length as a function of the remote stress compared to the numerical results for a specified strength couple. The determined strength couple provided agreement with the experimental observations, supporting the effectiveness of CZM in predicting fiber-matrix debonding.

The progressive damage induced by the CZM leads to a non-linear finite element calculation. As a result, the calculation time can increase considerably compared to a purely linear elastic calculation. For this reason, an alternative numerical approach for evaluating fiber-matrix debonding is presented in the following, namely the coupled criterion.

The coupled criterion

The coupled criterion was proposed by Leguillon [Leg02] to overcome the problem of crack initiation inherent to LEFM approach, namely Griffith's approach [Gri21] or Irwin's theory [Irw57]. Indeed, such theories are limited to predict the propagation

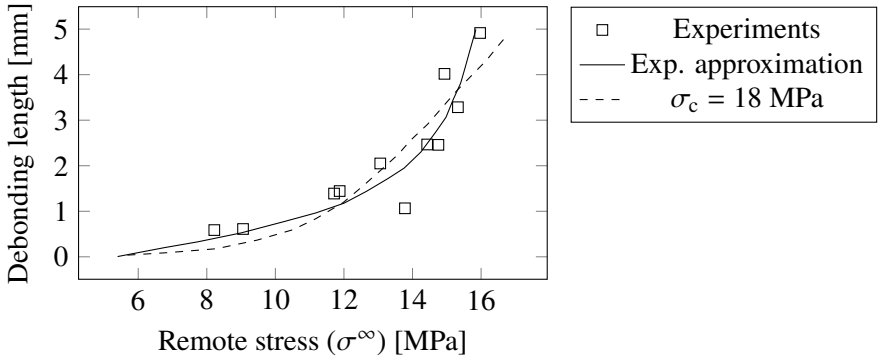

Figure II.29 – Experimental and numerical comparison of the debonding length as a function of the remote stress, from [Koy+09].

of an existing crack but fail to predict its initiation. Griffith's condition for crack propagation is given in Equation (II.24):

$$G > G_c, \tag{II.24}$$

where G represents the ERR and G_c its critical value. According to Griffith's theory, the ERR can be derived from the infinitesimal variation in the potential energy per infinitesimal crack surface increment. Consequently, the theory is unable to assess crack initiation, since both the ERR and the crack surface tend towards 0 when no initial crack is present.

Leguillon [Leg02] therefore proposed a criterion which combines two conditions to overcome this problem. The author stated that a crack can initiate if and only if both stress and energy conditions are simultaneously fulfilled. The solution to such a criterion provides the crack surface and loading level at initiation. As with CZM, the CC needs the input data of the critical ERR and the tensile strength. The two conditions necessary for the initiation of a crack are recalled in Equation (II.25) and depend on the boundary condition U:

$$\begin{cases} \sigma\left(\vec{x}, U\right) \geq \sigma_c, \forall\, \vec{x} \in \Gamma, \\ G_{inc}(S, U) \geq G_c. \end{cases} \tag{II.25}$$

On the one hand, the stress condition requires that, before initiation, the stress exceeds the strength at any location in the future crack path Γ. This crack zone can be either a curve (length ℓ) in 2D or a surface (area S) in 3D. On the other hand, the energy condition of the CC derives from the energy conservation principle before and after crack nucleation over a finite surface S. It consists in a balance of the variation of external work forces (ΔW_{ext}), kinetic energy (ΔW_k), elastic strain energy (ΔW_{el}), crack

surface creation energy ($G_c S$) and energy dissipated into other mechanisms (ΔW_d) such as plasticity, diffused damage or friction for instance, see Equation (II.26).

$$\Delta W_k + \Delta W_{el} + \Delta W_d + G_c S = \Delta W_{ext} \tag{II.26}$$

This energy balance rewrites in a form similar to Griffith's criterion in which the ERR is replaced by the IERR (Incremental Energy Release Rate) G_{inc} (Equation (II.27)):

$$G_{inc}(S,U) = \frac{\Delta W_{ext} - \Delta W_k - \Delta W_{el} - \Delta W_d}{S} = G_c. \tag{II.27}$$

The ERR and IERR can be obtained from each other using the relationships listed in Equation (II.28):

$$\begin{cases} G_{inc}(S) = \frac{1}{S}\int_\Gamma G(s)\,\mathrm{d}s, \\ G(S) = G_{inc}(S) + S\,\frac{\mathrm{d}G_{inc}}{\mathrm{d}S}. \end{cases} \tag{II.28}$$

It is worth mentioning that the energy condition of the CC reverts to Griffith's condition when the crack surface tends towards 0 [CSC16; Doi+17b]. From both above conditions, the initiation loading level U_c and the crack topology Γ_c (which corresponds to a crack length ℓ_c or surface S_c) can be determined at initiation. In the often-encountered particular case of linear elasticity and small deformation assumption, the stress and IERR are proportional respectively to the loading and the square of the loading. The CC therefore turns into Equation (II.29):

$$\begin{cases} G_{inc}(S,U) = A(S)U^2 \geqslant G_c, \\ \sigma(S,U) = k(S)U \geqslant \sigma_c. \end{cases} \tag{II.29}$$

This formulation facilitates the use of inverse identification procedure since the fracture properties are only required during the post-processing of the FE calculation needed to obtain the function A and k [Doi+20].

The two CC conditions can be represented as a function of crack size. There are different representations: the first involves a direct representation of the two criteria, while the second displays the displacement required to meet the two criteria. There is a third representation which consists in presenting both the loading and corresponding surface at initiation, but it is not presented here. Figure II.30 illustrates both possibilities [Doi+23]. Basically, the crack is likely to initiate close to a stress concentration or singularity. The stress condition therefore decreases as the crack size increases, see Figure II.30a. As a result, the displacement required to fulfill the stress condition (U_σ) increases with crack size, see Figure II.30b. On the contrary, the energy condition is small for a small crack size since the potential energy released depends on the crack size. The larger the crack size, the larger the IERR, see Figure

Figure II.30a. Consequently, the displacement required to fulfill the energy condition (U_G) decreases with increasing crack size (Figure II.30b).

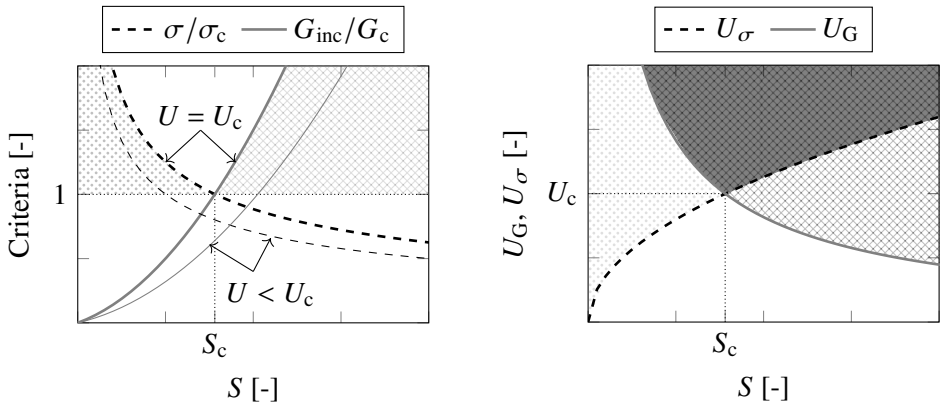

Figure II.30 – (a) Normalized stress (dashed line) and IERR (solid lines) variations as a function of the crack surface obtained for a loading (U) either smaller than (thin lines) or equal to (thick lines) the initiation loading (U_c). (b) Required loading to fulfill the stress (dashed line) or the energy (solid line) criteria as a function of the crack surface evidencing the configurations for which the CC is fulfilled (gray zone), from [Doi+23].

Figure II.30a shows the two criteria for two loading levels, where each is satisfied when it exceeds 1, corresponding to the hatched and dotted areas for the energy and stress conditions. For the lowest loading level, $U < U_c$, neither zone intersects the other, meaning that there is no solution. By increasing the loading level to $U = U_c$, the two zones now coincide with the intersection point describing the crack size S_c at initiation and U_c the corresponding initiation loading level.

Figure II.30b shows the displacement required to fulfill each criterion. The grey area shows the possible CC solution, and from the range of possibilities, corresponding to the intersection of the possibilities fulfilling the two criteria, the one that minimizes the displacement is therefore the most favorable. Thus, the CC conditions can be found using Equation (II.30):

$$\begin{cases} U_c = \min\limits_{S}\{\max\{U_G(S), U_\sigma(S)\}\}, \\ S_c = \{S, \max\{U_G(S), U_\sigma(S)\} = U_c\}. \end{cases} \tag{II.30}$$

However, the CC conditions can vary and become more complex depending on the geometry, the loading configuration and the mode mixity. Consequently, the two con-

ditions can no longer increase or decrease monotonically as shown in Figure II.30a. Further details on such a configuration will be presented later.

There are several possibilities for implementing the CC. Some authors have calculated stress and IERR based on analytical formulae, which are generally available for simple geometries and loads. For example, Sapora *et al.* [Sap+18] and Cornetti *et al.* [CS19] studied holes crack initiation. Similarly, Chao Correas *et al.* [Cha+21] and Ferrian *et al.* [Fer+23] applied the CC for cavities. Mantič [Man09] used the stress solution of Goodier [Goo33] combined with the analytical ERR formula proposed by Toya [Toy74], from which the IERR can be derived by integrating over the crack path, to apply the CC. Ultimately, the use of analytical formulas is an effective way of implementing the CC as it only requires solving on equation to determine the initiation loading and corresponding crack length.

The Matched Asymptotic (MA) approach of the CC was originally proposed by Leguillon [Leg02]. It consists in solving a two-scale problem. The problem is thus divided into an outer domain, where the crack that initiates is disregarded, and an inner domain where the displacement in the stress concentration vicinity can be obtained using Williams's expansions [Wil57]. The approach states the continuity of the displacements at the intersection of the two domains and that, combined with the inner domain fields formulation, stress and IERR solutions can be derived to solve the CC.

Finally, in more complex configurations, where the two previous methods cannot be applied, the FE solution may be an alternative. Like the other methods, the FE approach requires knowledge of the potential crack paths. Thus, the stress fields can be evaluated directly, while the critical IERR can be obtained by unbuttoning the nodes along the crack path. Some authors compared the MA approach with the FE approach and small discrepancies have been observed provided the initiation length remains small with respect to: i) the characteristic dimensions of the structures and ii) to the material characteristic length. For instance, [Mar+16] observed agreement provided the Irwin's length is small enough compared to the characteristic dimension of the structure.

Defining the crack path remains an open problem and is not straightforward. For example, in 2D, the length and orientation of the crack must be defined so that the configuration involving the minimum required displacement is likely to be the most favorable. In addition, when several potential initiation sites are in competition, all the configurations must be compared. For example, García *et al.* [GMG15] compared symmetric or asymmetric debonding at one or two poles of an embedded fiber. However, such an approach to determine the crack path becomes very computationally demanding in 3D. To overcome this drawback, Leguillon [Leg14] proposed to base the crack path on stress isocontours. The crack shape is thus efficiently extracted from the stress fields. This approach proved to be accurate compared to the 2D so-

lution. Leguillon found similar properties derived from both 2D and 3D using stress isocontours [Leg14]. Similarly, Doitrand and Leguillon [DL18b] proposed both 2D and 3D CC applications for predicting the failure of scarf joints, with the 3D approach predicting the failure loading slightly more accurately. The 3D applications of the CC were also extended to several configurations such as laminates failure in García *et al.* [Gar+16] and woven composite in Doitrand *et al.* [Doi+17a] and, more recently, to adhesive pores in [Car+21] or anisotropic fracture in nacre-like alumina [Dum+23]. In 3D, as shown in [Doi+23], the crack can be released in two distinct manners. Firstly, the nodes of the initial mesh located inside the stress isocontours can be doubled, then unbuttoned, but this results in a non-smooth crack front that depends on the mesh topology. Alternatively, the isocontours can be directly included in the geometry topology so that the crack front perfectly matches the isocontours. The difference between the two techniques has to be investigated. In addition, this approach bases the crack path on the stress condition, whereas the energy condition may also drive crack initiation. This means that the stress criterion is already satisfied along the entire crack path, although the energy condition may not. This configuration was encountered by Doitrand *et al.* [Doi+17a] for the prediction of cracks in composite materials. The authors based the CC solution on a parameterized crack geometry and an iterative approach to determine the favorable configuration. However, not all crack configurations have been studied, so the most favorable crack shape configuration remains unknown. So far, further studies are therefore required to evaluate all crack shape configurations among stress-isocontours and energy-based shapes.

Among the applications of the CC to composite materials, García *et al.* [Gar+16] and Doitrand *et al.* [Doi+17a] applied the CC to assess intralaminar failure. Mention should also be made of the original work of Mantič [Man09] who studied the initiation of debonding at the interface of an embedded fiber using the CC. The author studied glass-epoxy and carbon-epoxy configurations. The stress variation at the fiber is derived from Goodier's solution [Goo33] where the normal component decreases monotonically from the fiber pole whereas the maximum of the shear component is located between the fiber pole and the equator. Since the stress conditions involves solely the normal stress, the required displacement to fulfill the stress condition increases monotonically with the debonding size, here described by the debonding angle θ_{d}. Unlike the stress condition, the ERR exhibits a maximum in its variation, which is shifted when the critical ERR is introduced. The author used the relation of Hutchinson and Suo [HS91] to evaluate the critical ERR. The interface stress mixity changes from an opening mode to a shear mode as one moves from the pole of the fiber to the equator. The critical ERR therefore increases as the debonding angle increases. Consequently, the CC solution can be driven either by both conditions or by energy solely. Indeed, depending on the interface failure properties, the minimum of the two conditions can be located either in the IERR to critical ERR maximum,

or at the intersection of the two curves. Figure II.31 shows the normalized remote stress required to fulfill both stress and energy criteria for two different values of the interface brittleness number (Equation (II.31)), introduced by the author as follows:

$$\gamma = \frac{1}{\sigma_c}\sqrt{\frac{G_{IC}E^*}{r}}, \tag{II.31}$$

where σ_c and G_{IC} denote the tensile strength and the critical ERR in mode I, respectively. The parameter r is the fiber radius and E^* the harmonic mean of the effective elastic moduli of the two constituents.

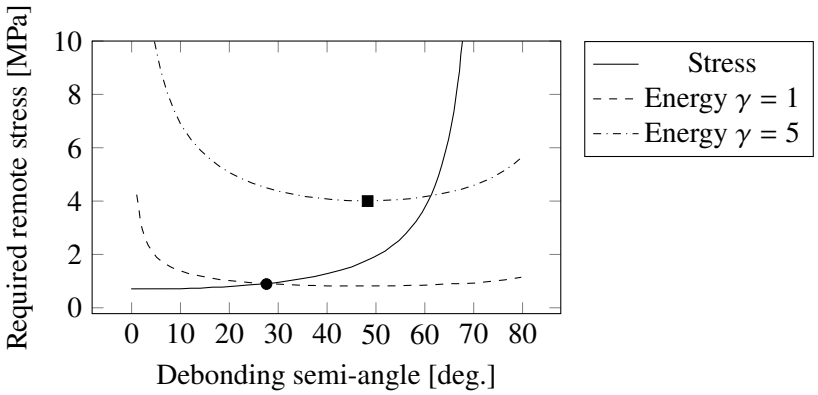

Figure II.31 – Normalized required remote stress to fulfill both stress and energy conditions with two different interface brittleness numbers, from [Man09]. The CC solutions are indicated with the markers.

For a small interface brittleness number, corresponding to a small critical ERR, the CC solution is described by the intersection of the two conditions, indicated by the round marker. For a larger critical ERR, the solution becomes that of the energy condition, since the stress condition is already fulfilled and no longer has any influence (square marker).

Similarly, García *et al.* [GMG15] investigated the favorable configuration between one or two symmetric debondings at fiber-matrix interface. The stress condition remains unchanged unlike the energy one which is less favorable with two symmetric debondings. Muñoz-Reja *et al.* [Muñ+16b] assessed debonding initiation in a two-fiber configuration under biaxial loading, varying the fiber intercenter distance between 2.25 and 2.5 times the fiber radius and compared two different inter-center angles. Asymmetric debonding locations with respect to the loading direction were obtained.

Since the CC and CZM share the same input parameters, *i.e.*, strength and critical ERR, a direct comparison between them can be achieved, which is presented in the sequel.

CC versus CZM

Numerous comparative studies have been carried out to compare the results of the CC with those of CZM. Among these, minor discrepancies have been observed between the initiation remote loading obtained with the two approaches [CSC16; Dim+17]. In particular, García *et al.* [GPM14] studied the single fiber composite using both the CC and CZM, focusing on the effect of fiber size. Tvergaard's CZM [Tve90] was used by the authors. With regard to the implementation of the CC, a Mohr-Coulomb stress criterion was used and fixed in order to obtain a critical ERR similar to that of CZM. The authors found similar remote stress at initiation for large fibers, while larger discrepancies were observed for smaller fibers. Similarly, Gentieu *et al.* [Gen+19] analyzed particle size effect on debonding initiation and compared both the CC and CZM. The authors also observed a transition in the CC solutions where both stress and energy-driven initiation take place for large particles while energy-driven configuration are encountered for small particles. Such mechanisms can be explained by the independence on the stress condition from the particle radius, see the solid black line in Figure II.32a.

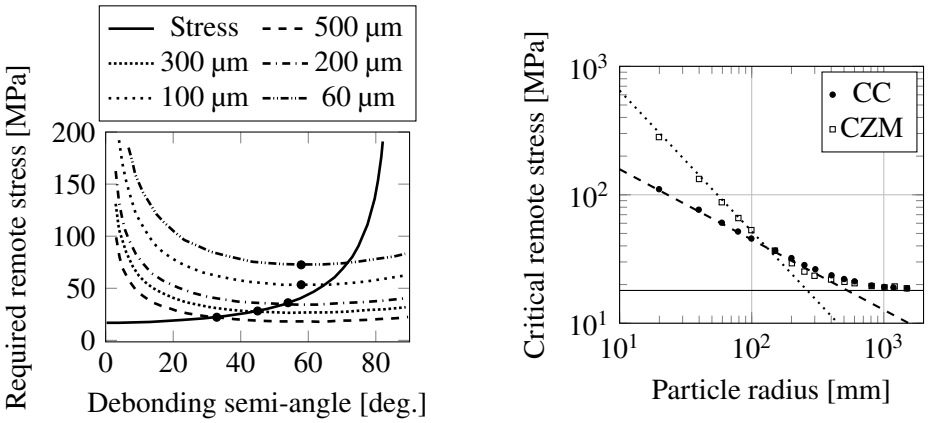

Figure II.32 – (a) Required remote stress to fulfill both stress (slide lines) and energy (dashed lines) criteria for different particle radius where the favorable solutions are depicted by round markers, from [Gen+19]. (b) Critical remote stress from both the CC and CZM as a function of the particle radius, from [Gen+19].

However, the energy condition, represented by the dashed lines in Figure II.32a, is strongly radius dependent, where a smaller radius implies a smaller IERR and therefore a larger remote loading to reach the critical ERR. Therefore, there is a transition where the CC solution is driven either by stress and energy or by energy only, the solutions being indicated by the markers in Figure II.32a. Similar phenomena are also observed with CZM. Figure II.32b shows the remote stress required for debonding initiation as a function of the square root of the particle size for the two numerical approaches. For large particles, agreement is observed between the CC and CZM. However, the decrease in particle size leads to larger discrepancies, where two different asymptotic regimes are encountered. The CC therefore follows an asymptotic variation of $1/\sqrt{r}$ while the CZM varies proportionally to $1/r$, r being the particle radius. The difference between the two asymptotic behaviors was explained by the presence of a process zone before debonding and the relative process zone size compared to the particle radius, which allows energy to be dissipated before crack initiation.

II.5 Summary and next challenges

Numerous experimental methods exist for assessing the fracture properties of the fiber-matrix interface. Among the different methods, most of them focus on the determination of shear properties such as pull-out test, fragmentation test, push-out test. However, there is a lack of experimental techniques for determining opening properties, despite the methods proposed in [KMM98]. It is worth mentioning that opening fracture properties are as important as shear properties, particularly when the composite is subjected to transverse loading. One major drawback highlighted previously is the lack of standardization of the different experimental techniques, where larger discrepancies can be observed between tests, and especially between operators. Therefore, a closer examination of the experimental set-up, combined with accurate modeling of the problem, could help to reduce discrepancies and determine more relevant fracture properties. Furthermore, the development of experimental techniques involving subjecting the fiber-matrix interface to mode I is necessary. To this end, the use of a single-fiber composite subjected to transverse tension appears to be advantageous since the debonding transitions from mode I to mode II. This technique enables the tensile and shear fracture properties to be determined. Consequently, similar single-fiber composites are used in this thesis work, with the emphasis on the experimental characterization of debonding that needs to be developed.

The modeling of fiber-matrix debonding has evolved from analytical models to finite element models coupled with dedicated fracture models. Analytical models are advantageous because they are very efficient when the configuration is simple. However, their implementation becomes a challenge when real and imperfect experimental

conditions are taken into account. Examples include fiber misalignment, an imperfect loading configuration, a defect in the sample manufacturing. In this sense, FE are a very useful tool for considering a realistic model. Among the most widespread models, the CC and the CZM appear to be a relevant compromise to numerically study the fiber-matrix debonding. The CC is efficient in the case of small deformation and linear elasticity, which is the case for the material considered in this thesis. Few studies have used the CC to assess debonding at the fiber-matrix interface. However, none of these studies has used the CC in conjunction with experimental observations to assess the fracture properties of the interface. The CC is thus applied in this work to the fiber-matrix debonding prediction using experimental observations of the debonding process. In addition, the CC and CZM predictions were mainly compared on the basis of the initiation loading only. CZM are therefore applied to fiber-matrix debonding on both initiation and propagation and compared with experimental observations and the CC predictions. Contrary to CZM, most of the CC application are nevertheless restricted to single crack location with known crack path. The main difficulty lies in determining the crack path, which can be theoretically described by an infinite number of configurations. Most current studies base the crack path on a parameterized shape or on stress isocontours, which do not take into account the energy aspect. An approach is therefore proposed in 2D to evaluate the CC solution based on stress isocontours-based and energy-based debonding shapes in a two-fiber configuration where the crack path is no longer symmetric and has to be determined. Additionally, the CC has not yet been applied to 3D fiber-matrix debonding. A 3D model of this configuration is thus studied, the results being compared with those in 2D to evaluate the relevancy of the 2D model in adequately predicting debonding initiation. However, determining the crack path in 3D can be computationally expensive, especially when the solution is energy-driven. Stress isocontours are first considered as a first assumption to describe the potential debonding shape, and then extended to energy-based debonding shapes. It is done with the aim of determining what are the optimal 3D shapes to be use for crack initiation simulation.

CHAPTER III

Experimental characterization of fiber-matrix debonding

Content

Some results presented in the following chapter can be found in the two following articles published in peer-reviewed journals:
Characterizing fiber-matrix debond and fiber interaction mechanisms by full-field measurements by Robert Livingston, Behrad Koohbor [LK22];
Experimental characterization of in-plane debonding at fiber-matrix interface using single glass macro fiber samples by Hugo Girard *et al.* [Gir+23a].

III.1 Introduction and motivation

From the previous chapters, optimizing the fiber and matrix fracture properties appears as an essential aspect for improving the performance of composite structure. Appropriate experimental characterization is therefore essential. Livingston and Koohbor [LK22] pointed out several challenges, consistent with those reported in Chap-

ter II, inherent in current methods of fiber-matrix interface characterization, which motivated their experimental campaign. Firstly, most current characterization methods focus on determining shear fracture properties, whereas tensile properties are also important. Another challenge is the scale at which debonding occurs. Indeed, composites made up of fibers with a few microns in diameter requires the use of SEM for accurate observation. Additionally, single-fiber samples are generally used, which does not correspond to the actual microstructure of composites, where neighboring fibers induce perturbations of the stress field for instance. Moreover, there is a lack of precise experimental observations of the debonding process in the literature. On the contrary, the numerical model of interface cracking has improved considerably recently, and therefore requires accurate experimental results for relevant experimental-numerical comparisons. In particular, digital image correlation has proved to be a relevant element for calibrating numerical modeling.

To this end, Livingston and Koohbor [LK22] proposed to characterize fiber-matrix debonding using glass macro-fibers (few mm in diameter) embedded in an epoxy matrix. Two different types of sample were studied in the sequel, a single-fiber sample and a double-fiber sample, the latter enabling the influence of a neighboring fiber to be assessed. Macro-fibers enable to extract significant quantities without the need for SEM or microtomography.

The following chapter is devoted to describing the experimental aspects of this thesis work. Several batches of samples are fabricated or studied, each with a specific reference. *Single fiber batch I* (SFI) refers to the single fiber samples prepared by Livingston and Koohbor [LK22]. *Single-fiber batch II* (SFII) corresponds to single-fiber samples prepared as part of a collaboration with Rowan University. Finally, *Double-fiber batch* (DF) refers to double-fiber samples prepared by Livingston [LK22]. Several experimental techniques have been developed in order to characterize the debonding topology as a function of the remote loading. More specifically, the following geometric quantities are extracted: i) the debonding angle at the free surface, ii) the debonding opening at the fiber pole relative to the loading direction, iii) the debonding length through the thickness at the fiber pole and iv) the shape of the debonding front along the interface. These latter quantities enable experimental-numerical comparison in the determination of the fracture properties of the fiber-matrix interface.

The experimental chapter is therefore divided as follows. Section III.2 presents the different aspects related to the materials used, the manufacturing process and the mechanical behavior of the samples. Techniques for characterizing the debonding are then described in detail in Section III.2, with a discussion of the results obtained. Finally, the experimental results are presented in Section III.3, alongside with current limitations.

III.2 Experimental methods and samples

III.2.1 Sample preparation and testing

Different batches of samples are studied in this work. Depending on the batch, different constituents are used. For the sake of clarity, the types of matrix and fiber used for the different batches are summarized in Table III.1, where d_f indicates the diameter of the fiber.

Batch	Ref.	Fiber	Matrix
Single-fiber batch I	SFI	Borosilicate GF, $d_f = 2$ mm	Epoxy ProMarine Supplies Co.
Single-fiber batch II	SFII	Quartz GF, $d_f = 1$ mm	Epoxy SD2505/SR1500, Sicomin
Double-fiber	DF	Borosilicate GF, $d_f = 2$ mm	Epoxy ProMarine Supplies Co.

Table III.1 – Summary of the constituents used in the different batches of samples.

The SFI and DF batches have the same constituents, unlike the SFII batch. All samples use glass fiber with an epoxy matrix, details of which can be obtained from the manufacturer.

Single-fiber batch I [LK22]

Two single-fiber composite samples are fabricated by Livingston and Koohbor [LK22] by embedding a glass macro-fiber in a thermoset epoxy resin. A room-temperature curable epoxy resin (ProMarine Supplies Co., MI, USA) is used to avoid any residual stress due to thermal expansion mismatch between fiber and matrix during high-temperature curing. The macro-fiber has a diameter of 2 mm, enabling high magnification optical observation of the debonding. Borosilicate glass fibers (McMaster-Carr, USA) are used because of their properties, which are similar to those of E-glass fibers. Three different tensile tests of neat epoxy are carried out to assess the elastic properties of the matrix, the stress-strain curves of which are shown in Figure III.1 [LK22]. Dog bone samples are prepared in a mold in accordance with ASTM D638 and tests are performed at room temperature under quasi-static loading. The behavior of the matrix shows an almost linear variation up to 1% strain, followed by a more pronounced non-linear phase. The elastic properties of the fiber and matrix are given in Table III.2, where E and ν denote Young's modulus and Poisson's ratio respectively. Fiber elastic properties are supplied by the manufacturer.

Property	Epoxy	Glass Fiber
E [GPa]	2.36 ± 0.10	63
ν	0.40 ± 0.04	0.3

Table III.2 – Elastic properties of the matrix and fiber [LK22].

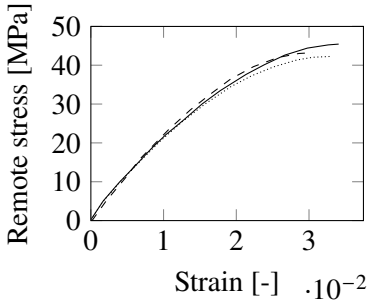

Figure III.1 – Stress-strain curves of epoxy samples loaded in tension [LK22].

The uncured epoxy mixture is poured into a silicone mold with dimensions conforming to ASTM D638, with a 13 mm wide and 6 mm thick cross-section. Figure III.2 shows the dimensions of the single-fiber sample, with the macro-fiber placed in the center.

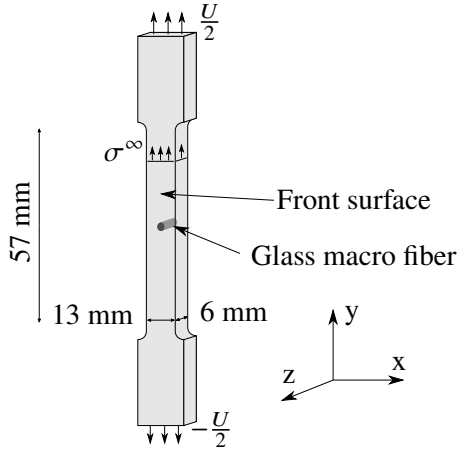

Figure III.2 – Single fiber specimen geometry and dimensions.

The fiber end which is in contact with the mold is further polished to achieve perfect flatness and prevent chipping of the fiber end, which could lead to premature debonding. Prior to insertion, the fiber surface is cleaned with isopropanol. A 3D-printed jig holder holds the fiber perpendicularly until the epoxy is fully cured. A curing time of 48 hours is adopted at room temperature. After curing, the front surface of the sample is lightly polished with fine sandpaper. The polished surface is then patterned for DIC purposes. The samples are tested under tension at a quasi-static constant cross-head speed of 5 mm/min. A 5 megapixel camera (Basler acA2440–75

µm, Germany) equipped with high magnification lens (Tokina atx-i 100 mm macro lens) is used to capture the front surface images at a rate of 1 image per second.

In the sequel, the two samples of batch I are designated as follows: SFI-1 and SFI-2 whose references are detailed below:

$$\underbrace{\text{SF}}_{\text{Single Fiber}}\ \underbrace{\text{I}}_{\text{batch I}}\ -\ \underbrace{1}_{\text{sample number}}\ ,$$

where SF indicates the Single Fiber sample, followed by the batch number, *i.e.*, I, and finally the number of the sample in the batch, *i.e.*, 1 or 2.

Single-fiber batch II

A second batch of single-fiber samples is made, as part of the collaboration with the Rowan University, to observe debonding on the front and side surfaces simultaneously, which are shown in Figure III.3.

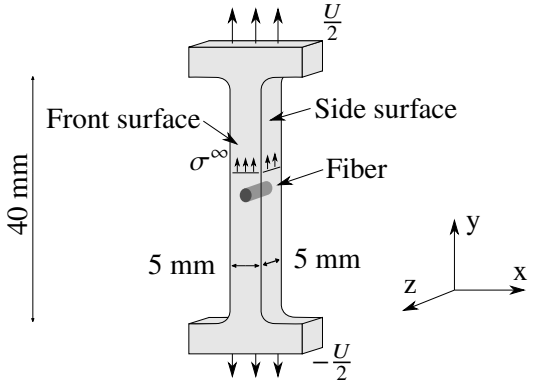

Figure III.3 – Single fiber specimen geometry and dimensions for the second batch.

The epoxy resin (SD2505/SR1500, Sicomin, France), which is different from SFI batch samples, is cured at room temperature with a curing time of one month to ensure that the resin is fully cured. Isotropic elastic properties of the epoxy matrix are determined in-house, using 5 samples with the same epoxy mixture as the single-fiber samples to avoid elastic properties depending on the mixture ratio of resin-hardener. Tensile tests are carried out on 3 samples at room temperature under quasi-static loading, whose stress-strain curves are shown in Figure III.4a.

All 3 samples show similar almost linear behavior up to fracture. The single-fiber samples from batch II exhibit slightly stiffer epoxy behavior than those from batch I. However, smaller failure strains are observed in batch II samples, as the shapes of the latter induce a stress intensification in the grips vicinity, leading to premature failure

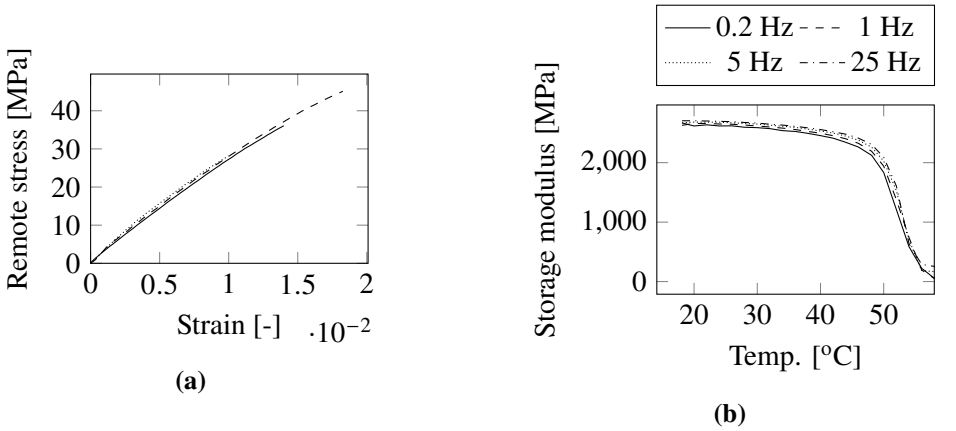

Figure III.4 – (a) Strain-stress curves for 3 different samples of neat epoxy. (b) Variation of the storage modulus as a function of the temperature for 4 different loading frequencies.

(see Figure III.3). Dynamic Mechanical Analysis (DMA) is also carried out on 2 samples to assess the influence of loading frequencies and temperature on epoxy elastic properties. Figure III.4b shows the variation in storage modulus, *i.e.*, Young's modulus, as a function of temperature for 4 different loading rates. The storage modulus varies slightly between 20 and 55°C, 55°C being assumed to be the glass transition temperature T_g. The glass transition temperature is confirmed at around 60°C by a differential scanning calorimetry test conducted on one sample. The elastic behavior of the epoxy is also independent of the loading rate, the storage modulus being identical for all loading rates. These results confirm the good curing of the resin. The average elastic properties obtained from the 5 samples are given in Table III.3, along with those of the 1 mm glass fiber supplied by the manufacturer. Although the fiber diameter is different from that of batch I, quartz glass fiber (McMaster-Carr, USA) is used in batch II compared with the borosilicate glass fiber (McMaster-Carr, USA) used in batch I.

Property	Epoxy	Glass Fiber
Young's Modulus [GPa]	2.7 ± 0.2	72
Poisson's ratio	0.41 ± 0.04	0.17

Table III.3 – Elastic properties of the matrix and fiber. The fiber properties are provided by the manufacturer and the matrix properties are averaged from 5 in-house measurements. The epoxy matrix used for the samples in batch SFII is different from that used in batch SFI.

Single fiber samples of batch II are made by embedding a 1 mm diameter quartz glass fiber in a clear, room-curable epoxy. The dimensions of the sample are defined for use in micro tensile testing machine (see Figure III.3). The final sample has a 5 mm wide and 5 mm thick cross-section. As for batch I, the single fiber is held in place using a 3D-printed jig. The surface of the fiber is cleaned with isopropanol to remove any unwanted substances from the surface. The matrix is then poured into a silicone mold, where the latter is drilled at the location of the fiber to allow it to protrude from the final sample. This eliminates the need to polish the end of the fiber itself. Curing time is also one month at room temperature. After curing, the front surface of the sample is slightly polished with fine sandpaper (10 µm grain size). The side surfaces are also polished, first using very fine sandpaper ($<$ 8 µm grain size), then using a rotating cotton disc coupled with a polishing solution to obtain a perfectly clear, flat side surface. The front surface is then patterned using spray paint for DIC.

Samples are tested under tension at a constant displacement rate of 0.18 mm/min. A dual-vision system consisting of two perpendicularly positioned cameras (FLIR Grasshopper GS3-U3-41C6M-C) is installed. This allows simultaneous observation of the front and side surfaces of the sample. Batch II samples are designated by the acronym SFII according to the nomenclature introduced for batch I, followed by the sample number, *e.g.*, SFII-1, SFII-2.

Double-fiber batch [LK22]

As with the two samples in batch I, double-fiber samples are fabricated and characterized by Livingston and Koohbor [LK22]. The manufacturing process and materials used are identical, see Section III.2.1, the single fiber being replaced by two fibers. Figure III.5 shows the geometry and dimensions of the sample, sized in accordance with ASTM D638 as for batch I.

Thirty samples are subjected to uniaxial tensile loading along the y-direction, leading to a remote stress (σ^{∞}). Tests are performed at room temperature under quasi-static loading. The inter-center angle (α) from the x-direction and distance (d) are varied in the range 0, 30, 45, 60 and 90 degrees and $2.5r$, $4r$ and $5r$, respectively, with r the fiber radius equal to 1 mm. It is worth noting that both fiber absolute positions do change between the configurations as they are rotated with respect to the inter-center midpoint. The experimental positioning of the fibers probably induced a slight shift of the fibers inside the matrix compared to the nominal position. Table III.4 thus shows the nominal and measured values of the angles and inter-center distances for each configuration, facilitating more accurate modeling of the experimental configurations [LK22].

A loading and camera configuration similar to that of batch I is used for double-fiber samples. In the sequel, the following designation is adopted for the different

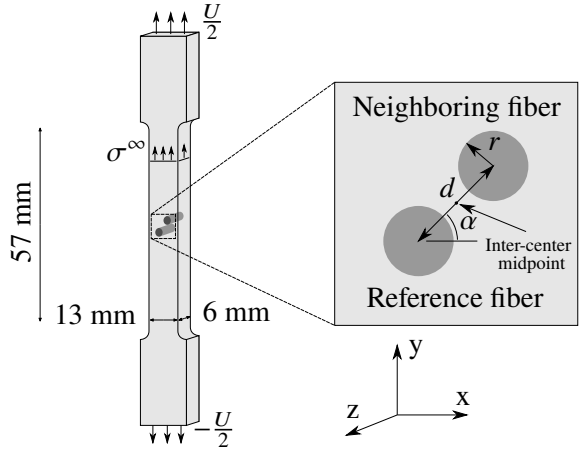

Figure III.5 – Double-fiber specimen geometry and dimensions including two fibers (radius r), where d is the inter-center distance and α is the angle between the x-direction and the direction passing through both fiber centers [LK22].

Inter-center distance d [mm]		Inter-center angle α [deg.]	
Nominal	Measured	Nominal	Measured
2.5r	2.9±0.3		5.4±1.3
4r	3.7±0.2	0	4.2±1.6
5r	4.7±0.1		0.4±0.1
2.5r	2.7±0.2		38.8±3.6
4r	3.9±0.2	30	32.8±1.7
5r	4.8±0.1		31.3±1.6
2.5r	2.5±0.1		46.7±2.1
4r	3.6±0.2	45	46.0±0.2
5r	4.8±0.1		48.5±1.5
2.5r	2.5±0.1		55.1±4.7
4r	4.1±0.2	60	62.1±2.1
5r	4.8±0.2		57.8±2.2
2.5r	2.5±0.0		90.6±5.5
4r	3.9±0.1	90	88.5±1.2
5r	4.9±0.1		91.0±0.1

Table III.4 – Nominal and measured values of inter-center angle and distance for each configuration of double-fiber sample where two samples are studied by configuration [LK22].

double-fiber samples:

$$\underbrace{\text{DF}}_{\text{Double Fiber}} - \underbrace{45}_{\text{angle}} - \underbrace{4.5r}_{\text{distance}},$$

where DF indicates the Double Fiber sample, followed by the fibers inter-center angle, α, and finally the inter-center distance, d.

III.2.2 Debonding characterization

Fiber-matrix debonding can be characterized using a variety of techniques, each requiring a specific experimental set-up. Analysis of the literature shows that a binary description of a crack, either damaged or not, is not always suitable [EF84; HW92]. A possible process zone may take place at the crack front vicinity. However, determining the size of the process zone from an experimental point of view is somewhat challenging. As a result, no process zone is considered in the description of the geometry in the sequel. Two states are thus used to describe the debonding: undamaged and damaged. The following geometrical parameters are used to describe the debonding geometry, translating a fully damaged interface zone. This description is adopted since the coupled criterion used in this thesis work relies on a binary vision of the crack. Thus, the proposed approach is suitable for its numerical implementation. Figure III.6 shows the parameters describing debonding geometry. Since straight-faced samples are used, debonding is likely to initiate at the free surface [OSK09].

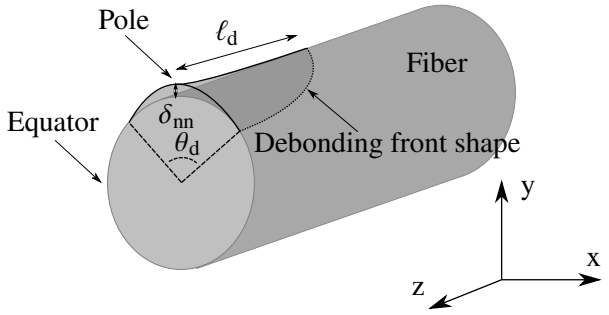

Figure III.6 – Fiber-matrix debonding geometrical parameters, where θ_d denotes the debonding angle at the free surface, δ_{nn} the debonding normal opening at the fiber free surface pole and ℓ_d the debonding length at the fiber pole.

Debonding can be described by the debonding angle θ_d at the free surface, measured by the angle between the two debonding tips. The quantity δ_{nn} corresponds

to the maximal normal debonding opening located at the pole of the fiber free surface with respect to the loading direction (*i.e.*, y-direction here), assuming symmetric debonding. The debonding opening actually reflects the distance separating the two lips of the crack. The length of debonding through the thickness is described by ℓ_{d}, which corresponds to the length of debonding in the z-direction at the pole of the fiber.

The following sections are devoted to the experimental procedure used to measure each parameter.

Debonding angle determination

The monotoring of the debonding angle as a function of the remote loading is of interest to calibrate numerical model and identify interface fracture properties. The determination consists of locating the debonding tips and thus derive the corresponding angle separating them. To observe the debonding process, a camera, whose reference is given previously in Section III.2, with high magnification lens, is placed parallel to the front side (see Figure III.2), and zoomed over the fiber location. This enables the *in-situ* extraction of images synchronized to the loading level. Two different methods allow for the debonding angle observation.

The first method implies optical observation of the debonding. Each image is imported into an image processing program [Sch+12] and zoomed in to observe the interface at the pole. Upon the debonding initiation, the formation of a debonded black area allows the identification of the two tips of the crack, enabling the measurement of debonding angle. Nevertheless, precise crack tip identification remains a challenge since the debonding opening becomes smaller when approaching the crack tip and also because the debonding opening may be small (*e.g.*, smaller than a pixel) in zones where the interface is solicited under dominant shear stress state. In addition, it raises the question of the presence of a process zone and therefore the definition of the actual crack tip. Since this method is highly operator-dependent, and in order to reduce the associated uncertainties, angle determination can be carried out by several operators.

The second strategy for estimating the debonding angle is to use DIC analysis with Ufreckles software [Ret18]. The correlation can locally not be achieved in the presence of a previously non-existent black debonded zone (*e.g.*, appearance of new black pixels). This results in high correlation residuals, highlighting the debonded zone [TRH16]. Consequently, the debonding angle can be determined by applying a threshold to the correlation residuals. The threshold is necessary to ensure that the debonding angle measurement is not affected by measurement noise at low loading levels prior to crack initiation. In addition, the DIC residual threshold is selected in such a way that for a large debonding angle, it converges towards optical observation.

Figure III.7 shows a qualitative comparison between the debonding observations obtained by the two methods. Both images are extracted for a similar imposed loading. Both methods yield similar debonding angles, but their location differs slightly. The location of the fiber is highlighted by red and white shaded areas in Figure III.7a and Figure III.7b, respectively.

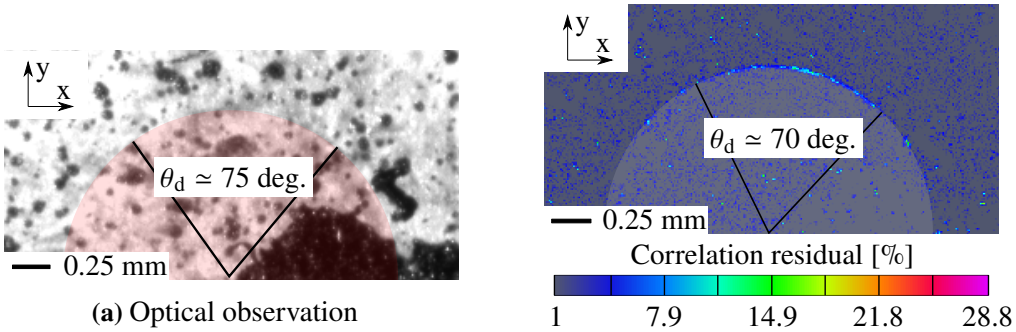

(a) Optical observation

(b) DIC residual

Figure III.7 – Determination of the debonding angle by (a) optical and (b) DIC residual approaches. The remote stress corresponding to both images is approximately 5 MPa. The debonding angle in (b) is identified based on a 1% threshold.

A primary drawback in determining the debonding angle is its dependence on the pixel size. The pixel size relative to the debonding opening must be significantly smaller. Thus, a suitable magnification needs to be chosen according to the fiber size. To overcome this limitation, other debonding dimensions, such as the debonding opening, may enable the capture of sub-pixel phenomena using DIC. Therefore, one possible approach may be to couple numerical simulation with experiment to provide a numerical debonding angle that leads to a debonding opening similar to that observed experimentally.

Debonding opening determination

The debonding normal opening can provide information about the debonding initiation remote loading to further perform inverse identification of the fiber-matrix interface fracture properties. Such a quantity requires the use of DIC analyses to determine the displacement fields from which the opening can be derived. To this end, a camera is positioned in a similar way to that used for the debonding angle, but the displacement fields are used instead of the correlation residual. Determination of the debonding opening is therefore possible at any point along the fiber-matrix interface. However, only the debonding opening at the pole of the fiber with respect to

the loading direction is studied in the following, since debonding is likely to start at this location. Two different DIC softwares are used here, namely VIC 2D [Cor] and Ufreckles [Ret18], both of which require a different procedure to obtain the debonding opening.

The VIC software offers the possibility of placing virtual extensometers to evaluate the variation in displacement between two material points. The extensometers are placed so that they encompass both the fiber and the matrix, and pass through the pole of the fiber. The length of the extensometer is chosen according to the step size, with a longer length being considered to accurately capture the debonding process. Before the debonding initiation, the relative displacement measured by the extensometer remains relatively low, since it corresponds to the deformation of both the fibers and the matrix in the vicinity of the interface. Once the debonding has initiated, the strain at the debonding lip vicinity tends toward zero, *i.e.*, no more loading transfer between both media through the interface. As a result, the actual displacement difference measured by the extensometer is representative of the debonding opening. Thus, the measured debonding opening is assumed to be independent of the extensometer length.

This assumption is confirmed by FE calculations in which a 2D plane strain model of an embedded circular inclusion is established. Elastic properties similar to those of the epoxy matrix and glass fiber are taken into account, see Table III.2. The real numerical debonding opening is determined as the nodal distance between the fiber and matrix nodes located at the pole. As with the VIC approach, the extensometer length variation obtained from virtual extensometers with lengths ranging from $r/3$ to $r/1.5$ is calculated to analyze the influence of the extensometer length. Figure III.8 shows the variation in numerical extensometer length as a function of debonding angle for the three different initial lengths, compared with the actual debonding opening.

Although the debonding opening displacements show difference at small angles, for debonding angles larger than 40 deg., the opening measured by the extensometer provides an accurate estimate (with relative differences smaller than 3%) whatever the extensometer length. Differences obtained for smaller angles are due to the interface debonding angle being too small so that the obtained quantity is representative of the displacement due to the fiber and matrix local stretches rather than the actual opening of the debonded interface.

The second approach in determining the debonding opening involves the use of Ufreckles software [Ret18], from which displacement fields can be derived. This second technique is primarily used in this thesis work. Figure III.9 shows an example of the U_y displacement field with removed rigid body motion obtained using 2D DIC at the fiber vicinity, superimposed with the associated image where the fiber location can be identified in-between the two displacement discontinuities by the black circle.

The displacement field in Figure III.9 results from a loading in the y-direction.

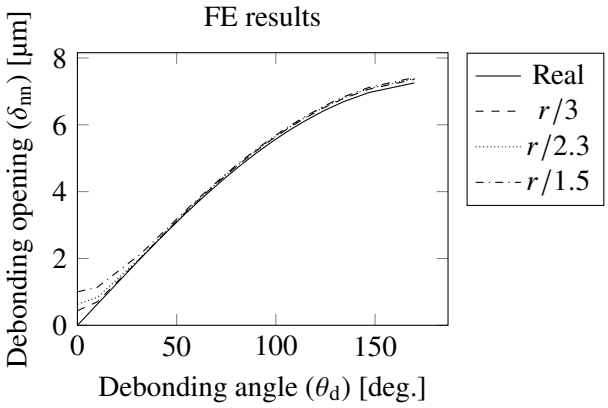

Figure III.8 – Normal debonding opening obtained with a FE calculation at the fiber pole as a function of debonding angle for three extensometer lengths of $r/3.0$, $r/2.3$, and $r/1.5$. The actual displacement of the interface opening due to debonding, denoted real, is also included for reference.

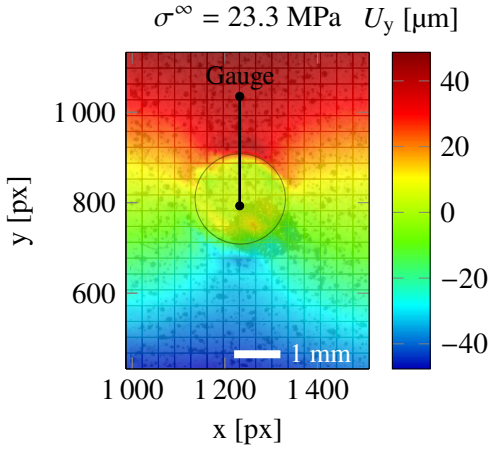

Figure III.9 – Displacement field U_y obtained at the fiber vicinity superimposed with the image and the mesh used for the DIC. Locations of the gauge and the fiber are indicated by the straight black line and the black circle, respectively.

DIC is performed using a mesh size of 35 pixels, the mesh being superimposed in Figure III.9. The pixel size corresponds to 10 µm. A 2.5 mm long virtual gauge aligned with the loading direction and passing through the fiber and the matrix at the

top pole is positioned as seen in Figure III.9. The U_y displacement is determined along the gauge as a function of the applied remote loading within both the fiber and matrix. The gauge size was chosen to embed several points of measurements (see the mesh in Figure III.9). Figure III.10 shows the variation in displacement along the gauge for several remote loadings.

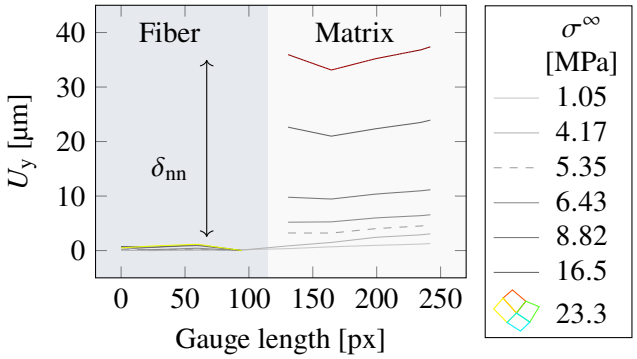

Figure III.10 – Displacement along the gauge for several loading levels.

The profile obtained for $\sigma^\infty = 23.3$ MPa is depicted with colors consistent with the associated displacement field shown in Figure III.9. For sufficiently small loading, *i.e.*, $\sigma^\infty < 4.2$ MPa, the displacement exhibits slight variations along the virtual gauge without any discontinuities at the fiber-matrix interface. The displacement presents larger variations within the softer matrix compared to the stiffer fiber. From a certain loading level, between $\sigma^\infty = 4.2$ and $\sigma^\infty = 5.4$ MPa, displacement discontinuously develops at the fiber-matrix interface, which can be associated with the debonding initiation. From this loading level, the displacement remains almost constant within either the matrix or the fiber, allowing the debonding opening δ_{nn} to be assessed by computing the displacement jump, as depicted in Figure III.10. It is noteworthy that the displacements are averaged in both phases to compute the debonding opening and the two extremes are used to compute the measurement uncertainties. This allows the remote loading at initiation and the corresponding debonding opening to be extracted. Therefore, opening variation can be assessed from this specific remote loading as shown in Figure III.11 for this example, with the associated uncertainties. Debonding initiation thus occurs at a remote stress ranging from 4.2 to 5.4 MPa in the configuration presented here. From the loading at which debonding is initiated until the sample is completely broken, debonding opening continues to increase, see Figure III.11.

Mesh size influence on the debonding opening variation is assessed in Figure III.12 in a similar configuration, *e.g.*, same sample and gauge location. Mesh sizes of 25, 35,

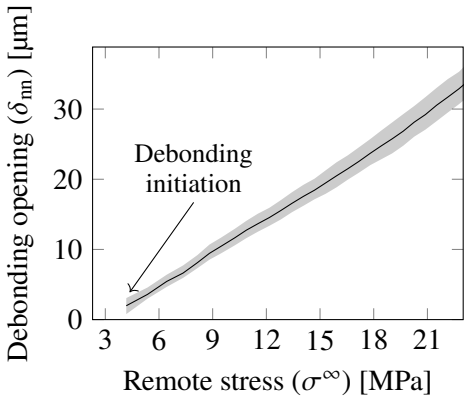

Figure III.11 – Debonding opening (δ_{nn}) extracted using the displacement fields as a function of the remote loading (σ^{∞}).

and 45 pixels are compared in terms of opening and associated uncertainties. Overall, computed openings reveal to be independent of the mesh size, unlike the uncertainties. Indeed, small and large mesh sizes provide increased uncertainties compared to intermediate size. Consequently, adequate intermediate mesh sizes have to be identified, with a corresponding size to be around $r/3$.

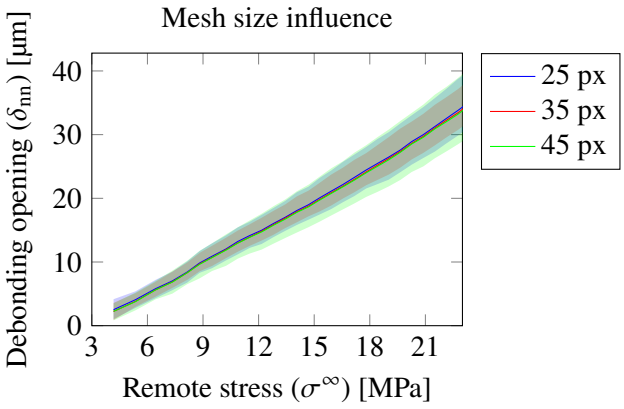

Figure III.12 – Debonding opening (δ_{nn}) extracted using the displacement fields as a function of the remote loading (σ^{∞}) for different mesh sizes using four nodes elements.

Unlike the regular mesh used above, results obtained with different mesh elements

and topologies are also compared. Figure III.13a shows a standard unstructured mesh composed of triangles. In order to accurately describe the debonding process, another mesh topology including the fiber-matrix interface is used, see Figure III.13b. Finally, the use of two distinct meshes respectively located in the fiber and in the matrix is also investigated, see Figure III.13c.

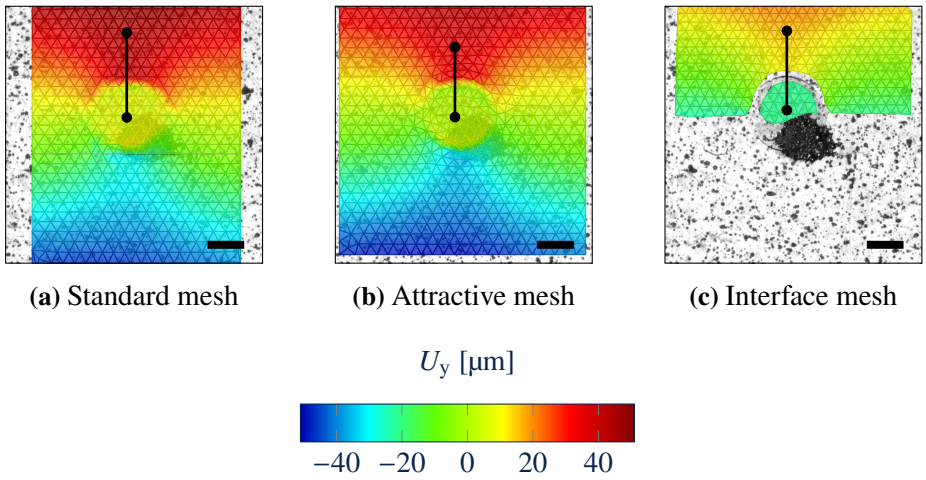

(a) Standard mesh **(b)** Attractive mesh **(c)** Interface mesh

Figure III.13 – Different mesh topologies using unstructured triangular elements: (a) a standard, uniform mesh topology is used with a 30 px mesh size, (b) the mesh topology follows the fiber-matrix interface with a 30 px mesh size and (c) two separate meshes are used in the fiber and matrix with a 25 px mesh size. All scale bars correspond to 1 mm.

Similar to the approach presented above for the determination of the debonding opening, the latter quantity is extracted using the different mesh elements and topologies. The location of the gauges is shown in Figure III.13 for each configuration. A comparison is also made with the opening obtained using the 2D VIC method. Figure III.14 shows the variation of the debonding opening as a function of remote loading for all mesh element and topology configurations.

With regard to the results obtained with Ufreckles, the openings remain in agreement from debonding initiation to sample failure, where opening relative differences no larger than 40% are observed. This observation confirms the accuracy of the standard mesh in capturing the debonding opening, which requires less implementation effort compared to other mesh topologies. Similarly, small discrepancies are observed between VIC and Ufreckles, ranging from 70% relative difference at initiation to 9% before failure. Both methods yield similar debonding opening, with the second re-

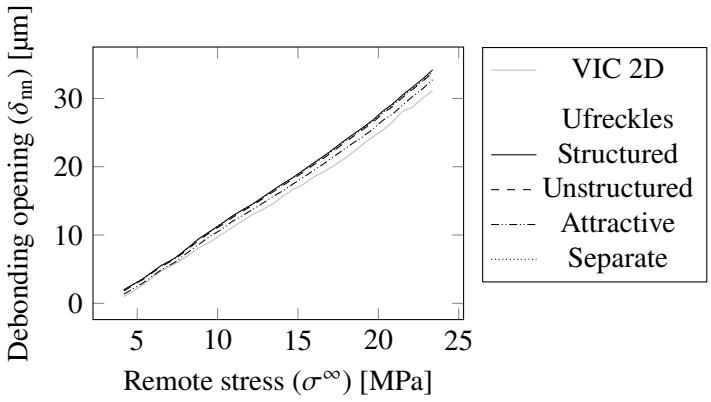

Figure III.14 – Debonding opening (δ_{nn}) extracted using the displacement fields as a function of the remote loading (σ^{∞}) for the different software, mesh elements and topologies.

quiring slightly more computational implementation to extract the quantity compared to VIC integrated tool.

Debonding length determination

The debonding length determination consists of observing and monitoring the debonding propagation through the thickness of the sample, *i.e.*, in the z-direction. Since debonding is likely to initiate and propagate at the fiber pole with respect to the loading direction due to the maximum stress attained at this location, the latter also corresponds to the maximum possible debonding length ℓ_d. The length is thus determined as the distance between the debonding tip at the fiber pole and the free surface pole of the fiber. This quantity is extracted using a camera placed parallel to the side surface of the sample (see Figure III.3). The camera is coupled with a high-magnification lens, zoomed in over the fiber location. Two light sources are positioned to highlight the two fiber poles. The images are extracted *in situ*, synchronized with the loading level. As with the determination of the debonding angle, two distinct methods are used to assess the debonding length.

The first method consists of an optical observation of the debonding. The side images are imported into image processing software, ImageJ [Sch+12], and zoomed in at the interface pole. Such measurements are possible due to the different refractive indices of both the fiber and the matrix. Since the two indices are different, light is reflected differently at the interface. The debonding causes a slight opening at the interface. This slight opening involves a third medium, *i.e.*, air, unlike an intact inter-

face, which means that light is reflected differently from that at the interface. Such a change in light reflection therefore allows for the identification of the crack location, as proposed in [Koy+09]. Figure III.15b shows an example of a side image where the debonded zone can be identified based on different gray intensity compared to undamaged interface (see Figure III.15a). The debonding tip location is indicated by the red triangle. The debonding length is thus determined as depicted in Figure III.15b, taking the maximum dimension of the debonded area. However, such debonding length measurements depend on the operator performing the observation. To reduce the uncertainty related to the operator, several measurements can be performed by several operators.

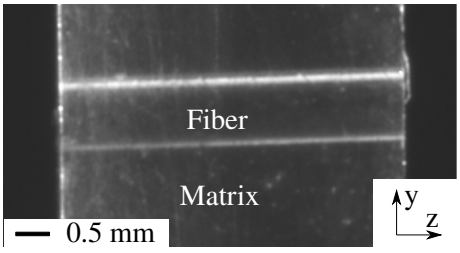

(a) Undamage interface

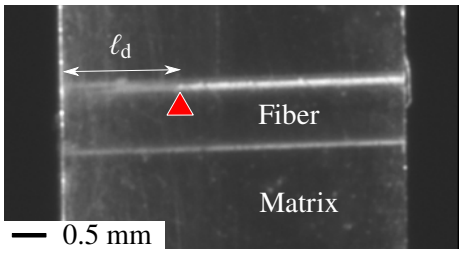

(b) Optical observation

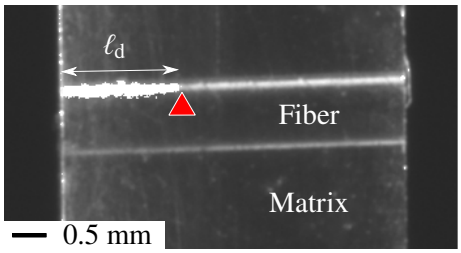

(c) Threshold

Figure III.15 – Side view of a single fiber sample where the debonding length is determined (b) optically by monitoring the gray level change and (c) using a threshold on image processing software. Image of the undamaged interface is added for reference in (a). The images (b) and (c) are extracted from a similar remote loading of 9.2 MPa.

The second method of determining debonding length consists of using an image processing software [Sch+12]. The side images are first imported into the software, then aligned to eliminate any motion induced by the tensile test, with the images shifted to match the previous one. In this way, the location of the fibers remains constant for several remote stresses, which facilitates identification of the debonding. The image preceding the onset of debonding is then selected, from which the gray level

difference for each pixel is performed with the subsequent images. As a result, the debonding area results in a large gray level difference compared to the initial image, while the other areas result in a difference close to 0. A threshold is then applied to the difference between the two images and superimposed on the real image. Pixels whose gray level difference is larger than the threshold are shown in white in Figure III.15c.

The new images with the debonded area highlighted can be imported into Python. The length of the debonded area is determined as the maximum distance within the threshold area, *i.e.*, the distance between the free surface and the red triangle in Figure III.15c. This second method is independent of any action by the operator, except for the definition of the threshold, which reduces uncertainties. It is also more efficient. The threshold is defined as a gray level difference. It is chosen so that the debonding length obtained corresponds to the optical observation of a large, well-defined debonding length. Two values are compared to ensure the accuracy of this method. Figure III.16 shows the debonding length as a function of remote stress obtained by the first method and the second method with two threshold values, namely 7% and 13% in gray level difference. The values are taken from a sample similar to that shown in Figure III.15. The second method provides consistent results regardless of the threshold chosen, with a difference of less than 0.02 mm.

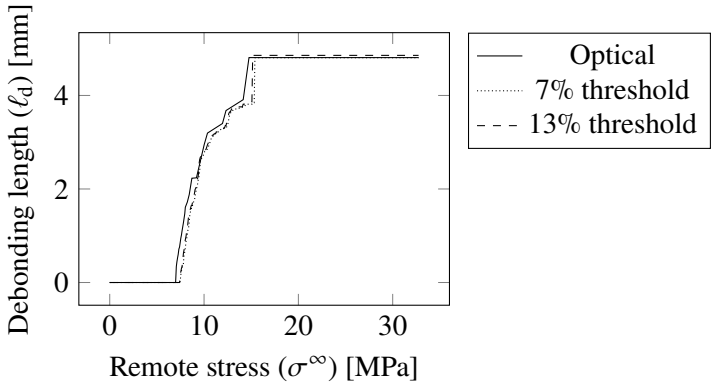

Figure III.16 – Debonding length as a function of remote stress for the two methods, with two threshold values being compared for the second.

The optical and threshold methods are in agreement and provide similar initiation remote loading, with the threshold results being slightly shifted. Optical determination provides earlier debonding than the threshold method, which may be explained by a too small gray level difference for a small debonding since debonding opening is small. The results of debonding length determination therefore appear to be independent of the technique employed. Consequently, all the above methods are suitable

for its determination, since regardless of the technique chosen, the influence on the result will be negligible.

Debonding shape determination

Alongside the method used to extract the debonding length from the zone obtained from the threshold, the shape of the debonding can also be extracted. This debonding shape may be of interest for further numerical modeling. As the debonding is likely to initiate from the free surfaces, the topology of the debonding between the free surface, *i.e.*, the debonding angle, and the debonding tip at the fiber pole, *i.e.*, the debonding length, still needs to be determined. The contour delimited by the debonded zone gives a description of the potential shape of the debonding, typically the debonding angle in all positions between the free surface and the tip of the debonding though the thickness at the fiber pole. The side images are then imported into Python. The position of the fiber pole is recorded from an image prior to the initiation of debonding so that the position of the debonding front relative to the fiber pole does not take into account the opening of the debonding. For a fixed y-coordinate from the free surface, the x-coordinate difference between the fiber pole and the debonding front is used to assess the through thickness debonding semi-angle. This semi-angle can be projected onto a cylindrical coordinate axis, corresponding to the fiber-matrix interface, to obtain a 3D shape of the debonding (see Figure III.17). The propagation of the debonding front can then be monitored as a function of remote loading.

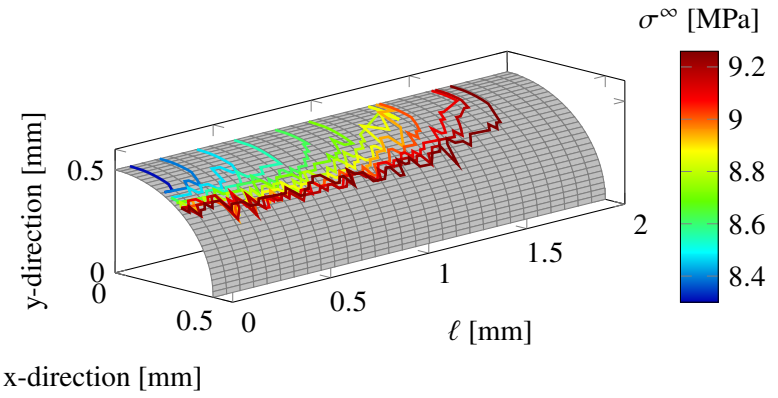

Figure III.17 – Debonding front as a function of the remote loading superimposed on a quarter of the fiber-matrix interface.

Figure III.17 shows the debonding front obtained from the side images as a function of remote loading for a single fiber sample. The loading is applied along the

y-direction. The gray surface corresponds to a quarter of the fiber-matrix interface, where the color gradient indicates the remote loading associated with each debonding shape. The debonding initiates from the free surface, *i.e.*, $\ell = 0$ mm, and then propagates along the pole of the fiber. In contrast to the slight increase in the debonding angle, there is strong propagation of the debonding through the thickness. The debonding fronts have a non-smooth topology which is explained by the resolution of the image. Consequently, this crack shape cannot be taken into account directly in a subsequent numerical model. One approach to address this issue is to smooth the data, for example using moving average of 5 points, see Figure III.18a.

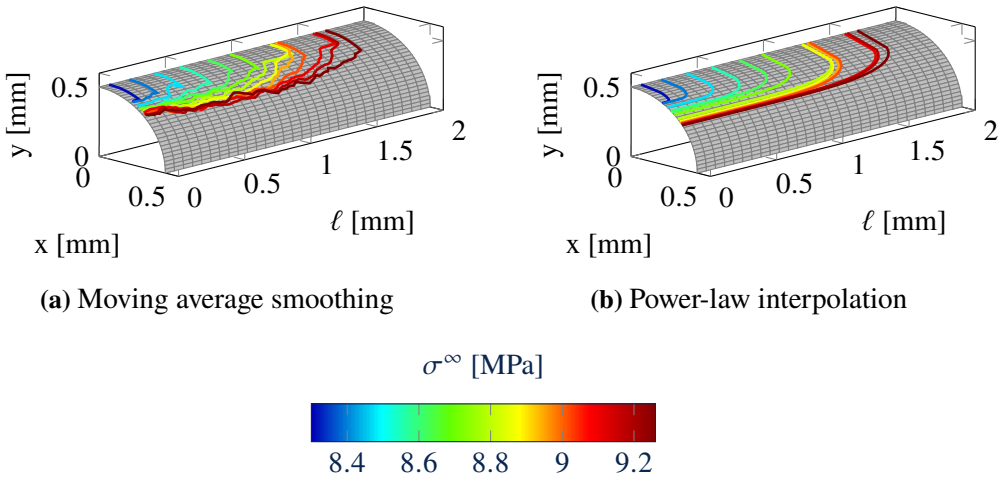

(a) Moving average smoothing **(b)** Power-law interpolation

Figure III.18 – (a) Smoothed debonding front as a function of remote loading with a moving average of 5 points. (b) Interpolation of the debonding front using a power-law and an exponent of 6.

Smaller variations in the debonding angle are observed along the front, but variations are still present with this method due to the large initial scattering. One approach to overcome these variations is to approximate the debonding front using a power-law, as shown in Figure III.18b. The power-law approximation seems appropriate because the exponent can be varied to appropriately match the apparent debonding angle at the free surface and the debonding length. This method is thus efficient in approximating the debonding front for subsequent numerical modeling. A power law exponent of 6 is shown to accurately describe the experimental debonding front.

One of the main drawbacks inherent to this determination of the shape of the debonding is the change in reflective index when the debonding is subjected to coupled compressive and shear loading as it approaches the fiber equator. The debonding

therefore propagates in shear rather than opening manner, which mitigates the presence of a third medium that causes changes in the reflective index. As reported by Koyanagi *et al.* [Koy+09], optical observation of the debonding at the fiber equator vicinity is challenging due to vanishing reflective index difference from the intact interface. A coupled experimental-numerical study is thus established to accurately determine the actual shape and angle of the debonding.

To overcome the above mentioned challenges, a numerical model is developed to assess the debonding shapes that best match the experimental observations; namely, the debonding opening at the free surface δ_{nn} and its length along the sample thickness ℓ_{d}. To this end, a 3D finite element model is established to reproduce the geometry of the sample and the boundary conditions of an observed experimental configuration. Tetrahedral elements are used to discretize the model under linear elasticity and small deformation assumptions. A mesh convergence study is achieved to ensure that the results are similar for a smaller mesh size. The displacement boundary condition is applied at the top surface of the model consistently with the experimental configuration, and the remote stress is computed using the summation of the nodal reaction forces at the model boundary. The elastic properties given in Table III.3 are used in this study for the matrix and the fiber since they correspond to the constituents employed experimentally.

Based on the front and side observations, two geometric parameters, *i.e.*, the debonding opening and length, can be extracted directly from the experimental observations (see sections above). However, the other two parameters that remain unknown and are required to define the complete debonding geometry are the debonding angle at the free surface and the debonding shape between the free surface and the crack tip at the fiber pole (see Figure III.6). Indeed, the debonding angle can be determined using the method proposed previously, however, this latter quantity is considered unknown in the sequel in order to assess the relevance of the side observation to provide the debonding shape and therefore the debonding angle throughout the thickness. The main objective of the numerical approach herein is to retrieve the experimental debonding opening for fixed debonding length, angle, and shape. Therefore, the suitable numerical solution would be able to match both experimental debonding opening and length simultaneously, providing quantitative data for the debonding angle and shape. It is noteworthy that each debonding stage corresponds to a specific loading level that is replicated in the numerical model. A range of 10 debonding angles from 20 deg. to 180 deg. are tested for each debonding length. Several possible debonding shapes are approximated using the expression given in Equation (III.1), where n can be varied from 2 to 6 to assess a wide range of shape options:

$$\ell(x) = \left(\ell_{\mathrm{d}} \left(1 - \left(\frac{x}{\sin\left(\frac{\theta_{\mathrm{d}}}{2}\right) r} \right)^{n} \right) \right)^{\frac{1}{n}}, \tag{III.1}$$

where r is the fiber radius. The determined shapes are drawn in the x-z plane and then projected onto the fiber surface. The interface nodes are unbuttoned within the surfaces defined by the debonding front shape. The debonding opening is further determined as the distance between the matrix and fiber nodes at the free surface pole of the fiber. This approach is also conducted by considering the opposite side debonding into consideration, *i.e.*, debonding initiated at the rear side of the sample propagating in -z direction. However, this opposite-side debonding propagation appeared to have a negligible influence on the opening quantities extracted, smaller than 1%. Figure III.19 shows the debonding opening observed experimentally as a function of the debonding length.

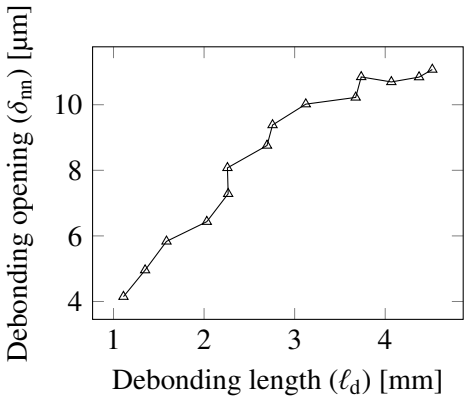

Figure III.19 – Variation of the experimental debonded interface opening δ_{nn} (in x-y plane) as a function of its length ℓ_{d} (along z-direction).

Figure III.20 shows the variation of the three previous quantities, namely debonding angle, interface opening, and length obtained from the numerical model using a fixed exponent $n = 4$. The debonding opening increases with the debonding angle and length. Similarly, for each value of n in Equation (III.1), a numerically determined debonding angle can be identified corresponding to a numerical interface opening that matches the experimentally measured values for a fixed crack length. The appropriate numerical debonding semi-angles are therefore superimposed on the numerical opening in Figure III.20 with a solid line and square markers.

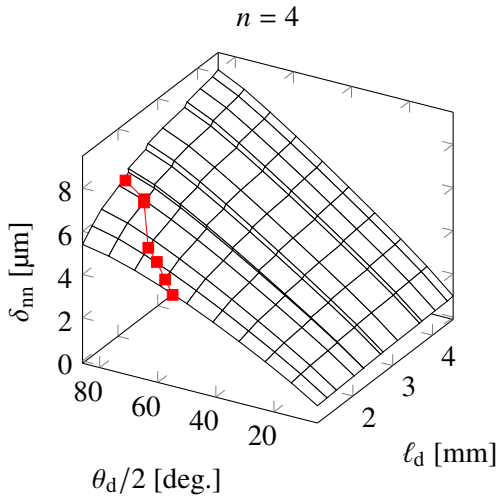

Figure III.20 – Variation of the debonding opening as a function of the debonding length and angle determined numerically. The numerical debonding parameters that correspond to the experimental debonding opening are depicted by the solid red line.

Figure III.21 shows the suitable numerical debonding angles for three different orders, *i.e.*, different n values.

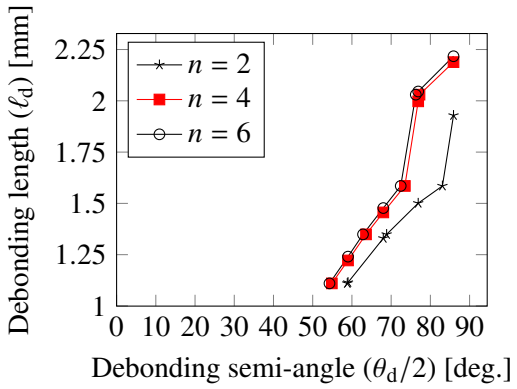

Figure III.21 – Numerical debonding angles that lead to similar openings for different debonding lengths.

The debonding angle starts between 55 deg. and 60 deg. and increases to 90

degrees. It can be observed that the debonding shape exponent plays only a minor role in the obtained debonding angle with differences smaller than 15 degrees. From a 2.25 mm debonding length, the numerical model failed to replicate the correct experimentally measured debonding openings, as the numerical results underestimated those measured experimentally. Such observation could be explained by the possibility of a gradual change of mechanical and interface properties along the sample thickness resulting from a spatially variable degree of cure of the along z-direction. If such variations in the degree of cure of the matrix exist, the sample center would be expected to exhibit softer behavior, leading to larger debonding openings obtained experimentally. It should be noted that the sample studied here is not part of the batch of samples presented above, so it has a curing time of one day. Regardless, further debonding length can thus be approximated by a 90 deg. debonding angle.

The numerically determined debonding shapes are shown on the fiber-matrix interface in Figure III.22a for $n = 4$.

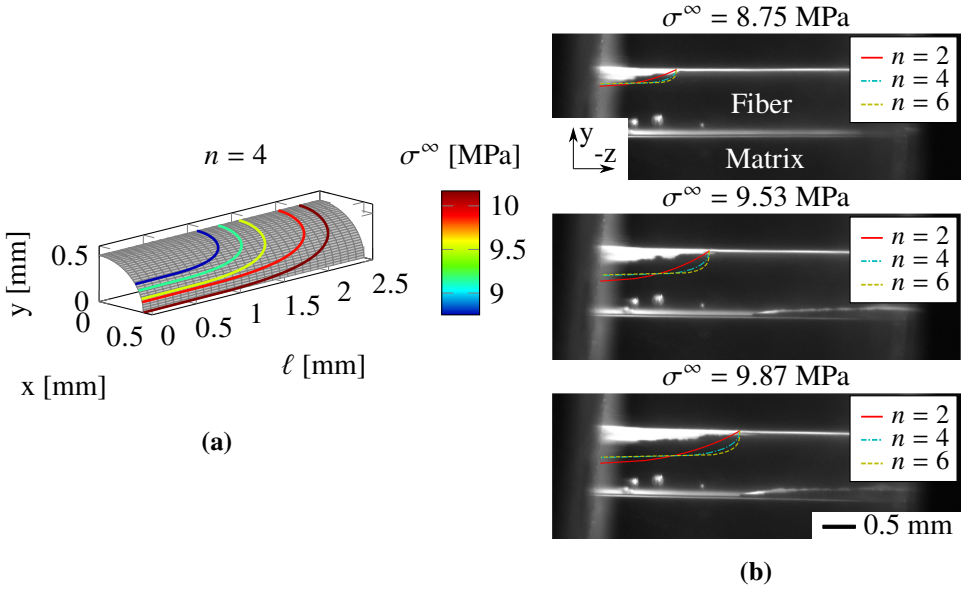

Figure III.22 – (a) Variation of debonding (crack tunneling) front as a function of remote stress based on the angles that best match the experimental opening and length, for $n = 4$. (b) Debonding front shapes for several loading stages superimposed on the optical images.

The debonding propagates significantly along the thickness while the increase in debonding angle remains less pronounced. Similarly, the determined debonding shapes are finally superimposed onto the side images obtained experimentally

in Figure III.22b. Overall good agreement is achieved at small remote stresses. The debonding shape encompasses the lighter area that is assimilated to the debonded zone. Nevertheless, larger discrepancies are obtained for larger stresses. Particularly, the numerically determined debonding areas are larger than the lighter areas observed on the side view images of the sample. The lighter zone seems to be representative of the actual fiber-matrix debonding except in areas loaded under combined shear and compression. In these zones, the presence of a debonding cannot be revealed only by the light contrast brought by the presence of a debonded interface.

It is important to mention that the debonding in this example is revealed by applying a threshold in the gray level intensity. However, the method introduced previously consists of a difference in gray level between an undamaged stage and a damaged stage. As a result, the results may be different and provide better correspondence with the actual debonding topology, as the actual method is less dependent on the operator who chose the threshold. The actual method is also compared in Section III.3 to assess its accuracy in determining the appropriate debonding angle.

The above conclusions can be confirmed by observing the debonding area for larger stresses, *e.g.*, a remote stress of 40 MPa. On the one hand, a fully debonded interface can be observed at the front surface (Figure III.23), meaning that a complete debonding angle is present.

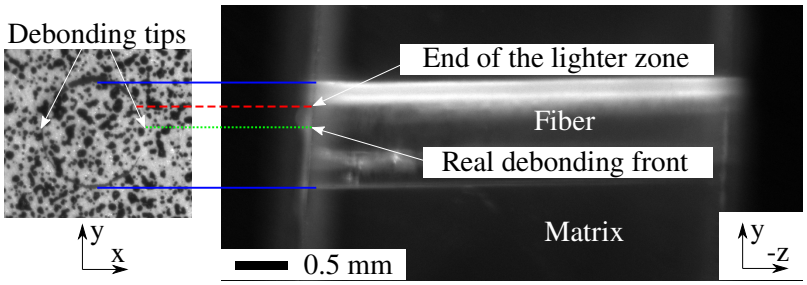

Figure III.23 – Comparison between the front view (left image) of the debonding angle corresponding to a fully debonded interface and the side view (right image) of the debonding for the similar remote loading, highlighting the discrepancies between experimental and numerical determination of the debonded shape.

On the other hand, Figure III.23 shows the side view where the lighter zone can be observed. The debonding angle derived from the lighter zone does not correspond to a fully debonded area. Such observation, therefore, confirms that lighter areas observed on the side view only enable partial capturing of the actual debonding shape and its corresponding area. Consequently, the side-view optical observations of the debonding only provide a correct debonding shape at the early stages of propagation.

Comparison with the front-view observations is actually required to confirm that the lighter areas observed on the side view correspond to the real debonding shape. As a result, only the length of debonding can be accurately determined using this technique, while the shape and angle of debonding must be verified numerically.

Debonding detection by acoustic emission

The debonding process is monitored by AE to capture the various stages. As debonding can initiate in a short time over a very small area, some aspects may be missed by DIC or optical observation. Two PICO sensors with MISTRAS PCI2 acquisition system are thus placed at 15 mm from the fiber, see Figure III.24. A medium-viscosity vacuum grease is used as a coupling agent between the sensors and the sample. Both sensors are held in place with PTFE tape to ensure correct positioning during mechanical testing. The acquisition parameters for the two channels are defined as follows: 40 dB preamplification, 30 dB threshold, 50 µs peak definition time, 100 µs hit definition time and 1000 µs hit lockout time. Different parameters of the AE signal, such as, *e.g.*, amplitude, energy, duration, counts, frequency centroid and rise time are recorded at the same time as the force in the tensile machine and the camera images. This enables to correlate the different debonding mechanisms to the AE signals.

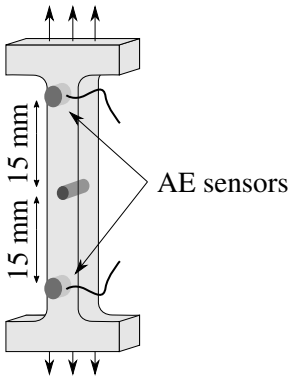

Figure III.24 – Location of the two AE sensors.

The AE wave velocity is required to accurately assess the location of each acoustic event. The velocity of the AE wave in the epoxy is determined outside the testing machine using a pencil-lead break procedure. Two sensors are placed at different locations in the sample and several pencil leads are broken at different locations. The difference in arrival time relative to the difference in location of the two sensors with respect to the breaking location of the pencil lead is used to estimate the wave velocity. The wave velocity is found to be equal to 1400 ± 200 m/s. Determining the wave

velocity enables AE events to be located during testing, so that only AE events located in the fiber vicinity are selected.

III.3 Results and discussion

The following sections are devoted to the presentation of the results obtained by the methods presented above. The batch of samples from which the results are extracted is indicated in the figures legend or title. The quantities that can be extracted from the two single fiber batches vary depending on whether one or two cameras are used to monitor the debonding process. Since debonding is likely to initiate from the free surfaces of the sample at the pole of the fiber relative to the loading direction, 4 preferred initiation sites can be defined. Figure III.25 shows the different preferential sites in relation to the positioning of the observation sides for the single fiber sample.

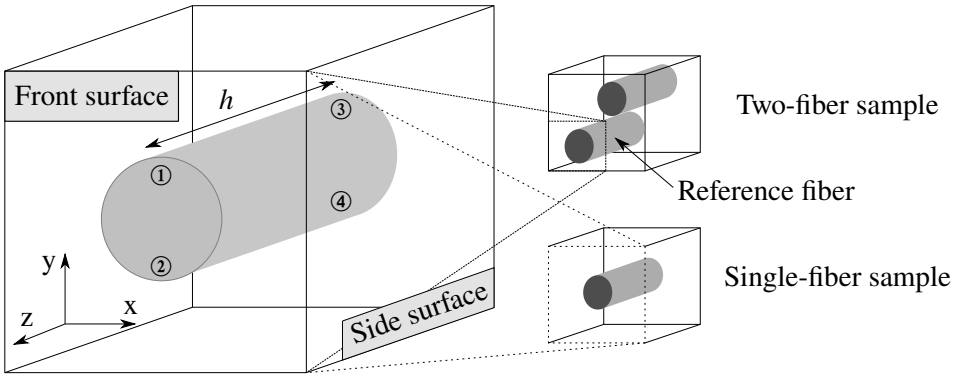

Figure III.25 – Schema of the preferential debonding initiation sites location in the single fiber sample.

It is worth recalling that the loading is applied along the y-direction. Initiation sites ① and ② are those on the front surface where the speckle pattern is applied. As a result, the debonding opening can only be extracted at these two sites, as without the use of a third camera, the DIC on the opposite side cannot be performed. In batch I, the single-fiber samples are observed using a single camera positioned parallel to the front surface. Consequently, no information about debonding on the opposite side can be extracted. In contrast, the samples from the second batch have a second camera positioned perpendicularly to the first one. Therefore, while the debonding opening cannot be identified on the opposite front side, the initiation of debonding can still be identified using the side view. Only the debonding length can therefore be extracted from the debonding initiating on the opposite front side.

Consequently, the use of a single camera limits observation to the debonding angle and the opening, whereas using two cameras enables the determination of the debonding length, as well as observation of any phenomena occurring on the opposite face. The two-camera configuration allows for thorough monitoring of the debonding process. Numerous debonding processes can take place, as debonding can initiate from sites located at the same pole, for instance, sites ① and ③ . Debonding can also initiate from one site and further propagate to another site at the same pole. Studying all debonding events emanating from each site would be both time-consuming and of limited relevance for subsequent modeling. As a consequence, only the first event of debonding initiation or those occurring at sites ① and ② will be considered in the following analysis, depending on which scenario occurs first.

Debonding opening

The debonding openings are monitored in the single-fiber batch I and II to determine the initiation remote loading and the opening variation as a function of the loading level. The following opening results are derived from DIC fields computed with Ufreckles [Ret18]. Only the initiation remote loadings are extracted from the double-fiber samples using the debonding opening.

Single-fiber batch I consists of two samples, allowing for the extraction of two opening variations from each pole of both samples. A black spot is placed at the fiber location on the front side to locate the fiber. This spot locally hides the fiber-matrix interface at the bottom pole, making the extraction of the debonding opening challenging. Figure III.26 shows the variation in debonding openings at both sites ① and ② for the two samples from batch I, with the uncertainties represented by the shaded area.

Similar debonding initiation remote loading occurs for both samples, between 4 and 5 MPa. The precise determination of the initiation loading is limited by the image rate acquisition. Similarly, symmetric debonding initiation takes place at both sites for the two samples. After initiation, similar variations in opening relative to the remote loading are observed for both samples, with SFI-1 exhibiting slightly larger opening values. It is worth mentioning that the debonding initiation extracted from SFI-1 is not straightforward, as the transition between the intact and damaged state is not perfectly defined, as observed in SFI-2. Particularly, the discontinuity in the displacement field at debonding initiation is less pronounced in SFI-1. However, the results are still presented and are consistent with SFI-2.

Optical determination of the debonding opening is performed for large remote loadings that result in large openings. Gray level intensity gauge is placed at SFI-2 site ① , at the exact position of the displacement gauge. The appearance of black pixels in the debonded zone leads to large variations in gray intensity compared to speckle

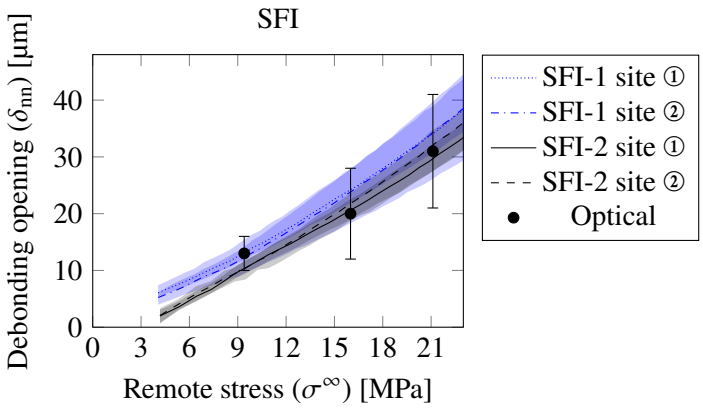

Figure III.26 – Debonding opening (δ_{nn}) extracted using the displacement fields as a function of the remote loading (σ^{∞}) for the two samples of the batch I. The shaded area corresponds to the measurement uncertainties.

pattern. The length of the variation zone allows for the derivation of the debonding opening by selecting gray level boundaries. The measured lengths, denoted as optical in Figure III.26, are superimposed on the debonding opening obtained with DIC. Small differences, no larger than 2 µm, are encountered with the DIC approach, with the optical observation slightly overestimating the opening for small remote loading. Such small discrepancies can be explained by the smooth transition at the two lips of the debonding, making the opening challenging to determine. It confirms the relevance of the DIC approach in assessing the debonding opening.

Table III.5 summarizes the debonding opening obtained for batch I at initiation. The lower limits describe the displacement variation just before debonding initiation, while the upper limits indicate the opening just after initiation. SFI-1 exhibits a larger debonding opening than SFI-2, the two poles being consistent.

Site	δ_{nn} [µm] lower bound	δ_{nn} [µm] upper bound
SFI-1 ①	6.2 ± 1.2	7.4 ± 1.2
SFI-1 ②	5.2 ± 1.1	6.2 ± 1.3
SFI-2 ①	2.1 ± 1.0	3.8 ± 0.8
SFI-2 ②	2.0 ± 1.2	4.1 ± 1.0
Average	3.9 ± 2.0	5.4 ± 1.7

Table III.5 – Debonding opening at initiation for single-fiber batch I.

Five samples of the single-fiber batch II enable DIC to be carried out on their

front surface. The samples are referenced as follows: SFII-1, SFII-2, SFII-3, SFII-4 and SFII-5, where the last two are coupled with AE. The debonding opening are also extracted from sites ① and ② . This batch of samples allows precise identification of the initiation site since the coupled side view allows simultaneous observation of all 4 sites. Consequently, only the samples whose debonding initiation is located on the front surface are studied in the following, *i.e.*, the samples referenced SFII-2, SFII-3 and SFII-4. In this sense, the debonding opening can be coupled to the length to evaluate the debonding angle according to the method presented in Section III.2.2. Figure III.27 shows the variation in debonding opening as a function of remote stress for these three samples. Particularly, Figure III.27a and Figure III.27b show opening extracted at the first and second initiation sites, respectively.

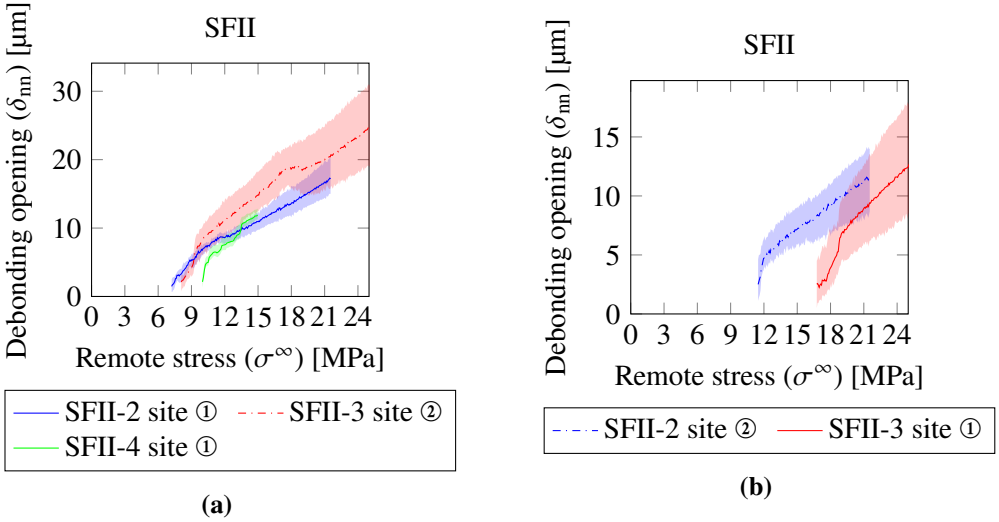

Figure III.27 – Debonding opening (δ_{nn}) as a function of the remote loading (σ^{∞}) for the samples of the batch II for (a) the first initiation site and (b) second initiation site. The shaded area corresponds to the measurement uncertainties.

Similarly to the samples from batch I, the samples from batch II show consistent remote loadings at initiation, varying from 7.2 to 9.9 MPa. Samples SFII-2 and SFII-3 exhibit different remote loading at initiation between both poles, ranging from 4 MPa difference, *e.g.*, SFII-2, to 8 MPa, *e.g.*, SFII-3. This phenomenon can be explained by debonding initiation located at the opposite side which propagates at the fiber pole to reach the front surface, as shown in Figure III.28 for sample SFII-2. Figure III.28 displays a side view of the debonding process, with the debonded area highlighted by white pixels. Initially, debonding begins at site ① , as seen in the opening in Figure III.27a under similar remote loading conditions. As the loading increases,

another debonding initiation occurs at site ④ , which is not captured by the DIC. Subsequently, this later debonding propagates from site ④ to reach site ② , leading to a sudden increase in opening, as also observed in Figure III.27b.

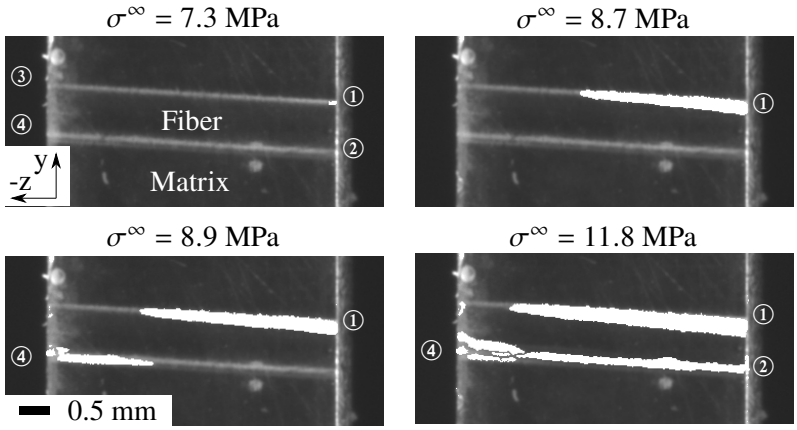

Figure III.28 – Side observation of the sample SFII-2 debonding initiation and propagation at different sites for several remote loadings.

No second debonding is observed for sample SFII-4 since complete sample failure occurred before the opposite side debonding reached the front surface. It is worth noting that the presence of a second debonding mitigates the opening at the opposite pole, as it can be observed for sample SFII-3 at $\sigma^\infty = 16$ MPa for site ② . Large scatterings are observed for sample SFII-3 due to slightly blurry images inducing larger scattering in the debonding opening determination. Table III.6 summarizes the debonding opening obtained for batch II at initiation. Overall agreement is obtained between samples with small discrepancies.

Site	δ_{nn} [µm] lower bound	δ_{nn} [µm] upper bound
SFII-2 ①	1.5 ± 1.0	1.7 ± 1.0
SFII-2 ②	2.6 ± 1.5	2.7 ± 1.5
SFII-3 ①	2.5 ± 2.0	2.6 ± 2.0
SFII-3 ②	2.1 ± 0.8	2. ± 1.0
SFII-4 ①	2.1 ± 1.0	3.0 ± 0.8
Average	2.2 ± 0.4	2.4 ± 0.5

Table III.6 – Debonding opening at initiation for single-fiber batch II.

Double-fiber sample are not presented herein since only the debonding initiation remote loading was extracted. Further studies on the debonding initiation remote

loading are presented in the Section III.3.

Debonding length

The debonding length is extracted from the second camera placed parallel to the side surface so that only the samples from batch II can be investigated. In addition to the debonding length, the side observation provides the corresponding remote loading at which the debonding initiates and propagates with the corresponding site. Consequently, even the debonding does not initiate on the front surface, the debonding can be monitored thanks to the second camera. However, only samples which provide initiation at the front surface are studied herein, since coupled with the debonding opening, the debonding angle can be derived numerically. In addition, only the debonding initiating from the front surface are considered. As a result, the samples referenced as SFII-2, SFII-3 and SFII-4 are investigated.

Figure III.29 displays multiple side images illustrating the debonding process, employing both optical and threshold methods denoted by left and right images, respectively, for different loading level.

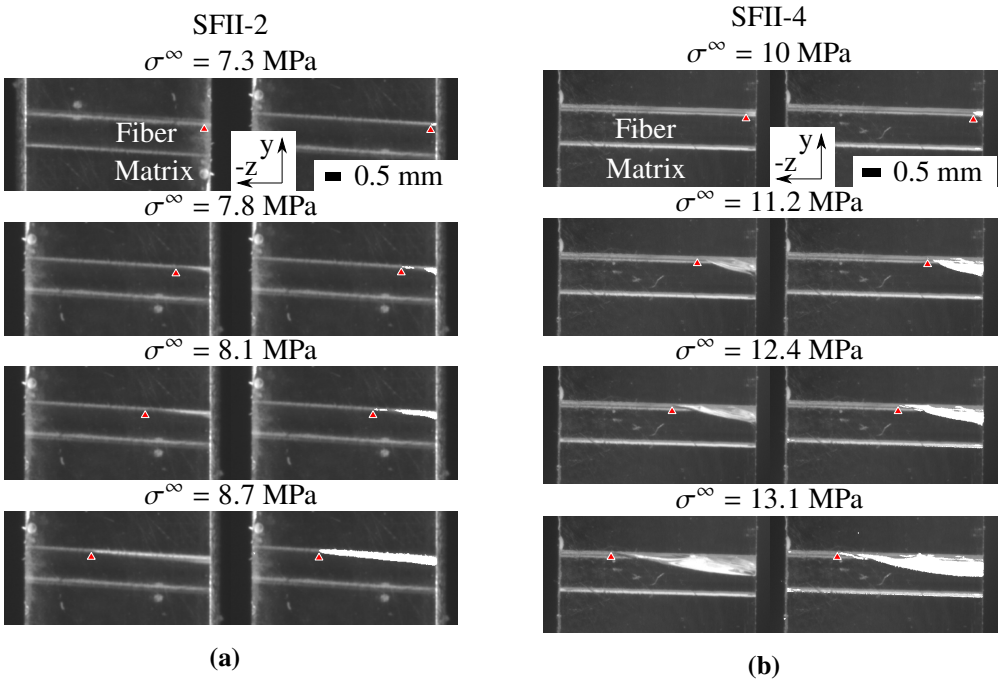

Figure III.29 – Debonding propagation observed optically (left column) and using a threshold (right column): (a) sample SFII-2 and (b) sample SFII-4.

The images correspond to samples SFII-2 and SFII-4. The location of the crack tip is identified by a red triangle marker, enabling the debonding length to be determined as the distance to the free surface. Notably, the fiber from sample SFII-2 is slightly tilted, approximately 4 deg. relative to the loading direction, potentially influencing the debonding shape topology.

Figure III.30 shows the normalized debonding length variation as a function of the remote loading. The debonding length is obtained following the methodology presented in Section III.2.2 and using a threshold of 17% difference in gray level intensity.

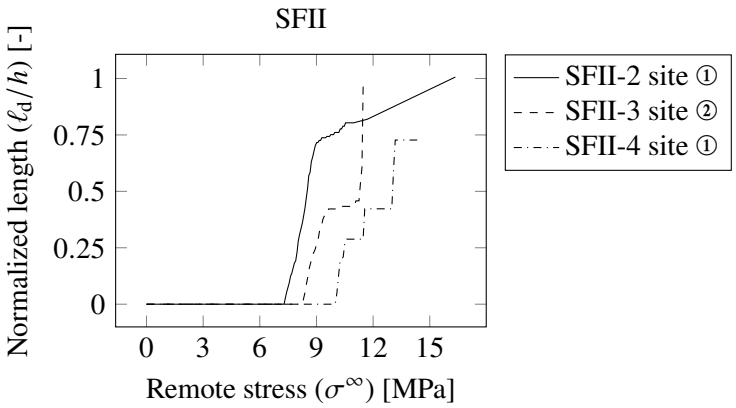

Figure III.30 – Normalized debonding length as a function of remote stress for the samples from batch II where the debonding is measured using a threshold of 17% difference in gray level intensity.

The three samples show a similar profile, with the remote initiation loading agreeing. The remote initiation loading corresponds to that obtained by monitoring the debonding opening by DIC (see Section III.3). Sample SFII-2 shows a relatively regular variation in length compared with samples SFII-3 and SFII-4, where the variation is rather step-like. In these latter cases, the debonding propagates by steps and even taking into account the camera images rate, constant debonding lengths are obtained for different successive images. In some cases, complete failure of the sample occurs before the debonding reaches the opposite side, which explains why sample SFII-4 has a partial debonding length at failure.

The variation in opening is superimposed on the variation in length in Figure III.31.

Overall, the debonding initiation remote loading coincides between both methods for all samples, although with slight shifts provided by the length measurement. Small debonding surface occurring after initiation may induce only a minor difference in

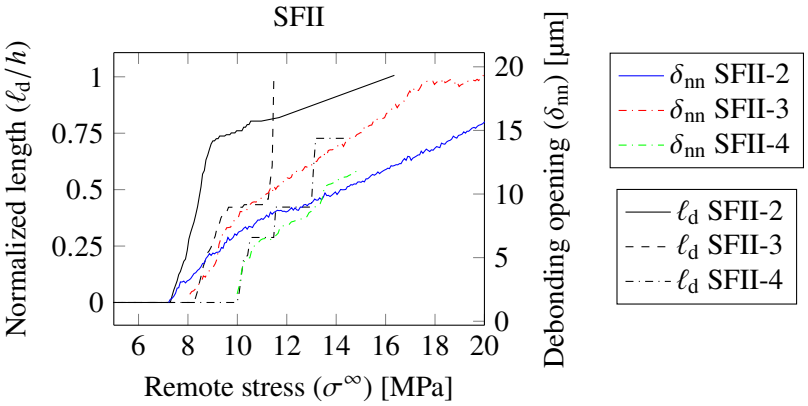

Figure III.31 – Variation of both normalized debonding length and opening as a function of the remote stress for three samples of batch II.

gray level, rendering the debonding difficult to identify. As a result, this method may lead to larger remote loadings at debonding initiation. Similarly, there are noticeable similarities in the variations observed. An increase in the debonding opening relative to remote loading results in an increase in length. Conversely, crack arrest induces smaller variations in debonding opening. These mechanisms can be explained by the initiation and propagation of debonding located at opposite poles, which may either dampen or promote the debonding process.

Debonding angle

The camera, positioned parallel to the front surface, facilitates the assessment of debonding angle variation as a function of the applied stress, employing the methods introduced in Section III.2.2. The debonding angle (θ_d) variation as a function of the remote stress (σ^∞) obtained using both approaches are shown in Figure III.32a for the sample SFI-1. As a reminder, one method involves optically detecting debonding. This method is performed independently by two operators to evaluate the measurement uncertainty due to, for instance, the sample pattern possibly obscuring the crack and the pattern black components that may be confused with the crack. A second method is based on DIC residuals. Only the debonding angle at site ① can be extracted since a black spot is placed close to the fiber location and locally hide the fiber-matrix interface at site ② .

Similar trends are obtained using both methods. The maximum difference is observed between the measurements of the two operators, mainly due to the difficulty

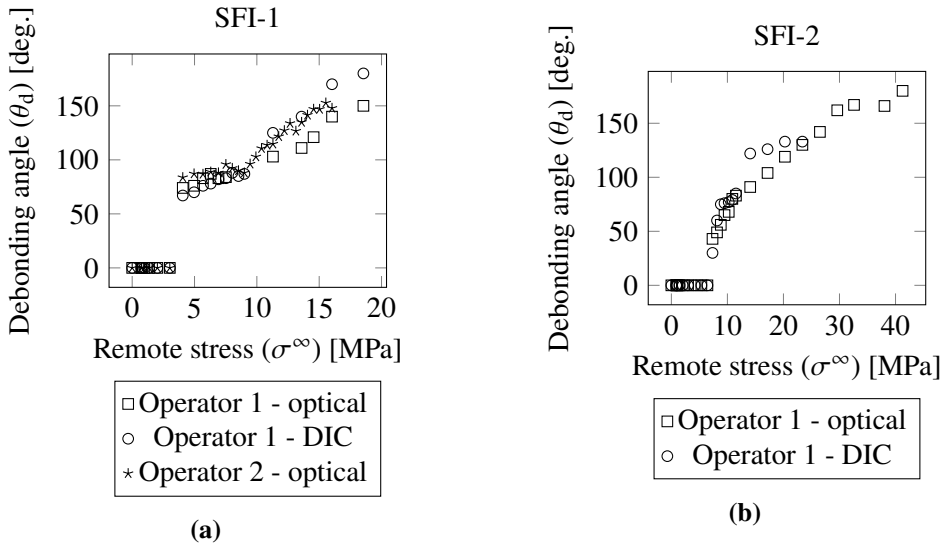

Figure III.32 – Variation of the debonding angle as a function of the remote stress for (a) sample SFI-1 and (b) sample SFI-2.

of identifying the crack tips. Observations highlight crack initiation over a significant debonding angle for loadings comprised between 3.0 MPa and 4.0 MPa, followed by a stable crack propagation phase for larger loading levels. Noticeably, the debonding angle after initiation is obtained for the same loading (*i.e.*, the same recorded image) level using both methods. This debonding initiation remote loading level coincides with that observed using the debonding opening in Section III.3. Debonding angles just after initiation in the range 67 to 83 deg. are obtained (20% relative difference). Angle difference no larger than 30 degrees (21% relative difference) is obtained during the propagation phase.

The debonding angles of sample SFI-2 are also extracted optically and by DIC by a single operator, the results being shown in Figure III.32b. Debonding initiation for a 7.3 MPa remote loading is observed. Overall, the debonding angle increases rapidly with remote loading for debonding angles smaller than 80 deg., and then stabilizes. The transition from the opening mode to the shear mode may explain the mechanisms observed, since the propagation in the opening mode is more favorable than that of the shear. Differences below 30 degrees are obtained between the optical and DIC measurements. The DIC results yield a larger debonding size for a similar remote loading, which can be explained by the difficulty in optically determining the location of the crack tips.

Angles determined in sample SFI-2 yield different results to those for sample

SFI-1, as shown in Figure III.33. Sample SFI-2 exhibits a larger debonding initiation remote loading, *i.e.*, 7.3 MPa, compared to sample SFI-1, *i.e.*, 4 MPa, whereas similar results were obtained for both samples using the debonding opening. This difference may be due to the difficulty of optically identifying the debonding at low remote loading. In summary, both samples exhibit sudden debonding initiation up to a finite angle. The initiation angle for sample SFI-2 is smaller than that of sample SFI-1, ranging from 30 to 42 deg. compared to 67 to 83 deg., respectively. This disparity may arise from challenges in accurately locating the crack tips, particularly due to sub-pixel phenomena. Following the unstable debonding phase, a stable debonding propagation occurs for both samples, at smaller angles for sample SFI-2.

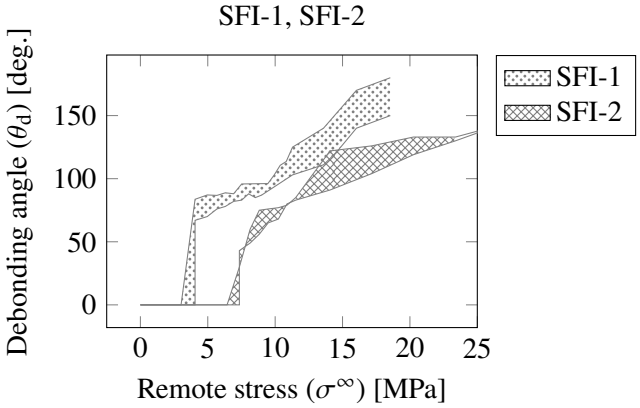

Figure III.33 – Variation of the debonding angle as a function of the remote stress for both samples SFI-1 and SFI-2. The dotted and hatched areas correspond to the interval associated with the various measurements.

Another alternative method for determining the debonding angle is to couple the experimental debonding opening with FE analysis. 2D FE model is implemented using the dimensions of the samples from batch I. Elastic properties similar to those of the epoxy matrix and glass fiber are taken into account. The actual numerical debonding opening is determined as the nodal distance between the fiber and matrix nodes at the pole. The numerical debonding opening is evaluated for debonding angles ranging from 10 to 170 degrees for a fixed remote loading. As linear elastic properties are used, the opening can be varied linearly with the remote loading. Figure III.34 shows the numerical debonding opening obtained for the range of angles as a function of remote loading. This approach is only carried out for sample SFI-2 because the opening derived for sample SFI-1 remains uncertain (see Section III.2.2) and in fact overestimates that obtained numerically. The experimental debonding opening is

also shown in Figure III.34, the intersection with the numerical opening provides the debonding angle at which the numerical and experimental openings coincide.

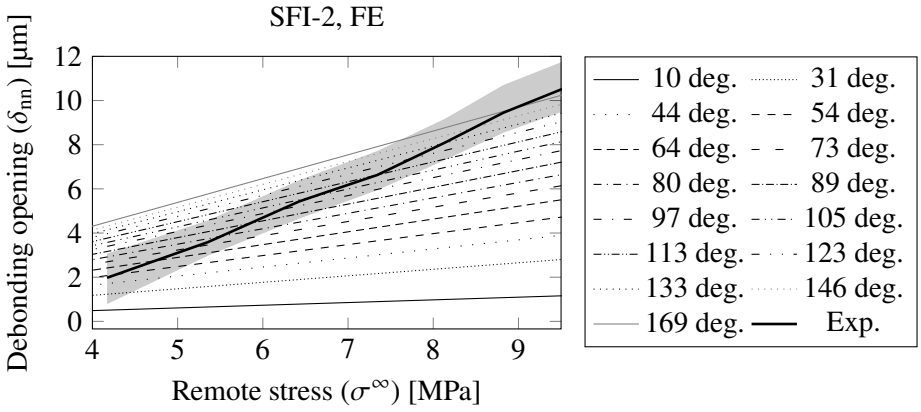

Figure III.34 – Variation of the debonding opening as a function of the remote stress obtained numerically for several fixed debonding angles superimposed to the experimental opening extracted from sample SFI-2.

The debonding angles obtained from the experimental-numerical dialogue show major discrepancies with those obtained using the optical and DIC approaches, as shown in Figure III.35. The obtained remote loading is smaller at initiation, *i.e.*, 4.2 to 7.3 MPa obtained otherwise, which corresponds to what is obtained using the debonding opening. This suggests that the optical and DIC approaches lack the debonding initiation, corresponding to a sub-pixel opening not captured by the images. As a consequence, both optical and DIC methods may therefore underestimate the actual size of the debonding since the debonding opening tends towards zero as it approaches the crack tip. Therefore, experimental-numerical coupling could help to validate the debonding angle obtained optically or by DIC. However, the debonding angle and the opening are observed on the free surface of the sample where singularities arise from the elastic fiber-matrix mismatch. Consequently, taking into account a 3D model can provide more accurate results but requires knowledge of the debonding length, which is not available for batch I samples. Such possibility is investigated for batch II samples.

Difficulties in determining debonding angles are encountered with single-fiber samples from batch II. The smaller size of the fibers compared with batch I results in a smaller crack size and the camera is thus unable to capture debonding at the free surface. The pixel size obtained with the front camera varies between 10 and 12 µm, whereas the DIC provides debonding initiation opening with a sub-pixel size of 1

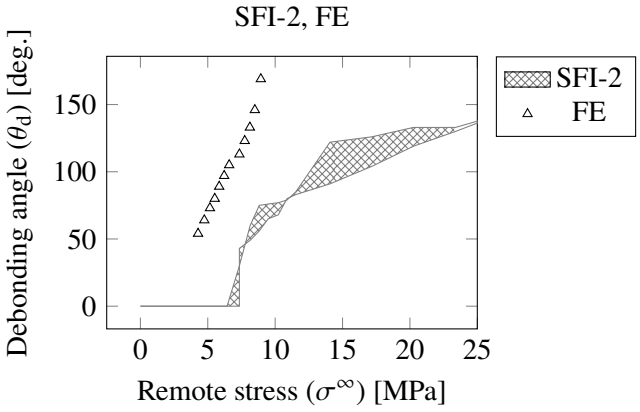

Figure III.35 – Variation of the debonding angle as a function of the remote stress for the SFI-2 sample, with measurement interval indicated by the hatched area, and those obtained with the coupled numerical-experimental approach using the debonding opening.

to 3 µm. Consequently, the resolution of the camera is not sufficient to capture the early stages of debonding at the free surface. Nevertheless, coupled experimental-numerical approach, similar to that proposed in Section III.2.2, is established to retrieve the debonding angle and shape that best matches the opening and debonding length measured experimentally. The approach consists of numerically comparing various debonding geometries approximated using a power-law, see Section III.2.2. The appropriate geometry thus gives the debonding angle at the free surface and the shape of the debonding front. Identification can be performed at several debonding stages, providing debonding angles as a function of remote loading. Debonding angles obtained from the coupled numerical-experimental approach are shown in Figure III.36, for the 3 studied samples from batch II. The debonding shapes are approximated by a power law of exponent 4.

Overall, the samples show an abrupt debonding initiation at a finite consistent angle ranging from 30 to 40 degrees. On the one hand, samples SFII-2 and SFII-4 progressively propagate to a fully debonded free surface, *i.e.*, a debonding semi-angle of 90 degrees. Sample SFII-3, on the other hand, rapidly reaches a full debonding angle at the free surface.

The debonding angle can also be assessed using the side observation, using results from Figure III.29. It has been shown previously that this method provides accurate results for the early stages of debonding, when the latter remains located at the pole of the fiber, withstanding primarily mode I. The debonding angles obtained by the side

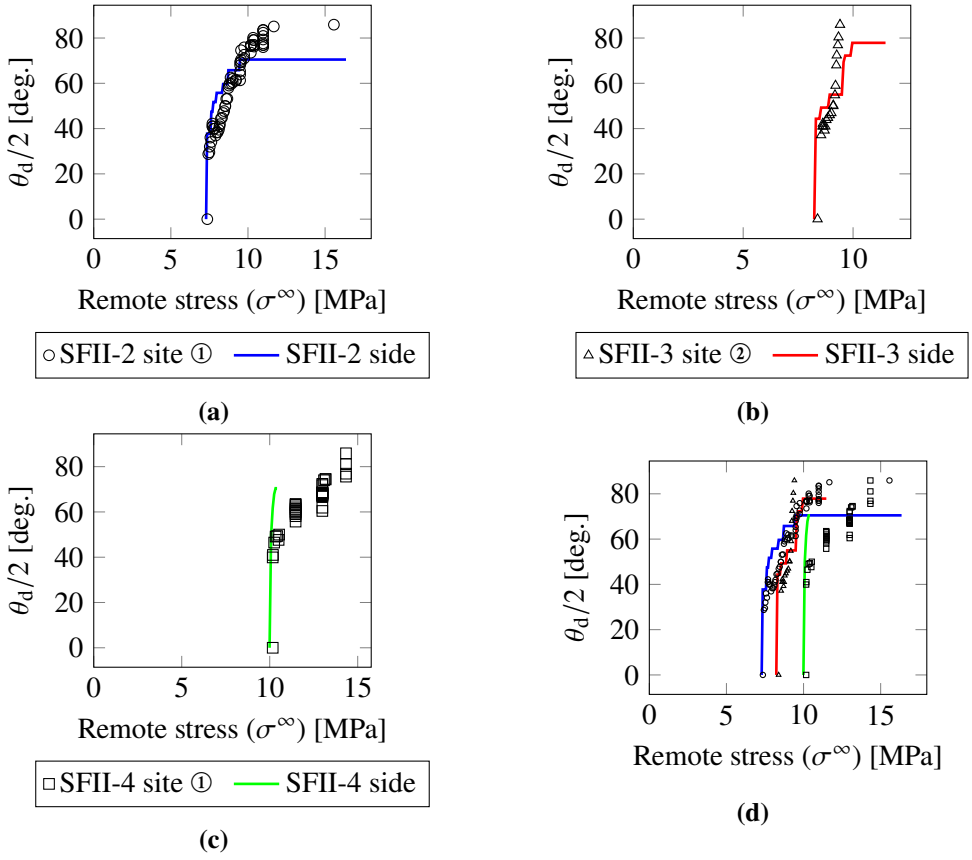

Figure III.36 – Variation of the debonding semi-angle as a function of the remote stress for the 3 samples from batch II, namely (a) SFII-2, (b) SFII-3, (c) SFII-4 and (d) all compared together. Semi-angles are extracted from numerical-experimental dialogue, as presented in Section III.2.2.

view are also depicted in Figure III.36 by solid lines. This method provides precise debonding angles for samples SFII-2 and SFII-3 for small angles, whereas it does not provide a precise description for large angles, *i.e.*, for semi-angles larger than 70 degrees. On the contrary, the side view of sample SFII-4 overestimates the actual debonding angle. This latter observation can be explained by the rapid debonding kinking into the matrix observed experimentally, which locally modified the gray intensity at the fiber equator vicinity. For this reason, it is not possible to determine suitable debonding angles for loading larger than that of the kink event. Nevertheless, the results obtained offer a better correspondence between the numerically determined angle and the side observation than those obtained in Section III.2.2. This difference

could be explained by the different methods used to reveal the debonding in the side observation. The method used in Section III.2.2 used only a threshold to highlight the debonding, whereas the method presented in this thesis work used a difference in gray level intensity between the undamaged and damaged stages. Therefore, the current method is more accurate in highlighting the actual topology of the debonding shape.

Debonding angles are also extracted from the double-fiber sample immediately after debonding initiation. They are determined using the residual DIC method presented in Section III.2.2. Only the first debonding initiation is taken into account in the determination of the debonding angle. As a reminder, two samples per inter-center distance and angle configuration are tested. Thus, an average debonding angle at initiation for both samples is shown in Table III.7 for each configuration.

α [deg.]	d [mm]	θ_d [deg.]	Site
0	2.5r	72.5 ± 26.1	①
	4r	52.5 ± 3.5	②
	5r	63.5 ± 9.2	①
30	2.5r	64.5 ± 5.0	①
	4r	59 ± 4.2	①
	5r	62.5 ± 3.5	②
45	2.5r	100 ± 0.0	①
	4r	76.5 ± 27.6	②
	5r	70 ± 0.0	①
60	2.5r	77.5 ± 19.0	①
	4r	52 ± 0.0	①
	5r	58.5 ± 6.4	②
90	2.5r	51 ± 4.2	②
	4r	58.5 ± 10.6	②
	5r	53 ± 5.7	②
	Average	64.8	
	Deviation	13.1	

Table III.7 – Debonding angles observed at initiation for the double-fiber samples using the DIC residual. The debonding initiation site is extracted from the reference fiber (see Figure III.25).

Consistent debonding angles at initiation are obtained from the different configurations, with a standard deviation of 13 degrees. The influence of neighboring fibers on the debonding angle at initiation appears to be negligible. The average angle of 65 degrees is in agreement with those observed on batch I single-fiber samples. No par-

ticular trend in debonding site can be observed. The site location is extracted from the reference fiber (see Figure III.25). However, only a front observation is carried out on the double-fiber samples. As a result, debonding may have initiated on the opposite side, so, initiation at sites ③ and ④ could have been the origin of debonding.

Coupling of the different characterization

The SFII-4 sample enables the various characterization techniques described above to be combined. As a reminder, two cameras placed in front of the front and side surfaces allow in-plane and out-of-plane monitoring of the debonding process. In addition, as two sensors are placed at both ends of the sample, AE events are localized. AE events are therefore limited to those located in the vicinity of the fiber. The debonding opening and length extracted from sample SFII-4 are shown in Figure III.37, as a function of the remote stress. The corresponding cumulative AE events energy are also shown in Figure III.37. Cumulative energy is obtained by summing the energy of the signals measured as its integral over its duration.

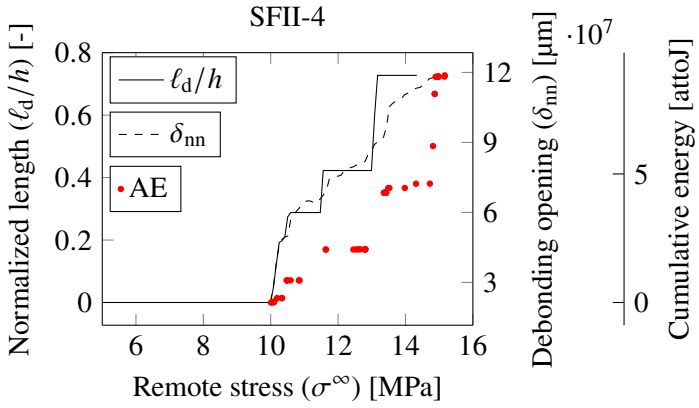

Figure III.37 – Coupling of the normalized debonding length (ℓ_d/h) and opening (δ_{nn}) to the AE events, extracted from sample SFII-4, as a function of the remote stress (σ^∞).

Generally, all the debonding characteristics share a similar remote loading at initiation for a remote stress of 10 MPa. The first localized AE event is consistent with the other observations. Furthermore, they agree in terms of the debonding process, which appears to proceed by steps. Significant propagation phases are interrupted by crack arrest. Such process can be observed on each quantity. During propagation phases, a larger increase is observed in debonding length, as well as in debonding opening.

Additionally, there is a notable increase in cumulative energy during each debonding propagation phase. This can be attributed to the energy released by the debonding during the debonding propagation, which results in large signal energy, while a plateau is observed during crack arrest. Interestingly, debonding opening continues to increase even during crack arrest. This phenomenon may be explained by the development of a local process zone or local stretching of the crack free surface. The final jump in the EA cumulative energy can be attributed to the sample final failure.

Debonding initiation remote loading

The common quantity that can be extracted from all characterization techniques is the debonding initiation remote loading. Indeed, debonding initiation results in a significant increase in each characteristic. For example, a sudden increase in debonding angle is encountered at initiation. More gradual increases are generally observed for the length and opening of the debonding. As debonding may have initiated from sites ③ and ④ , only the side observation is suitable. However, these observations have not been reported previously, as only remote loading and debonding length can be derived. To this end, all remote loadings at initiation for each sample are summarized in the sequel. Table III.8 summarizes the remote loadings at debonding initiation obtained by each technique from single-fiber samples of batch I.

Sample	Site	σ^∞ [MPa]	σ^∞ [MPa]	σ^∞ [MPa]
		δ_{nn}	θ_d opti.	θ_d DIC
SFI-1	①	4.1 - 5.0	3.0 - 4.1	3.0 - 4.1
	②	4.1 - 5.0	/	/
SFI-2	①	4.2 - 5.4	6.4 - 7.3	6.4 - 7.3
	②	4.2 - 5.4	/	/

Table III.8 – Debonding initiation remote loading extracted from samples from batch I using the different techniques.

Similar remote loadings are obtained using the debonding opening at both fiber poles. Likewise, techniques involving debonding angles, whether optical or DIC determination, align in terms of remote loading. A black spot is placed near the fiber to locate its position after the sample has been patterned. The latter locally hides the fiber-matrix interface on site ② , so that no debonding angle can be extracted. For SFI-1, a lower remote loading is observed through the debonding angle relative to the debonding opening. This is surprising, DIC can capture sub-pixel phenomena, unlike optical determination, which is limited to pixel size. However, the above hypothesis is confirmed by SFI-2, where a larger remote initiation loading is observed using the debonding angle compared to the opening angle. Overall, the different techniques

deliver consistent remote loads at initiation, ranging from 3 to 7 MPa depending on the sample.

Table III.9 summarizes the remote loading from single fiber - batch II samples obtained using opening and debonding length measurements.

Sample	Site	σ^∞ [MPa]	σ^∞ [MPa]	σ^∞ [MPa]
		δ_{nn}	ℓ_{d}	AE
SFII-1	④	/	6.9	/
SFII-2	①	7.2-7.3	7.3	/
SFII-3	②	8.1	8.1	/
SFII-4	①	10.0	10.0	10.0
SFII-5	③	/	5.6	6.9

Table III.9 – Debonding initiation remote loading extracted from samples from batch II using the different techniques. The first AE event localized is used.

In addition to the samples studied previously, those on which debonding initiations are located on the opposite site are also taken into account, *e.g.*, for instance site ③ or ④ . Samples SFII-2, SFII-3 and SFII-4 show similar remote loading regardless of the technique used. This confirms the accuracy of the side view, even though it may be unable to capture the sub-pixel mechanism. However, the side view consists of a projected observation of the debonding surface, enabling the debonding to be observed even if it has a very small opening. Samples SFII-1 and SFII-5 initiated at a slightly smaller remote loading on the opposite side, where only the side view is able to capture the phenomenon. Overall, the remote loading at initiation shows a good correspondence, ranging from 5.6 to 10 MPa. The remote loading obtained by AE for sample SFII-5 provides a larger value than that from lateral observation. This can be explained by the fact that the size of the debonding initiation is very small and the amplitude of the AE signal is below the threshold. Although the materials are different from those of batch I, the initiation loadings are comparable. For the sake of efficiency, the remote loading initiation of double-fiber samples is extracted using only the debonding opening. Four gauges are placed across the poles of the two fibers, aligned with the loading direction. Initiation loadings are averaged from the 4 gauges of the two samples per configuration, and the results derived are given in Table III.10. The difference between the remote loadings is used to estimate the standard deviation.

Initiation remote loadings are in the same order of magnitude, varying between 3 and 6.5 MPa. Small differences in the results are reflected in a standard deviation of less than 1 MPa. No particular trend can be observed with regard to the influence of distance and angle between the two fibers. It appears that the distance between the fibers neither promotes nor dampens debonding initiation. Likewise, whatever the

α [deg.]	d [mm]	σ^{∞} [MPa]
0	2.5r	5.1 ± 0.6
	4r	5.0 ± 1.4
	5r	4.3 ± 0.9
30	2.5r	4.4 ± 0.3
	4r	3.0 ± 0.6
	5r	4.3 ± 0.4
45	2.5r	4.0 ± 0.2
	4r	3.9 ± 0.3
	5r	4.5 ± 0.0
60	2.5r	4.0 ± 0.6
	4r	3.2 ± 0.5
	5r	3.8 ± 0.2
90	2.5r	4.9 ± 0.5
	4r	6.5 ± 0.6
	5r	5.3 ± 0.3
	Average	4.4
	Deviation	0.9

Table III.10 – Debonding initiation remote loading extracted from double-fiber samples using the opening technique.

inter-fiber angle, similar loadings are encountered. The average loading at initiation distance is in line with that of the batch I single-fiber samples.

III.4 Conclusion

Techniques for characterizing fiber-matrix debonding are discussed in the present chapter. These techniques involve mechanical testing of single-fiber and double-fiber samples. On the one hand, the 1 and 2 mm diameter glass macro fibers used herein enable accurate monitoring of fiber-matrix debonding without the need for SEM or microtomography. On the other hand, contrary to classical microcomposite test focusing on shear properties solely, the single-fiber samples used herein exhibit a debonding propagation transitioning from an opening to a shear mode along the fiber circumference. Such test thus simultaneously provides key experimental results for the determination of tensile and shear interface fracture properties. Furthermore, double-fiber samples provide information on the influence of fiber proximity in the debonding process.

The above-mentioned mechanical tests are combined with various characteriza-

tion techniques of the debonding geometry. The following parameters are monitored: i) the opening at the fiber pole, ii) the debonding angle at the front surface, iii) the though thickness length at the fiber pole and iv) its shape along the fiber-matrix interface.

Characterization is carried out using two cameras positioned perpendicular to each other. The front camera provides displacement fields by DIC but does not allow observation of the debonding that initiates on the opposite side. The use of the second camera therefore makes it possible to capture the debonding propagation through the thickness, regardless of where the debonding initiates.

The debonding opening is evaluated by DIC on the front surface using VIC 2D and Ufreckles software, both of which provide similar results. Overall, mesh size have negligible effect on the opening results, unlike uncertainties where adequate intermediate mesh size have to be determined. It was found that the topology of the DIC mesh and the elements have a negligible influence on the opening extracted. At a sufficiently advanced stage of debonding, the debonding opening obtained by DIC aligns with that observed optically. The debonding opening therefore provides the remote loading at initiation as well as the opening throughout the debonding process.

The debonding length is determined optically by monitoring the change in gray level intensity. Another technique is to differentiate the gray level between an intact and a damaged state, where a greater difference appears in the debonded area. Overall, both methods yield similar results in terms of remote loading at initiation and length throughout the debonding process. Side observation enables the shape and angle of debonding to be determined, *a priori*. It has been shown to provide an accurate debonding shape for a sufficiently small debonding size, *i.e.*, located at the pole of the fiber. However, the methods do not describe the correct debonding shape for larger debonding sizes where the debonding undergoes significant shear. Indeed, the influence of shear attenuates the difference in reflective index that characterizes the debonded zone. Experimental-numerical coupling overcomes this problem by determining the debonding shape that minimizes the difference with the experimental opening and debonding length.

The debonding angle is determined either optically or by the large DIC residuals in the debonded area. Both methods yield similar results in terms of debonding size. However, this approach is limited to debondings larger than the pixel size. As a result, it may overestimate the initiation loading compared to the opening method. In addition, for a small fiber diameter, no debonding angle can be extracted without the help of FE simulation. The debonding size induced by such a fiber size remains smaller than the pixel size. This method is therefore unable to provide a consistent debonding angle for small fibers.

Finally, all the samples provided similar remote loading at initiation, regardless of the batch considered. The remote loading extracted using each technique gives

similar results. The double-fiber samples show negligible influence of the inter-fiber distance and angle on the remote loading at initiation or on the debonding size. Overall, the different samples provide relevant experimental results for further numerical modeling in identifying the fracture properties of the fiber-matrix interface.

The major drawback inherent in the experimental campaign carried out is the lack of reproducibility. A maximum of 2 samples per configuration were tested for the SFI and DF batches. In addition, other characterization methods could be used, such as micro-tomography to assess the topology of the debonding in 3D for different remote loadings. Other matrix behaviors could also be studied to induce non-linearity in the response. The alignment of the fibers with respect to the loading direction could be modified to induce more or less mode mixity and see the influence on the debonding process.

CHAPTER IV

Inverse identification of the fiber-matrix interface fracture properties

Content

Some results presented in the following chapter can be found in the following articles published in peer-reviewed journals:
Experimental characterization of in-plane debonding at fiber-matrix interface using single glass macro fiber samples by Hugo Girard *et al.* [Gir+23a];
Numerical simulation of fiber–matrix debonding: Inverse identification of interface properties by Hugo Girard *et al.* [Gir+23b].

IV.1 Introduction and motivation

Debonding initiation and propagation at the fiber-matrix interface of a single-fiber composite loaded transversely can be assessed using both CZM and the CC. On the one hand, CZM are usually employed, see [Koy+09; GPM14; Gen+19], being particularly advantageous as they predict the debonding process autonomously and allow for several simultaneous debonding events [Kus+11]. However, such advantages may imply a large computational cost. On the other hand, the CC can also assess debonding initiation, propagation and predict the associated loading and size, yet being numerically efficient when a single crack is studied, making it suitable for inverse identification. The CC reverts to LEFM when employed to assess further debonding propagation for a sufficiently long crack (*i.e.*, retrieving LEFM hypothesis), as employed in Sandino *et al.* [SCP16] and Velasco *et al.* [VCP20]. This approach was first applied to fiber-matrix debonding by Mantič [Man09], and the approach was then extended to assymetric debondings by García *et al.* [GMG15] or two-fiber sample by Muñoz-Reja *et al.* [Muñ+16b]. However, the CC applications related to fiber-matrix debonding are primarily based on numerical aspects and lack experimental verification. Similarly, the CC and CZM have been compared numerically in the case of inclusion debonding, investigating the influence of the inclusion size on the initiation remote loading [Gen+19], but have not yet been confronted simultaneously to experimental results.

Drawbacks inherent to 2D modelings are their ability to describe only the debonding angle and opening in a given plane perpendicular to the fiber. As a result, 2D modelings fail to describe the debonding length (ℓ_d) and the variation in debonding angles (θ_d) through the thickness of the sample. Additionally, experimental quantities provided by 2D modelings are extracted at the sample free surfaces, where there is a 3D stress singularity due to the fiber-matrix elastic mismatch. Such singularity can be represented through 3D modeling. However, the 3D application of the CC raises challenges, such as crack shape determination. Leguillon [Leg14] attempted to

determine the crack shapes based on stress isocontours and proposed a comparison between 2D and 3D applications of the CC to bi-material interface debonding. Properties derived from inverse identification based on both models were in the same order of magnitude. Similarly, Doitrand and Leguillon [DL18b] proposed a CC application in both 2D and 3D for scarf joint failure prediction, where the 3D approach slightly more accurately predicted the failure loading.

In this regard, Section IV.2 aims at confronting the CC predictions with the experimental characterization of debonding initiation and propagation angles in order to identify the fracture properties of the fiber-matrix interface. A similar approach is then employed in Section IV.3 using CZM to assess their ability to describe the debonding process and identify the fracture properties of the fiber-matrix interface. The results obtained using the 2D CC and 2D CZM models are then compared. For a more detailed description of the fiber-matrix debonding process, a 3D model of a single fiber specimen is finally developed in Section IV.4 to perform the inverse identification of interface fracture properties using the CC and quantify the accuracy of 2D models.

IV.2 2D inverse identification using the Coupled Criterion

The following inverse identification approach is performed based on the debonding angle observed from batch I samples at the site ① , *i.e.*, sample SFI-1 and SFI-2. The samples experience symmetric debonding initiation at both fiber poles for a similar remote stress according to the variation in debonding opening (see Chapter III).

IV.2.1 2D numerical model

A 2D plane strain model under linear elasticity and small deformation assumptions is set up. A schematic representation of the model geometry is shown in Figure IV.1. The FE model geometry is bounded along y- and x-directions at 50 and 6.5 mm from the fiber center, respectively, which is sufficiently large to provide local stress fields corresponding to a fiber embedded in an infinite media and subjected to a remote tensile stress. A displacement U is applied at both top and bottom surfaces, which magnitude is adapted to provide a selected remote stress $\sigma_{yy} = \sigma^{\infty}$ level sufficiently far from the fiber. Fiber-matrix interface debonding initiation and propagation is predicted using the CC, which requires the calculation of the stresses before debonding and the elastic energy variation as a function of the debonding angle θ_d. The angular position at the fiber-matrix interface, from the equator to the pole, is denoted by θ_f. Two simultaneous debondings are considered at both fiber poles accordingly to the experimental observations. From an energy point of view, symmetric debonding leads to a slightly different amount of energy released compared to asymmetric debonding,

as shown by Garcia *et al.* [GMG15], and observed experimentally by Martyniuk *et al.* [Mar+13]. Four-node linear elements are used. The elastic properties given in Table III.2 are assigned to each component. Mesh convergence is performed in order to choose a mesh size that ensures difference on both elastic strain energy and stress no larger than 1% for a finer mesh size (see Appendix A.1 for an example of mesh convergence analysis).

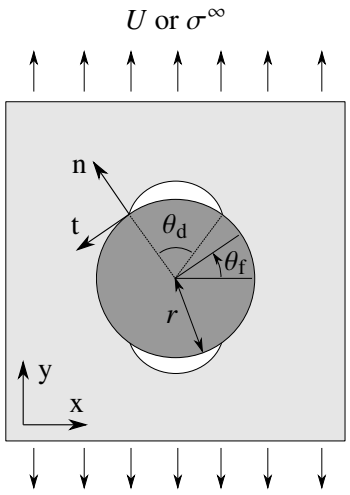

Figure IV.1 – Schema of the single-fiber numerical model.

The methodology to implement the CC [Leg02] is similar to Mantič's approach [Man09]. The CC predicts crack initiation by combining two conditions: sufficiently high stress field along the crack path before initiation and high enough energy released by the crack opening. Conditions that fulfill the CC form a two-equations system (Equation (IV.1)) whose solution provides the loading and crack size at initiation. Both conditions presented in Equation (IV.1) must be satisfied to make initiation possible:

$$\begin{cases} f(\underline{\sigma}(\theta_\mathrm{d}, \sigma^\infty), \sigma_\mathrm{c}, \tau_\mathrm{c}) \geq 1, \\ G_\mathrm{inc}(\theta_\mathrm{d}, \sigma^\infty) \geq \overline{G_\mathrm{c}}. \end{cases} \tag{IV.1}$$

The stress criterion at the interface, denoted by f, can either corresponds to a tensile or quadratic criterion, see Section IV.2.2. G_inc represents the IERR, obtained from the elastic strain energy (W) variation per unit thickness of the model (Equation (IV.2)).

$$G_\mathrm{inc}(\theta_\mathrm{d}, \sigma^\infty) = \frac{W(0, \sigma^\infty) - W(\theta_\mathrm{d}, \sigma^\infty)}{r\theta_\mathrm{d}} \tag{IV.2}$$

The global interface critical energy release rate denoted $\overline{G_c}$, which depends on the debonding angle, is detailed in the sequel. The change in elastic strain energy is calculated by unbuttoning the interfacial nodes located within a specified debonding angle. The interfacial nodes are doubled and an equation is established between the two nodes using a reference point to ensure continuity of displacement. Depending on their location, the equation is deactivated between the nodes and the reference point so that no continuity occurs between the doubled nodes, leading to two newly created crack lips without any reaction. The elastic strain energy of the model is then evaluated for different debonding angles.

IV.2.2 CC implementation

Stress condition

The first condition involved in the CC depends on the stress field at the fiber-matrix interface. The interfacial stress components are calculated at the fiber-matrix interface at each node. As for the calculation of the variation in elastic strain energy, the interfacial nodes are doubled and an equation is established between the two nodes using a reference point to ensure continuity of displacement. This results in a reaction force RF at the reference point which is used to evaluate the normal stress σ_{nn} and shear stress σ_{nt} components using Equation (IV.3).

$$\begin{bmatrix} \sigma_{nn} & \sigma_{nt} \\ \sigma_{nt} & \sigma_{tt} \end{bmatrix} \times \begin{pmatrix} 1 \\ 0 \end{pmatrix} = \frac{1}{S_{node}} \times \begin{bmatrix} \cos(\theta_T) & \sin(\theta_T) \\ -\sin(\theta_T) & \cos(\theta_T) \end{bmatrix} \times \begin{pmatrix} RF_x \\ RF_y \end{pmatrix} \tag{IV.3}$$

The surface of the zone surrounding the node is denoted S_{node} and θ_T represents the angle between the main coordinate system (x,y) and the interfacial coordinate system (n,t), see Figure IV.1.

Different stress criteria can then be used, from a normal stress criterion (Equation (IV.4)), to a quadratic criterion (Equation (IV.5)), involving both normal and shear stress tensor components.

$$f(\underline{\sigma}(\theta_d, \sigma^\infty), \sigma_c, \tau_c) = \frac{\sigma_{nn}}{\sigma_c} \geq 1 \tag{IV.4}$$

$$f(\underline{\sigma}(\theta_d, \sigma^\infty), \sigma_c, \tau_c) = \sqrt{\left(\frac{\sigma_{nn}}{\sigma_c}\right)^2 + \left(\frac{\sigma_{nt}}{\tau_c}\right)^2} \geq 1 \tag{IV.5}$$

Interface properties σ_c and τ_c correspond to the interface tensile and shear strengths, respectively, and enable to define $\mu = \tau_c/\sigma_c$, the shear to tensile strength ratio. An equivalent stress can therefore be defined (Equation (IV.6)) including the parameters listed in Equation (IV.5), similarly to Martin *et al.* [Mar+20] and Doitrand *et al.* [Doi+20].

$$\sigma_{\text{eq}} = \sqrt{\sigma_{\text{nn}}^2 + \frac{1}{\mu^2}\sigma_{\text{nt}}^2} \geq \sigma_{\text{c}} \tag{IV.6}$$

With this, the influence of considering the shear fracture properties for a range of μ can be evaluated. Figure IV.2 shows the influence of μ on the equivalent stress variation at the fiber-matrix interface.

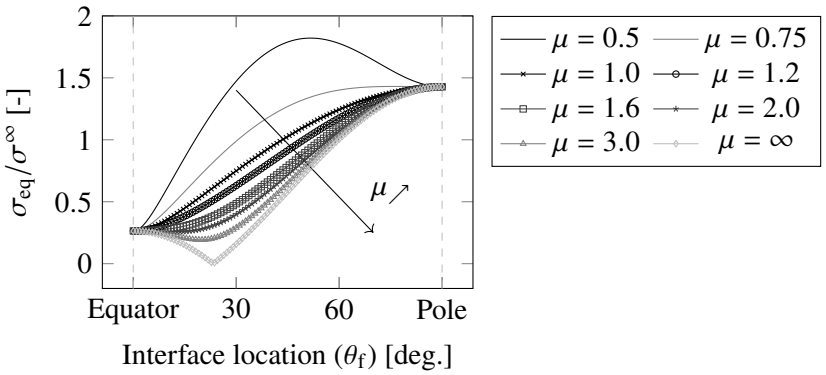

Figure IV.2 – Equivalent to remote stress ratio variation at the fiber-matrix interface from the fiber equator to the pole for different $\mu = \tau_{\text{c}}/\sigma_{\text{c}}$.

Figure IV.2 shows the equivalent stress variation from the fiber equator, *i.e.*, $\theta_{\text{f}} = 0$ deg., to the fiber pole, *i.e.*, $\theta_{\text{f}} = 90$ degrees. The larger the shear to tensile strength ratio, *i.e.*, μ, the closer the variation is to that of the normal stress criterion $\mu = \infty$, if the absolute value of the normal stress is considered. Therefore, as the debonding moves from the pole to the equator of the fiber, the equivalent stress tends towards 0 as the normal stress component changes from tension to compression. The minimum value of the equivalent stress at every angular location θ_{f} located in the debonding angle θ_{d} is retained in the stress condition of the CC, whether or not the stress decreases monotonically from the pole of the fiber.

Two configurations can be encountered by varying the shear to tensile strength ratio, as observed in Figure IV.2:

- Tensile-stress induced debonding initiation: the equivalent stress reaches a local peak located at both fiber upper and lower poles ($\mu > 0.75$);

- Shear-stress induced debonding initiation: the equivalent stress reaches two local peaks per fiber half-circle ($\mu < 0.75$), symmetrically with respect to the y-direction.

Based on experimental observation of tension-induced debonding initiation, configurations for which the stress maximum is attained at the fiber pole are considered in the sequel. The minimum acceptable value of μ is 0.75 in order to maintain a monotonic decrease in the equivalent stress from the pole. Therefore, for larger μ, the $\sigma_{\text{eq}}/\sigma^{\infty}$ ratio exhibit a monotonic decrease with increasing debonding angle. For the same applied loading and similar interface strengths, the use of the quadratic criterion leads to a larger debonding angle for which the stress criterion is fulfilled compared to a normal stress criterion. For debonding angles larger than 140 degrees, the interface experiences shear and compressive stresses. Therefore, it is not likely that debonding initiation occurs for angles larger than 140 degrees since it would correspond to debonding initiation under compression. For the sake of simplicity, only mode II is considered above this angle and the influence of the compressive stress being neglected. This explains the condition introduced in Equation (IV.7) for $\sigma_{\text{nn}}(\theta_{\text{d}}) < 0$.

$$\psi(\theta_{\text{d}}) = \begin{cases} \arctan\left(\frac{|\sigma_{\text{nt}}(\theta_{\text{d}})|}{\sigma_{\text{nn}}(\theta_{\text{d}})}\right), & \text{if } \sigma_{\text{nn}}(\theta_{\text{d}}) \geq 0 \\ \frac{\pi}{2}. & \text{if } \sigma_{\text{nn}}(\theta_{\text{d}}) < 0 \end{cases} \tag{IV.7}$$

The mode mixity parameter ψ defines the proportion of shear to normal stress ratio. The normalized variation in normal and shear stresses evaluated at the location of the future debonding tip on an undamaged interface, is shown in Figure IV.3a, as a function of the debonding angle.

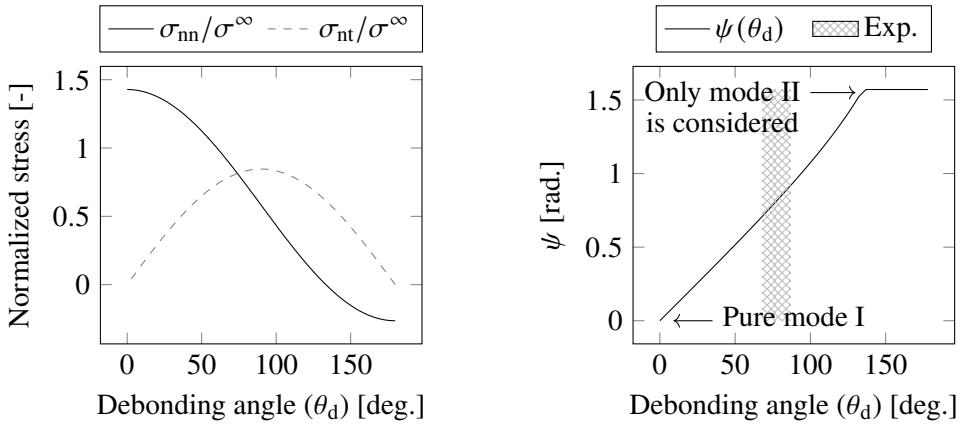

Figure IV.3 – (a) Variation in normalized normal and shear stresses at the location of the debonding tip on an undamaged interface. (b) Mode mixity variation as a function of the debonding angle, highlighting the mode mixity range corresponding to the experimentally-measured initiation debonding angles (hatched zone).

The interface experiences pure tensile stress at the fiber poles and shear combined to compressive stress at the fiber equators, see Figure IV.3a. The debonding angle measured experimentally just after initiation lies between 67 and 83 degrees, see Section III.3. In this angle range, indicated in Figure IV.3b by the hatched area, the influence of shear stress is not negligible, which justifies the use of the quadratic criterion in the sequel. Finally, the equivalent stress σ_{eq}, introduced in Equation (IV.6), must be larger than the tensile strength along the area on which the debonding initiates to fulfill the stress criterion.

Energy condition

The second condition of the CC for crack initiation prediction compares the IERR to the interface critical ERR, Equation (IV.2) and Equation (IV.8), respectively. The local critical energy release rate $G_{\text{c}}(\psi)$ accounts for the local mode mixity such that it varies from G_{IC} under pure opening mode to G_{IIC} under pure shear mode following the relationship proposed by Hutchinson and Suo [HS91] and recalled in Equation (IV.9). The global interface critical ERR, $\overline{G_{\text{c}}}$, corresponds to the average of the local interface critical ERR over the initiation crack path θ (Equation (IV.8)). The local mode mixity is calculated at an angle of 0.3 deg. ahead of the crack tip for a given debonding angle θ_{d}. The critical ERR (Equation (IV.9)), G_{c}, depends on the parameter λ which defines the ratio between G_{IIC} and G_{IC}. For instance, $\lambda = 1$ corresponds to $G_{\text{IIC}} = G_{\text{IC}}$ and $\lambda < 1$ corresponds to $G_{\text{IIC}} > G_{\text{IC}}$.

$$\overline{G_{\text{c}}} = \frac{1}{\theta_{\text{d}}} \int_0^{\theta_{\text{d}}} G_{\text{c}}(\psi(\theta)) \mathrm{d}\theta \tag{IV.8}$$

$$G_{\text{c}}(\psi(\theta_{\text{d}})) = G_{\text{IC}} \left[1 + \tan^2 \left[(1-\lambda)\,\psi(\theta_{\text{d}})\right]\right] \tag{IV.9}$$

Figure IV.4a shows the IERR to critical ERR ratio and Figure IV.4b shows the ratio between the loading ($\sigma^{\infty}_{\text{req}}$) to fulfill the energy criterion and the applied loading (σ^{∞}) as a function of the debonding angle for various values of λ.

Each curve exhibits a similar trend: for a small crack angle, a small amount of elastic strain energy is released which corresponds to a large imposed stress to fulfill the energy criterion. Therefore, there exists an optimal angle which maximizes the incremental ERR to critical ERR ratio and, therefore, minimizes the imposed stress to fulfill the energy criterion. Additionally, decreasing λ causes increasing G_{IIC} relative to G_{IC}. This results in larger $\overline{G_{\text{c}}}$ for large angle since the interface transitions from opening to shear as the debonding angle increases. As a result, larger loadings are required to fulfill the energy criterion when λ decreases, particularly for debonding angle larger than 60 degrees.

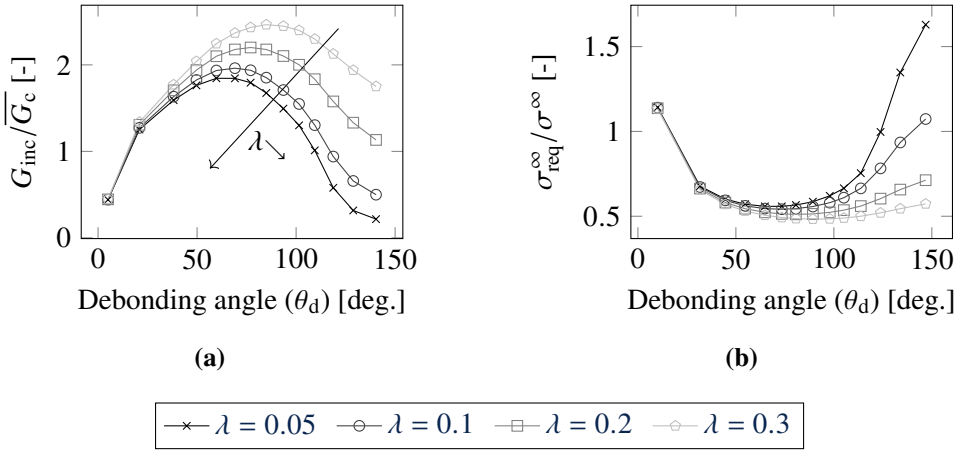

Figure IV.4 – (a) Incremental to critical ERR ratio denoted λ and (b) normalized required stress to fulfill the energy criterion variations as a function of the debonding angle, for various G_{IC}/G_{IIC} ratio.

Coupled stress and energy criteria

The CC consists in determining the minimum loading and corresponding debonding angle θ_{ini} for which the stress and the energy conditions are simultaneously fulfilled. The equivalent stress decreases monotonically whereas the incremental to critical ERR ratio exhibits a maximum. Therefore, as reported by Mantič [Man09] or Gentieu *et al.* [Gen+19], two scenarios can be identified:

- Scenario 1 (Figure IV.5a) - stress and energy driven configuration: when the intersection point of the two curves (dashed and solid) corresponds to an angle smaller than that corresponding to the maximum of the incremental to critical ERR, the favorable configuration corresponds to the intersection of the two curves (round red marker);
- Scenario 2 (Figure IV.5b) - energy-driven configuration: when the intersection point of the two curves (dashed and solid) corresponds to an angle larger than that corresponding to the maximum of the incremental to critical ERR, the favorable configuration is therefore the angle maximizing the IERR to critical ERR ratio (square red marker).

IV.2.3 Interface debonding propagation

Once interface debonding initiates, LEFM can be applied to assess its propagation. The condition for interface debonding propagation states that the ERR must exceed

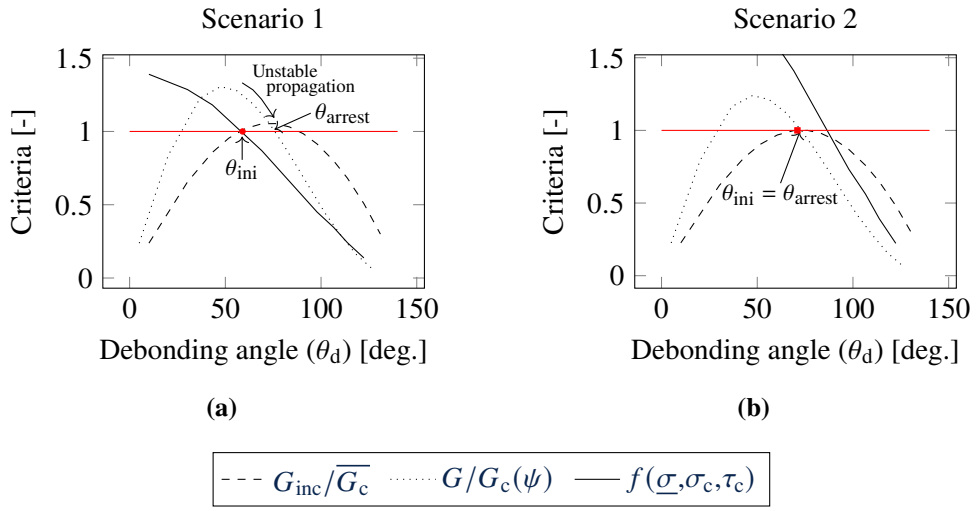

Figure IV.5 – IERR to critical ERR, ERR to critical ERR and stress criteria variation as a function of the debonding angle for (a) scenario 1 (stress and energy driven) and (b) scenario 2 (energy driven).

the local critical energy release rate, see Equation (IV.10).

$$G \geq G_c(\psi) \tag{IV.10}$$

For scenario 2, the crack remains stable just after initiation, because $G_{inc} = G = G_c$ at debonding initiation. Conversely, for scenario 1, $G > G_c$ at initiation therefore the debonding propagates in an unstable manner until $G < G_c$.

Stable crack propagation phase after initiation, see Section III.3, is observed experimentally. Considering the limitations associated with the image-based experimental analysis performed in this work, see Chapter III, an accurate assessment of the unstable crack propagation step is impossible. In particular, the image acquisition rate applied (one frame per second) is not large enough to provide any meaningful information regarding the unstable propagation step. As such, interface appears to remain undamaged until a finite crack increment. This observation can be attributed to the direct stable crack $\theta_{ini} = \theta_{arrest}$, *i.e.*, scenario 2, or to the end of the unstable crack propagation θ_{arrest}, as described in scenario 1.

The ERR is evaluated numerically as the opposite of the elastic strain energy derivative with respect to the debonding surface, obtained by successively unbuttoning the nodes along the interface. The normalized equivalent stress, IERR and ERR variations as a function of debonding angle obtained for the debonding initiation loading are shown for both scenarios in Figure IV.5. Figure IV.5a shows a configuration

where crack initiation is triggered by both stress and energy conditions. θ_{ini} corresponds to the initiation debonding angle. At debonding initiation, $G(\theta_{\text{ini}}) > G_c(\theta_{\text{ini}})$, there is an unstable propagation of the debonding until a debonding angle θ_{arrest} verifying $G(\theta_{\text{arrest}}) < G_c(\theta_{\text{arrest}})$. Since no increase in the loading is necessary so that the debonding propagates up to θ_{arrest}, the unstable propagation following initiation is expected to occur simultaneously. Therefore, the debonding angle measured experimentally can be compared to θ_{arrest} rather than to θ_{ini}. Figure IV.5b shows a configuration where crack initiation is driven by the energy condition. The initiation debonding angle corresponds to the maximum of the normalized IERR, which verifies $G(\theta_{\text{ini}}) = G_c$ and $\mathrm{d}G/\mathrm{d}\theta_d(\theta_{\text{ini}}) < 0$. Therefore, the initiation debonding angle is also an arrest angle in this configuration so that $\theta_{\text{arrest}} = \theta_{\text{ini}}$.

IV.2.4 Unstable propagation? Identification of the finite crack length

The approach to identify the arrest angle led to the identification of the debonding angle lower limit denoted θ_l in Figure IV.6.

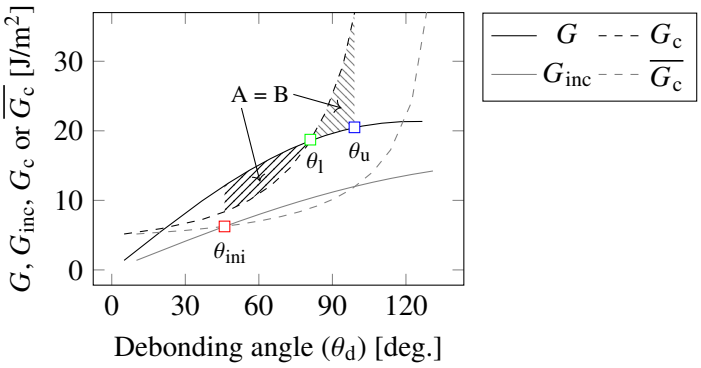

Figure IV.6 – Variation of G, G_{inc}, G_c and $\overline{G_c}$ as a function of the debonding angle for a loading leading to crack initiation.

However, during the unstable propagation phase from θ_{ini} to θ_l, there is an excess energy ($G > G_c$) that has not been consumed for crack propagation (hatched zone A in Figure IV.6). This excess energy may be consumed by further propagation of the crack, which enables defining an upper bound for the arrest angle, θ_u. This upper bound actually verifies that A and B areas (Figure IV.6) are identical.

Figure IV.7 shows the initiation debonding angle (θ_{ini}) as well as the lower (θ_l) and upper (θ_u) bounds for the arrest debonding angle (θ_{arrest}) obtained for several interface property couples. These curves are superimposed for sufficiently small tensile strengths ($\sigma_c < 4$ MPa) or sufficiently large critical ERR ($G_{IC} > 8$ J/m^2), corre-

sponding to configurations driven only by the energy criterion, *i.e.*, scenario 2. However, configurations driven by both stress and energy conditions are retrieved for large enough tensile strengths and small enough critical ERR, resulting in different lower and upper bounds of the debonding angle.

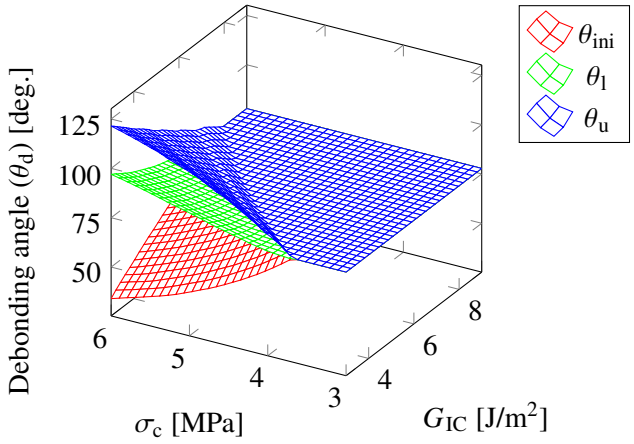

Figure IV.7 – Variation of the initiation angles as a function of the interface fracture properties for $\tau_c = 1.2\sigma_c$ and $\lambda = 0.2$.

The differences between the initiation and arrest angles are larger for either larger tensile strengths or smaller critical ERR. Increasing σ_c or decreasing G_c actually results in decreasing the material characteristic length:

$$\ell_{mat} = \frac{EG_c}{(1-\nu^2)\sigma_c^2}. \tag{IV.11}$$

Since the debonding angle obtained using the CC is a fraction of the material characteristic length [DML20; Mar+16; Mar+18], it explains that a decrease in the material characteristic length results in a decrease in the initiation angle and an increase in the arrest angle. Larger debonding arrest angles are finally obtained in configurations driven by both conditions rather than in configurations driven only by the energy condition.

IV.2.5 Inverse identification for sample SFI-1

The inverse identification procedure for sample SFI-1 is based on the following strategy:

Step 1: identification of a range of σ_c, τ_c, G_{IC} and G_{IIC} leading to a debonding initiation remote stress (σ^∞) consistent with experimental observations;

Step 2: definition of a range of σ_c, τ_c, G_{IC} and G_{IIC} leading to a debonding arrest angle (θ_{arrest}) close to that found experimentally;

Step 3: definition of a range of G_{IC} and G_{IIC} leading to crack propagation stress (σ^∞) and angles (θ_d) similar to those found experimentally.

The first two steps rely on the debonding initiation, the third one on its propagation.

Properties identification based on crack initiation (step 1 and 2)

Step 1: according to the experimental measurements, the remote stress corresponding to crack initiation is comprised between 3.02 and 4.05 MPa (see Section III.3). Because of linear elasticity and small deformation assumptions, the interface properties can be varied only during the post-processing step of the FE calculations, which makes the interface property determination computationally efficient. Figure IV.8 shows the set of interface properties identified leading to remote stress at debonding initiation σ^∞ = 4.05 MPa for λ = 0.22.

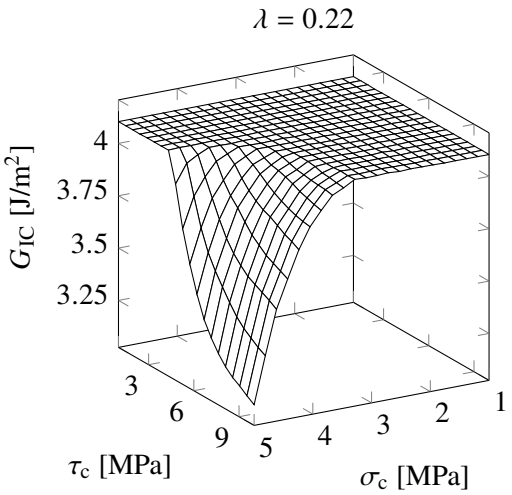

Figure IV.8 – Interface fracture properties leading to a crack initiation at a remote stress applied of 4.05 MPa, λ is set to 0.22 as an example.

For sufficiently small tensile or shear strengths, a constant G_{IC} is identified. This is related to configurations driven only by the energy criterion. In such configurations, the stress criterion is already fulfilled and crack initiation depends only on the normalized IERR maximum. However, configurations driven by both stress and energy

conditions are encountered for sufficiently large tensile and shear strengths, which results in the decrease of G_{IC} with increasing shear or tensile strength.

The debonding arrest angle θ_{arrest} variation is also related to G_{IC} (Figure IV.9). It is considered equal to θ_l in the sequel, see Section IV.2.4. For configurations driven only by the energy condition, *i.e.*, assimilated to the G_{IC} plateau, a constant debonding angle corresponding to the normalized IERR maximum is obtained. For interface properties leading to a smaller G_{IC}, the debonding angle is larger than the value at the plateau.

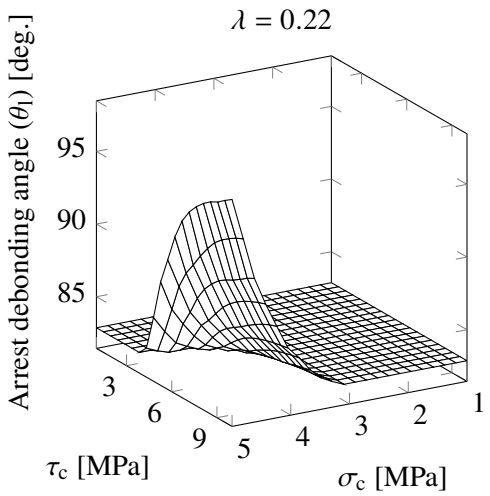

Figure IV.9 – Arrest debonding angle ($\theta_{arrest} = \theta_l$) variation as a function of interface fracture properties.

Step 2: restriction on the range of properties is pursued so that the arrest debonding angle corresponds to the one measured experimentally, *i.e.*, between 67 deg. and 83 degrees. Figure IV.10 shows the debonding arrest angle variation as a function of the tensile and shear strengths obtained for the interface properties verifying $\sigma^{\infty} = 4.05$ MPa for various λ values.

The debonding angle at the plateau mainly depends on λ, which enables determining an upper bound, $\lambda = 0.22$ (Figure IV.10a) above which a too large debonding angle is obtained. Conversely, using $\lambda = 0.03$ (Figure IV.10b) leads to the minimum acceptable value to keep the plateau within the two experimental limits. Figure IV.11 shows the variation in debonding angle at the plateau for a range of λ superimposed on the experimentally observed limits of the debonding angles, *i.e.*, the dotted area. Overall, the plateau value increases as λ increases. This trend can be attributed to the reduction in shear fracture properties, which consequently facilitates debonding at the fiber equator. The λ range is therefore restricted which provides a debonding angle

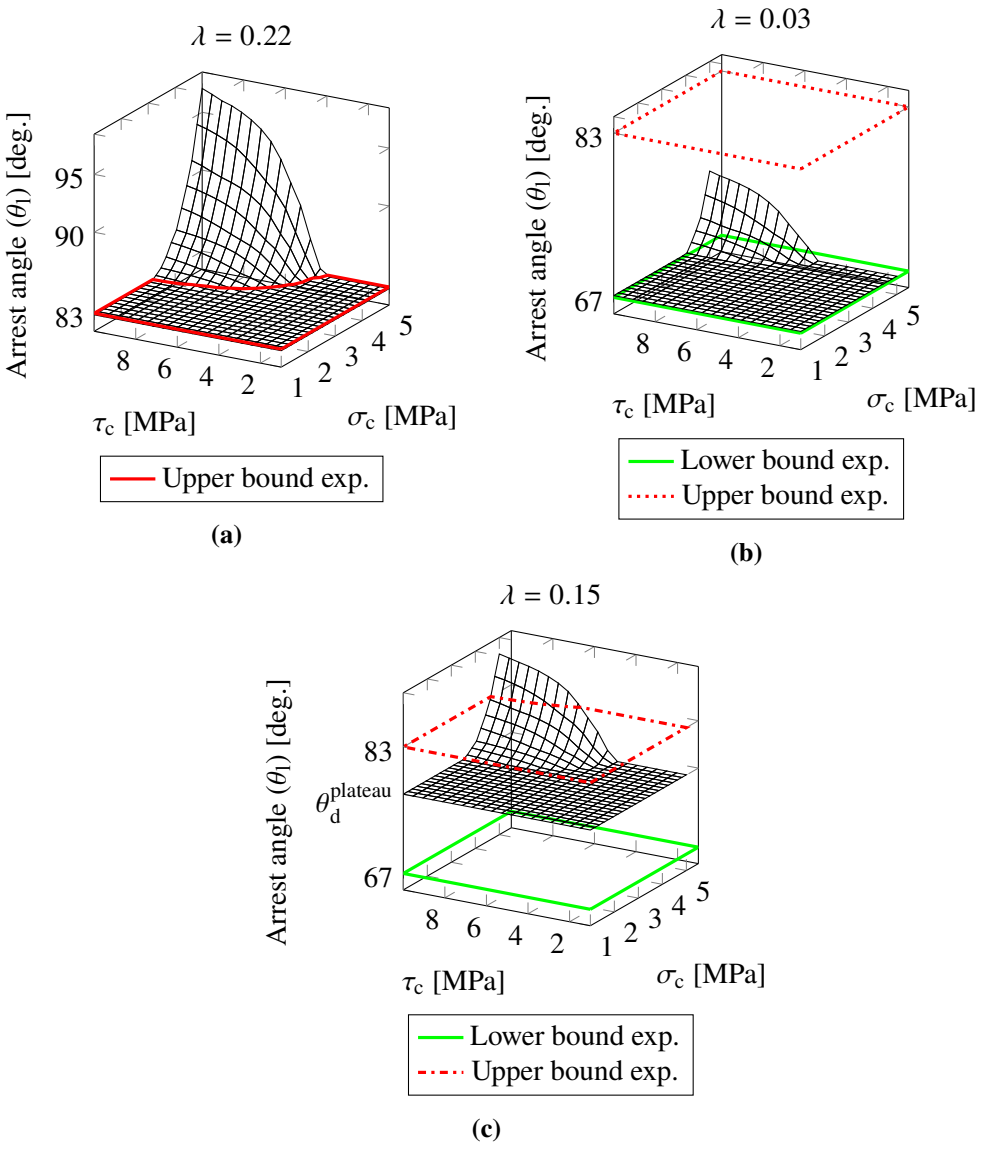

Figure IV.10 – Variation of the lower bound of the arrest angle ($\theta_{\text{arrest}} = theta_{\text{l}}$) as a function of tensile and shear strengths, for (a) $\lambda = 0.22$ (b) $\lambda = 0.03$ (c) $\lambda = 0.15$, with their corresponding boundaries.

at the plateau between the two experimental limits. Smaller values of λ can also be obtained for large tensile and shear strengths but further result in large differences in terms of debonding angle variation as a function of applied stress. They are therefore

disregarded in the following.

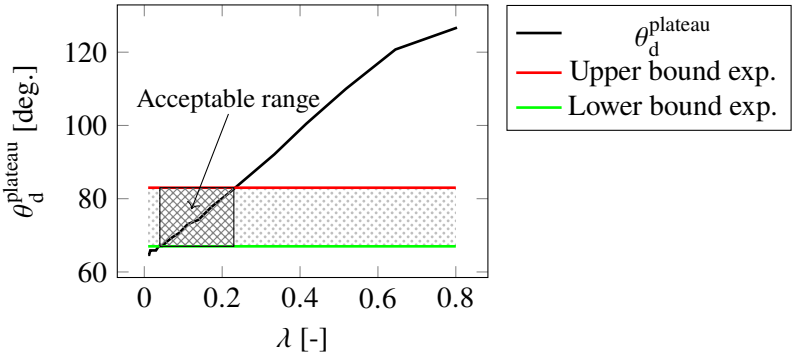

Figure IV.11 – Debonding angle at the plateau obtained for a range of λ.

The application of the restriction of the debonding angle has no influence on the smallest values of λ because all the couples lie between the two boundaries, see Figure IV.10b. Nevertheless, increasing this parameter leads to couples outside the acceptable range, as shown by the red upper boundary in Figure IV.10c and Figure IV.10a. For these configurations, the proportion of unacceptable strength and energy parameters increases with λ. Moreover, to ensure a parameter μ greater than 0.75, additional restrictions are applied to the obtained range of σ_c and τ_c. Figure IV.12 and Figure IV.13 summarize these restrictions for the strength and energy interface properties respectively.

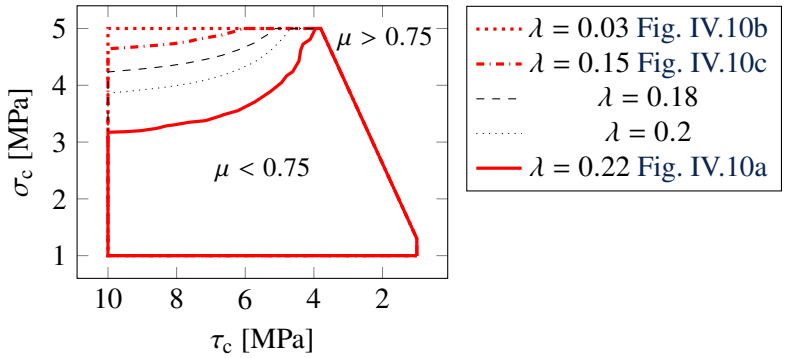

Figure IV.12 – Stress couples restriction for several values of λ. The upper bounds depicted in red are directly related to the upper bounds of the angle restriction shown for three values of λ in Figure IV.11.

Ultimately, increasing λ leads to decrease the range of acceptable tensile and shear strengths (Figure IV.12) as well as critical ERR, for which a lower bound can be

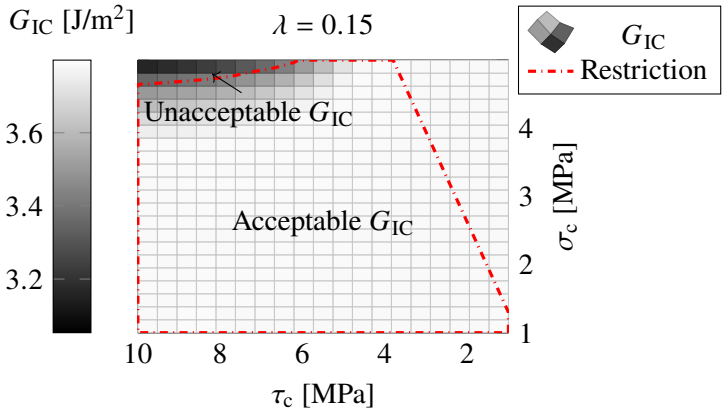

Figure IV.13 – G_{IC} restriction for $\lambda = 0.15$. The lower bound depicted in red is directly related to the upper bound of the angle restriction shown for $\lambda = 0.15$ in the Figure IV.10c.

determined for a given λ (Figure IV.13).

Further property restriction based on crack propagation (step 3)

Step 3: this last step of the inverse identification approach depends only on an energy condition, so that only the energy parameters are involved. The influence of fracture energy properties is investigated in Figure IV.14. Focusing on Figure IV.14a, a similar debonding arrest angle at initiation is obtained whatever G_{IC} whereas a larger remote loading at initiation is encountered by increasing G_{IC}. Since debonding initiation occurs at the pole of the fiber, which experiences predominantly mode I, it is likely that the opening fracture properties controls the remote loading at initiation. In contrast, the debonding angle at initiation is driven by the shear properties, as shown in Figure IV.14b. Increasing G_{IIC} leads to a decrease in λ and a decrease in the debonding arrest angle. This can be explained by the influence of the shear between the pole of the fiber and the equator. Similarly, a large G_{IIC} requires a larger remote loading to achieve a large debonding angle compared to small G_{IIC}. It is worth noting that G_{IIC} has a slight influence on the remote loading at initiation, as shown in Figure IV.14b, with the remote loading at initiation slightly increasing with G_{IIC}. This is due to the fact that the initiation angles are located in zones with combined opening and shear loadings. Thus, the G_{IC} properties have a significant influence on the remote loading at initiation, while G_{IIC} governs the debonding arrest angle.

Consequently, studying the debonding propagation phase enables the determination of G_{IIC} and λ. The aim is to minimize a difference ($\mathcal{F}_1$) between the experimental

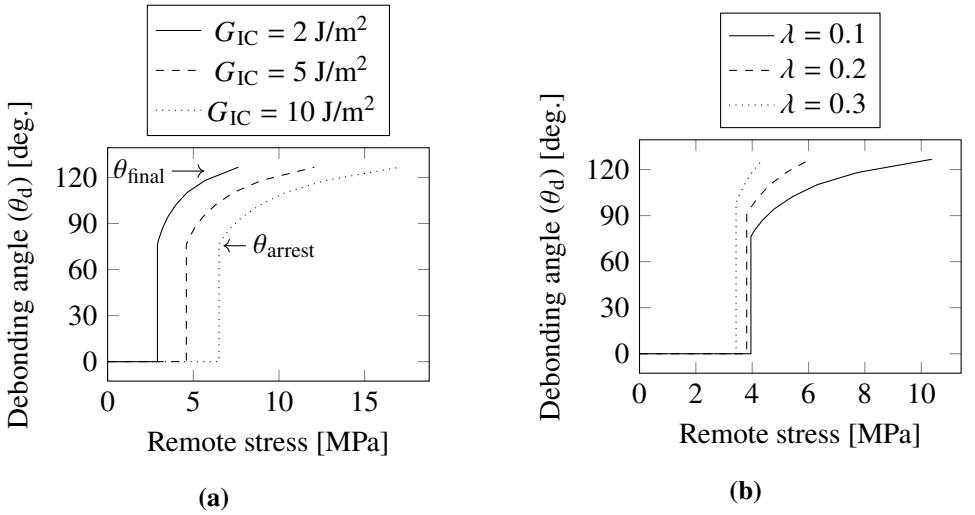

Figure IV.14 – Debonding stable propagation phase obtained for (a) three G_{IC} values with $\lambda = 0.1$ and (b) three λ values with $G_{IC} = 3.7$ J/m^2.

and numerical remote loadings for different angles from after initiation (θ_{arrest}) up to a large debonding angle (θ_{final}), see Figure IV.14a. The difference calculation is detailed in Equation (IV.12), where σ^{∞}_{sim} and σ^{∞}_{exp} denote the remote stress obtained from the simulation and experiments respectively.

$$\mathcal{F}_1 = \left(\frac{1}{\theta_{final} - \theta_{arrest}} \int_{\theta_{arrest}}^{\theta_{final}} \frac{\left| \sigma^{\infty}_{exp}(\theta) - \sigma^{\infty}_{sim}(\theta) \right|}{\sigma^{\infty}_{exp}(\theta)} d\theta \right) \times 100 \tag{IV.12}$$

The difference $\mathcal{F}_1$ is evaluated for a range of λ and G_{IC}, as shown in Figure IV.15a.

The surface exhibits a valley where the difference is minimal, with a difference $\mathcal{F}_1$ around 20%. Consequently, the adequate couples should be inside the valley. Coupling the previous restriction obtained in the first two steps and the results of the $\mathcal{F}_1$ calculation leads to the identification of a relevant set of fracture properties. Figure IV.15b superimposed the difference isocontours to the previous restriction obtained based on the debonding initiation (dashed red line). The (G_{IC}, λ) couple that best meets all the restrictions is represented by the square mark in Figure IV.15b and corresponds to the interface properties presented in the first row of Table IV.1. The properties are consistent with other glass fiber epoxy matrix interfaces fracture properties (Table IV.2). It is worth noting that the properties presented depend strongly on the characterized interface and the method used, as developed in Section II.2. Thus, a direct comparison cannot be performed, nevertheless the comparison of the orders of magnitude leads to a good correspondence.

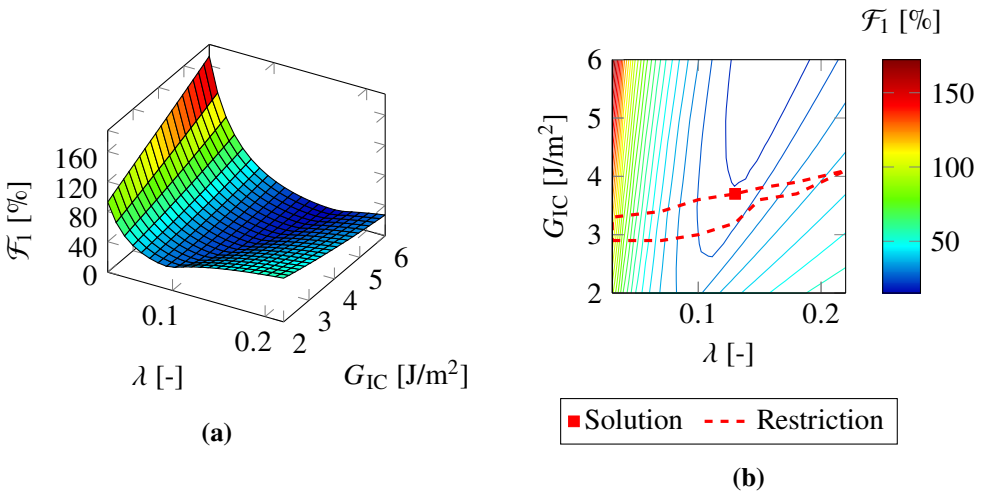

Figure IV.15 – (a) Difference $\mathcal{F}_1$ as a function of the energy parameters λ and G_{IC}. (b) Isocontours of the difference $\mathcal{F}_1$ with the addition of the previous restriction due to crack initiation.

	G_{IC} [J/m^2]	G_{IIC} [J/m^2]	λ	σ_c [MPa]	τ_c [MPa]
Initiation-based	3.7	90	0.13	1 - 5	1 - 10
Propagation-based	16	90	0.27	1 - 5	1 - 10

Table IV.1 – Identified interface fracture properties using the CC approach.

The debonding angle variation as a function of the applied stress is compared with that observed experimentally in Figure IV.16 for the identified optimal set of parameters. The initiation debonding angle and applied stress as well as the debonding angle propagation as a function of the applied stress for debonding angles larger than 120 deg are well captured. Between 90 and 120 deg. the debonding angle is slightly overestimated due to properties identification that mainly focuses on debonding initiation.

Parameter identification based solely on crack propagation

Since crack initiation may be prone to some variability, for instance due to the presence of a defect, another approach can be used to identify the interface properties by first disregarding debonding initiation and focusing on propagation only (**step 3**). This approach yields the interface properties given in the second row of Table IV.1.

The debonding angle variation as a function of the applied stress corresponding to these parameters is shown in Figure IV.16. A better description of the debonding angle variation as a function of applied stress is obtained for the propagation phase,

Materials	σ_c [MPa]	τ_c [MPa]	G_{IC} [J/m^2]	G_{IIC} [J/m^2]	
GF / Ep.[2]	18 - 25	18 - 22	5.5	11	[Koy+09]
GF / Ep.	31				[OSK09]
GF / Ep. (NOCA)			2	6	[VBE97]
GF / Ep.	37				[TKC16]
GF / Ep.		6			[Cha02]
GF / Ep.		12			[TTK00]
GF / Ep.	10 - 13				[Age+99]

[1]Epoxy

Table IV.2 – Interface properties obtained from previous works.

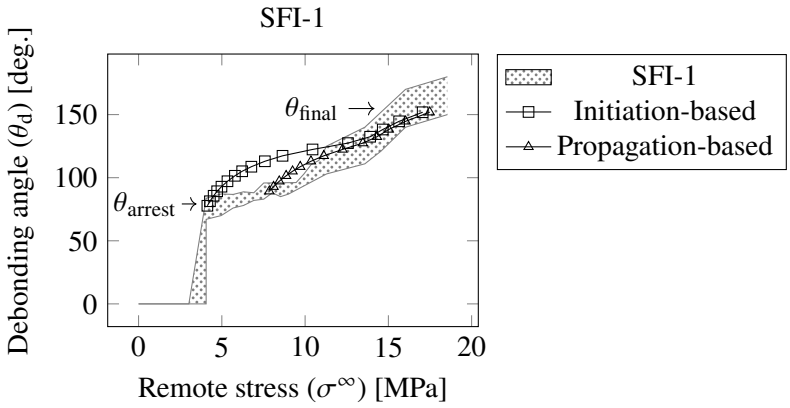

Figure IV.16 – Variation of the debonding angle as a function of the remote stress applied. Comparison between the experimental measurements and simulations performed with the identified properties using both initiation- and propagation-based approaches (see Table IV.1). The dotted area represents to the experimental measurement interval.

the initiation debonding angle also being well reproduced. Nevertheless, the applied stress at debonding initiation tends to be overestimated by the latter approach.

IV.2.6 Inverse identification for sample SFI-2

A similar inverse identification can be undertaken for sample SFII-2, which has a remote initiation loading of 7.34 MPa and initiation debonding angles ranging from 30 to 43 degrees. The initiation arrest debonding angle is therefore smaller than that of

sample SFI-1, which complicates the inverse identification since this range of angles cannot be captured by the CC. Indeed, Figure IV.11 shows the minimum initiation debonding angle that can be attained as a function of the critical ERR ratio. The minimum debonding angle is therefore close to 65 degrees, which is larger than the experimental observations.

One approach to identify the interface fracture properties would therefore consist in:

Step 1: identifying a range of σ_c, τ_c, G_{IC} and G_{IIC} leading to a crack initiation remote stress (σ^∞) consistent with experimental observations (7.35 MPa) and disregard the arrest debonding angle obtained at initiation;

Step 2: restricting the range of G_{IC} and G_{IIC} based on the stable debonding propagation after initiation using the remote stress (σ^∞) and angles (θ_d) similar to those found experimentally.

Regarding **step 1**, Figure IV.17 shows the range of fracture properties identified for a fixed λ of 0.13.

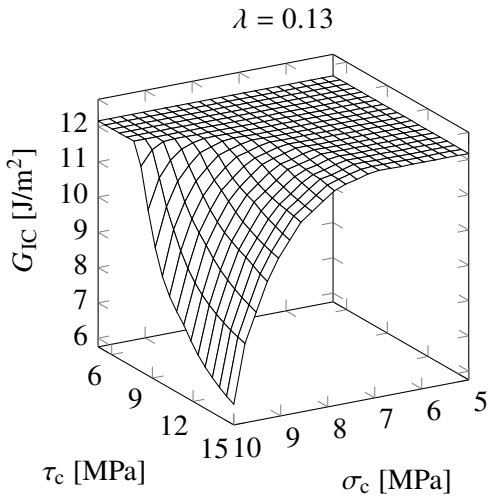

Figure IV.17 – Interface fracture properties leading to a crack initiation at a remote stress applied of 7.35 MPa. The parameter λ is set to 0.13.

Since the arrest debonding angle obtained after initiation is not considered for this sample, similar ranges of properties can be identified for the entire λ range. The properties identified yield a plateau for the energy driven configurations. The remaining properties are identified until there is no longer an intersection between the two

CC conditions. Based solely on debonding initiation, it is possible to identify an infinite number of fracture properties. Regarding **step 2**, the numerical-experimental difference $\mathcal{F}_1$ on the remote stress during the propagation phase is calculated using Equation (IV.12). The difference is shown for a range of critical ERR in mode I and λ in Figure IV.18a.

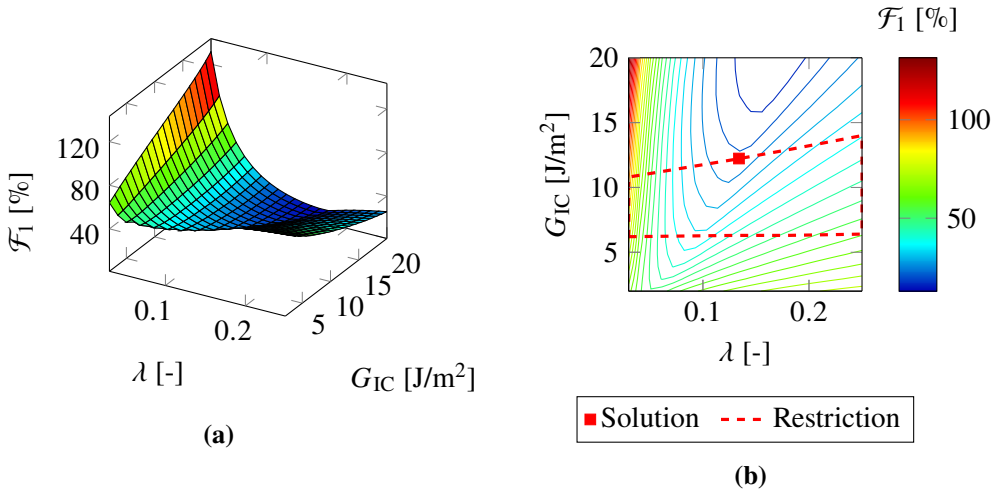

Figure IV.18 – (a) Calculation of the difference $\mathcal{F}_1$ as a function of the energy parameters λ and G_{IC}. (b) Isocontours of the difference $\mathcal{F}_1$ with the addition of the previous restriction due to crack initiation.

The difference yields a valley, similar to the SFI-1 sample, where the difference during the propagation phase becomes smaller. The appropriate solution (G_{IC}, λ) should be located inside the valley, but there is still an infinite number of solutions. A restriction based on the initiation phase can be considered. Figure IV.18b shows the difference isocontours, highlighting the valley for the intermediate λ. The extremes G_{IC} identified for each value of λ are thus superimposed on the isocontours, red dashed line, defining the admissible interval of (G_{IC}, λ). Note that the acceptable zone is wider than that of the SFI-1 sample because no restrictions on debonding angle at initiation can be applied. The optimal solution can be defined as the one that minimizes the difference within the new acceptable zone (dashed red line). In fact, it corresponds to the value inside the valley for the largest G_{IC}. The optimal solution is highlighted by a red square marker in Figure IV.18b. The range of fracture properties identified is summarized in Table IV.3.

A λ of 0.13 is identified, in line with that of sample SFI-1 with the same procedure. A larger G_{IC} is identified, consistent with the difference in remote initiation stress between the two samples. Similarly, larger strengths are identified with sample

	G_{IC} [J/m^2]	G_{IIC} [J/m^2]	λ	σ_c [MPa]	τ_c [MPa]
Initiation-based SFI-1	3.7	90	0.13	1 - 5	1 - 10
Initiation-based SFI-2	12.2	296	0.13	5 - 10	5 - 15

Table IV.3 – Identified interface fracture properties using the CC approach for the two samples from batch SFI.

SFI-2, corresponding to the range shown in Figure IV.17. A large value of G_{IIC} is identified compared to other values reported in the literature. This raises the question of the validity of the description of the critical ERR used here or the determination of the debonding which is limited by the pixel size. However, the propagation phase is correctly described by the model when the variation in the debonding angle is compared with the experimental observations, as shown in Figure IV.19.

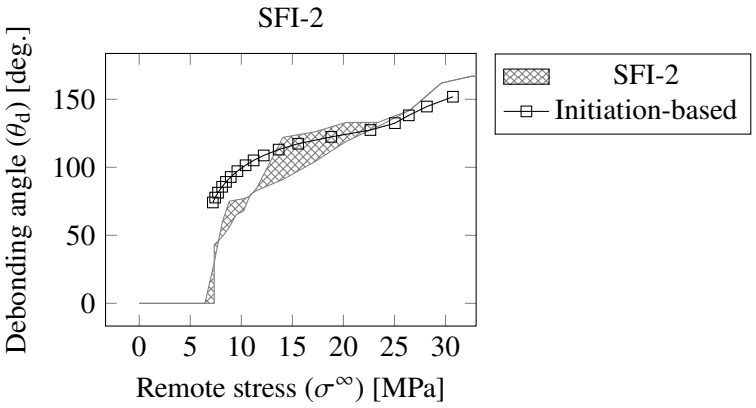

Figure IV.19 – Variation of the debonding angle as a function of the remote stress applied. Comparison between the experimental measurements and the simulation performed with the identified parameters. The hatched area corresponds to the experimental measurement interval.

As expected, the arrest debonding angle is overestimated as it cannot be captured with the current approach. The debonding angle is then overestimated for the stable propagation phase between 7 and 13 MPa remote stress, with the difference decreasing with remote stress. The numerical predictions are finally in line with the experimental predictions for a large debonding angle up to almost complete debonding.

IV.2.7 Current limitations

The proposed approach enables the determination of σ_c, τ_c, G_{IC} and G_{IIC}, using a model based on a binary description of fracture considering either interface debonding or no debonding. As a consequence, the possible presence of a process zone is not considered, as in cohesive zone models, for instance. Measured debonding angle may however account for the fully damaged and process zones, whereas the above identification considers a fully damaged zone. The current method of measuring the debonding angle cannot distinguish between the process zone and the fully cracked zone. One approach would be to compare the DIC fields at the fiber vicinity for different loadings and compute the numerical debonding that minimizes the difference in DIC fields for different angles.

IV.3 2D inverse identification using Cohesive Zone Model

The inverse identification approach using CZM was carried out in collaboration with Benjamin Bert as part of his internship at the laboratory. It is performed on the sample SFI-1.

IV.3.1 2D numerical model

A numerical model similar to that used in Section IV.2 is used where cohesive elements are placed at the fiber-matrix interface. Overall, the model consists of 2D plane strain elements under the assumption of linear elasticity and small deformations. An implicit dynamic algorithm is used to avoid convergence issues due to unstable crack propagation under quasi-static conditions. The elastic properties given in Table III.2 are employed. A density of 1.1 gr/cm^3 is assigned to the matrix and 2.5 gr/cm^3 to the fiber, these values being supplied by the manufacturers. A mesh size of 0.02 mm is assigned to the cohesive elements to ensure that the difference observed in the debonding angle relative to the remote stress with fixed fracture properties is less than 5% compared with a converged solution.

The CZM requires a traction-separation profile that involves mode mixity since the fiber-matrix interface is likely to experience both mode I and mode II. The CZM and the CC share similar interface fracture properties, namely the critical tensile and shear strength, σ_c and τ_c, respectively, and the critical ERR in both mode I and II, G_{IC} and G_{IIC}, respectively. The following quadratic stress criterion is used to assess the damage initiation in the cohesive elements:

$$\left(\frac{\sigma_{nn}}{\sigma_c}\right)^2 + \left(\frac{\sigma_{nt}}{\tau_c}\right)^2 = 1. \tag{IV.13}$$

Also, there is no longer any traction in the element when the following energy criterion is fulfilled:

$$\frac{G_{\mathrm{I}}}{G_{\mathrm{IC}}} + \frac{G_{\mathrm{II}}}{G_{\mathrm{IIC}}} = 1. \tag{IV.14}$$

An artificial stiffness is further implemented into the cohesive profile to guarantee the continuity of the displacement fields for any separation smaller than the damage initiation separation. The artificial stiffness is determined so that the difference induced on the debonding angle variation is smaller than 2%. Figure IV.20 shows the triangular traction-separation profile used herein. The artificial stiffness corresponds to the slope for separation smaller than δ_0 and can be calculated by $\sigma_{\mathrm{c}}/\delta_0^{\sigma}$ or $\tau_{\mathrm{c}}/\delta_0^{\tau}$ for opening or shearing modes.

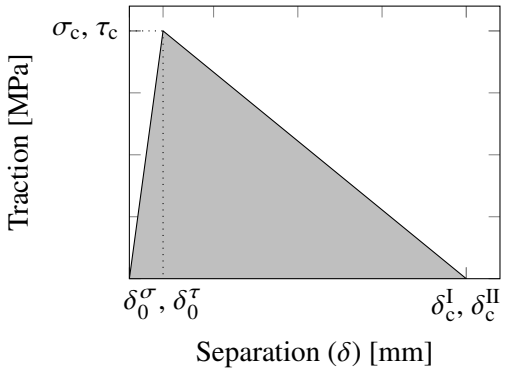

Figure IV.20 – Triangular profiles implemented into the CZM to assess debonding initiation and propagation.

The two triangular profiles can be related to each other using Equation (IV.13) and Equation (IV.14).

IV.3.2 Influence of the interface fracture properties

The debonding process observed experimentally in Section III.3, *via* the debonding angle, can be divided into several stages:

1. Increase in remote loading until debonding is initiated (——);
2. Debonding initiation for a remote stress ($\sigma_{\mathrm{req}}^{\infty}$);
3. Unstable debonding propagation up to an arrest angle (θ_{arrest}) (- - -);

4. Stable debonding propagation (·····).

Figure IV.21 provides a schematic illustration of the various stages described above.

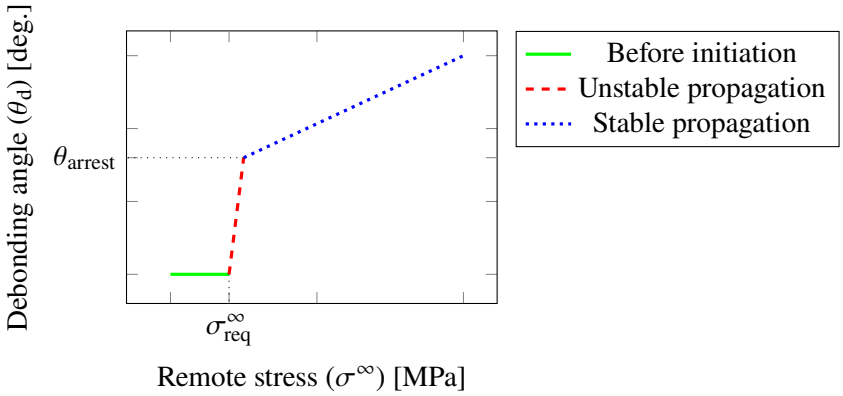

Figure IV.21 – Schematic illustration of the different phases of the debonding process, manifested by the debonding angle variation as a function of the remote stress.

The interface fracture properties influence each phase of the debonding process since both opening and shear modes are involved in the debonding process. Only completely damaged cohesive elements are taken into account in the calculation of the debonding angle to be consistent with the binary vision of the crack considered by the CC.

Figure IV.22 shows the influence of the critical ERR in mode I (G_{IC}) on the debonding process while the other fracture properties are fixed (σ_c, τ_c and G_{IIC}).

Overall, the critical ERR in mode I mainly influences the remote stress at initiation. (σ^{∞}_{req}). The larger the critical ERR, the larger the loading required for debonding initiation. The parameter σ_c influences the debonding process in the same way. These parameters only influence the initiation loading, while the arrest angle θ_{arrest} and the propagation phases remain unchanged.

Figure IV.23 shows the influence of the critical ERR in mode II, G_{IIC}. This fracture property, together with τ_c, primarily influences the arrest angle (θ_{arrest}) obtained after the unstable propagation phase. The larger these two parameters, the smaller the arrest angle will be since the interface mainly experiences shear for sufficiently large debonding angle. Similarly, the larger the parameters τ_c and G_{IIC}, the larger the loading required to propagate the debonding after the unstable propagation phase. Shear fracture properties also slightly influence the debonding initiation loading suggesting that debonding also experiences shear at debonding initiation.

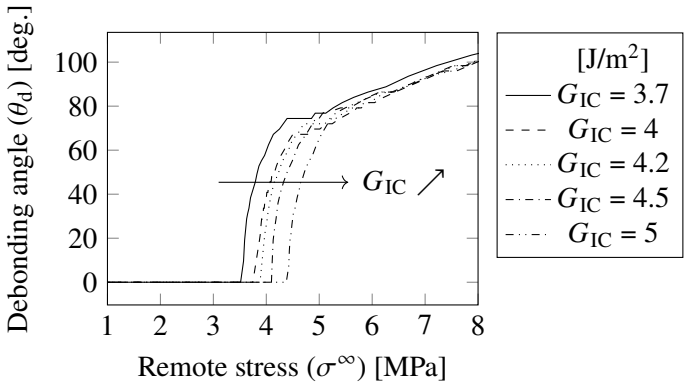

Figure IV.22 – Influence of the G_{IC} on the debonding process with σ_c = 3 MPa, τ_c = 4 MPa and G_{IIC} = 10 J/m^2.

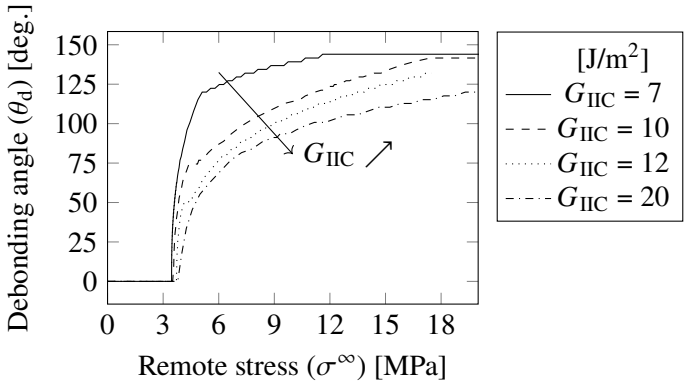

Figure IV.23 – Influence of the G_{IIC} on the debonding process with σ_c = 3 MPa, τ_c = 4 MPa and G_{IC} = 3.7 J/m^2.

The influence of each parameter on the different phases of the debonding process therefore enables the identification of a range of optimum fracture properties that minimizes the difference with the experimental results.

IV.3.3 Inverse identification

As CZM involves non-linearity, the approach is not as efficient as the CC in identifying optimal fracture properties since one FE calculation per fracture parameter set must

be performed. Therefore, a different approach is developed herein. Several indicators are used to quantify the agreement between simulations and experimental results:

- Initiation remote loading ($\sigma^{\infty}_{\text{req}}$);
- Arrest angle after the unstable propagation phase (θ_{arrest});
- Slope of the debonding angle relative to the remote stress provided by the stable propagation phase.

The influence of each parameter on the experimental-simulation agreement is quantified in order to obtain a range of acceptable interfacial fracture properties. Calculations are therefore undertaken with large ranges of fracture properties during a preliminary study, the aim being to minimize these ranges iteratively.

The preliminary study reveals that G_{IC} is of the order of 2 to 5 J/m^2 and G_{IIC} of the order of 6 to 15 J/m^2. Similarly, σ_{c} is found to be close to 3 MPa and τ_{c} must be larger than σ_{c} to ensure that debonding initiation takes place at the pole of the fiber and not on its equator. A second study is carried out to minimize the range of properties obtained. The first step is to determine the optimum G_{IIC}. The other parameters are then fixed at the mean values of the ranges obtained during the preliminary study. In order to minimize the difference with the experimentally observed arrest angle and stable propagation phase, G_{IIC} is found to be between 8 and 11 J/m^2. In a second step, a similar approach is used with the parameter G_{IC}. The latter mainly influences the loading at initiation, and the agreement between experiment and simulation is satisfactory for values of G_{IC} between 2.5 and 4.2 J/m^2. Finally, the influence of the two parameters σ_{c} and τ_{c} is evaluated iteratively until experimental-simulation agreement is obtained. The optimum range for the parameter σ_{c} lies between 3 and 3.5 MPa and between 3.5 and 4.5 MPa for τ_{c}.

Table IV.4 summarizes the ranges of fracture properties identified with the CZM and those obtained with the CC initiation-based approach in Section IV.2.

Fracture properties	CZM SFI-1	CC SFI-1
σ_{c} [MPa]	3 - 3.5	1 - 5
τ_{c} [MPa]	3.5 - 4.5	1 - 10
G_{IC} [J/m^2]	2.5 - 4.2	3.7
G_{IIC} [J/m^2]	8 - 11	90

Table IV.4 – Comparison of the interface fracture properties identified using the CC and the CZM.

Similar interface fracture properties are obtained with both the CC and CZM, except for G_{IIC} which is larger with the CC. However, the properties identified are

dependent on the criterion used. The energy condition involves a sum of two criteria for the CZM, whereas the CC uses the Hutchinson and Suo [HS91] relationship to describe the critical ERR. This difference may explain the differences obtained for G_{IIC}.

In addition, the presence of the process zone may have influenced the results for relatively large debonding angles. Some authors have found a significant difference between the CC and CZM approaches, particularly for small fibers [GPM14; Gen+19]. García *et al.* [GPM14] showed the influence of the interface brittleness number, which is detailed in Equation (II.31), on the CC and CZM predictions. The configuration studied here leads to a brittleness number of $\gamma \simeq 1.4$. According to García *et al.* [GPM14], such a value should result in a CC-CZM agreement, explaining the similar opening fracture properties identified. Nevertheless, no study or comparison of the two approaches on debonding propagation has yet been performed.

Figure IV.24 shows a comparison of the experimental results superimposed on the results obtained using the CC and CZM approaches.

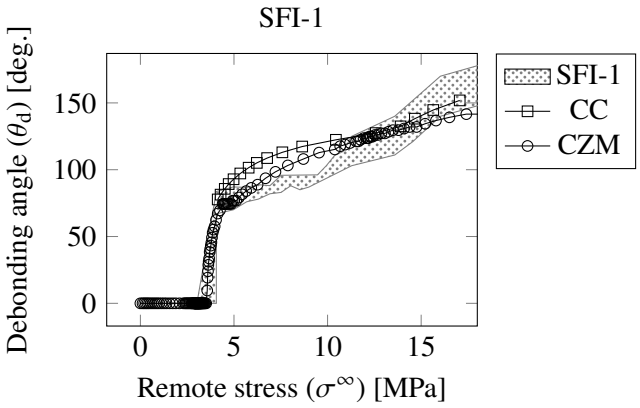

Figure IV.24 – Variation of the debonding angle as a function of the remote stress applied. Comparison between the experimental measurements and the simulations based on both the CC and CZM approaches. The dotted area corresponds to the experimental measurement interval.

Both approaches agree with the experimental results. The remote loading at initiation and the angle at which unstable propagation stops are correctly predicted by both approaches. There is a slight difference at the beginning of the stable propagation phase, particularly for the CC, which slightly overestimates the angle. All in all, the properties identified with the CZM are also consistent with other glass fiber epoxy matrix interfaces (Table IV.2).

IV.3.4 Current limitations

Similarly to the CC approach presented in Section IV.2, the CZM is based on 2D calculations whereas the experimental observations are carried out at the free surface of the sample, where there is a 3D stress singularity. The 2D modeling disregards the stress singularity, which may lead to an underestimation of the fracture properties by the CZM approach. Furthermore, the debonding initiation may not be uniform along the specimen thickness, as shown previously by the experimental observations of Martyniuk *et al.* [Mar+13]. It is expected that considering a 3D model would therefore enable capturing the 3D stress singularity.

Furthermore, the proposed approach mainly depends on the experimental variation of the debonding angle as a function of the remote stress. However, the determination of the debonding angle is dependent on the pixel size. Another possibility would therefore be to use the debonding opening rather than the angle, since this characterization method allows the sub-pixel phenomenon to be observed.

IV.4 3D inverse identification using the Coupled Criterion

A 3D model of a single fiber specimen is developed to perform the inverse identification of interface fracture properties and quantify the accuracy of the 2D models introduced previously. The following inverse identification approach is performed based on the debonding opening observed from the SFI-2 sample at site ① since uncertainties in the determination of the debonding opening at initiation is observed for sample SFI-1 (see Chapter III). The latter shows symmetric debonding initiation at both fiber poles for a similar remote stress.

IV.4.1 3D numerical model

Model presentation

Figure IV.25 depicts the dimensions of the corresponding 3D numerical model (right), along with the geometry of the sample (left), where the proximity of the free surface to the fiber-matrix interface induces a 2% difference in the stress fields compared to a fiber embedded in infinite medium.

To reduce computational costs, the sample geometry is simplified and limited to 1/8. Symmetry boundary conditions are applied to the ($x = 0$), ($y = 0$) and ($z = 0$) faces, with the origin (0,0,0) being located at the fiber center point. Displacements are applied to the top face to replicate the remote loading. The calculations are performed assuming linear elasticity and small deformations using linear hexahedral elements. The elastic properties of the constitutive materials used are summarized in Table III.2. In the sequel, debonding initiation is assessed based on both stress and energy criteria.

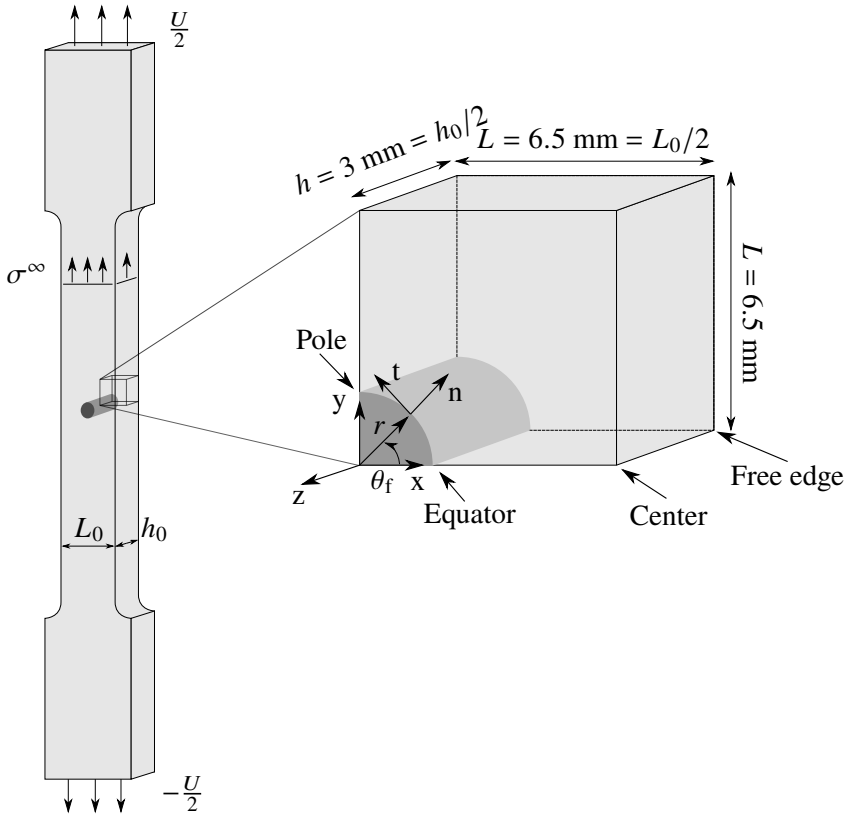

Figure IV.25 – Tensile specimen dimensions and associated numerical models where r denotes the fiber radius, σ^∞ the remote stress and θ_f the angular position from the fiber equator to pole along the interface.

Therefore, two mesh convergence campaigns are performed to account for both stress and energy aspects. Due to the elastic properties mismatch between the fiber and the matrix, there is a singularity at the free surface interface, so that the stress locally tends to infinity. To ensure that the mesh size is small enough to accurately describe the stress gradient, the interface stress isocontours location are compared for each mesh size. Convergence is achieved when the element size does not affect the stress isocontours thereby ensuring that the smallest debonding surface (see Section IV.4.1) is not influenced. A subsequent campaign is conducted to assess the suitable mesh size, ensuring that the difference in released elastic strain energy for fixed areas are smaller than 1.5% (see Appendix A.1 for an example of mesh convergence analysis). It results in $\simeq$ 15 µm mesh size along the fiber matrix interface.

Debonding shape determination

The CC implementation requires the definition of the debonding shape along which the crack is likely to initiate. Considering a 2D simulation results in symmetric initiation from the fiber pole which can be thus described by a single parameter, *i.e.*, the debonding angle θ_d, see Section IV.2 and Section IV.3. However, a 3D simulation involves a third dimension to describe the crack shape, *i.e.*, the crack front topology, which is initially unknown. Monitoring the debonding shape along the thickness is possible experimentally (see [Koy+09], [Mar+13]). It only yields observations of already propagated debondings after initiation. Approaches have emerged to overcome this challenge. Using stress isocontours to determine the crack shape yielded promising results, as shown for instance by [Leg14], [DL18a], [DL18b] and [Car+21]. Since it is much more efficient numerically than determining debonding shape based on the energy condition, stress isocontours based debonding shape determination is adopted in the sequel for the inverse identification procedure. Further analysis about the debonding shapes is proposed in Chapter VI.

Figure IV.26 shows the variation in normalized normal stress as a function of angular position ($r\theta_f$) and through-thickness z-direction. The normal stress component increases and tends towards infinity when approaching the free surface (-z = 3 mm).

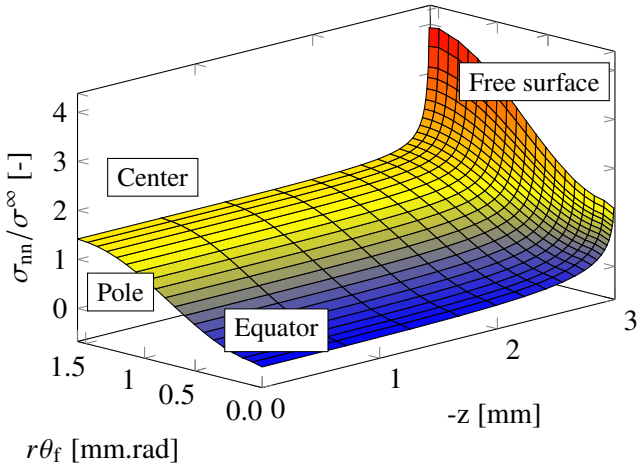

Figure IV.26 – Variation of the normalized normal stress (σ_{nn}) along the fiber-matrix interface emphasizing the stress singularity for -z = 3 mm, with r = 1 mm.

Likewise, maximum values are attained at the fiber pole ($r\theta_f = \pi/2$ mm.rad.). The normal stress component stabilizes at a constant value when moving away from the free surface for a given angular position. Figure IV.27 shows the normal stress

isocontours and highlights the singularity in the vicinity of the free surface. It should be mentioned that whether remote stress or displacement is imposed as a boundary condition, it has no significant influence on the variation of interface stresses, with differences smaller than 3% on the equivalent stress σ_{eq}, see Equation (IV.15). Thus, in the sequel, only displacement boundary conditions will be considered. Stress isocontours delineate different potential debonding shapes where the normal stress is strictly larger than a specified stress level.

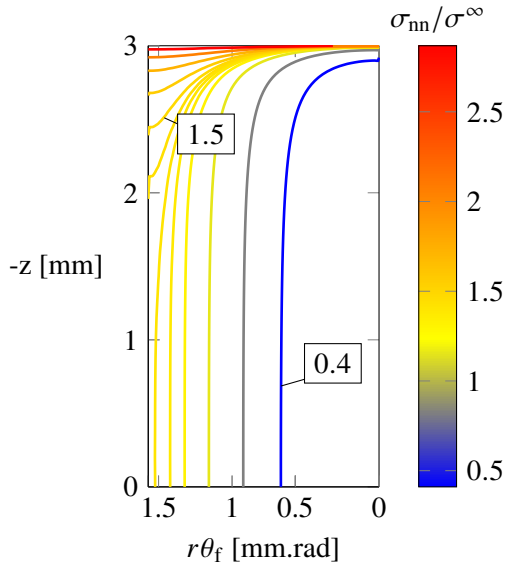

Figure IV.27 – Normalized normal stress isocontours along the fiber-matrix interface.

Figure IV.28a shows a 3D representation of a debonding surface delimitation, for a normal stress level of $\sigma_{nn}/\sigma^{\infty} = 1.5$, on the fiber interface represented by the grey surface. Stress isocontour, *e.g.*, the solid yellow line, encompasses a S surface, *e.g.*, the shaded yellow area, which corresponds to the debonded zone. Figure IV.28b shows the isocontour for a normal stress level of $\sigma_{nn}/\sigma^{\infty} = 0.4$ and a larger debonding surface is obtained. The lower the stress level associated with an isocontour, the larger the debonding surface. Overall, the debonding evolves from a localized debonding in the free surface vicinity to the creation of a tunnel reaching the other free surface debonding. This debonding process closely resembles what was experimentally observed by [Mar+13], for a single fiber sample loaded in uniaxial tension.

The benefit of basing debonding shapes on normal stress isocontours is that no interface properties are *a priori* needed. Consequently, the determination of isocontours becomes significantly more efficient, as the crack shape remains independent

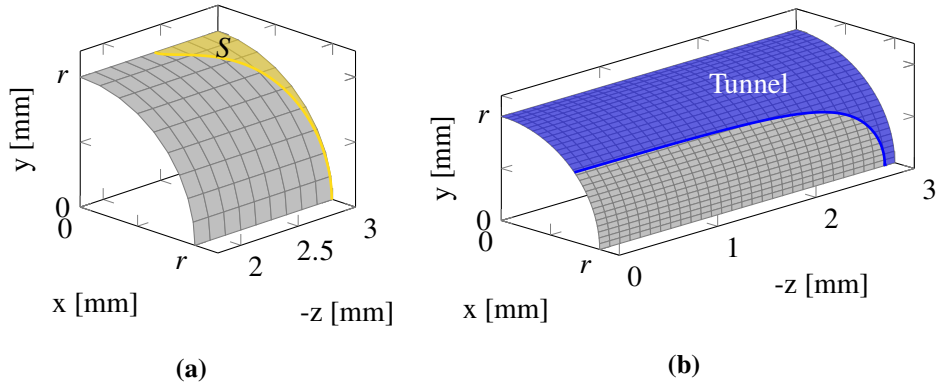

Figure IV.28 – Debonding surface delimitation for given stress isocontours (a) $\sigma_{nn}/\sigma^{\infty} = 1.5$ so that the debonding remains close to the free surface and (b) $\sigma_{nn}/\sigma^{\infty} = 0.4$ resulting in the two debondings merging by tunneling between each others.

of fracture properties. However, the fiber interface may experience both opening and shear modes from the pole to the equator of the fiber. An equivalent stress, presented in Equation (IV.15), is employed to account for the complex stress field and both phenomena:

$$\sigma_{eq} = \sqrt{\sigma_{nn}^2 + \frac{1}{\mu^2}(\sigma_{nt}^2 + \sigma_{nz}^2)}, \tag{IV.15}$$

yet again $\mu = \tau_c/\sigma_c$ describes the ratio between the shear strength τ_c and the tensile strength σ_c. The quantity σ_{nn} represents the normal tensile stress at the fiber-matrix interface, while σ_{nt} and σ_{nz} correspond to the in-plane and out-of-plane shear stresses respectively.

Similarly to the representation shown in Figure IV.26 focusing on the normal stress only, the variation in equivalent stress along the interface can be computed. Since both normal and equivalent stresses decrease monotonically from the free surfaces, an efficient approach to consider the equivalent stress using normal stress-based isocontours is to provide the equivalent stress values along each isocontour. This assumption results in a non-constant equivalent stress, and the minimum stress value is retained, accordingly with the stress condition proposed by [Leg02], recalled in the sequel.

Figure IV.29 shows the normalized equivalent stress as a function of the debonding surface for different values of μ. The larger the value of μ, the closer the variation in equivalent stress is to the variation in normal stress. Consequently, when μ is large,

the equivalent stress isocontours revert to the normal stress isocontours. Isocontours based solely on normal stress therefore induce a smaller error. Reducing μ to 1 (*e.g.*, $\sigma_c = \tau_c$) results in a slight deviation of the equivalent stress from the trends observed with larger μ values (*e.g.*, 3 and larger). Using the variation of equivalent stress based on normal stress isocontours seems to be a suitable approach for enhancing the efficiency of the numerical model. Moreover, the disparity between equivalent stress and normal stress remains minimal, highlighting the insignificance of shear in calculating the equivalent stress in comparison to the normal stress component. As a result, the use of the equivalent stress may become unnecessary, and the identification of shear strength based on equivalent stress could hold little significance. Nonetheless, in the subsequent sections, equivalent stress condition is used to maintain consistency with previously developed 2D models (see Section IV.2 and Section IV.3), where shear has a more pronounced influence.

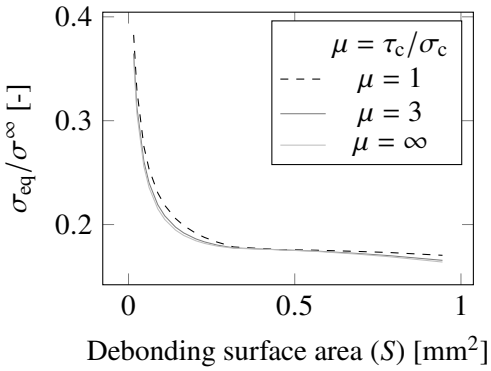

Figure IV.29 – Minimum value of σ_{eq} calculated along each isocontours obtained from the σ_{nn} variation along the fiber-matrix interface (equivalent to isocontours based on σ_{eq} with $\mu = \infty$).

CC implementation

Once the potential initiation debonding shapes are determined, the CC can be implemented in a similar way to that presented in the Section IV.2, but using a surface S instead of an angle θ_d. The methodology used to determine the interfacial stress tensor is similar to that presented in Section IV.2.2, extended to a 3D configuration. As a reminder, the stress components are determined using the RF of the reference point placed between the doubled interfacial nodes. In order to provide the initiation loading and the debonding size, the CC combines two conditions as summarized in

Equation (IV.16):

$$\begin{cases} \sigma_{\text{eq}}\left(\vec{x}, \sigma^{\infty}\right) \geq \sigma_{\text{c}}, \forall \vec{x} \in \Gamma, \\ G_{\text{inc}}(S, \sigma^{\infty}) \geq \overline{G_{\text{c}}}(S). \end{cases} \tag{IV.16}$$

The equivalent stress σ_{eq} has to exceed the tensile strength σ_{c} at any location on the debonding area Γ before initiation. Likewise, the minimum σ_{eq} has to exceed σ_{c} over the isocontour as the stress decreases monotonically. G_{inc} refers to the IERR which is the variation of the elastic strain energy W per unit crack surface S (Equation (IV.17)).

$$G_{\text{inc}}(S, \sigma^{\infty}) = \frac{W(0, \sigma^{\infty}) - W(S, \sigma^{\infty})}{S} \tag{IV.17}$$

G_{inc} must be larger than the global critical ERR $\overline{G_{\text{c}}}$, which is defined in Equation (IV.18), to fulfill the energy criterion.

$$\overline{G_{\text{c}}} = \frac{1}{S} \int_0^S G_{\text{c}}(\psi(s)) \mathrm{d}s. \tag{IV.18}$$

IERR calculation

The IERR is obtained by computing the change in elastic strain energy between two states: without and with crack. Both states are assessed by debonding some interfacial nodes, as presented in Section IV.2.2, located in the debonding zone. From a numerical point of view, cracks can be defined either based on the initial interface mesh, or after remeshing so that the new mesh topology coincides with the stress isocontours trajectory. The first method is easier to implement because it does not require remeshing, but also yields an approximate, non-smooth crack shape depending on the mesh size. In this context, the IERR obtained using both methods have to be compared.

In Figure IV.30a, a comparison of the IERR obtained using two different methods is presented. For the first method, denoted **1**, a converged mesh size is adopted.

With the first method based on the original interface mesh, a constant mesh size along the interface is used as well as near the free surfaces and then gradually increased once the tunnel has started (see Figure IV.27). The second method, involving remeshing and identified as **2**, also undergoes a mesh convergence study. This validation is essential to ensure the validity of the comparison, given that this method yields a more accurate representation of the isocontours topology. Both methods yield overall comparable results in terms of IERR. For small debonding surfaces, method **1** yields a slightly smaller IERR compared to method **2**. This difference may emanate from the presence of a relatively small debonding surface near the free surfaces, making the surface difficult to be captured using a constant mesh size that may be too

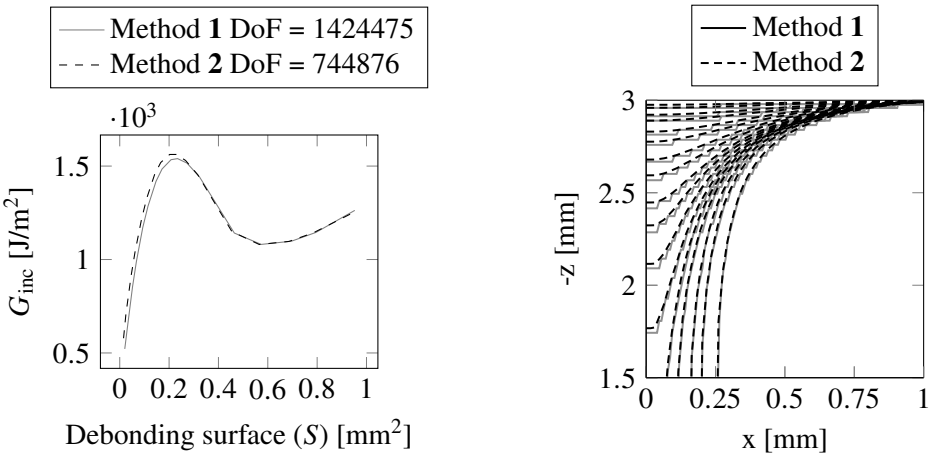

Figure IV.30 – (a) IERR variation as a function of the debonding surface and meshing strategy (DoF translates the number of Degrees of Freedom of the model). (b) Debonding surface with relatively large mesh size to highlight the potential difference observed between the two strategies.

large. The remeshing method thus has an advantage because the mesh size is varied accordingly to the surface geometry. Contours of the debonding surfaces obtained using the two methods are depicted in Figure IV.30b. Using a large mesh size effectively highlights the contrast between the surface contours derived from remeshing and the shape defined by the original mesh. Hence, the area encompassed by method **1** might be larger for the same isocontour level, potentially explaining the observed shift in the IERR. For larger debonding surfaces, method **1** aligns with method **2** IERR. Furthermore, the overall gain of the method **2** over the method **1** in terms of IERR is negligible, about 3% difference for converged solutions. This highlights the larger computational cost of the method **1** to be converged, twice the DoF number in the method **2**, as it requires a finer mesh over the entire isocontour that contributes to an expanded numerical model.

The first method is easier to implement but requires a finer mesh to accurately capture the isocontours shapes. While the second method is more challenging to model but may involve larger mesh size to precisely describe the isocontour. As a result, the first method may involve a longer calculation time, whereas the second approach might require larger implementation time but is more computationally efficient. All in all, both methods remain relevant due to their negligible disparity; however, the second method could allow small debonding surfaces to be captured more accurately

and reduce the number of DoF.

Critical ERR calculation

The global critical ERR $\overline{G_c}$ (Equation (IV.18)) is determined by calculating the average of the local critical ERR G_c over the entire debonding front. The local critical ERR is calculated according to the formulation introduced by [HS91] (Equation (IV.19)).

$$G_c(\psi(S)) = G_{IC}\left[1 + \tan^2\left[(1-\lambda)\,\psi(S)\right]\right] \tag{IV.19}$$

The parameter λ is a function of the G_{IC} to G_{IIC} ratio, and more information about its influence can be found in Section IV.2 and in [Doi+23]. The critical ERR is denoted G_{IC} in opening mode (mode I) and G_{IIC} in shear mode (mode II) . The global and local critical ERR depend on the mode mixity ψ that is the ratio between shear and tensile stresses acting at the debonding front. This quantity is averaged at the interface, at a distance of 7.5 µm, corresponding to half the element size, beyond the crack front according to the method used in 2D by [Man09] and also employed in Section IV.2.

Besides, a condition may be applied to the calculation of the mode mixity ψ, as employed in Section IV.2, when the interface experiences compression in order to only account for the shear-induced propagation at this location (Equation (IV.20)):

$$\psi(S) = \begin{cases} \arctan\left(\frac{|\tau(S)|}{\sigma_{nn}(S)}\right), & \text{if } \sigma_{nn}(S) \geq 0 \\ \frac{\pi}{2}. & \text{if } \sigma_{nn}(S) < 0 \end{cases} \tag{IV.20}$$

In the above condition, the shear component $\tau(S)$ can be affiliated to i) in-plane shear σ_{nt} with respect to the free surface, ii) out-of-plane shear σ_{nz}, iii) the maximum of the two shear stresses or iv) an average shear stress. Figure IV.31 shows the variation in both mode mixity ψ (Figure IV.31a) and critical ERR $\overline{G_c}$ (Figure IV.31b) for the above calculation possibilities as a function of debonding surface.

Taking $\tau(S) = \max(\sigma_{nt}, \sigma_{nz})$ will increase the influence of shear on the calculation of the critical IERR since larger ψ are considered. This results in an increase in the critical ERR, see Figure IV.31b, as the mode II critical ERR is often larger than the mode I one. Taking the out-of-plane shear into account increases the mode mixity for small debonding surface because the debonding is close to the free edges. In this region, the elastic mismatch between the fiber and the matrix induces a large out-of-plane shear stress compared to the normal stress. In addition, the in-plane shear acts mainly on the equators of the fiber interface, at a specific distance from the free edge. Therefore, taking into account the in-plane shear stress in the mode mixity calculation increases the critical ERR for a larger debonding surface. Finally, an average of the

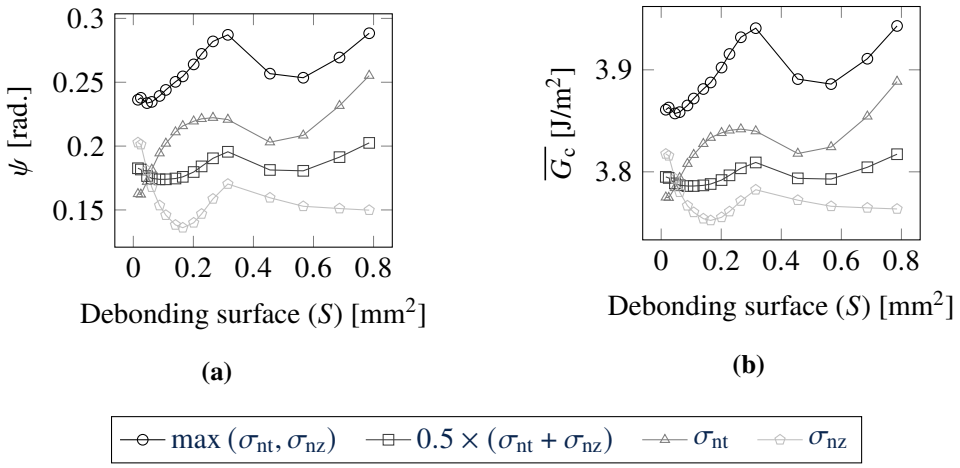

Figure IV.31 – (a) Mode mixity and (b) global critical ERR as a function of the debonding surface for the different calculations with the interface properties identified previously in Section IV.2: $G_{IC} = 3.7$ J/m^2, $\lambda = 0.13$.

shear stresses $\tau(S) = 0.5\times(\sigma_{nt}+\sigma_{nz})$ will reduce the influence of shear by considering an intermediate value. It should be mentioned that opting for the maximum of the two shear stresses results in a more important assessment of the mode mixity, involving larger critical ERR. This is due to the initial evaluation of the mode mixity at multiple positions along the debonding front for each surface. Subsequently, these values are averaged by alternating the maximum shear stresses along the debonding front whether it is σ_{nt} or σ_{nz}. This approach yields higher values compared to considering in-plane or out-of-plane shear stresses independently. Consequently, the initiation process on a surface dominated by shear will either be dampened or intensified, depending on the selected mode mixity calculation. Interestingly, the variation in $\overline{G_c}$ shown in Figure IV.31b remains small since the mode mixity is close to 0 meaning that the interface experiences mostly mode I. Consequently, the selected mode mixity calculation has a negligible influence on the critical ERR determination in the present example. Furthermore, it is noteworthy that while the consideration of one critical shear ERR is included, there are potentially two critical ERR that can be accounted for (G_{IIC}^{nt} and G_{IIC}^{nz}). However, for the sake of simplicity, the subsequent analysis will focus on a single critical shear ERR, employing the maximum shear stresses for the mode mixity calculation.

ERR calculation

The CC provides the debonding initiation loading and surface. Two configurations can be encountered at initiation depending on the IERR and the critical ERR. On the one hand, $\mathrm{d}(G_{\mathrm{inc}}/\overline{G_{\mathrm{c}}})/\mathrm{d}S = 0$ leading to a stable debonding after initiation such that the initiation debonding surface corresponds to the arrest surface. On the other hand, $\mathrm{d}(G_{\mathrm{inc}}/\overline{G_{\mathrm{c}}})/\mathrm{d}S > 0$ leading to $G/G_{\mathrm{c}} > 1$ and further propagation of the debonding without any increase in the remote loading until $G/G_{\mathrm{c}} = 1$ occurs. Thus, in the second configuration, the ERR is evaluated using Equation (IV.21) as the opposite of the elastic strain energy W derivative with respect to the debonding surface S.

$$G = -\frac{\mathrm{d}W}{\mathrm{d}S} \tag{IV.21}$$

Consequently, debonding shape associated with unstable debonding propagation must be determined. Exploring all the shape possibilities starting from the debonding initiation one would be computationally time-consuming. As a result, for the sake of efficiency, in particular to perform an inverse identification, the debonding shapes based on stress isocontours are used.

IV.4.2 Comparison between 2D and 3D models

In addition to the 2D inverse identification undertaken in Section IV.2, the 2D front model is again studied here on the basis of different quantities. A new 2D side model is also studied, the study was carried out after the one presented in Section IV.2, so the results are kept in the next section.

Models and debonding opening

The use of a 2D numerical model instead of a 3D model enables a reduction in computational costs. For example, the models used in Section IV.2 have 110946 DoF, whereas the 3D model considered in this section has 744876 DoF, a relative difference of 40%. Considering the problem of a single fiber subjected to remote tension can be modeled in 2D using either plane strain (PE) or plane stress (PS) assumptions. The subsequent results are presented for homogeneous fixed material and interface properties. Two distinct 2D models are suitable for assessing debonding initiation and propagation. Figure IV.32a shows the front model which corresponds to a stiff circular cylindrical inclusion within a softer squared medium. This model, employed in Section IV.2 and Section IV.3, allows monitoring the debonding angle (θ_{d}) relative to the imposed displacement (U) or corresponding remote stress (σ^{∞}). While it accurately describes the fields around the specimen center, it does not account for the singularity at the free surfaces caused by elastic property mismatch. Figure IV.32b

shows the current 3D modeling of the problem which considers simultaneously the debonding angle (θ_d), the debonding length (ℓ_d) and the debonding surface (S) as a function of the remote stress or the imposed displacement. Finally, Figure IV.32c shows the side model which provides information on the debonding length and offers a more accurate description of the free surface singularity at the fiber pole compared to the front model.

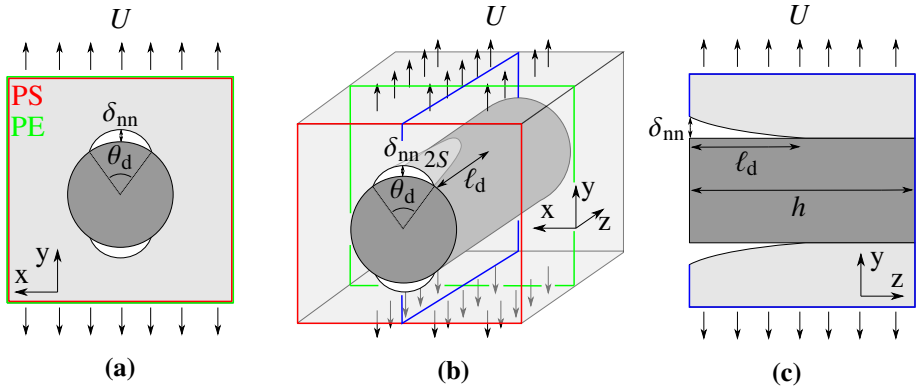

Figure IV.32 – Schematic of (a) the 2D front model, (b) the 3D model and (c) the 2D side model. The 2D representations are depicted in color on the 3D schema. The quantity δ_{nn} denotes the debonding normal opening extracted at the free surface, shared by all the models. Note that PS and PE stand for plane stress and strain, respectively.

It is worth noting that the only debonding metric shared by the three models is the maximum normal opening at the free surface, δ_{nn} (Figure IV.32).

Figure IV.33a shows the variation in normal opening as a function of debonding angle for the PS and PE front models and the 3D model. The two front 2D models exhibit similar relationship between the two quantities, presenting relatively large debonding openings for any fixed angle compared to 3D modeling. In contrast, the 3D model provides a small opening even for a complete debonding. The 3D model therefore rapidly provides large debonding angle at the free surface for fixed debonding opening, whereas the 2D models provide a more progressive increase. The previous observations could be attributed to the debonding shape that exhibits a large debonding angle associated to small debonding length. A more concave than convex trend could result in a better correspondence between the 2D and 3D models.

Figure IV.33b shows the variation in opening as a function of debonding length for the side and 3D models. For a small debonding length, the side and 3D models show good correspondence. Beyond a certain point ($\ell_d/h \simeq 0.05$), corresponding to the initiation of the tunnel effect, the 3D opening stops increasing, while the 2D

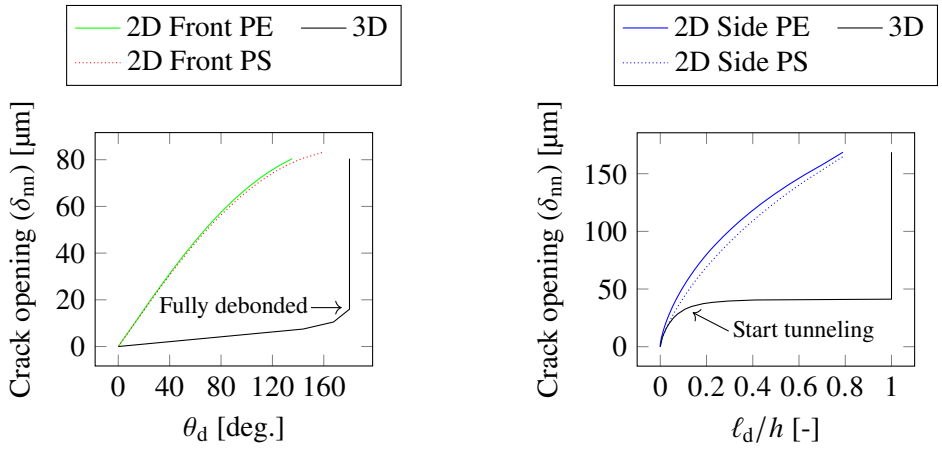

Figure IV.33 – (a) Comparison of the debonding opening (δ_{nn}) as a function of the debonding angle (θ_d) for the 3D and 2D front models. (b) Comparison of the crack opening as a function of the normalized debonding length (ℓ_d/h) for the 3D and 2D side models.

front models continue to increase. This tunnel effect leads to complete debonding across the sample thickness, resulting in a constant debonding length increase for larger debonding openings. Once the tunneling starts, the debonding propagation influence on the opening becomes negligible. This effect is not considered by the side model, which predicts a progressive increase in opening as a function of debonding length.

As mentioned already, the debonding opening is the only parameter shared by the three models. It will thus be used to compare the stress and energy fields between the 2D front, 2D side and 3D models, as well as a full CC comparison, which are detailed hereafter.

Stress comparison

Figure IV.34 shows the variation of equivalent stress (σ_{eq}) as a function of debonding opening (δ_{nn}) for the front, side and 3D models.

Consequently, the remote stress varies according to models for a similar imposed displacement, as indicated in Table IV.5.

These values are calculated as the total reaction forces divided by the cross-section or length per unit thickness. In the following, all the calculations are performed with a prescribed displacement, which magnitude is adapted to obtain a given remote stress.

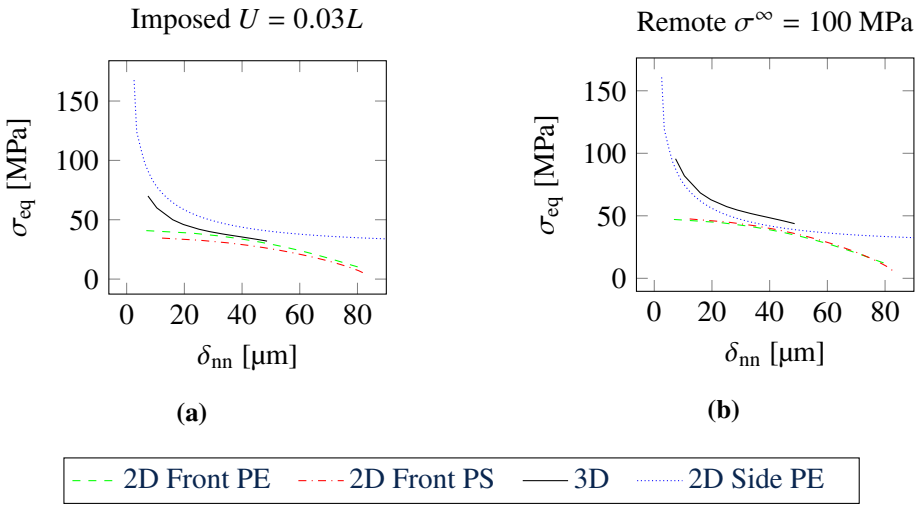

Figure IV.34 – Equivalent stress (σ_{eq}) variation as a function of the debonding opening (δ_{nn}) for a similar (a) imposed displacement and (b) remote stress.

Model	3D	2D front PE	2D front PS	2D side PE
Remote stress (σ^∞) [MPa]	73.2	86.7	72.7	104.3

Table IV.5 – Remote stress extrapolated for each model under an imposed displacement of $U = 0.03L$ mm.

As a result, differences in both stress and energy fields are obtained, whether a configuration with given displacement magnitude (Figure IV.34a) or remote stress level (Figure IV.34b) is considered. Another possibility would be to impose a specific remote stress as a boundary condition (not considered here). For the sake of simplicity, only the results for the side PE model are provided since the trends are similar for the side PS model.

Contrary to the convex trends of the front models, the side model varies in a concave manner. The side model effectively captures the stress singularity originating from the free surfaces, exhibiting a pronounced downward trend. Furthermore, the side model concave trend is similar to the 3D model one. Both front models also show a decreasing convex trend as a function of the debonding opening, but converge to a finite stress value for vanishing debonding opening. Consequently, the front models are not preferable for accurately replicating the actual stress trends observed in 3D. Nonetheless, for a similar imposed displacement, the front PE model exhibits good correspondence in terms of stress levels with the 3D model for $\delta_{nn} > 20$ µm, with a relative difference smaller than 15%. For a similar remote stress, the side model

better matches the 3D stress levels, exhibiting a similar downward trend.

Energy comparison

Figure IV.35 shows the variation of IERR as well as the IERR to critical ERR ratio as a function of debonding opening for the four models, all characterized by identical G_{IC} and λ.

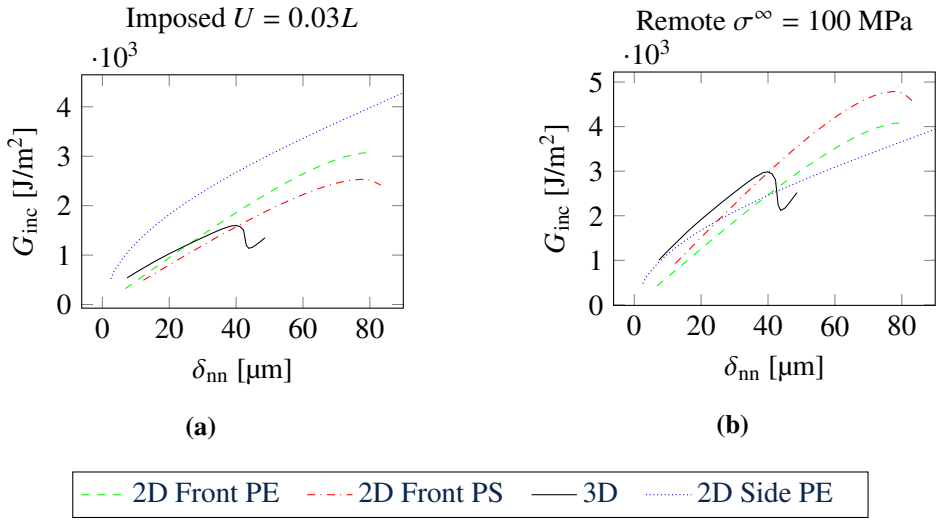

Figure IV.35 – IERR as a function of the debonding opening for a similar (a) imposed displacement and (b) remote stress.

For a similar imposed displacement (Figure IV.35a), the energy released per surface increment by the 3D and front models are close, implying that 2D front models are valid options for describing the IERR in this loading configuration. The IERR obtained by the side model is larger than that of the 3D model. For a similar remote stress (Figure IV.35b), the side model more accurately coincides with the behaviors of both 3D and 2D front models. However, the difference with the front PE model becomes more pronounced, while the front PS model maintains good correspondence with the 3D model. In both loading cases, the IERR shows a monotonic increase with the debonding opening for the 2D models, while the 3D model exhibits a maximum. Actually, the front PS model also shows a maximum for a larger opening. However, neither the front nor the side 2D models are able to accurately describe the maximum position of the 3D curve in terms of debonding opening. This maximum is particularly noteworthy given the assumption of a constant G_c. Such a maximum could therefore result in a stable growth of the debonding after initiation (see Section IV.2).

However, as mixed modes are taken into account in the calculation of G_c, it may induce a maximum in the $G_{inc}/\overline{G_c}$ profile based on the stress state (*i.e.*, ψ) acting at the interface.

In this regard, Figure IV.36a and Figure IV.36b illustrate the influence of mode mixity on the IERR to critical ERR ratio.

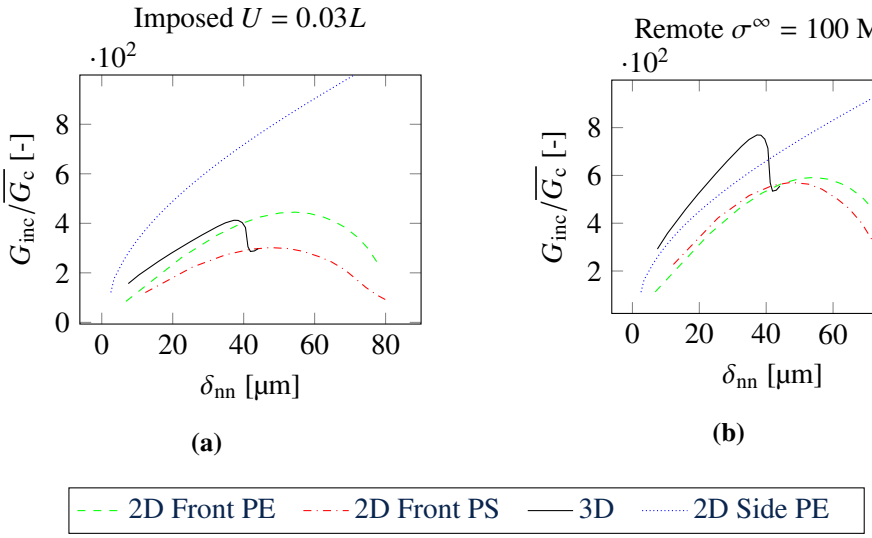

Figure IV.36 – IERR to critical ERR as a function of the debonding opening for a similar (a) imposed displacement and (b) remote stress.

For both 3D and side models, a trend similar to the one depicted for G_{inc} is obtained, suggesting that mode mixity remains relatively constant with changes in debonding size. Such finding is further explored in Figure IV.37 where the mode mixity at the crack front is displayed as a function of the debonding opening.

Both the 3D and side models maintain a nearly constant mode mixity close to 0 indicating that the interface predominantly experienced mode I loading (as described in Equation (IV.20)). Consequently, G_c maintains an almost constant value throughout the debonding propagation, ensuring that the trends in IERR remain unaffected. In contrast, the front models show an increase in mode mixity as a function of the debonding opening. The migration of the crack tip from the fiber pole to the fiber equator leads to a shift from tensile-induced propagation to shear-induced propagation of the debonding. Consequently, the value of G_c rises as mode mixity increases. This increase in G_c consequently influences the trends observed in $G_{inc}/\overline{G_c}$ (Figure IV.36a-IV.36b), which now emphasize a different maximum position compared to the IERR alone. This suggests that the front model might undergo stable debonding growth following initiation, but for a larger opening. However, even when considering

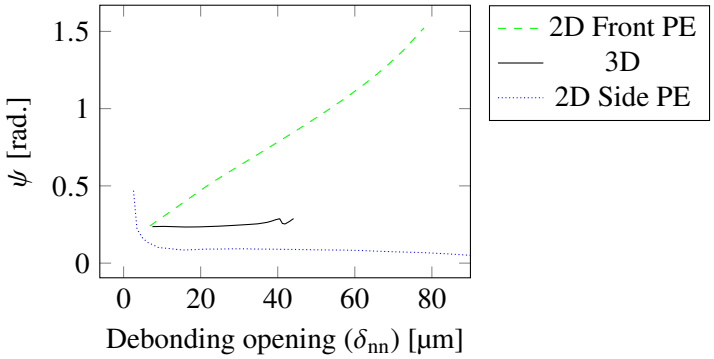

Figure IV.37 – Mode mixity evaluated at the crack front for front PE, side PE and 3D models.

variations in λ, the front models fail to accurately predict the 3D model maximum prediction. Notably, varying λ in the 3D model does not influence the opening position determined by the maximum in $G_{\text{inc}}/\overline{G_{\text{c}}}$, as discussed in the sequel.

Only the side model does not exhibit a maximum in $G_{\text{inc}}/\overline{G_{\text{c}}}$. Once the debonding has initiated, crack propagation can be assessed by calculating the ERR (G) which can be derived from the IERR using Equation (IV.22).

$$G\left(S\right) = G_{\text{inc}}\left(S\right) + S \times \frac{\mathrm{dG_{inc}}}{\mathrm{d}S} \tag{IV.22}$$

Consequently, in the side PE model where debonding is predominantly driven by mode I, resulting in a constant G_{c}, the IERR shows a monotonic increase. According to Equation (IV.22) the ERR also follows a monotonically increasing trend, along with the ERR to critical ERR ratio. It means that unstable propagation takes place after crack initiation, and no arrest length can be deduced from the side model. This model is unsuitable for performing inverse identification based on arrest length and is therefore disregarded in the following.

Comparison of the CC solution

Figure IV.38 shows the CC solution obtained from the two front models and the 3D model for similar fixed interface fracture properties.

Both strategies devoted to the required displacements or the remote stresses to fulfill the CC solution are investigated. As a result, the 2D model that best matches the 3D model and the corresponding imposed conditions can be defined. As expected, increasing the strength or the critical ERR leads to an increase in the required dis-

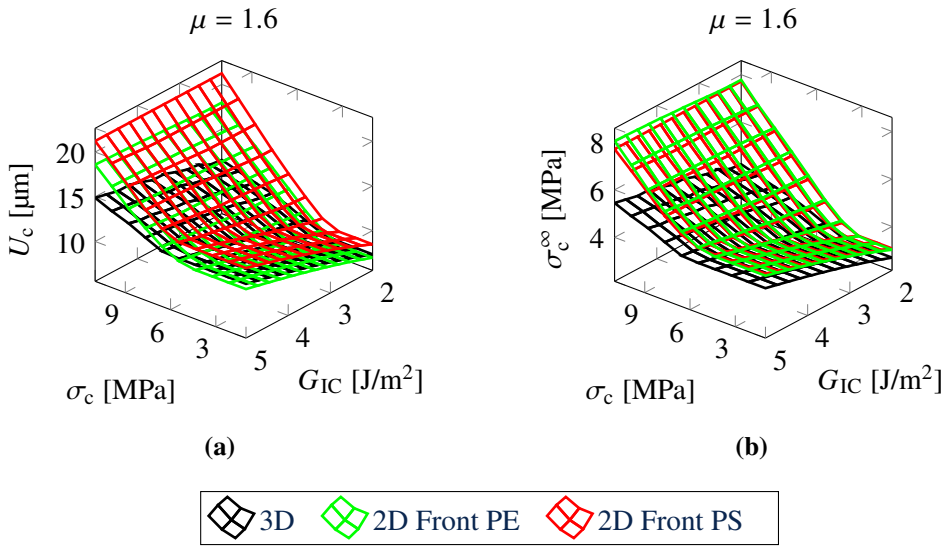

Figure IV.38 – Required (a) displacement and (b) remote stress to fulfill the CC as a function of a range of strengths and critical ERR.

placement and remote stress required to fulfill the CC. For sufficiently low strengths, an insensitivity with respect to σ_c is obtained, describing an energy-driven configuration where only the critical ERR drives the CC solution. On the one hand, the remote stress required to fulfill the CC is similar for the two 2D front models, where the solutions closely align (Figure IV.38b). However, the 2D front models slightly overestimate the solution of the 3D model. On the other hand, the displacement necessary to fulfill the CC for the two 2D models exhibits a more significant difference, with the disparity being more pronounced in the plane stress assumption (Figure IV.38a). Notably, the difference with the 3D model is more prominent in this scenario. The plane strain model provides a more accurate representation of the 3D model solution, especially in cases involving small strengths and configurations with large critical ERR. This observation is supported by the similarity in the maximum values of G_{inc}/G_c for the same imposed displacement, as depicted in Figure IV.36a. These results highlight the significance of the 2D front PE model in accurately describing the 3D model solution, particularly when considering cases with imposed displacement. However, for the sake of consistency with the 2D identification performed in Section IV.2 and Section IV.3, remote stress solutions are compared in the sequel, where experimental measurements are used to identify interface fracture properties.

IV.4.3 Inverse identification

In contrast to the approaches employed in Section IV.2 and Section IV.3, which consist of an inverse identification based on the debonding angle, the following inverse identification is performed on the basis of the debonding opening. This approach would enable more accurate identification, since the debonding angle remains a challenge to determine accurately, as it is limited by the size of the pixel. The sample referenced SFI-2 is used to identify the fracture properties, in particular the opening observed at site ① , since uncertainties in the detection of debonding initiation are observed in sample SFI-1 (see Section III.3).

Identification based on remote stress at initiation

Since linear elastic properties are considered for the fiber and the matrix, FE calculation with several debonding configurations at a single imposed displacement are required to solve the CC for any interface fracture properties. The inverse identification process is similar to the approach used in Section IV.2.

The first step in the inverse identification is to identify a range of properties (*i.e.*, σ_c, τ_c, G_{IC} and G_{IIC}) leading to the debonding initiation remote stress between 4.2 and 5.4 MPa. The initiation stress level observed slightly differs from the one obtained in Section IV.2 since it is a different sample. Although debonding could have occurred between 4.2 and 5.4 MPa, the smaller value is chosen as the target to be consistent with that observed using the debonding angle and sample SFI-1 in Section IV.2 and Section IV.3, *i.e.*, 4.1 MPa.

Figure IV.39a shows range of G_{IC} identified for a range of strengths leading to the debonding initiation at a remote stress of 4.2 MPa. For sufficiently small strengths (< 6 MPa), a plateau is reached where constant G_{IC} value is identified. In such a configuration, the energy condition drives the initiation where the solution is described by the maximum in the IERR to critical ERR ratio. As a result, tensile and shear strengths no longer influence the CC solution, since the stress condition is already fulfilled; constant critical ERR are therefore sufficient to match the experimental remote stress. Conversely, for larger strengths, both stress and energy conditions drive debonding initiation. As tensile and shear strengths increase, decreasing critical ERR are required to counterbalance the increasing stress condition. Figure IV.39b shows the G_{IC} plateau values identified as a function of λ where the latter depends on the G_{IIC} to G_{IC} ratio. It shows that λ has a negligible influence on the range of identified G_{IC} values, given that the interface mainly experiences mode I loading, whereas λ mostly denotes the influence of mode II. In fact, each range of identified G_{IC} values, based on a fixed λ, enables the identification of the corresponding G_{IIC}.

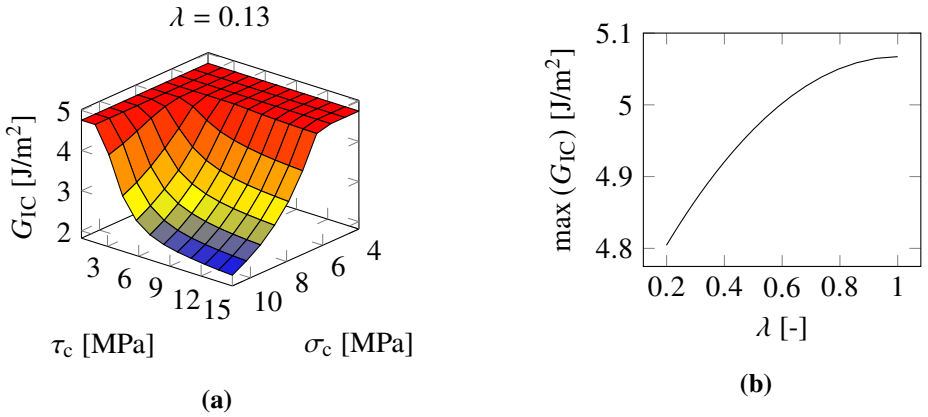

Figure IV.39 – (a) Range of critical opening ERR as a function of both tensile and shear strengths leading to a debonding initiation at a remote stress of 4.2 MPa and (b) maximum critical ERR in mode I identified as a function of λ, corresponding to the plateau value.

Properties restriction based on debonding opening at initiation

Once a range of properties is deduced from debonding initiation, a second step involving additional constraints can be undertaken. The arrest opening given by the CC solution is compared with the experimental debonding opening obtained after initiation, recalled in Table IV.6, enabling the determination of upper and lower opening limits.

Site	δ_{nn} [µm] lower bound	δ_{nn} [µm] upper bound
SFI-2 ① (Section III.3)	2.1 ± 1.0	3.8 ± 0.8

Table IV.6 – Debonding opening at initiation for sample SFI-2.

Figure IV.40 shows the debonding opening $\delta_{nn}^{plateau}$ corresponding to either the crack length or surface maximizing $G_{inc}/\overline{G_c}$ as a function of λ.

Since the $\overline{G_c}$ calculation relies on the mode mixity, the maximum location remains constant for the 3D results due to the dominance of mode I configuration at the interface. As a result, the shear mode has a negligible influence on the calculation of $\overline{G_c}$, and consequently, the maximum location will correspond to that of G_{inc}. On the contrary, the 2D front model undergoes a transition from mode I to mode II as the opening increases, that corresponds to an increase in debonding angle. The smaller the value of λ, the larger the value of G_{IIC}, leading to a smaller arrest opening and requiring larger loading to propagate the debonding.

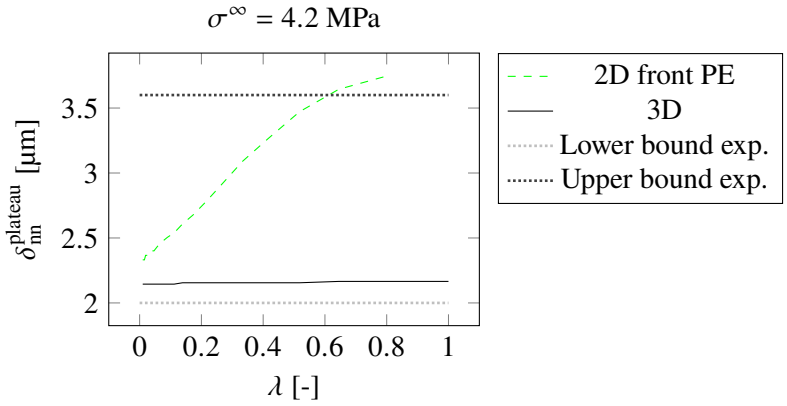

Figure IV.40 – Debonding opening corresponding to the $G_{inc}/\overline{G_c}$ maximum for both front and 3D models as a function of λ and compared with the experimental upper and lower bounds (dark gray and light gray solid thick lines respectively).

With a fixed remote stress of 4.2 MPa, which corresponds to the experimental remote stress observed at initiation, the corresponding debonding opening can be deduced for both models. When debonding initiation is solely driven by the energy condition, stable debonding occurs, resulting in the smallest possible arrest opening, which corresponds to the location of the maximum $G_{inc}/\overline{G_c}$. However, when both stress and energy conditions drive the initiation, larger arrest openings are observed. As a result, the openings shown in Figure IV.40 correspond to the minimum arrest openings that can be obtained with both models. The 3D model shows a good correspondence with experimental opening whereas the front model overestimates the results for λ larger than 0.6 since the 2D model overestimates δ_{nn} for a given angle θ_d (see Figure IV.33b). Therefore, the front model is able to perform inverse identification based on δ_{nn} only for small λ; such a configuration would imply large G_{IIC} to restrain debonding opening at initiation since the arrest opening is primarily driven by shear in 2D. As a consequence, $\lambda = 0.13$ could still be identified in Section IV.2 based on the debonding angle which also results in debonding opening consistent with experiments. The 3D model does not allow for the identification of λ, as the latter does not influence the arrest opening. A meaningful identification of G_{IIC} is no longer feasible using the 3D model and based on δ_{nn} solely. Possible identification of G_{IIC} could be achieved based on debonding propagation located at the specimen center, where the 2D PE model is applicable. However, this would imply observing the debonding propagation on the fiber equator, not performed on SFI-2 sample. Nonetheless, additional constraints could be applied to G_{IC} based on arrest openings

obtained from further unstable growth.

Figure IV.41 shows the arrest debonding opening (δ_{nn}^{arrest}) as a function of a range of strengths identified during the first identification step.

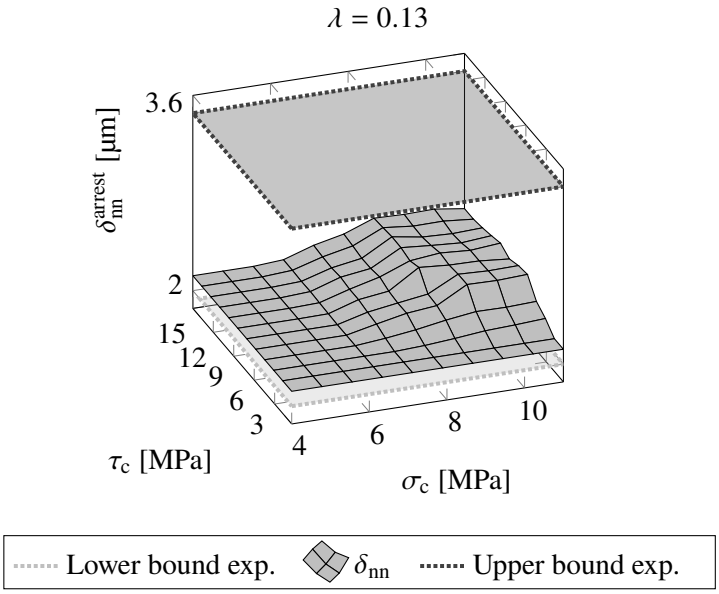

Figure IV.41 – Arrest debonding opening (δ_{nn}^{arrest}) as a function of range of strengths with lower and upper bound obtained from the experimental observation.

Similarly to the first step, when dealing with small strengths, an energy-driven configuration prevails for stable debonding, *i.e.*, $G = G_c$ at initiation. Hence, there is no additional unstable propagation of debonding, with the initiation opening depending only on constant ERR over such a range of strengths. Consequently, constant arrest openings, equivalent to initiation openings, are obtained, leading to the formation of a plateau. With larger strengths, there is a possibility of unstable propagation of the debonding, resulting in additional opening growth until $G < G_c$. These configurations therefore induce a larger arrest opening. By comparing the numerical arrest opening with the experimental bounds, the range of identified strengths can be validated since the arrest openings remain within the two experimental bounds. No additional restrictions can be applied to the range of strengths. Similarly, since the complete range of strengths matches the experimental observations, the identified range of critical ERR can also be approved.

IV.4.4 Comparison with 2D identified properties

Table IV.7 compares the properties identified with the 3D model with the ones obtained with the 2D CC PE model in Section IV.2 and the 2D CZM PE model in Section IV.3 to quantify the relevance of a 2D model in accurately identifying the interface properties.

Fracture properties	CZM 2D PE	CC 2D PE	CC 2D PE	CC 3D
Sample	SFI-1	SFI-1	SFI-2	SFI-2
σ_c [MPa]	3 - 3.5	1 - 5	5 - 10	4 - 11
τ_c [MPa]	3.5 - 4.5	1 - 10	5 - 15	/
G_{IC} [J/m^2]	2.5 - 4.2	3.7	12.2	2.2 - 4.7
G_{IIC} [J/m^2]	8 - 11	90	296	/

Table IV.7 – Comparison of the interface fracture properties identified using the CC in 2D and 3D and the CZM.

The properties identified with the SFI-2 2D model are based on different remote loadings at initiation observed between the debonding angle (σ^∞ = 4.2 MPa) and the opening (σ^∞ = 7.3 MPa), see Table III.8. It is likely that the properties identified can no longer be compared. Properties identified in 2D for the SFI-1 sample and in 3D with the SFI-2 sample, for a similar remote loading at initiation, can nevertheless be compared. Even though, the stress components experienced by the interface in both models are different, the 2D SFI-1 model is consistent with the 3D SFI-2 obtained properties regarding the critical ERR in mode I. The 2D SFI-1 model slightly underestimates the tensile strengths as it does not account for the singularity at the free surface. However, due to the fact that the 3D model involves less shear at the interface compared to the 2D model, differences in shear properties are likely and raise questions about the relevance of such identification. On the one hand, the choice of an equivalent stress in 3D might be justifiable since it closely aligns with a normal stress criterion. The shear strengths deduced from this stress condition might be erroneous because regardless of the chosen properties, their influence on the stress condition is negligible, so that comparison between the two models is thus no longer feasible. On the other hand, the identification of λ is challenging since it does not drive the arrest opening. Consequently, it is not possible to identify any critical ERR in mode II due to the unknown value of λ. It would require analyzing further debonding propagation with larger debonding angle in the specimen middle plane where shear has larger influence. It is worth mentioning that debonding shapes are based on stress isocontours while the energy-based shapes could also be suitable. Such energy-based debonding shapes may yield debonding topology experiencing more shear and allow for a better capture of both τ_c and G_{IIC}. Furthermore, these new debonding shapes may better de-

scribe debonding angles observed experimentally with a variation of δ_{nn}. However, the determination of energy-based debonding shapes is challenging to implement and will be developed in Chapter VI.

IV.5 Conclusion

Inverse identification of the fiber-matrix interface fracture properties is carried out using several 2D and 3D numerical approaches based on the CC and CZM. Using a 2D model results in more efficient calculations. Both 2D and 3D model are nevertheless compared to assess the validity of the 2D model in accurately describing the debonding process at the free surface despite it does not account for the free surface singularity.

The experimentally observed abrupt debonding propagation over a finite angle can be captured by the CC. The initiation debonding angle either corresponds to an arrest debonding angle (if the initiation is driven by the energy condition) or is followed by unstable crack propagation up to the arrest debonding angle (if the initiation is driven by both stress and energy conditions) depending on the material tensile and shear strengths and opening and shear critical ERR. Restricting the simulated arrest debonding angles to the range measured experimentally enables determining a range of admissible interface critical ERR and tensile and shear strengths. An optimum set of parameters is finally determined by confronting the debonding angle variations as a function of the applied stress for the stable propagation phase. The fracture properties identified are of the same order of magnitude as those determined in other work for a similar configuration.

CZM can be used to accurately capture the debonding process, in particular the initiation, for a certain loading, followed by unstable propagation up to an arrest angle followed by a stable propagation. Opening properties primarily control the initiation remote loading while the shear properties influence the arrest debonding angle and the propagation phase. A two-stage methodology enables the identification of an optimum set of interface fracture properties in agreement with those obtained using the CC. Larger differences are nevertheless observed on the critical ERR in mode II, possibly due to the choice of a different criterion. The fracture properties identified provide a variation in the debonding angle close to that obtained experimentally. However, the inverse identification approach is not as efficient as the CC approach, as the CZM implies non-linearities.

Initiation of fiber-matrix debonding is assessed using 3D and 2D front and side models and the CC. However, the implementation of the CC in 3D raises a challenge since the latter resolution requires knowledge of the crack path. Deriving shapes based on normal stress isocontours is a relevant solution since it does not rely on any fracture

properties, yet constant throughout the entire interface. An equivalent stress can also be derived from these isocontours, and small discrepancies compared to normal stress are observed regardless of the shear to tensile strength ratio. As a result, shear contribution can be neglected, and a normal stress criterion might be sufficient to describe the stress condition. The mode mixity of the three models differs: side and 3D models primarily exhibit mode I with a constant mode mixity. In contrast, front models transition from mode I to mode II as the debonding angle expands towards the equator region, resulting in an increase in $\overline{G_c}$. When comparing the CC solution, 3D solution and the 2D front PE solution are in agreement for a similar imposed displacement. This configuration becomes particularly relevant for comparison purposes.

Finally, the properties identified using the front model and sample SFI-1 in Section IV.2 and Section IV.3 align with those in 3D and sample SFI-2 concerning tensile strength and mode I critical ERR. This makes the front PE model with the CC relevant for efficiency purposes in identifying the interface fracture properties even though the front model yields a slight underestimation of the tensile strength. This underestimation might be due to the fact that the 2D stress fields do not account for the singularity. A good correspondence is observed between IERR to critical ERR levels using both the 2D front CC and 3D models, leading to close identification of G_{IC}. The shear properties of the interface can no longer be identified using the 3D model since μ has no influence and the equivalent stress variation that actually closely corresponds to the normal stress variation. Similarly, λ no longer has any influence, so that it is impossible to identify G_{IIC}. Therefore, a comparison of shear properties with the 2D models becomes unfeasible. One approach could involve observing debonding propagation on the fiber equator at the sample center, where the interface experiences larger shear. This would require the use of SFII samples, involving imaging the front and side surfaces. However, the approaches presented above have not yet been implemented for SFII samples. Additionally, stress-based isocontours might lead to non-optimal debonding shapes in terms of energy. Energy-based debonding shapes might offer a more consistent representation of the observed debonding angle at the free surface, and provide a more pronounced shear influence during debonding initiation. A methodology for investigating other possible debonding shapes is discussed in Chapter V and Chapter VI.

CHAPTER V

Influence of nearby fiber on fiber-matrix debonding

Content

Some results presented in the following chapter can be found in the following article published in a peer-reviewed journal:
Influence of nearby fiber on fiber-matrix debonding: Coupled Criterion prediction and debonding shape determination by Hugo Girard *et al.* [Gir+24].

V.1 Introduction and motivation

Previous studies have mainly focused on a single fiber in an infinite matrix. However, a more realistic composite microstructure involves numerous fibers with varying relative positions (which can be for instance quantified by inter-center distances and angles with respect to the loading direction). Several authors have investigated the influence of neighboring fibers on the debonding process. Muñoz-Reja *et al.* [Muñ+16a; Muñ+16b] assessed debonding initiation in a two-fiber configuration under tensile loading, varying the inter-center distance between 2.25 and 2.5 times the fiber radius and compared two different inter-center angles. Asymmetric debonding locations with respect to the loading direction were obtained. It was shown that the smaller the inter-center distance, the smaller the remote tensile loading required for the debonding to initiate. Sandino *et al.* [SCP16] studied the influence of angle and distance between fibers center on debonding propagation. Inter-center angle influenced the debonding arrest angle and remote loading required for propagation. Moreover, the influence of the nearby fiber vanishes after a certain distance. Within the same framework, Velasco *et al.* [VCP20] and Zhuang *et al.* [ZTV18] proposed a similar analysis in the presence of a pre-existing debonding and found that the debonding of another fiber may either be delayed or enhanced by the pre-existing debonding depending on its location. It was also found that the debonding kink into the matrix was affected by the neighboring fiber and was either damped or reinforced depending on whether there was a pre-existing debonding. Kushch *et al.* [Kus+11] used CZM for the prediction of debonding initiation with a two-fiber configuration and focused on interface stresses and debonding locations that vary with the inter-center angle, either at the top or bottom poles. However, most of the aforementioned studies do not focus on a configuration that is asymmetric with respect to the loading direction, so that the debonding location and propagation remain symmetric. Besides, there is a lack of experimental confrontation to validate the numerical approach employed.

The asymmetric debonding shape leads to some difficulties in the implementation of the CC which requires the *a priori* definition of the crack shape. Such shape of the debonding can be prescribed symmetric in the case of a single inclusion [Man09; PCM06]. However, multi-fiber configurations induce a perturbation of the fields at the interface and the debonding no longer remains symmetric with respect to the loading direction [Muñ+16b; Kus+11]. To overcome this shape identification problem, some authors estimated the crack shape based on stress isocontours [DL18a; DL18b; Car+21]. This solution led to an efficient way of determining the crack shape (see Chapter IV). However, it does not take into account any energy aspects which, in some cases, can drive the initiation of debonding, see Chapter IV and [Man09; Doi+17a; Mar+08]. In this regard, García a *et al.* [Gar+16] and Doitrand *et al.* [Doi+17a] proposed an iterative approach by comparing the CC solution based on a parameterized

crack geometry in the vicinity of the stress concentration which, therefore, considers the energy aspects. Yes, the two above-mentioned approaches do not consider all possible crack geometries. As a consequence, it is yet not established which initiation crack shape among all possible crack shapes is the most favorable, *i.e.*, results in the minimum imposed loading at initiation.

The present study aims at determining the CC solution in the case of an asymmetric debonding by simultaneously considering all possible crack shape configurations. In Section V.2, the CC solution is compared to the stress- and energy-based debonding shape solutions to quantify the accuracy of the stress isocontours assumption in terms of debonding angles and remote loading. The blind predicted CC solutions are then confronted to experimental observations from the DF batch samples using the fracture properties identified in Chapter IV. CZM are then used in Section V.3 for the different configurations with the fracture properties identified in Chapter IV and the predictions are then compared with the experimental and the CC results.

V.2 Coupled criterion predictions

V.2.1 2D numerical model

Two-fiber specimens under uniaxial tensile loading are considered to study the influence of a nearby fiber on fiber-matrix debonding initiation and propagation. Experimental results are summarized in Section III.3. Figure V.1 describes the model geometry.

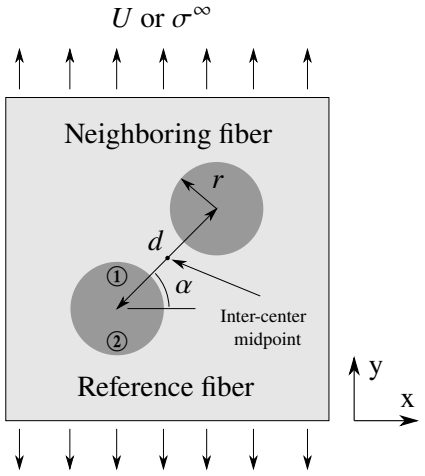

Figure V.1 – Schema of the double-fiber numerical model.

Samples are subjected to uniaxial tensile loading along the y-direction, leading to

a remote stress σ^∞. The inter-center angle (α) from the x-direction and distance (d) are varied in the range 0, 30, 45, 60 and 90 degrees and $2.5r$, $4r$ and $5r$, respectively, with r the fiber radius equal to 1 mm (see Section III.2 for further details). It is worth noting that both fiber absolute positions do change between the configurations as they are rotated with respect to the inter-center midpoint. Both fiber and matrix isotropic elastic properties are detailed in Table III.2 and are similar to those used in Chapter IV. In the sequel, the fibers are referred to as respectively reference and neighboring fibers and all quantities will be referring to the reference fiber in the sequel (see Figure V.1). As the neighboring fiber induces field perturbation, debonding is likely to be initiated at either half-circle of the fiber. Therefore, a denomination similar to Chapter III is adopted to describe the initiation site, where the top half-circle is referred to as ① and the bottom half-circle as ② (see Figure V.1).

A 2D plane strain FE model is implemented under the assumption of linear elasticity and small deformations. As a consequence, the stress is proportional to the applied loading whereas the elastic strain energy is proportional to the square of the applied loading. In the sequel, the calculations are performed with a $\sigma^\infty = 6.85$ MPa remote stress. A 0.02 mm mesh size is chosen at the fiber-matrix interface, which ensures that the difference on the stress and elastic strain energy is smaller than 1% for a finer mesh (see Appendix A.1 for an example of mesh convergence analysis). The geometry of the model is limited to 50 mm and 13 mm along the longitudinal y-direction and transverse x-direction with prescribed nodal displacements.

V.2.2 CC implementation

Debonding initiation is assessed using the CC, which combines two conditions to provide the initiation loading and debonding angle ranges. The implementation is similar to that employed in Chapter IV. On the one hand, the stress condition must be satisfied at any location over the entire debonding path Γ before initiation. As a consequence, the stress requirement is not a point stress but a nonlocal condition since it must be fulfilled all over the debonding path before initiation. It can thus be employed even in the case of a nonuniform stress field, particularly advantageous given the perturbation induced by the second fiber. On the other hand, the IERR must be larger than the interface average critical ERR. These two conditions are summarized in Equation (V.1).

$$\begin{cases} \sigma_{\text{eq}} = \sqrt{\sigma_{\text{nn}}^2 + \frac{1}{\mu^2}\sigma_{\text{nt}}^2} \geq \sigma_{\text{c}} \; \forall \, \vec{x} \in \Gamma, \\ G_{\text{inc}}(\theta_{\text{d}}, \sigma^\infty) \geq \overline{G_{\text{c}}}(\theta_{\text{d}}). \end{cases} \tag{V.1}$$

The parameter μ denotes the τ_{c} to σ_{c} ratio, which are respectively the shear and tensile strengths. The IERR is denoted by G_{inc} and $\overline{G_{\text{c}}}$ is the average critical ERR.

The normal and shear stresses at any location on the interface are denoted σ_{nn} and σ_{nt}, respectively. The calculation of all these quantities is detailed in the sequel. Contrary to the CC application to single-fiber configuration, see Chapter IV, where the initiation debonding location is *a priori* known and symmetric with respect to the y-direction, the initiation debonding configuration may now depend on the nearby fiber (inter-center distance and angle, see Figure V.1). As a consequence, solving the CC requires to determine not only the remote imposed stress causing debonding initiation but also the initiation debonding configuration, which is addressed in the sequel.

V.2.3 Debonding shape determination

As introduced in Section V.2, the debonding trajectory can no longer be considered symmetric with respect to the loading configuration and must now be determined. The angular position at the interface of the reference fiber is denoted θ_f, see Figure V.2. Based on the CC, debonding can initiate provided the stress and energy criteria given in Equation (V.1) are fulfilled. As a consequence, it is likely that the potential debonding configurations do not lie far from the ones maximizing either the equivalent stress or the elastic strain energy variation. Figure V.2 shows the variation of the equivalent stress (σ_{eq}) and elastic strain energy variation ($-\Delta W$) computed as a function of the angular position along the fiber-matrix interface (θ_f).

The equivalent stress variation as a function of θ_f is obtained based on a calculation without debonding. The evaluation of $-\Delta W$ is performed by releasing one interface node at a given angular position θ_f. A constant mesh size along the interface is used to ensure that the angular location maximizing $-\Delta W$ also maximizes the IERR. For a single-fiber configuration under remote tensile loading, the equivalent stress and $-\Delta W$ profiles are symmetric and both their maxima are attained at the fiber pole (90 deg. angular position, see Figure V.2a). Asymmetry in the equivalent stress and elastic strain energy variation nevertheless occurs for a two-fiber configuration, as shown in Figure V.2b in a case where $\alpha = 45$ deg. and $d = 2.5r$. More precisely, both quantities reach a maximum at a similar 100 deg. angular position, different from the single fiber configuration. In the following θ_i is used to define the angular position θ_f maximizing the stress or the elastic strain energy variation, where debonding could most likely initiate from. Table V.1 lists the angles maximizing the strain energy released ($\theta_i^{-\Delta W}$) or the equivalent stress criterion ($\theta_i^{\sigma_{eq}/\sigma_c}$) for different inter-center angles at a fixed inter-center distance of $2.5r$, distance for which the fields are most affected.

The ratio between the two angles are presented in Table V.1. All ratios remain close to 1 whatever the configuration meaning that both angles are close to each other, even for highly perturbed configurations ($\alpha \simeq 60$ deg.).

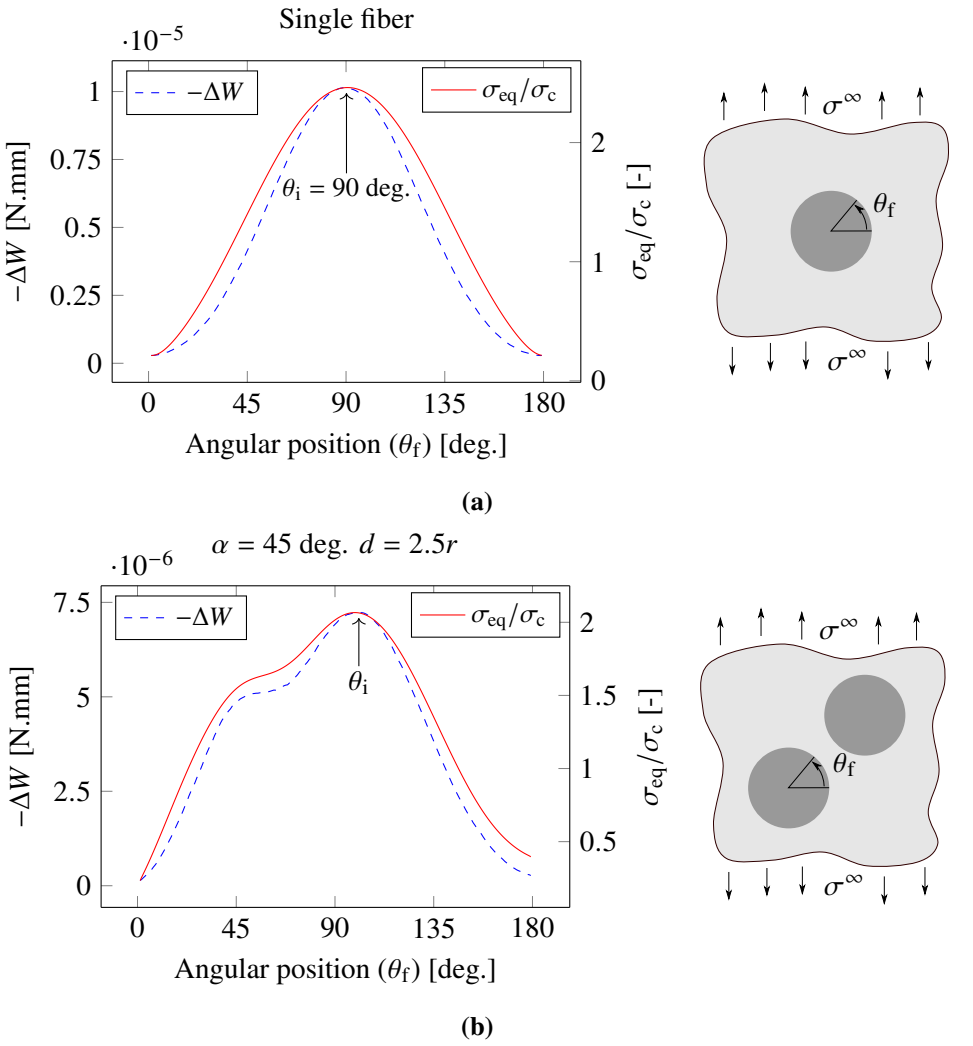

Figure V.2 – Equivalent stress and elastic strain energy variation as a function of the angular position along the fiber-matrix interface a constant $\mu = 1.5$: (a) single-fiber configuration (Chapter IV) (b) two-fiber configuration for a constant $\mu = 1.5$. The angular location θ_i corresponds to the θ_f maximizing the stress or the elastic strain energy variation,

Figure V.3 illustrates the field perturbation reporting the angle $|\theta_i|$ for the equivalent stress is maximum for several fiber inter-center distances and angles.

This angle is calculated at both top, *i.e.*, site ① Figure V.3a, and bottom, *i.e.*,

α [deg.]	0	30	45	60	90
$\theta_i^{\sigma_{eq}/\sigma_c}$ [deg.]	87	93	98	63	90
$\theta_i^{-\Delta W}$ [deg.]	89	95	102	60	90
$\theta_i^{-\Delta W}/\theta_i^{\sigma_{eq}/\sigma_c}$ [-]	1.02	1.00	1.03	0.96	1.02

Table V.1 – θ_i variation for various inter-center angles where $d = 2.5r$ and $\mu = 1.5$, evaluated at the reference fiber top half circle. The upperscripts refer to the energy or stress conditions used for the angular position determination. Ratio between the two angles are added to highlight the small discrepancy between the two approaches.

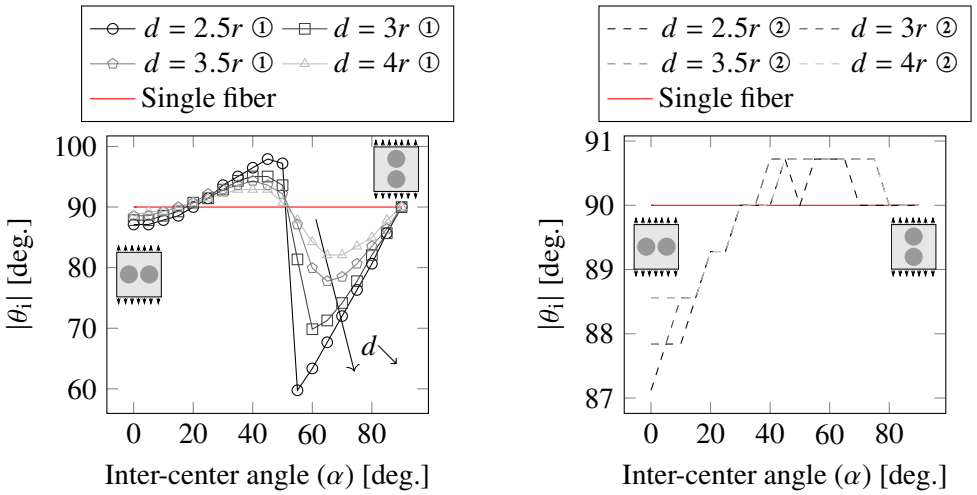

(a) **(b)**

Figure V.3 – Angle $|\theta_i|$ for which the maximum equivalent stress is attained at the top (a) and bottom (b) fiber half circles as a function of the fiber inter-center distance and angle for $\mu = \infty$.

site ② Figure V.3b, half circles of the reference fiber. The larger the difference from 90 degrees, the higher the perturbation of the fields with respect to the single fiber configuration. Noticeably, the stress fields at the fiber bottom half circle (Figure V.3b) are only slightly influenced since the angles remain within the 90 deg. vicinity (+ or - 3%) whatever the inter-center distance. On the contrary, at the top half circle of the fiber (Figure V.3a), the smaller the inter-center distance, the larger the perturbation. Additionally, θ_i differs the most from 90 degrees for an inter-center angle close to 60 degrees. This configuration may thus result in strongly asymmetric crack initiation. In contrast, θ_i reverts to 90 deg. when $\alpha = 90$ deg. as the direction through the two fiber centers is parallel to the loading direction.

Starting from an initiation debonding angular position θ_i, the debonding shape can then be described by increments of angles on each side of this initial location, denoted by $\Delta\theta^+$ and $\Delta\theta^-$, as detailed in Figure V.4. The sum of these two debonding increments corresponds to the total debonding angle θ_d. In the sequel, different approaches are assessed to determine the possible initiation debonding configurations, based on stress, energy or both stress and energy.

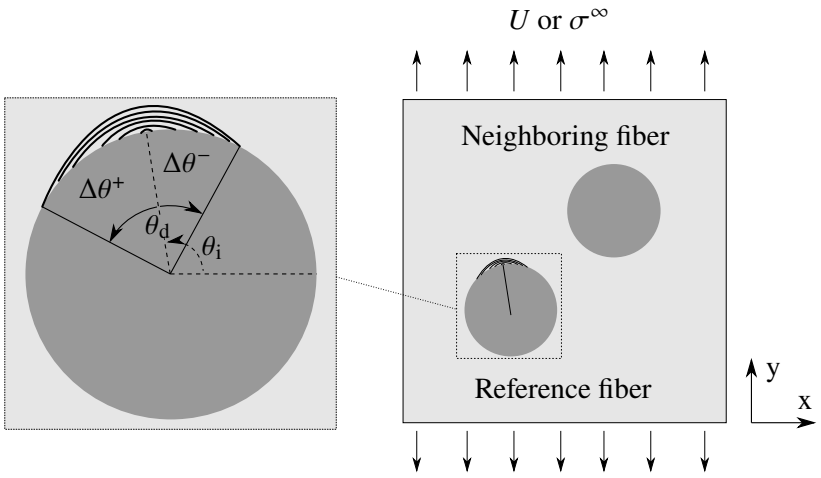

Figure V.4 – Schematic of the debonding shape including the initiation debonding angular position θ_i and the debonding increments $\Delta\theta^+$ and $\Delta\theta^-$ on each side of the initiation location at the reference fiber top interface. The sum of both debonding increments correspond to the total debonding angle θ_d.

Debonding configuration based on stress criterion

A convenient crack shape determination approach consists in defining the possible crack configurations based on the stress isocontours [DL18a; DL18b; Car+21]. The stress isocontour-based crack definition consists in considering angle configuration which strictly fulfill the stress criterion for a given imposed loading and specified interface strengths. As a consequence, it reverts to determining the debonding configuration described by θ_i, $\Delta\theta^+$ and $\Delta\theta^-$ for which the stress criterion is fulfilled before initiation (see Figure V.4). The two debonding tips correspond to angles $\theta_i + \Delta\theta^+$ and $\theta_i - \Delta\theta^-$, respectively. The advantage of this approach is that, for given shear and tensile strengths, the possible crack surfaces can be determined based on a single calculation without crack and that the stress criterion is strictly fulfilled for each possible crack. Figure V.5 shows an example of the variation of the equivalent stress along the fiber-matrix interface at the reference fiber top half circle for a given sample geometry

and varying strength ratios. Two configurations can be encountered depending on the tensile and shear strength magnitudes (that is a variation in the μ ratio):

- Tension-induced crack initiation leading to one equivalent stress maximum per half circle;
- Shear-induced crack initiation leading to two equivalent stress maxima per half circle.

More precisely, for μ larger than 1.5, the equivalent stress decreases monotonically from the maximum peak, inducing a single initiation site. On the contrary, for μ smaller than 1.5, the equivalent stress exhibits two local yet uneven maxima thus corresponding to two possible (yet non equiprobable) initiation sites. It is worth mentioning that experimental observations often show a single initiation site at one or both half circles of the fiber, which could indicate tension induced debonding initiation for the studied fiber-matrix interface. Nevertheless, without the use of a high speed camera that would enable capturing either tension- or shear-induced crack initiation, it is not possible to draw a clear conclusion on this statement. Additionally, the many stochastic effects resulting from imperfections or heterogeneity could also influence debonding location. As a consequence, shear-induced crack initiation are also studied for comparison purposes.

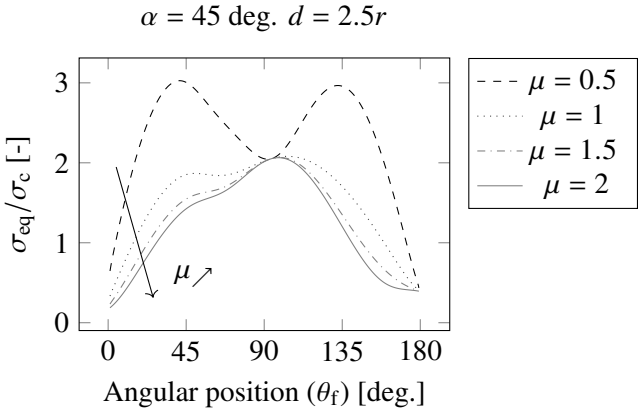

Figure V.5 – Equivalent stress to tensile strength ratio variation as a function of the angular position along the reference fiber top half-circle interface for various μ values.

Tension-induced crack initiation

In case of tension-induced crack initiation ($\mu > 1.5$), the equivalent stress reaches a single maximum, which leads to a straightforward definition of the possible debond-

ing configurations based on equivalent stress isocontours. Figure V.6 shows the minimum equivalent stress to normal strength over the debonding angle corresponding to $\theta_i + \Delta\theta^+$ and $\theta_i - \Delta\theta^-$ according to the stress condition introduced by Leguillon [Leg02].

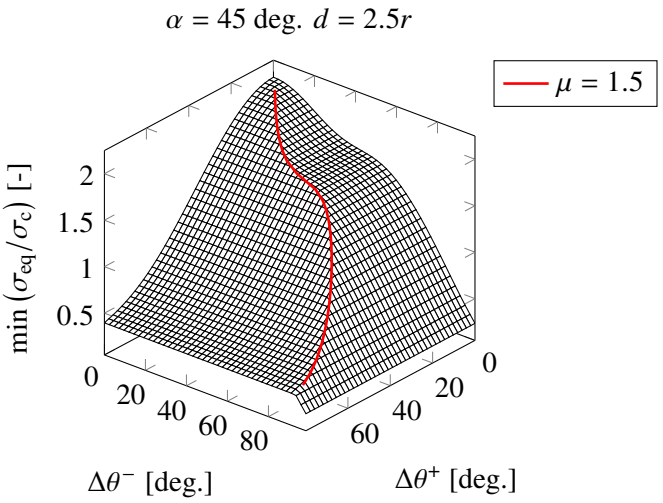

Figure V.6 – Minimum equivalent stress to tensile strength for any angular location θ_f such that $\theta_i - \Delta\theta^- \leq \theta_f \leq \theta_i + \Delta\theta^+$, as a function of angle increments.

This curve is obtained as the minimum stress attained over the whole crack path prior to debonding. The equivalent stress to tensile strength ratio decreases with increasing both angle increments from θ_i. The possible initiation debonding configurations based on the stress isocontours are depicted by the red line in Figure V.6 and Figure V.7. The admissible initiation debonding angles correspond to configurations where σ_{eq} is larger than σ_c. Figure V.7 shows the debonding shape based on the stress criterion isocontours for several values of μ larger than or equal to 1.5. $\Delta\theta^+_{TC}$ indicates the transition angle between the areas undergoing tension or compression. Note that the range of μ presented in Figure V.7 results in θ_i differences smaller than 3 degrees. The debonding shape is thus slightly influenced by the interface shear to tensile strength ratio. Ultimately, the increase of μ results in a debonding shape close to that obtained with a normal stress criterion (corresponding to $\mu = \infty$).

The average difference between the debonding shapes for a normal stress criterion and the equivalent stress criterion for various μ values is evaluated. By comparing for fixed $\Delta\theta^+$, the difference in $\Delta\theta^-$ between debonding shapes obtained using the equivalent stress ($\Delta\theta^-_{\sigma_{eq}}$) or the normal stress criterion ($\Delta\theta^-_{\sigma_{nn}}$) is evaluated using Equation (V.2).

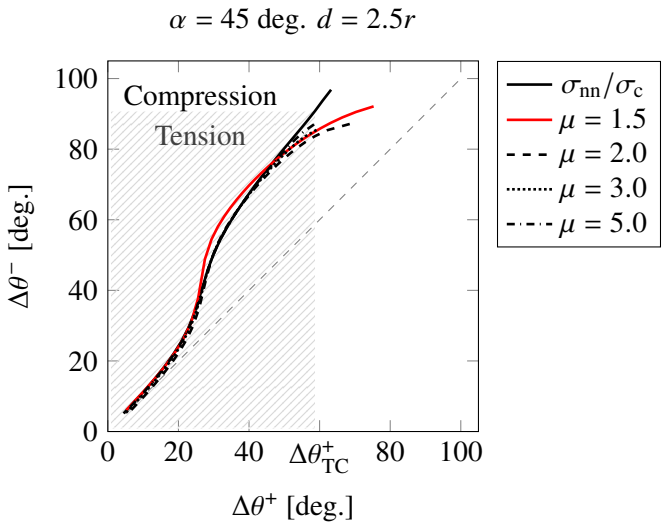

Figure V.7 – Stress isocontours for several values of μ where tension zone ($\sigma_{nn} > 0$) and compression zone ($\sigma_{nn} < 0$) are highlighted. The transition increment angle from tension to compression is indicated by $\Delta\theta^+_{TC}$. The dashed lightgray line corresponds to symmetric configuration.

$$\mathcal{F}_2 = \left(\frac{1}{\Delta\theta^+_{TC}} \int_0^{\Delta\theta^+_{TC}} \frac{\left| \Delta\theta^-_{\sigma_{eq}}(\Delta\theta^+) - \Delta\theta^-_{\sigma_{nn}}(\Delta\theta^+) \right|}{\Delta\theta^-_{\sigma_{nn}}(\Delta\theta^+)} \mathrm{d}\Delta\theta^+ \right) \times 100 \qquad \text{(V.2)}$$

For all the configurations covered, the average difference turns out to be no larger than 6%. Only debonding angles located in the tensile zone are considered because a crack does not initiate under compressive stress. All in all, whatever the shear to tensile strength ratio, the normal stress-based debonding configuration provides a good estimate of the stress-based debonding shape obtained under the equivalent stress criterion. Importantly, the advantage of using the debonding shape based on the normal stress rather than on the equivalent stress is that it allows defining possible initiation configurations that do not depend on fracture properties. As a consequence, it is numerically more efficient for inverse identification approach. The same study is performed for several angles and inter-center distances to ensure that this observation is valid for any fiber inter-center distances and angles and the maximum differences never exceeded 10%. The difference becomes more pronounced for a smaller inter-center distance and at the top half-circle location, *i.e.*, site ① , which corroborates what is observed with regard to the stress field perturbation (see Figure V.3). It is worth

mentioning that the difference vanishes for a symmetric configuration with respect to the loading direction, *i.e.*, inter-center angle equal to 90 degrees.

Shear-induced crack initiation

For μ smaller than 1.5, the equivalent stress shows two often uneven local maxima (Figure V.5). This configuration could then lead to various initiation scenarios:

- Single debonding initiation at one stress maximum;
- Two debonding initiations at both maxima.

García *et al.* [GMG15] showed that two simultaneous debonding initiations at both half circles of a single fiber were not favorable compared to a single initiation site. Similar approach is employed here to compare the IERR of a single or double initiation located on the same half circle of the fiber. The same isocontours are determined based on each stress maximum and the nodes are released on the corresponding angles. Table V.2 summarizes the IERR obtained for a randomly selected isocontour for $\mu = 0.5$ where $\alpha = 45$ deg. and $d = 2.5r$, see Figure V.7.

	2 sites	1 site	
	Both maxima	$\theta_f \simeq 40$ deg. maximum	$\theta_f \simeq 132$ deg. maximum
G_{inc} [J/m^2]	3.97	4.13	3.7

Table V.2 – IERR for a given initiation configuration considering single initiation site separately or both sites.

The debonding configuration maximizing the IERR can be considered as the favorable initiation site. Thus, a single initiation site is energetically more favorable. Interestingly, it corresponds to the location where the equivalent stress is maximum (see Figure V.5). Finally, in case of shear-induced crack initiation, possible debonding configurations can be determined following stress isocontours by considering only one debonding location that corresponds to the global equivalent stress maximum.

Debonding configuration based on energy criterion

The second approach consists in determining the debonding shape based on the configurations maximizing the IERR. To this end, nodes at the fiber-matrix interface are successively released on both sides of θ_i in increments of $\Delta\theta$ to compute the IERR for a given debonding angle (θ_d) using Equation (V.3), where W denotes the elastic strain energy of the model and r the fiber radius:

$$G_{\text{inc}}(\theta_{\text{d}}, \sigma^{\infty}) = \frac{W(0, \sigma^{\infty}) - W(\Delta\theta^{+} + \Delta\theta^{-}, \sigma^{\infty})}{r(\Delta\theta^{-} + \Delta\theta^{+})}. \tag{V.3}$$

The local critical ERR is evaluated at both crack tips by means of the Hutchinson and Suo relation [HS91] similarly to the approach employed in Chapter IV. This relation links the interface opening (G_{IC}) and shear (G_{IIC}) critical energy release rates to the local critical ERR (G_{c}) using the mode mixity defined as $\psi(\theta_{\text{d}}) = \arctan(|\sigma_{\text{nt}}| / \sigma_{\text{nn}})$ (Equation (V.4)). The mode mixity is assessed at a distance of 0.015 mm from the two crack tips for each configuration according to [Man09] and the maximum of the two G_{c} is retained.

$$G_{\text{c}}(\psi(\theta_{\text{d}})) = G_{\text{IC}} \left[1 + \tan^2\left[(1 - \lambda)\,\psi(\theta_{\text{d}})\right]\right] \tag{V.4}$$

As a reminder, the parameter λ is linked to the ratio between G_{IC} and G_{IIC}. The average interface critical ERR, $\overline{G_{\text{c}}}$, corresponds to the average of the local interface critical ERR, *i.e.*, for each debonding angle θ, over the complete debonding shape, corresponding to θ_{d} (Equation (V.5)).

$$\overline{G_{\text{c}}} = \frac{1}{\theta_{\text{d}}} \int_{\theta_{\text{i}} - \Delta\theta^{-}}^{\theta_{\text{i}} + \Delta\theta^{+}} G_{\text{c}}(\psi(\theta))\mathrm{d}\theta \tag{V.5}$$

Figure V.8 shows the IERR to critical ERR ratio as a function of debonding increments on each side of the debonding initiation location.

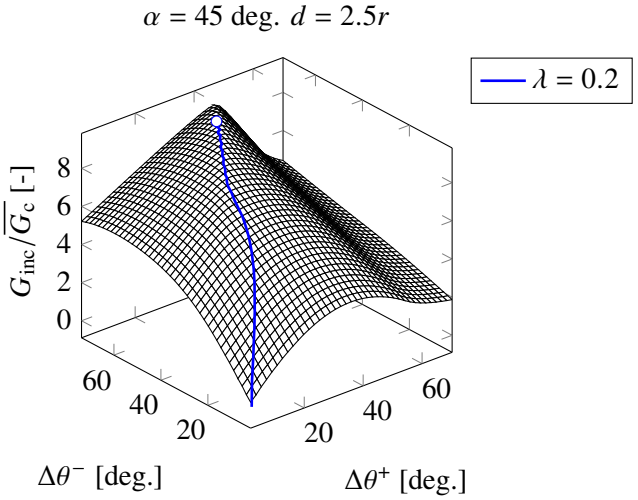

Figure V.8 – IERR to critical ERR variation as a function of angle increments.

For a small debonding angle, the energy released is too small to fulfill the criterion. By increasing the debonding angle, the criterion is fulfilled and the surface exhibits a maximum, corresponding to an optimal angle maximizing the criterion. Therefore, this maximum corresponds to the favorable condition for the debonding to initiate, meaning that the loading to apply in order to fulfill the energy criterion is minimal. The debonding shape can be evaluated by maximizing the surface gradient until the maximum is reached, denoted by the blue marker in Figure V.8 and Figure V.9.

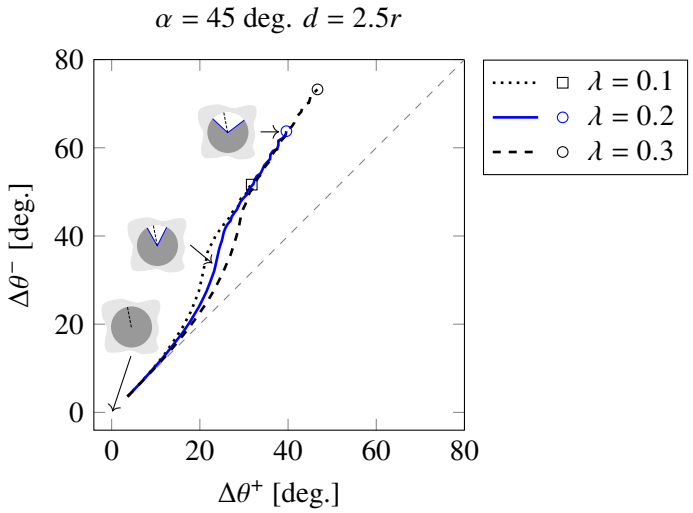

Figure V.9 – Debonding shape for several values of λ. The dashed lightgray line corresponds to symmetric opening around θ_i.

The G_{IIC} to G_{IC} ratio, related to the parameter λ, influences the shape of the debonding as well as the configuration maximizing $G_{inc}/\overline{G_c}$. Figure V.9 shows the shapes obtained from three different values of λ for the studied configuration. The debonding initiation angle remains the same for a fixed value of λ. Setting $\lambda = 1$ results in $G_{IC} = G_{IIC}$ and a smaller value of λ corresponds to $G_{IC} < G_{IIC}$. Decreasing λ leads to an increase in the critical ERR and G_{IIC} for a fixed G_{IC} and mode mixity. Therefore, no shape change is observed for a fixed value of λ as the ratio between G_{IC} and G_{IIC} remains the same.

Coupled stress and energy criterion

Coupling both stress and energy conditions allows the determination of the minimum loading to apply in order to initiate a debonding as well as the corresponding debonding angle. When both conditions are involved, the initiation debonding is sought as

the angle for which both criteria are fulfilled for a minimum applied loading. As a consequence, it is likely that the initiation debonding configuration lies between the debonding shapes determined based on either the stress isocontours or maximizing the IERR. Figure V.10 shows the applied remote stress required to fulfill both conditions ($\sigma^{\infty}_{\text{req}}$) for a range of angle increments. The loading required to fulfill the equivalent stress condition increases monotonically with increasing debonding angle whereas the one required to fulfill the energy condition reaches a minimum. Combining both criteria thus results in determining the debonding configurations and corresponding applied stress for which the CC is fulfilled. Among these debonding configurations, the initiation debonding configuration is determined as the one minimizing the applied stress.

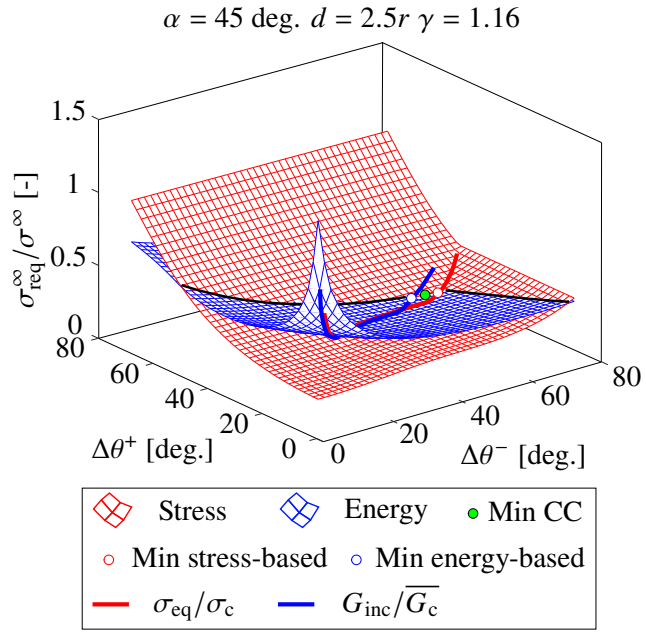

Figure V.10 – Required loading to fulfill stress or energy conditions. The solid lines indicate the configurations corresponding to either stress-based or energy-based possible debonding shapes and the circles indicate the corresponding initiation configurations minimizing the imposed loading.

The debonding configuration for which both criteria are fulfilled for a minimum loading (*i.e.*, the initiation debonding configuration) is highlighted on Figure V.10 and Figure V.11a with a green marker. Figure V.11a shows the isocontours of the loading required to fulfill the CC. The same approach is employed to determine the minimum remote stress that follows either the stress-based or energy-based debond-

ing configurations, also highlighted in Figure V.10 and Figure V.11a. These minima differ slightly from the CC solution, both in terms of the required remote stress and debonding angle.

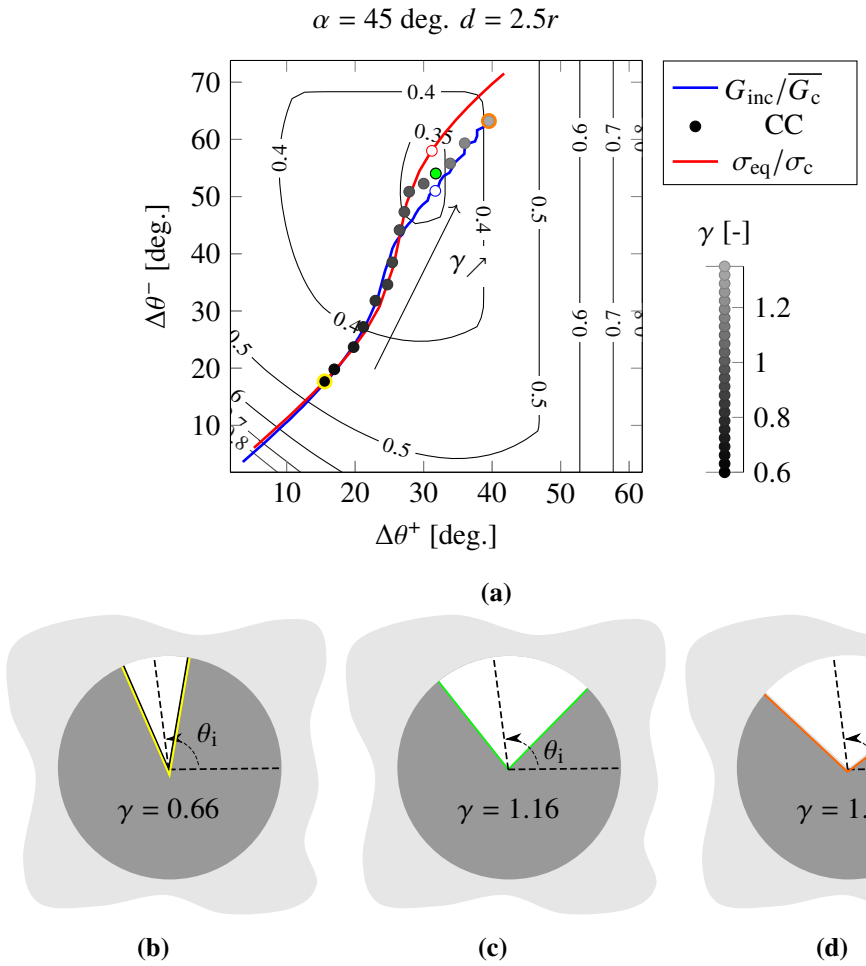

Figure V.11 – (a) Isocontours of the loading required to fulfill the CC emphasizing the minimum indicated in Figure V.10 and minima obtained for various other properties range, the smaller the gray intensity, the larger γ is. Visualization of $\theta_i \simeq 100$ deg. and associated debonding angle at initiation, before any potential unstable growth, taken from Figure V.11a for several values of γ, (b) $\gamma = 0.66$ with $\theta_d = 33$ deg. (yellow circle), (c) $\gamma = 1.16$ with $\theta_d = 85$ deg. (green marker) and (d) $\gamma = 1.45$ with $\theta_d = 102$ deg. (orange circle).

For given λ and μ, the debonding configuration minimizing the loading required

to fulfill the CC actually depends on the interface brittleness number γ which was introduced by Mantič [Man09] and recalled in Equation (V.6):

$$\gamma = \frac{1}{\sigma_c}\sqrt{\frac{G_{IC}E^*}{r}}. \tag{V.6}$$

Each marker in Figure V.11a corresponds to the CC solution with a different γ, where E^* denotes the harmonic mean of the effective elastic moduli of the two constituents. For small enough γ (< 1.), the debonding configuration obtained using the CC is close to the debonding shape predicted based on stress isocontours, which is also close the one determined by maximizing $G_{inc}/\overline{G_c}$. However, for large enough γ (> 1.2) the debonding configuration retrieves the debonding shape determined by maximizing $G_{inc}/\overline{G_c}$. Whatever the interface brittleness number, the debonding initiation configuration actually lies between the debonding shapes determined based on either stress isocontours or maximizing $G_{inc}/\overline{G_c}$. The debonding angles at initiation obtained for various increasing γ are shown in Figure V.11b-V.11c-V.11d, superimposed on the favorable fiber location for debonding initiation. A small γ results in a small debonding angle at initiation but is likely to induce a larger unstable debonding phase after initiation, initiation being driven by the stress condition (see Chapter IV). In contrast, a large γ induces a large debonding angle at initiation with a smaller unstable debonding phase.

Figure V.12 shows the stress-based, energy-based and CC-based debonding configurations obtained for inter-center angles of 90, 60 and 0 degrees with $d = 2.5r$. For the 90 degrees inter-center angle, a symmetric configuration is observed with respect to the loading direction. The stress-based, energy-based and CC-based debonding shapes are similar since there is no asymmetric perturbation of the fields. Similarly to the previous example, for inter-center fiber angles different from 90 degrees (Figure V.12b and Figure V.12c), the debonding configuration predicted using the CC always lies between the stress-based and energy-based debonding configurations. Moreover, it is also consistent with the stress-based debonding shape for small γ and with the energy-based debonding shape for large γ. For intermediate γ, there is a transition zone for which the debonding configuration does not correspond to neither shapes. Figure V.12b shows the predicted debonding configurations for a 60 deg. inter-center angle for which the transition from stress-based to energy-based occurs abruptly, *i.e.*, all debonding configurations predicted by the CC are close either to the stress-based or the energy-based debonding configuration whatever γ. On the contrary, Figure V.12c shows a smoother transition, where the debonding configuration predicted by the CC does not correspond to stress-based or energy-based debonding configuration for a significant range of γ (from 0.96 to 1.36).

It is noteworthy that even in the case of a strongly influenced initiation loca-

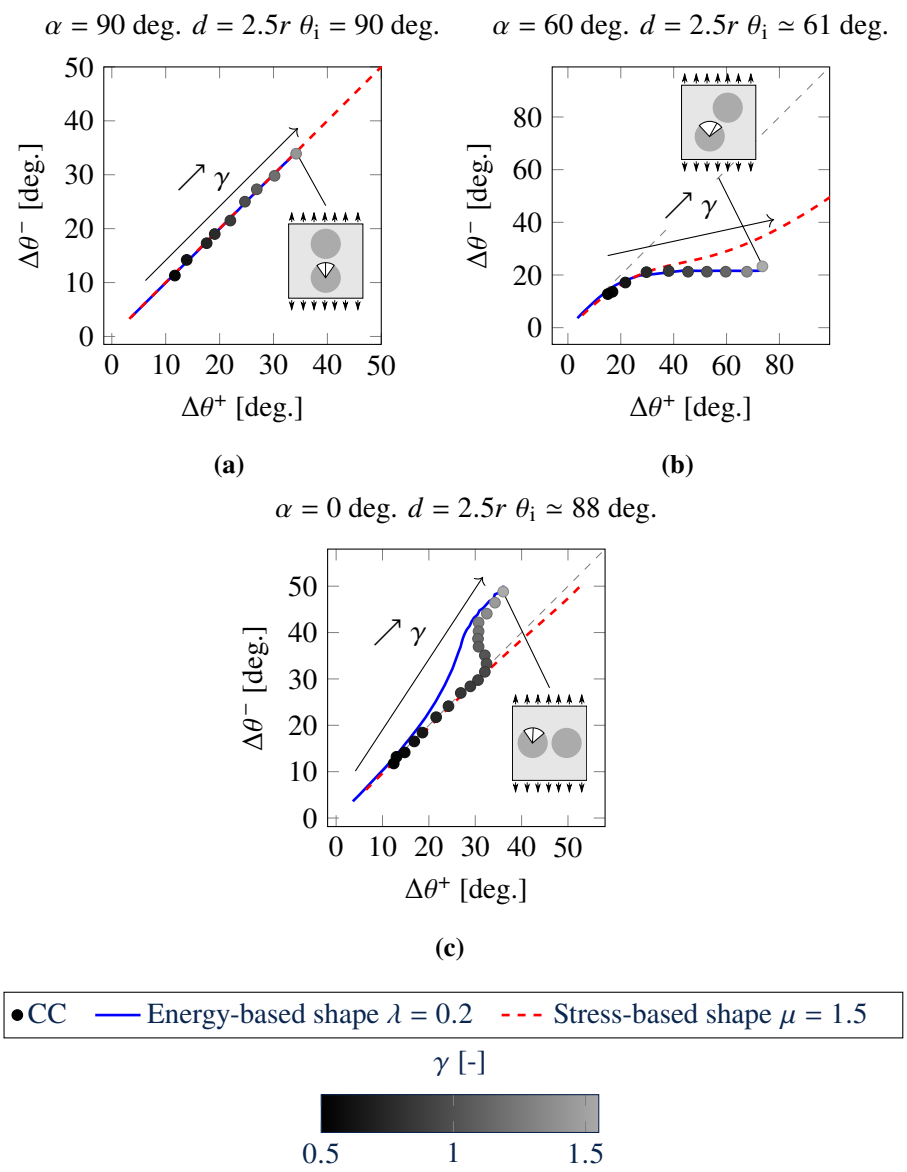

Figure V.12 – Comparison between debonding shapes for configuration where $d = 2.5r$ and (a) $\alpha = 90$ deg. (b) $\alpha = 60$ deg. and (c) $\alpha = 0$ degrees. The markers denotes the CC solutions for various γ values (increasing γ with decreasing gray intensity) and dashed lightgray lines correspond to symmetric openings on both sides from θ_i whose values are given in Table V.1.

tion (when θ_i is much larger or smaller than 90 deg.), the debonding initiation angle tends to recover a symmetric configuration with respect to the loading direction. Figure V.12b highlights this last observation with a $\alpha = 60$ deg. then the increment of angle $\Delta\theta^-$ is small compared to the increment of angle $\Delta\theta^+$ tending towards an initiation angle centered at about 90 degrees. The same observation was obtained by Mantič *et al.* [Man+15] who numerically found that, wherever debonding initiation might occur, propagation will tend towards the loading direction as the amount of available elastic strain energy is larger.

Stress isocontours allow efficient numerical prediction of the debonding shape because they can be derived from a purely linear elastic calculation without node release. The difference induced by the stress-based debonding shape from the favorable configuration can be evaluated. The stress-based solution is determined by locating the minimum on surface $\sigma^{\infty}_{req}/\sigma^{\infty}$ (Figure V.10) that follows the stress-based debonding shape and directly comparing it to surface global minimum, corresponding to the favorable CC configuration. Figure V.13a shows the variation of the relative difference in terms of remote loading between the two solutions as a function of γ for inter-center angles of 60 and 0 degrees.

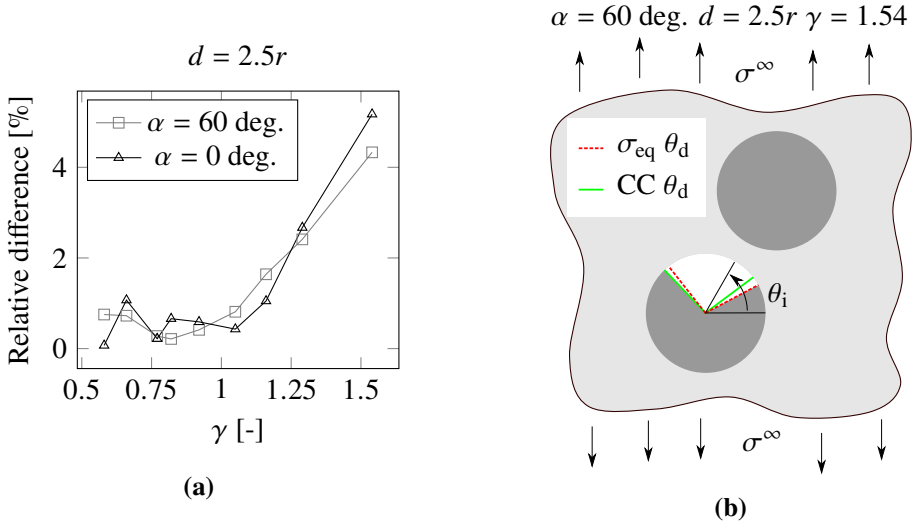

Figure V.13 – (a) Relative difference between CC and stress-based debonding shape solution as a function of γ. (b) Schematic comparison of the debonding location and angle at initiation predicted based on both stress ($\theta_d \simeq 100$ deg.) and CC ($\theta_d \simeq 97$ deg.) shapes with $\theta_i \simeq 61$ degrees.

The relative difference shows increasing trends with γ. The maximum relative difference remains smaller than 5.1 % and the maximum is reached for the largest

values of γ ($\gamma = 1.54$) when the configuration tends towards energy-based debonding shape. It is noticeable that the difference induced by the stress remains small and arguably not worth the computation time cost it requires. Therefore, basing the crack shape on the stress isocontours could be a good compromise to determine the debonding initiation remote loading. Figure V.13b shows the location of the debonding based on the CC and the stress at initiation for $\alpha = 60$ deg. and $\gamma = 1.54$. The debonding angles at initiation predicted by the two shapes are identical, but their locations differ slightly with respect to θ_i. The location of the debonding based on the CC solution is equivalent to the energy solution in this case, tending to maximize the energy released by being symmetric with respect to the loading direction.

V.2.4 Unstable crack propagation

After debonding initiation, it is possible to assess its propagation based on Griffith's criterion $G(\theta_\mathrm{d}) = -\mathrm{d}W/\mathrm{d}\theta_\mathrm{d} \geq G_\mathrm{c}(\psi(\theta_\mathrm{d}))$. The ERR G can actually be obtained from G_inc based on the following relation (Equation (V.7)), where S denotes the debonding surface, *i.e.*, $r\theta_\mathrm{d}$ or $r\,(\Delta\theta^+ + \Delta\theta^-)$ in the studied configuration:

$$G(\theta_\mathrm{d}) = G_\mathrm{inc}(\theta_\mathrm{d}) + S \times \frac{\mathrm{d}G_\mathrm{inc}}{\mathrm{d}S}. \tag{V.7}$$

When $G_\mathrm{inc}/\overline{G_\mathrm{c}}$ maximum is reached, $\mathrm{d}(G_\mathrm{inc}/\overline{G_\mathrm{c}})/\mathrm{d}S = 0$ so that $G_\mathrm{inc}/\overline{G_\mathrm{c}} = G/G_\mathrm{c}$ (see Appendix B.1). Therefore, two configurations can be encountered after the initiation of debonding. On the one hand, if $\mathrm{d}(G_\mathrm{inc}/\overline{G_\mathrm{c}})/\mathrm{d}S \geq 0$, then G/G_c is larger than 1 which implies further unstable debonding phase without increasing the applied loading until $G/G_\mathrm{c} = 1$. On the other hand, $\mathrm{d}(G_\mathrm{inc}/\overline{G_\mathrm{c}})/\mathrm{d}S = 0$ for the initiation debonding configuration so that $G_\mathrm{inc}/\overline{G_\mathrm{c}} = G/G_\mathrm{c} = 1$, resulting in no further propagation of debonding after initiation, as $\mathrm{d}/\mathrm{d}S(G/G_\mathrm{c}) < 0$ (see Appendix B.2).

The debonding has two different crack tips, which may separately or simultaneously propagate. One approach to identify the unstable debonding shape is to consider the direction that maximizes the ERR to critical ERR ratio. This enables the determination of the arrest angle corresponding to an angle for which G/G_c becomes smaller than 1.

Figure V.14 shows the unstable propagation phase of the crack in the configuration driven by both stress and energy for $\gamma = 1.1$. The debonding propagates in an unstable manner from the debonding angle solution, at initiation, obtained using the CC to the angle where G/G_c becomes smaller than 1, after unstable propagation phase.

Figure V.15 shows the unstable propagation shape of the debonding for several values of γ. Larger values of γ result in an energy-driven configuration where no further propagation of the debonding is possible after initiation ($\gamma = 1.5$). On the opposite, a large unstable debonding phase is encountered when γ decreases, leading

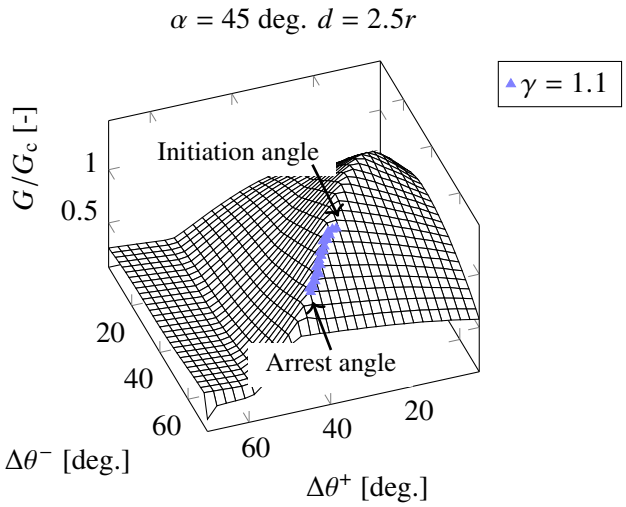

Figure V.14 – ERR to critical ERR variation as a function of angle increments.

to a larger arrest debonding angle ($\gamma = 1$). Although the initiation debonding angle differs from the location maximizing G/G_c, the unstable debonding retrieves an identical shape regardless of the interface properties.

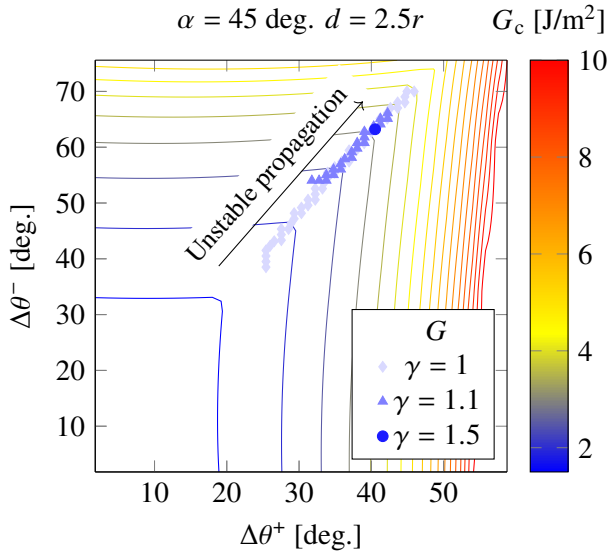

Figure V.15 – Isocontours of the critical ERR (G_c) and unstable debonding shapes obtained for several values of γ.

Configuration with 0 deg. inter-center angle highlights a transition zone where neither stress-based nor energy-based debonding shapes describe the CC solution (see Figure V.12c). By computing the favorable solution that minimizes the loading necessary for initiation based on either stress, energy or CC shape, several starting angles can be used to assess the unstable debonding phase. Figure V.16 shows the three corresponding debonding shapes.

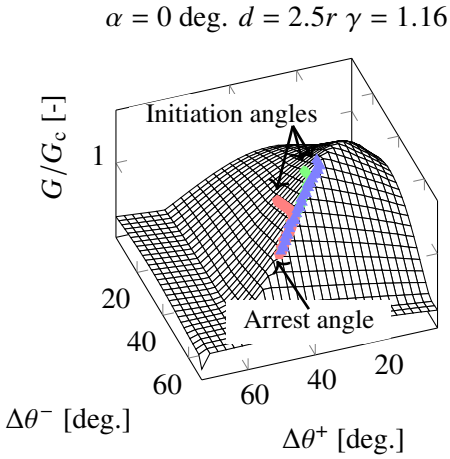

θ_d [deg.]	CC	Stress	Energy
Initiation	67.6	75.7	63.6
Arrest	99.4	100.0	99.2

Figure V.16 – Unstable debonding shape obtained from the stress-based, energy-based and CC-based initiation debonding angle. Table shows the associated debonding initiation angle and arrest angle obtained after unstable propagation phase.

As the required remote loadings for the three solutions have relative differences smaller than 1%, the ERR to critical ERR ratio surface presented is based on the CC solution for illustration purposes. However, the ERR calculation differs because the three solutions have different initiation remote loadings, so that the shape could be slightly different. All cases provide a similar debonding arrest angle with the same location regarding θ_i even with a slightly different initiation remote loading. Moreover, all shapes retrieve the same trajectory that maximizes the ERR to critical ERR ratio. Regardless of the type of shape used (stress, energy, CC), a configuration driven by both stress and energy will propagate to approximately the same debonding arrest angle, as the remote loading required for both solutions are close. Some limitations exist for energy-driven configuration, where a stress-based debonding shape solution could lead to an unstable propagation phase while the energy-based solution leads to a stable propagation. However, the final solution can be obtained using the local ERR released for each configuration, that is computationally expensive to determine.

V.2.5 Nearby fiber influence on debonding initiation

Perturbation induced by the neighboring fiber influences the debonding location along the fiber-matrix interface. However, fields intensity are also influenced by the neighboring fiber, both in terms of stress and energy, depending on the geometrical parameters d and α. Stress fields at the fiber-matrix interface are therefore either intensified or damped and the same observation can be made concerning the elastic strain energy released by the debonding initiation. For similar interface properties, debonding initiation location (top or bottom) and debonding angle range vary as a function of both inter-center angle and distance.

Figure V.17a shows the variation of the maximum normal to far field stress ratio evaluated at both top ① and bottom ② half circles of the reference fiber as a function of the neighboring fiber position (varying d and α). AS observed already, the bottom half circle is less affected than the top half circle. The latter is more affected by the neighboring fiber, highlighting a larger variation in the stress field. Also, with the distance between the top half circle and the neighboring fiber reduces, larger stress perturbations occur. The stress intensification reaches a maximum for 90 deg. configuration. For a configuration close to 45 deg., the top half circle stress intensity decreases, resulting in a larger stress at the bottom half circle.

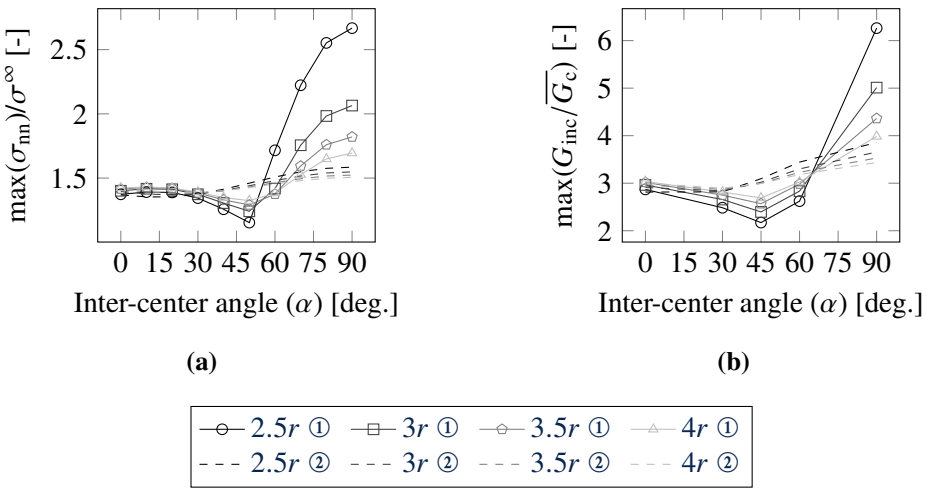

Figure V.17 – (a) Maximum normal to remote stress ratio variation and (b) maximum IERR to average critical ERR ratio variation as a function of the inter-center angle and distance, for an arbitrary remote loading.

Figure V.17b shows the variation of the maximum IERR to critical ERR ratio which is influenced similarly to the stress fields. The latter is obtained by releasing debonding based on the tensile stress isocontours. Larger IERR to critical ERR ratio

is observed for angles close to 90 degrees, where the stress intensity is maximum. However, for inter-center angle range from 20 to 60 degrees, IERR to critical ERR ratio appears to be larger at the bottom half circle. Based on the latest observations, it is more likely that debonding would occur at the top half circle for inter-center distances close to 90 degrees at a lower imposed loading. The smaller the distance between the centers, the smaller the loading required for debonding to initiate. Conversely, for an inter-center angle close to 45 degrees, debonding could most likely occur at the bottom half circle.

The perturbation of the stress and energy fields at the fiber-matrix interface could therefore have a significant influence on:

- The debonding initiation location;
- The required loading for debonding to initiate.

In the following, the CC solution is compared to experimental observations for different geometrical configurations.

V.2.6 Comparison with experimental observations

An application of the CC for all configurations is carried out in the following. The debonding initiation stresses at the top and bottom fiber half circles obtained using the CC and debonding shapes based on stress isocontours are compared with experimental measurements obtained in Chapter III. Furthermore, considering the relevance of the CC, the comparisons will allow to challenge or validate the accuracy of the interface properties determined in Chapter IV and recalled in Table V.3.

G_{IC} [J/m^2]	G_{IIC} [J/m^2]	λ	σ_c [MPa]	τ_c [MPa]
3.7	90	0.13	3	5

Table V.3 – Interface fracture properties used for the blind prediction of debonding initiation identified in Chapter IV.

The debonding initiation sites (reference fiber top, *i.e.*, site ① , or bottom, *i.e.*, site ② , half circle) are compared with the experimental observations in Table V.4. For various geometrical configurations, debondings that are found to be favorable at the top or bottom half circle are designated as indicated in Chapter III for the favorable initiation site. Concerning the simulations, when the remote loading difference between the top and bottom half circles is less than 1% relative error, the location of the debonding is designated as "① / ② ". The debonding locations show no particular trend as a function of the angle and distance inter-center. The experimental results show poor agreement with the CC solution, especially for an inter-center angle of

90 degrees. The difference observed may be associated with the idealized loading employed numerically whereas the experimental loading can differ from a simplified far-fields loading. Additionally, the single camera used in the DF batch samples allows one single free surface to be observed at a time, while the initiation of debonding may occur on the other side due to geometric imperfections for instance.

		α				
	Exp. / Sim.	0 deg.	30 deg.	45 deg.	60 deg.	90 deg.
d	2.5r	① / ① / ②	① / ②	① / ②	① / ②	② / ①
	4r	② / ① / ②	① / ①	② / ① / ②	① / ②	② / ① / ②
	5r	① / ① / ②	② / ①	① / ② / ① / ②	② / ②	② / ① / ②

Table V.4 – Debonding location for several inter-center distances (columns) and angles (lines), see Figure V.1. Within a single cell, the upper right term corresponds to the experimental result and the lower left value to the computed CC one.

Figure V.18 shows the loading required to initiate debonding as a function of the inter-center angles. These values are evaluated experimentally in Chapter III and using the CC for three different inter-center distances. Uncertainties of the experimental results are obtained by tracking a sudden change of slope in the extension of the virtual gauges located at each fiber pole, see Section III.3.

For all angles and inter-center distances, the CC solutions are indicated by round and square markers for the top and bottom location, respectively. The CC solution that requires a minimum loading is the favorable configuration. The latter depends on the inter-center angle and distance. For angles close to 0 degrees, both the top or bottom locations are favorable (difference in $\sigma^{\infty}_{\text{req}}$ smaller than 1%) whatever the inter-center distances. For angles between 30 and 60 degrees, the favorable initiation site is located at the bottom half circle for small distance ($d = 2.5r$). Finally, for angles close to 90 degrees and small distance, the top half circle seems to be the most favorable initiation site. The larger the inter-center distance, the smaller the difference between the top and bottom solutions, due to lower field perturbation, see Figure V.17 and Figure V.18.

The overall comparison leads to an agreement between the CC solution and the experimental observation. This observation attests to the accuracy of the interface properties determined previously. However, a larger difference is observed for an inter-center angle of 90 degrees for all three inter-center distances, possibly due to

the aforementioned difficulties in the identification of the experimental debonding initiation remote loading, with an opening probably smaller than the pixel size.

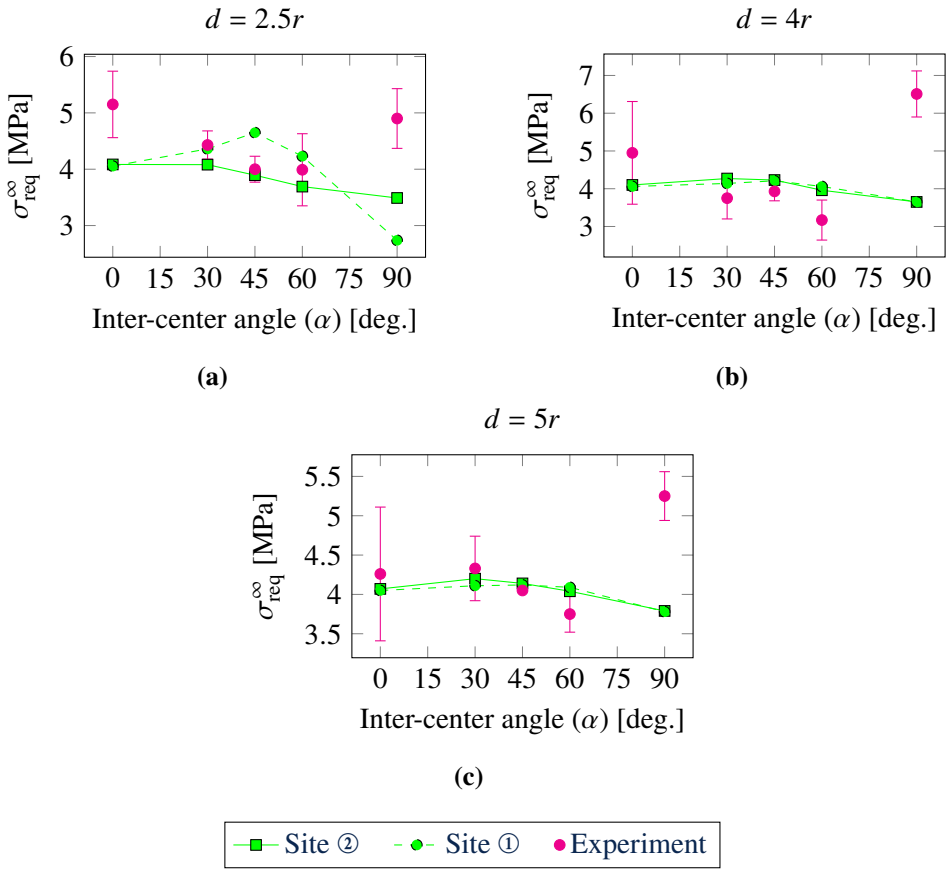

Figure V.18 – Loading required for debonding initiation as a function of the inter-center angle for (a) $d = 2.5r$ (b) $d = 4r$ (c) $d = 5r$. The scatter bars associated with the experimental data points represent variations between several independent tests and the different fiber poles measurements.

The experimental determination of the debonding angle at initiation after the potential unstable propagation is relatively difficult. The main difficulty lies in the identification of the locations of the two crack tips, possibly masked by the DIC speckles or considered as a process zone. Moreover, experimental capture of the unstable propagation phase remains impossible without the use of a high-speed camera. In the sequel, experimental debonding angles are therefore compared to arrest angles obtained numerically. The CC solutions provide an almost identical debonding angle

after initiation, with an average value of 77 deg., whatever the inter-center angle and distance. Figure V.19 shows the variation of the debonding angles as a function of the inter-center angles.

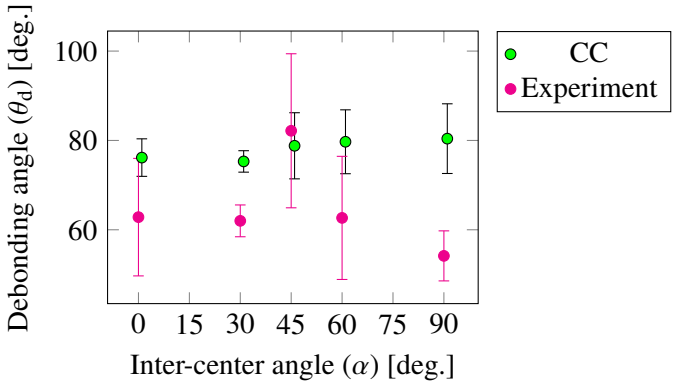

Figure V.19 – Experimental and numerical (CC) debonding arrest angles as a function of the inter-center angles.

The experimental values correspond to the debonding angles averaged and their standard deviation observed at initiation for all inter-center distances with fixed inter-center angle. Only small variations are seen with an average value of 62 degrees. The latter is close to the averaged CC solution, with 24% relative difference, as the CC solutions slightly overestimate the experimental observations. Figure V.20 shows the location and size of the debonding angles predicted by the CC using the stress isocontours and the corresponding experimental results, for the smallest distance ($d = 2.5r$), extracted from a half circle of one of the two samples. The CC solution accurately describes the location of the debonding by providing an upper limit to the experimental angle as observed on the overall trend (Figure V.20). The CC solution and the experimental angle locations and sizes are in good agreement, endorsing the stress isocontour as an effective approximation to describe the debonding shape. Moreover, even in the presence of the neighboring fiber, the experimental debonding is approximately centered at 90 degrees. The same result is obtained with the CC solution which validates the previous numerical observation (see Section V.2.3) concerning the debonding initiation angle obtained with a strongly influenced θ_i.

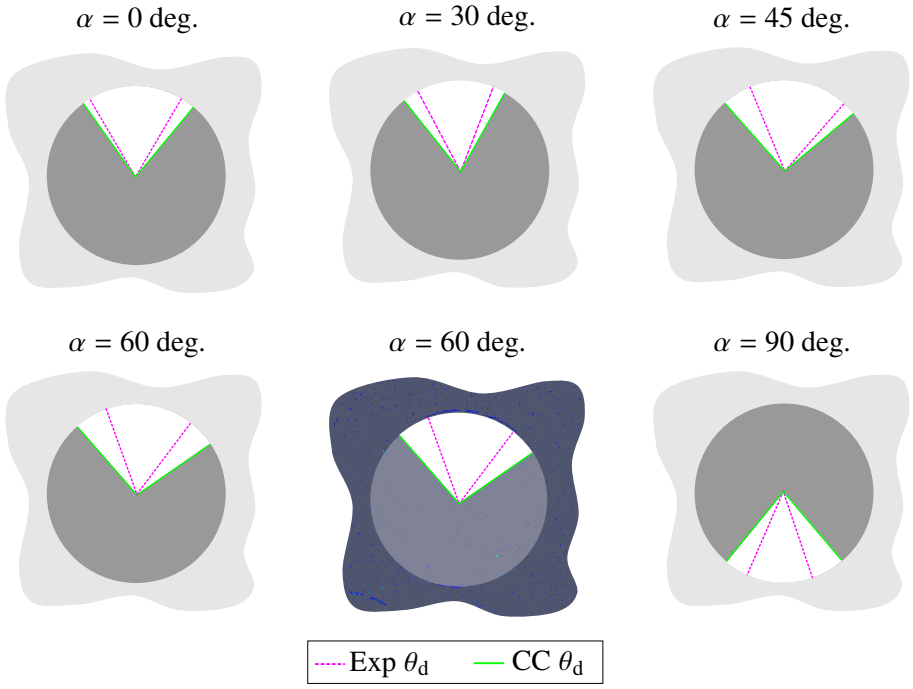

Figure V.20 – Representation of the debonding angle and location predicted by the CC and obtained experimentally with $d = 2.5r$ from a half circle of one of the two samples. The corresponding DIC residual is shown for $\alpha = 60$ deg. to illustrate the experimental angle extraction process, more details can be found in Chapter III.

V.3 Cohesive zone model predictions

V.3.1 2D numerical model

A numerical model similar to that used in Chapter IV is used in which cohesive elements are placed at the fiber-matrix interface of the two fibers. Overall, the model consists of 2D plane strain elements under the assumption of linear elasticity and small deformations. An implicit dynamic algorithm is used. The elastic properties given in Table III.2 are assigned to each component. A density of 1.1 gr/cm^3 is assigned to the matrix and 2.3 gr/cm^3 to the fiber, these values being supplied by the manufacturers. A mesh size study similar to that of Chapter IV is carried out, as well as a similar triangular traction-separation profile is used.

The CZM method requires less computational effort to determine the crack path compared to the CC approach. Therefore, in configurations where asymmetric fields occur, CZM proves to be a relevant option as it predicts debonding initiation and propagation autonomously. In the following, as for the CC, a blind prediction of the

experimental results is performed using the CZM with the fracture properties identified in Chapter IV.

V.3.2 Comparison with experimental observations

As with the CC in Section V.2, the CZM predictions for the DF batch of samples are compared with the experimental data to validate the fracture properties identified in Chapter IV. The normal and shear strengths are selected within a range of acceptable strengths and summarized in Table V.5.

G_{IC} [J/m^2]	G_{IIC} [J/m^2]	σ_c [MPa]	τ_c [MPa]
3.7	10	3	4

Table V.5 – Interface fracture properties used for blind prediction of debonding initiation.

The location of the first debonding initiation is compared with that obtained experimentally and with the CC. The results obtained by the CC and CZM are summarized in Table V.6 and compared with the experimental results. As a reminder, favorable initiation at the top half-circle is called ① and at the bottom half-circle ② . When the relative difference between the two initiation locations remote loading is less than 1%, the location is called "① / ② ".

α	0			30			45		
d	2.5r	4r	5r	2.5r	4r	5r	2.5r	4r	5r
Exp.	①	②	①	①	①	②	①	②	① / ②
CC	① / ②	① / ②	① / ②	②	①	①	②	① / ②	① / ②
CZM	①	①	①	②	①	①	②	②	②

α	60			90		
d	2.5r	4r	5r	2.5r	4r	5r
Exp.	①	①	②	②	②	②
CC	②	②	②	①	① / ②	① / ②
CZM	①	①	②	②	②	②

Table V.6 – Debonding location at initiation, comparison between experimental results, CZM and the CC.

The CZM predictions are in agreement with the experimental data, particularly for samples with an inter-center angle of 90 degrees. The CC describes the location site of the debonding initiation less accurately. The non-consideration of the process zone is perhaps the cause of these discrepancies. Indeed, the influence of the process

zones developed simultaneously at both half-circles of the fiber with the CZM may explain this difference, whereas the CC only considers one initiation site at a time.

Figure V.21 shows the debonding initiation remote loading as a function of the inter-center distances and angles obtained with the two numerical approaches and experimentally. The CC solutions are assessed independently at the bottom and top half-circles. In contrast, CZM take into account both phenomena simultaneously. Thus, debonding can initiate at one half-circle at the same time as the interface at the opposite half-circle begins to be damaged.

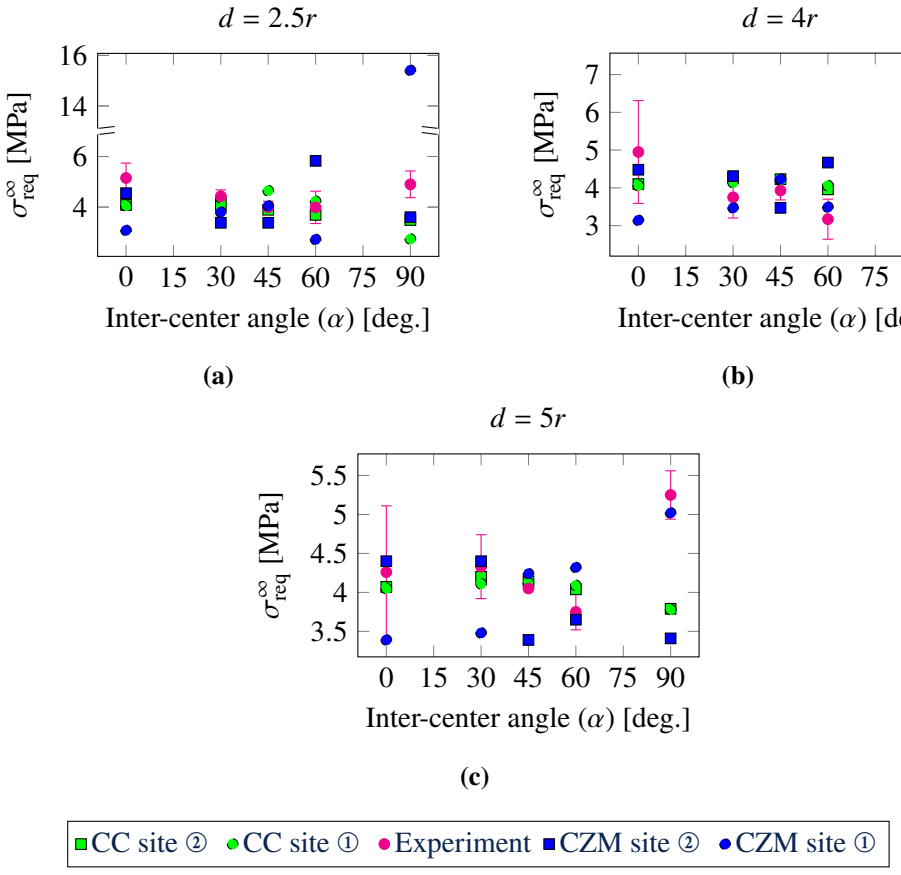

Figure V.21 – Loading required for debonding initiation as a function of the inter-center angle for (a) $d = 2.5r$ (b) $d = 4r$ (c) $d = 5r$ obtained experimentally, using the CC and CZM. The scatter bars associated with the experimental data points represent variations between several independent tests.

Overall, the results obtained from the CZM and the CC are close to those ob-

tained experimentally. Configurations with an inter-center angle of 90 deg. predict either much larger or much smaller loadings compared with the other configurations. The CZM predictions embed the experimental results in this configuration. The experiment-simulation comparison thus validates the consistency of the properties obtained by the two numerical models during the inverse identification approaches in Chapter IV. Similarly, the CZM results embed the CC predictions. The difference in initiation loading between the two half-circles is large with the CZM. The energy released by the initiation of a first debonding will require a larger loading in order to initiate the second opposite debonding. The required loading will therefore be larger than that of the first one. On the contrary, the CC considers each debonding independently, so no damage at the opposite half-circle is considered, resulting in a lower difference in initiation loading between both half-circles. To assess different simultaneous debonding locations with the CC, one solution would be to compare the propagation of one debonding with that of the initiation of a second one located at the opposite half-circle.

Figure V.22 shows the variation of the debonding angle after the unstable propagation phase as a function of the inter-center angles.

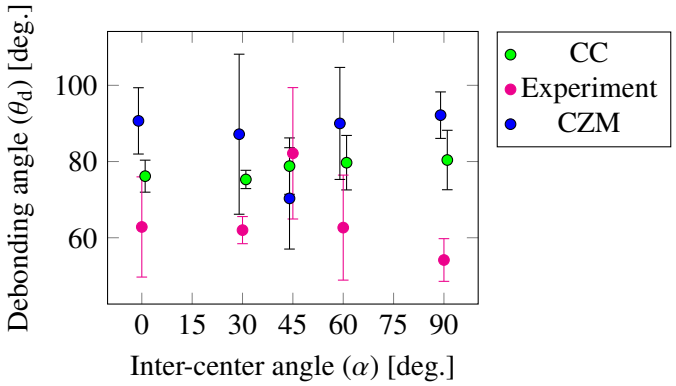

Figure V.22 – Comparison of the debonding arrest angles obtained experimentally and with the CC and CZM as a function of the inter-center angles.

The experimental data correspond to an average of the debonding angles and their standard deviation observed at initiation for all the inter-center distances with a fixed angle. Similarly, for each angle, the CZM and CC results are averaged and the standard deviation used to quantify the uncertainty. Only small variations are encountered and the experimental results are close to 62 deg. whatever the inter-center angle. The CZM results give almost identical angles at initiation, centered around 90 degrees. They slightly overestimate the experimental and CC results, with a relative error of 45% compared with the experimental results. The CC results give an almost identi-

cal debonding angle after initiation, close to 77 degrees, whatever the angle and the inter-center distance, which is closer to the experiment results. It is worth noting that each debonding is treated independently with the CC, so the results do not consider potential pre-damage to the interface on the other fiber.

V.4 Conclusion

Debonding initiation and propagation are assessed using both the CC and CZM on a two-fiber sample subjected to remote uniaxial tensile loading.

Regarding the CC, the debonding shape is predicted on the basis of stress- and energy-based isocontours and predictions provided by both approaches are compared. Using normal stress-based or equivalent stress-based debonding configurations lead to an almost identical initiation configuration. Normal stress-based debonding configurations can be efficiently extracted without introducing any fracture properties and therefore appear as a relevant compromise to describe the stress-based debonding configurations. The debonding angle size and location predicted by the CC lies between possible debonding configurations based on energy or stress isocontours. Depending on the interface properties, *e.g.*, the interface brittleness number γ, three different configurations can be encountered:

- Small γ: the stress-based debonding prediction provides a reasonable approximation for the possible initiation debonding shapes;
- Intermediate γ: the possible initiation debonding shapes lie in-between the stress-based and energy-based debonding predictions;
- Large γ: the energy-based debonding prediction provides a good approximation, as the solution tends to be energy driven.

Despite the difference observed between the three possibilities, similar initiation remote loadings are obtained using either the stress-based, the energy-based or the CC-based debonding configurations. The stress-based debonding configurations therefore appear to be a good compromise as it is numerically much more efficient since it can be extracted based on a single calculation without crack. However, it is not possible to accurately describe the unstable debonding phase based on stress isocontours because the stress-based and energy-based debonding configurations may differ widely for some configurations. Therefore, the final location of the angle described by the two shapes could be slightly different. However, basing the debonding configuration on stress isocontours and assessing the unstable debonding phase on energy isocontours leads to the same debonding arrest angle, but is computationally more expensive.

Blind application of the CC and comparison with experimental results showed overall agreement both in terms of required remote loading and debonding angle after propagation using previously identified interfacial shear and tensile strengths and critical opening ERR in Chapter IV. The debonding angle after initiation is slightly overestimated by the CC, which could be explained by an underestimation of the critical shear ERR that strongly influences the debonding arrest angle. The CC results obtained for a 90 deg. inter-center configuration differ from the experimental results, which could be explained by the idealized loading applied numerically or by an experimental inter-center angle slightly different from 90 degrees. It is also important to mention that the properties used are determined using a 2D simulation without considering the singularity acting at the free surface. Although the opening properties are similar in 2D and 3D, there may be differences in the shear fracture properties, see Chapter IV.

Regarding the CZM, comparisons with the results from two-fiber specimens showed that CZM are better at predicting the loading at initiation and the location of the debonding (site ① or site ②). The advantage of the CZM is that they simultaneously consider interface damage at different locations, whereas the CC considers each possibility for initiation independently. Both the CZM and the CC correctly describe the debonding angle at initiation, but the CZM overestimates the angle more than the CC, which could be explained by shear properties that are too low.

Finally, certain geometric configurations can promote or mitigate debonding initiation. For example, the inter-center distance promotes debonding initiation for small distances, whereas the influence almost vanishes for large distances, larger than $4r$. In addition, fibers aligned with respect to the loading direction yield premature debonding according to the CC.

CHAPTER VI

Towards the determination of optimal initiation 3D crack shapes

Content

VI.1 Introduction and motivation

Several possibilities exist for describing the potential crack shape required to implement the CC. In Chapter V, all possible 2D geometrical debonding shapes are compared using a 2D model. Among the configurations, stress isocontours-based and energy-based shape solutions, corresponding respectively to the shapes maximizing either stress or energy conditions, are compared to the optimal CC solution. The stress

isocontour-based shapes are numerically efficient because they can be derived from a single linear elastic calculation without releasing any nodes. In addition, they provide the optimal CC solutions for relatively small interface brittleness numbers. For larger brittleness numbers, they yield differences in the initiation loading no larger than 5% from the optimal solution even when the optimal solution corresponds to energy-based shape. There exists a transition zone though, for intermediate brittleness numbers, where neither the stress nor the energy isocontours-based shapes are able to provide the optimal CC solution. Overall, only small differences are obtained between the initiation debonding angles obtained with the different approaches.

Determining the crack path in 3D is challenging because the third dimension increases the number of possible crack shapes. To overcome this drawback, García *et al.* [Gar+16] used parametrized rectangle shape whose dimensions can be varied using two variables. Leguillon [Leg14] attempted to determine the crack shapes based on stress isocontours and proposed a comparison between 2D and 3D applications of the CC. Properties derived from both models were in the same order of magnitude. Similarly, Doitrand and Leguillon [DL18b] proposed a CC application in both 2D and 3D for scarf joint failure prediction, where the 3D approach predicted slightly more accurately the failure loading. The 3D applications of the CC were also extended to adhesive pores in Carrère *et al.* [Car+21] or anisotropic fracture in nacre-like alumina Duminy *et al.* [Dum+23] using both parametrized shapes and the stress isocontours-based shapes. However, Doitrand *et al.* [Doi+17a] were unable to apply stress isocontours-based shapes to describe potential crack shapes in woven composites when the CC solution was found to be driven by the energy condition solely. In such a configuration, idealized crack surfaces spanning the whole ply thickness and having straight crack fronts were assumed. These surfaces may not be the optimal ones compared to energy-based shapes to describe the 3D potential crack shapes when dealing with energy-driven configurations. With regard to the 3D fiber-matrix debonding configuration studied previously, stress isocontours-based shapes do not allow the identification of shear fracture properties because they are mainly subjected to mode I loading, see Chapter IV. In addition, they provide concave debonding shapes and large debonding angles that are not observed experimentally, see Chapter III. In this sense, energy-based shapes or intermediate shapes lying in between stress isocontours-based or energy-based ones could better describe the experimentally observed debonding shapes and allow for the shears fracture properties to be determined. However, their determination is computationally expensive, as an infinite number of possible debonding shapes need to be investigated.

A methodology is therefore developed in Section VI.2 to efficiently determine the optimal debonding initiation shapes provided that debonding initiates from the fiber pole located at the free surface. The CC predictions obtained with the stress isocontours- and energy-based shapes are then compared for a wide range of interface

fracture properties in Section VI.3 to assess the relevance of the stress isocontours-based or energy-based shapes in adequately describing the optimal solution. Finally, inverse identification of the fracture properties of the SFII batch samples is performed in Section VI.4 using both approaches to quantify the differences they yield.

VI.2 Debonding shape determination

The initiation of debonding is predicted by means of the CC similarly to Chapter IV and Chapter V. A 3D model is established to compare stress isocontours-based and energy-based debonding shapes. The model consists of either 1/4 or 1/8 simplification of the real geometry, using ten-node quadratic elements under the assumption of small deformation and linear elasticity. A 1/4 simplification is used for the calculation of energy-based shapes, as it allows a single initiation site to be studied. A second 1/8 simplified model is used with stress isocontours-based shapes as they provide a two-site initiation so that additional symmetry can be added to the model, see 3D model in Chapter IV. Two mesh convergence studies are performed since the CC involves both stress and energy conditions. Overall, a similar approach to that employed in Section IV.4 is used to obtain a difference of less than 2% on the stress fields and IERR compared to a converged solution. A mesh size of 20 µm is thus adopted at the fiber-matrix interface. The implementation of the CC requires the crack path to be known, with stress isocontours-based or energy-based debonding shapes being a relevant assumption for delineating the possible crack shape, but a methodology for determining energy-based debonding shapes has yet to be determined. Overall, the debonding topology can be characterized using several geometrical parameters detailed in Figure VI.1. In the sequel, one eighth of the fiber-matrix interface is used to show the debonding topology, as shown on the right-hand side of Figure VI.1.

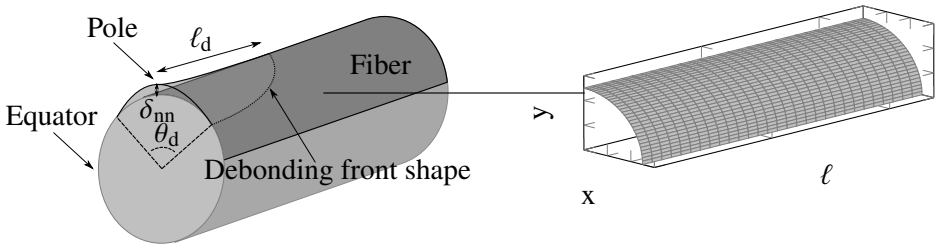

Figure VI.1 – Fiber-matrix debonding geometrical parameters. One eighth of the fiber-matrix interface is represented in the sequel in order to show the debonding front shape, a representation similar to the one on the right-hand side is used.

VI.2.1 Stress isocontours-based shapes

Unlike a 2D model where the debonding shape is characterized by a single geometrical parameter, *i.e.*, the debonding angle, using a 3D model involves a third dimension to describe the debonding path, which complicates significantly the determination of the potential debonding shape. The use of the normal stress isocontours as debonding shapes is numerically efficient since the potential crack shapes can be determined independently of all fracture properties. It is shown in Section IV.4 that, whether a normal or quadratic stress criterion is used, only small differences are observed in the equivalent stress when μ, which denotes a shear to tensile strengths ratio, is larger than 1. As a reminder, the equivalent stress is evaluated along each isocontour from the normal stress, which results in a non-constant variation of the equivalent stress, the minimum value being retained, in accordance with the stress condition proposed by Leguillon [Leg02]. A slight difference is observed between the variation of the normal stress and the equivalent stress, suggesting the insignificance of shear along the stress isocontours. The equivalent stress used in the sequel is recalled in Equation (VI.1).

$$\sigma_{\text{eq}} = \sqrt{\sigma_{\text{nn}}^2 + \frac{1}{\mu^2}(\sigma_{\text{nt}}^2 + \sigma_{\text{nz}}^2)} \tag{VI.1}$$

Figure VI.2 shows the debonding shapes for debonded surface of different areas obtained from the stress isocontours, noting that the debonding surface S corresponds to the area encompassed between the pole/free surface and the colored isocontours. As in Section IV.4, debonding is likely to initiate from the free surface due to the singularity. The debonding then evolves from a localized debonding in the vicinity of the free surface to the creation of a tunnel reaching the other free surface debonding for $S > 0.13$ mm^2.

A debonding surface increases abruptly as the tunnel is created, for relatively small surface area, as can be seen between the white and light blue isocontours in Figure VI.2. Debonding shapes are evaluated up to the stress isocontour level corresponding to $\sigma_{\text{nn}} = 0$ since no debonding initiation is possible for larger surface under compressive loading.

VI.2.2 Energy-based shapes determination

Determining energy-based debonding shapes is challenging because they cannot be extracted directly from elastic strain energy fields prior to crack initiation, but it requires computing the elastic strain energy difference between the states with and without crack. It thus requires one FE calculation for a given crack shape and there is theoretically an infinite number of 3D crack shapes to be evaluated. The determination of energy-based crack shapes involves defining the debonding shape that maximizes

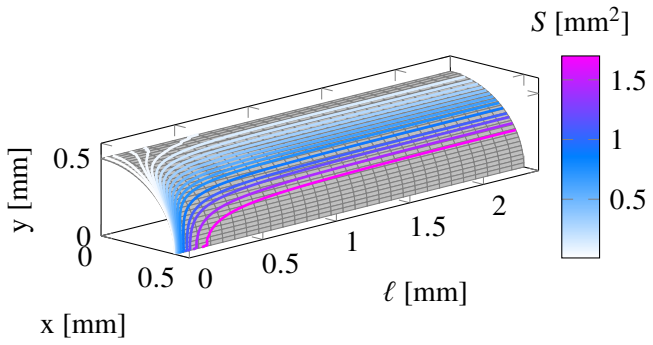

Figure VI.2 – Potential debonding shapes delimitation obtained using normal stress isocontours superimposed on one eighth of the fiber-matrix interface.

the IERR relative to the critical ERR for a given crack surface increment. However, it is not possible to test an infinite number of debonding shape configurations. Therefore, assumptions about the potential debonding shape are made in the following. On the one hand, since the stress field reaches a peak at the pole of the fiber at the free surface, it is likely that the debonding emanates from this location, as supposed in Chapter V. This process has also been experimentally observed in the present work based on front or side observations. On the other hand, it is assumed that the shape of the debonding is either concave or convex. For instance, Martyniuk *et al.* [Mar+13] observed rather concave debonding shapes.

The potential debonding shapes are therefore approximated using a power-law relationship, involving geometric parameters proposed in Figure VI.1. The location of the debonding front at the free surface is determined by the debonding angle (θ_d), while the debonding length (ℓ_d) determines the location at the pole of the fiber through the thickness. The topology of the debonding front, connecting these two points, can therefore be approximated using a power-law whose exponent n can vary from 0.6 to 4, see Equation (VI.2), where r is the fiber radius.

$$\ell(x) = \left(\ell_\mathrm{d} \left(1 - \left(\frac{x}{\sin\left(\frac{\theta_\mathrm{d}}{2}\right) r} \right)^n \right) \right)^{\frac{1}{n}} \tag{VI.2}$$

Figure VI.3 shows the influence of the three parameters on the topology of the debonding front.

Three parameters can be varied, namely θ_d, ℓ_d and n. The influence of the debonding angle is shown in Figure VI.3a, while the order and length are arbitrarily fixed.

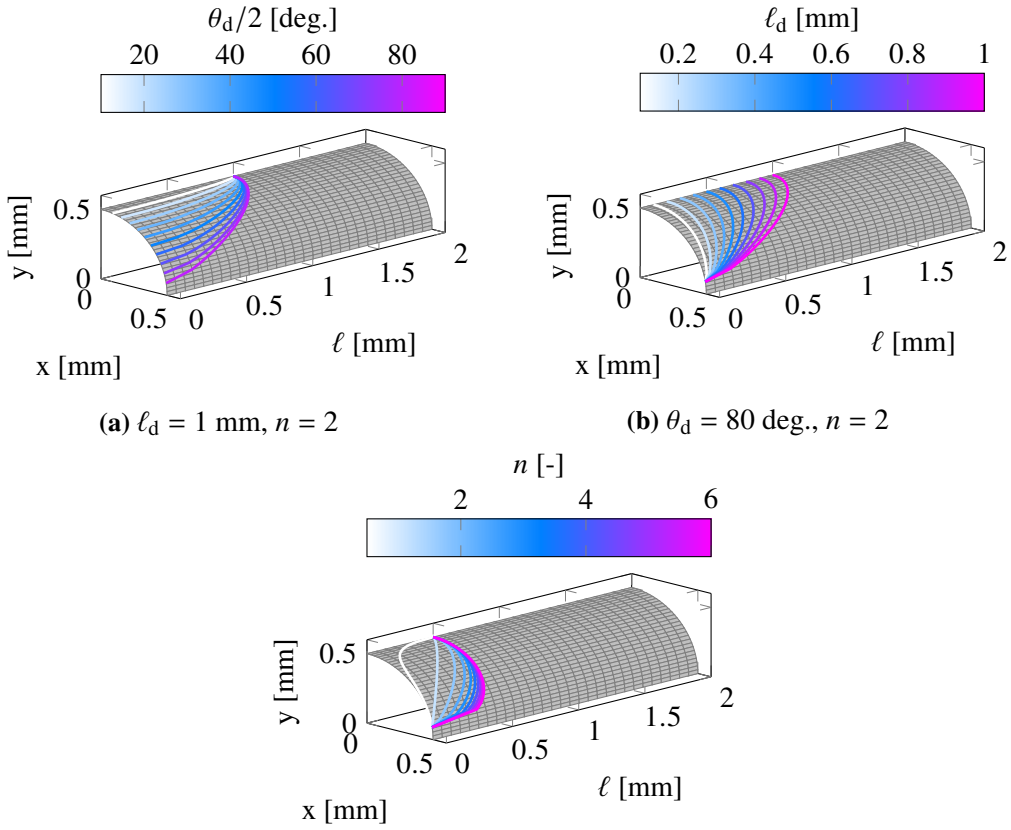

(a) $\ell_d = 1$ mm, $n = 2$ **(b)** $\theta_d = 80$ deg., $n = 2$

(c) $\ell_d = 1$ mm, $\theta_d = 80$ deg.

Figure VI.3 – Possible debonding shapes superimposed on the fiber-matrix interface obtained by varying (a) the debonding angle, (b) the debonding length and (c) the exponent of the power-law description.

The debonding half-angle $\theta_d/2$ can be varied between 10 and 80 degrees to assess a wide range of debonding shapes. The influence of debonding length is shown in Figure VI.3b and the power-law exponent in Figure VI.3c, yet again the other parameters being fixed. The debonding length varies between 0.05 and 1 mm in Figure VI.3b, in line with what was observed experimentally in Chapter III. The variation in exponent induces a transition from a concave shape, *e.g.*, for an exponent smaller than 1, similar to that provided by stress isocontours-based shapes, to a convex shape, *e.g.*, for an exponent larger than 1, tending towards a squared debonding shape for a large exponent. Using the above geometrical parameters, a wide range of debonding shapes can be evaluated to determine energy-based debonding shapes.

An iterative procedure is established to determine the energy-based debonding shapes by exploring all possible configurations for each exponent n of the power-law description. The first step consists in to identifying the couples of debonding angle and length leading to the same surface for a fixed exponent. Figure VI.4 shows the variation in debonding surface as a function of both debonding angle and length for a fixed exponent of $n = 1.5$.

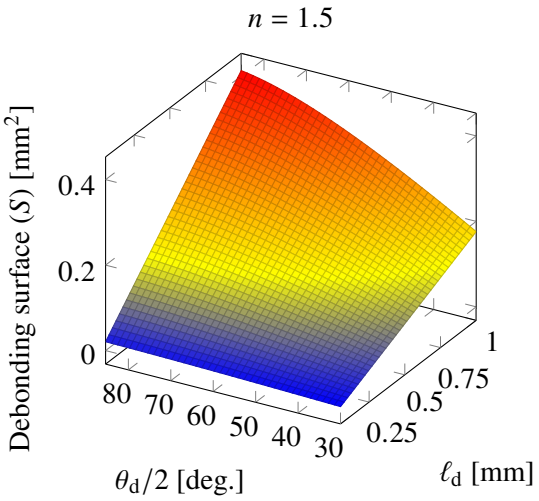

Figure VI.4 – Variation of the debonding surface as a function of the debonding angle and length for a fixed exponent $n = 1.5$.

Increasing both the debonding angle and the length leads to increasing debonding surfaces. Consequently, several couples of angle and length, leading to the same surface, can be determined using the isocontours of the solutions in Figure VI.4. These isocontours are shown in Figure VI.5, their color corresponding to that of Figure VI.4.

Several debonding surfaces can be selected by defining the magnitude of the isocontour, which is indicated on each isocontour in Figure VI.5. The minimum debonding surface considered is 0.001 mm^2, with surfaces smaller than 0.01 mm^2 not presented in the sequel for the sake of clarity. All couples of angles and lengths located on the isocontours lead to a similar surface. Ten (ℓ_d, θ_d) couples are selected for each isocontour, *i.e.*, for each debonding surface. The different debonding shapes obtained for two selected surfaces of 0.18 mm^2 and 0.3 mm^2 are shown in Figure VI.6, noting that only five couples of angles and lengths are displayed for the sake of clarity.

This illustrates the variation in debonding angle and length for a similar debonding surface. On the one hand, the debonding shapes corresponding to a surface of

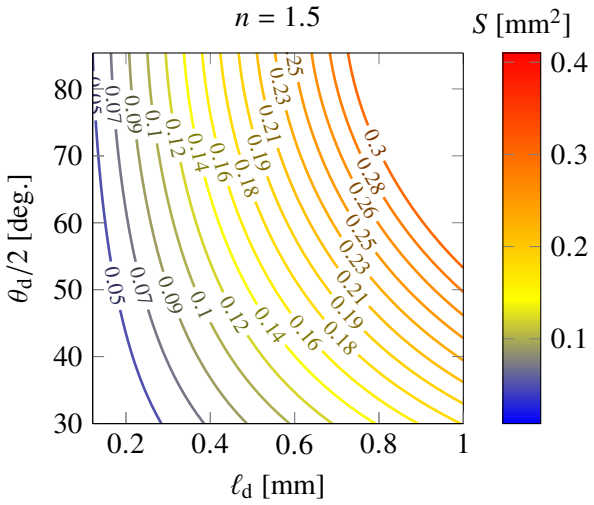

Figure VI.5 – Debonding surfaces isocontours highlighting the ranges of debonding angle and length couples leading to a similar debonding surface.

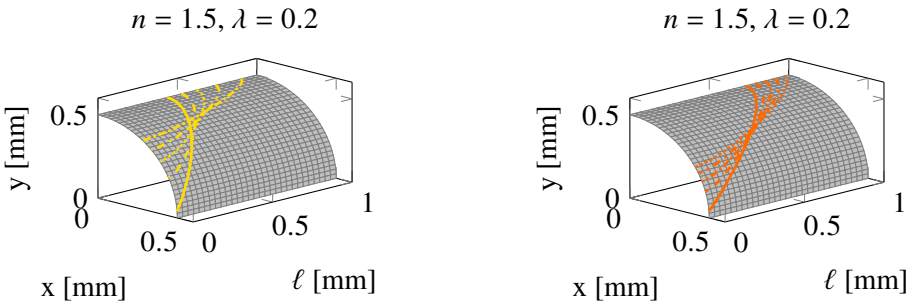

(a) $S = 0.18$ mm^2 **(b)** $S = 0.3$ mm^2

Figure VI.6 – Debonding shape with varying couples of debonding angle and length obtained for a similar debonding surface of (a) 0.18 mm^2 and (b) 0.3 mm^2.

0.18 mm^2 show large variations in length and angle (see Figure VI.6a). On the other hand, since a maximum value is set on the length range to conform to experimental observations, smaller variations are encountered for a surface of 0.3 mm^2 (see Figure VI.6b).

The IERR corresponding to each couple can be evaluated by releasing the nodes inside the area delimited by the angle, the length and the description obtained for the defined exponent. The following relationship (Equation (VI.3)) is used to evaluate

the IERR:

$$G_{\text{inc}}(S, \sigma^{\infty}) = \frac{W(0, \sigma^{\infty}) - W(S, \sigma^{\infty})}{S} \tag{VI.3}$$

It is worth noting that the debonding shape is projected onto the fiber-matrix interface so that the mesh topology matches the geometrical configuration perfectly. This method involves remeshing, as opposed to using a similar mesh for each configuration and directly releasing the nodes inside the surface. This second method, as discussed in Section IV.4, produces a non-smooth crack shape that follows the mesh topology. In addition, it requires a larger computational effort and is therefore not used here.

The average critical ERR is calculated using the Hutchinson and Suo [HS91] relationship, which depends on the mode mixity ψ. A condition is applied to the mode mixity to consider only shear when the interface undergoes compression, see Chapter IV for more details. Mode mixity is evaluated locally which gives a local value of G_c that is averaged on the anticipated crack path. In this way, the critical ERR becomes directly an average critical ERR, see Equation (VI.4), which can be compared with the IERR.

$$\overline{G_c}(S) = \frac{1}{S} \int_0^S G_{\text{IC}} \left[1 + \tan^2 \left[(1 - \lambda)\, \psi(s)\right]\right] \mathrm{d}s \tag{VI.4}$$

As a reminder, the parameter λ is related to a mode II to mode I critical ERR ratio. All the following results are evaluated for a fixed parameter $\lambda = 0.2$. This approach differs from that used previously, which consists of evaluating the mode mixity ahead of the crack front. However, a comparison of the different methods for assessing mode mixity is given in Appendix C.1 and relative differences smaller than 0.3% are found between the two methods.

The IERR to critical ERR ratio is shown in Figure VI.7a as a function of θ_d for each selected (ℓ_d, θ_d) couples and varying surfaces. The variation of IERR to critical ERR ratio is shown as a function of the debonding angle of the couple, which could alternatively be shown as a function of the corresponding debonding length.

Similar colors to those used to describe the debonding surfaces in Figure VI.4 are used to describe the IERR to critical ERR ratios obtained for each surface. Overall, each surface possesses a (ℓ_d, θ_d) couple that maximizes the energy criterion, *i.e.*, the IERR to critical ERR ratio, indicated by a round marker. Consequently, these couples lead to the geometrical configuration that is favorable from an energy point of view. The maximum of IERR to critical ERR ratio obtained from each surface is shown in Figure VI.7b, with a similar marker color, as a function of the corresponding debonding surface. It yields the maximum value of IERR that can be attained as a function of the crack surface for given exponent n and λ parameter.

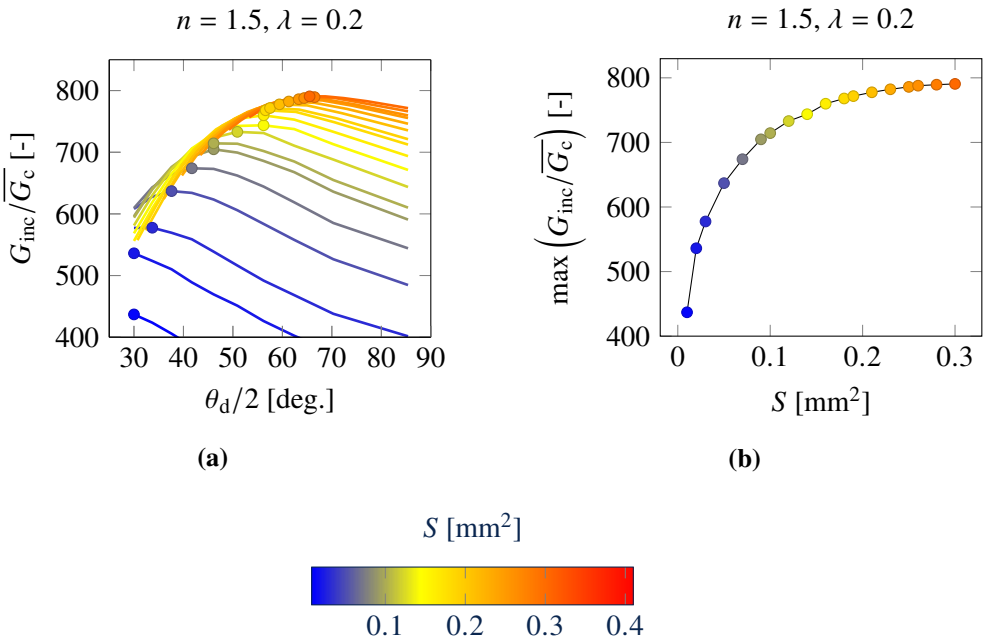

Figure VI.7 – (a) IERR to critical ERR variation obtained for different debonding surfaces and the corresponding debonding angle, that has a corresponding debonding length. The maximum is indicated by a marker for each surface. (b) Maximum IERR to critical ERR obtained for each debonding surface.

The debonding angle and length corresponding to the couples that maximize the IERR to critical ERR ratio are shown in Figure VI.8a. These couples therefore correspond to the most energetically favorable geometrical configuration. Since only the debonding initiation is studied here, the angle and length of debonding do not necessarily have to increase monotonically. Consequently, a decrease in the debonding angle is observed as the debonding surface increases, see Figure VI.8a for surfaces close to 0.4 mm^2 (ℓ_d close to 0.8 mm).

The configuration corresponding to the favorable debonding shape is superimposed onto the fiber-matrix interface in Figure VI.8b. The debonding remains localized near the free surface fiber pole for small surface areas. For a larger debonding area, there is a more pronounced increase in debonding length with respect to the angle.

The debonding shapes shown in Figure VI.8b are therefore those that maximize the energy condition. However, they are obtained for a fixed power-law exponent n. Thus, the optimum energy conditions obtained for different power-law exponents can be compared to determine the configurations which maximize the energy conditions.

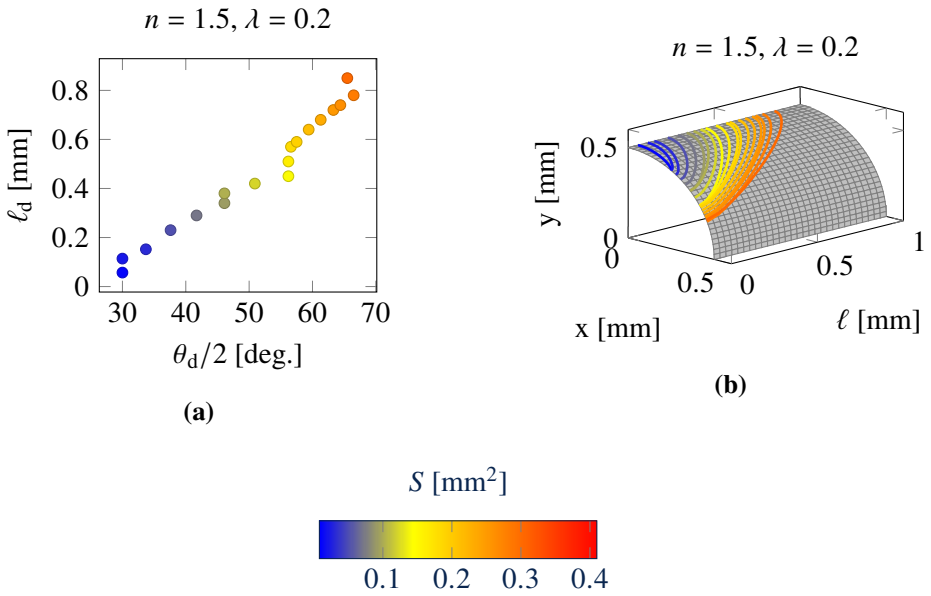

Figure VI.8 – (a) Debonding angle and length couples corresponding to the maximum in IERR to critical ERR ratio in Figure VI.7a, with the colors corresponding to the debonding surfaces. (b) Optimal potential debonding shape determined from an energy point of view with an exponent of 1.5, superimposed onto the fiber-matrix interface (gray surface).

Figure VI.9 shows the variation in the IERR to critical ERR ratio obtained for different exponents.

The exponent providing the largest energy condition for each debonding surface is therefore the one corresponding to the energy-based debonding shapes. It is worth noting that the obtained debonding shapes are also valid for a fixed λ, which may influence the optimal configuration obtained. For $\lambda = 0.2$, the interpolated shape with an exponent of 1.5 turns out to be the most favorable, over the entire range of the debonding surface, from an energy point of view. This process is repeated for a range of λ to assess the optimum exponent. An exponent of 1.5 is found to be the optimum exponent whatever the λ considered. This power-law exponent is then used to assess energy-based debonding shapes, whatever the critical ERR used.

VI.2.3 Influence of the critical ERR

The fiber-matrix interface undergoes both opening and shear modes simultaneously. Consequently, the mode I to mode II critical ERR ratio λ can influence the loading

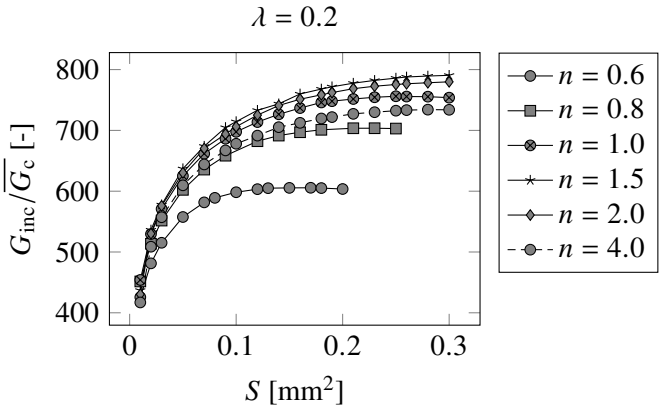

Figure VI.9 – Variation of the optimal IERR to critical ERR ratio as a function of the debonding surface for different power-law exponents, emphasizing the optimal exponent of 1.5 for the defined $\lambda = 0.2$.

required to fulfill the energy condition. Figure VI.10a shows the influence of λ on the magnitude of the IERR to critical ERR ratio.

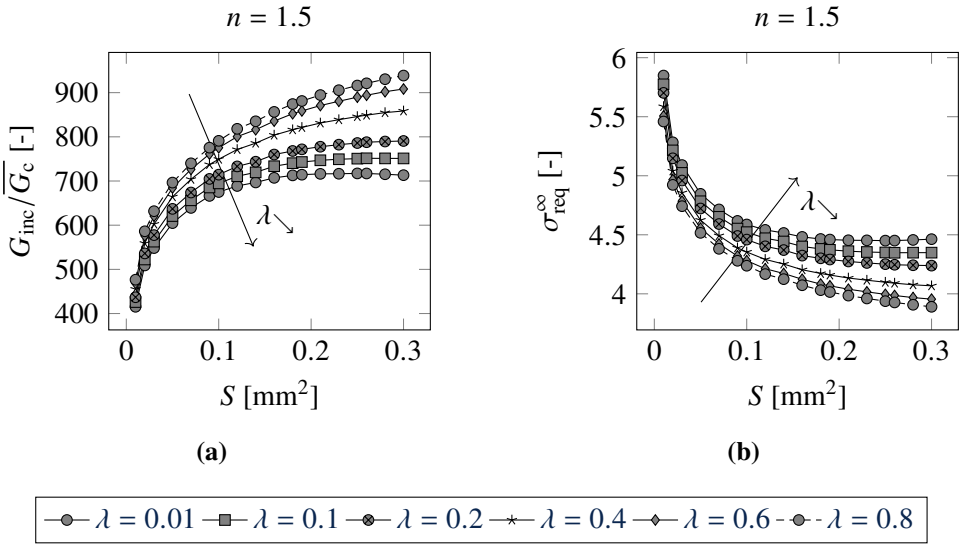

Figure VI.10 – Influence of λ on (a) the IERR to critical ERR ratio and (b) the loading required to fulfill the energy criterion for a fixed exponent of 1.5.

The opening critical ERR G_{IC} is fixed while the G_{IIC} increases, leading to a de-

crease in λ. The critical ERR in mode II appears to influence the profile of the energy criterion over the full range of the debonding surface, suggesting that small variations in mode mixity are encountered on the different debonding shapes. Overall, increasing G_{IIC} leads to a decrease in the level of the energy criterion. Consequently, a larger loading is required to fulfill the energy criterion as G_{IIC} increases, see Figure VI.10b. However, the difference in required loading induced by λ is small, less than 0.5 MPa for a fixed debonding surface. Consequently, the shear component appears to be negligible on the energy-based shapes determined.

Although shear has little influence on the loading required to fulfill the energy condition, it can influence the (ℓ_{d}, θ_{d}) couples that describe the energy-based shapes. Figure VI.11a shows the (ℓ_{d}, θ_{d}) couples corresponding to energy-based shapes for two extreme λ.

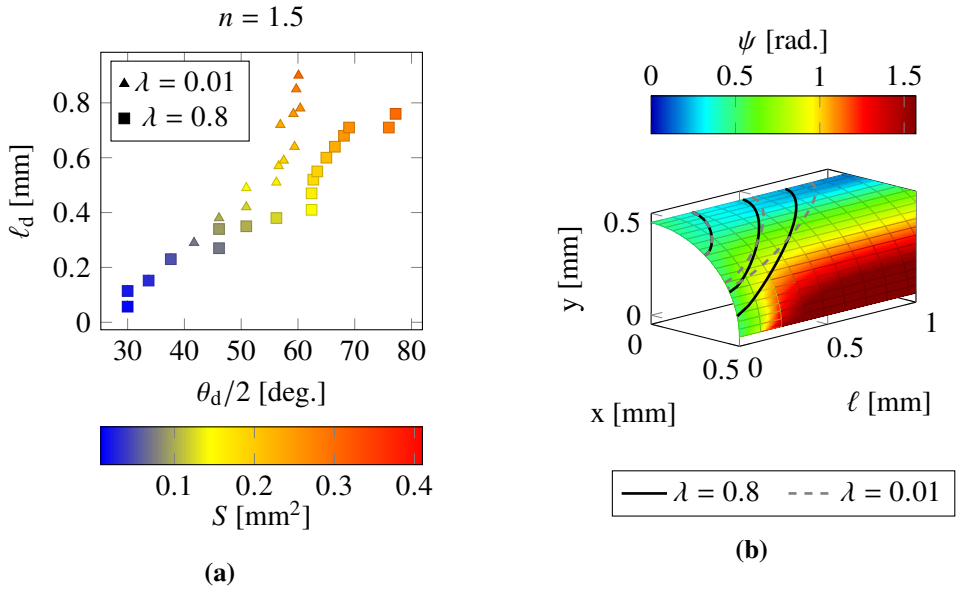

Figure VI.11 – (a) Debonding geometrical parameters (ℓ_{d}, θ_{d}) corresponding to the energy-based debonding shapes for two extremes values of λ. (b) Energy-based shapes obtained for three surfaces and three λ values highlighting the influence of the mode mixity whose variation is shown at the fiber-matrix interface.

For a relatively small debonding area, λ has little influence, since the energy-based shape is identical. However, for a larger debonding surface, smaller angles result from smaller λ. This difference can be explained by mode II loading, which acts primarily in the vicinity of the fiber equator, *i.e.*, at large debonding angles. Consequently, the increase in the critical ERR in mode II makes debonding initiation for a large

angle less favorable than for a small G_{IIC}. The optimum debonding shapes obtained for three different debonding surfaces and the two extreme values of λ are shown in Figure VI.11b, superimposed on the variation in mode mixity at the fiber-matrix interface. It is worth recalling that the zone with a mode mixity of $\pi/2$ corresponds to the interface area experiencing compression. Overall, mode mixity is similar to that observed with a front 2D modeling (see Section IV.2) for a sufficiently large distance from the free surface. As with the stress and energy fields, mode mixity is affected at the free surface due to the elastic mismatch between fiber and matrix. Additionally, as for the geometrical parameter couples corresponding to the energy-based shapes, similar shapes are observed for small surfaces since they are mainly undergoing mode I. However, as the debonding surface increases, the debonding angle also increases, tending towards a zone where the shear level is larger. Consequently, for a similar debonding surface, a smaller angle and larger length are encountered for an increase in G_{IIC} as initiation at the fiber equator becomes less favorable.

VI.3 Comparison of the CC predictions

Once the potential initiation debonding shapes based on both stress isocontours or energy are determined, the CC can be implemented. In order to provide the initiation loading and the debonding surface, the CC combines two conditions, recalled in Equation (VI.5):

$$\begin{cases} \sigma_{\mathrm{eq}}\left(\vec{x}, \sigma^{\infty}\right) \geq \sigma_{\mathrm{c}}, \forall \vec{x} \in \Gamma, \\ G_{\mathrm{inc}}(S, \sigma^{\infty}) \geq \overline{G_{\mathrm{c}}}(S). \end{cases} \tag{VI.5}$$

The equivalent stress σ_{eq} has to exceed the tensile strength σ_{c} at any location on the debonding area Γ before initiation. Likewise, the minimum σ_{eq} has to exceed σ_{c} over the debonding front as the stress decreases monotonically. The CC solution actually depends on the interface brittleness number γ, see Equation (II.31), which can induce initiation driven by either the stress or energy condition.

The loading required to fulfill both criteria is compared in Figure VI.12 on the basis of the stress isocontours-based and energy-based debonding shapes, red and blue lines, respectively. The minimum of the two criteria provides the initiation loading and corresponding debonding surface, which are indicated by the round marker for the stress isocontours-based and energy-based debonding shapes. The CC conditions are evaluated for two brittleness numbers regarding the usual fracture properties of the fiber-matrix interface, see Chapter IV.

For both stress isocontours-based and energy-based debonding shapes, the stress condition increases monotonically since the equivalent stress decreases with the debonding surfaces. Regarding the energy condition, that obtained with the energy-based

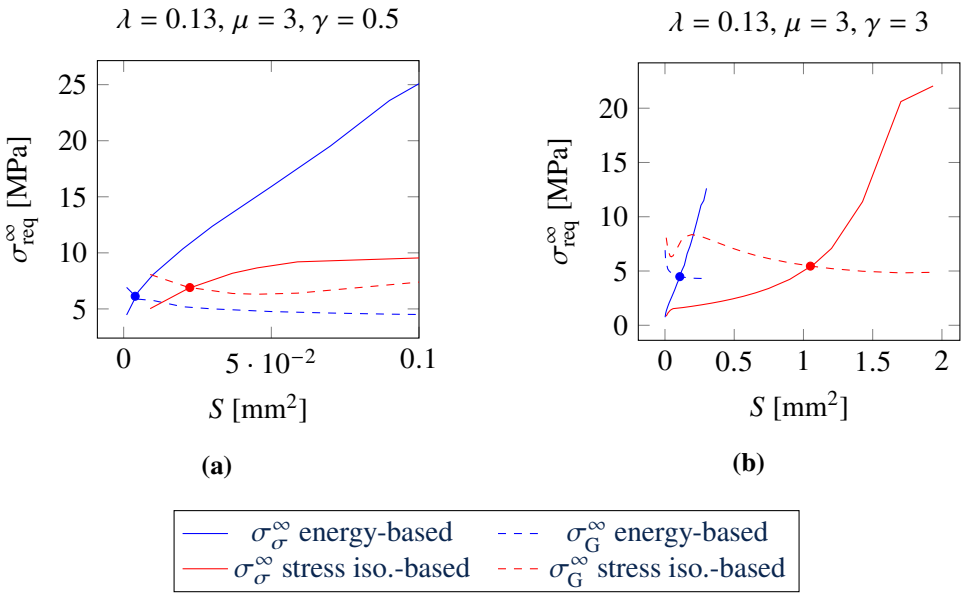

Figure VI.12 – Required loading to fulfill both the stress (solid lines) and energy (dashed lines) criteria obtained using the stress isocontours-based and energy-based shapes. Two interface brittleness numbers are investigated, (a) a relatively small one $\gamma = 0.5$ and (b) a relatively large one $\gamma = 3$.

debonding shapes does not present a minimum, unlike that obtained using the stress isocontours-based shapes which provide two minima. Consequently, no stable debonding can be obtained using the energy-based debonding shapes since $G > G_c$ at initiation , see Chapter IV.

Overall, the stress isocontours-based shapes result in the most favorable solution in terms of stress conditions, whatever the debonding surface considered, consistently with their definition. On the contrary, the energy condition provided by energy-based shapes is smaller than that of stress isocontours-based shapes, whatever the debonding surface. Since energy-based shapes are derived from the debonding surfaces shape that maximize the IERR to critical ERR ratio, it is likely that these shapes minimize the loading required to fulfill the energy criterion.

For a relatively small brittleness number (Figure VI.12a), the energy-based shapes provide the most favorable configuration compared to that provided by the stress isocontours-based shapes. This differs from what is obtained in 2D, where the stress isocontours-based shapes are the optimal debonding shapes for a small brittleness numbers, *i.e.*, smaller than 1. In 3D, the energy condition, which is significantly larger for the stress isocontours-based shapes, appears to control debonding initiation

even for a small brittleness number. The stress isocontours-based and energy-based shapes provide debonding initiation surfaces with relative difference of 140%.

For a relatively large brittleness number (Figure VI.12b), the energy-based debonding shapes also lead to the most favorable configuration for predicting debonding initiation. The stress isocontours-based shapes require a larger loading to fulfill the energy condition. A similar result was obtained in 2D for large brittleness numbers. The debonding initiation surface (S_c) obtained for the stress isocontours-based and energy-based debonding shapes and the two brittleness numbers are compared in Figure VI.13.

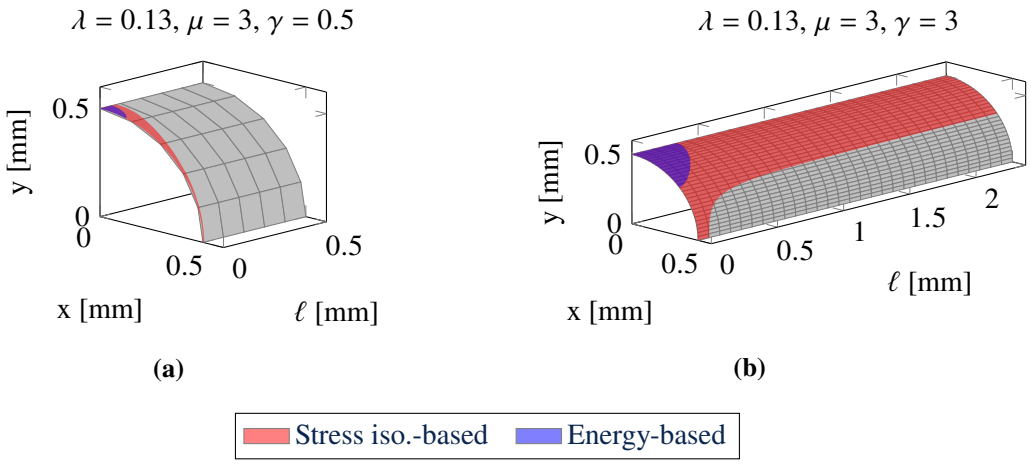

Figure VI.13 – Comparison of the debonding initiation surfaces (S_c) obtained in Figure VI.12 with the stress isocontours-based and energy-based debonding shapes and two interface brittleness numbers: (a) $\gamma = 0.5$ and (b) $\gamma = 3$.

For a small brittleness number, the stress isocontours-based surface remains close to the free surface with a debonding angle spanning over the whole fiber circumference. The energy-based surface has a smaller angle and length, thus a smaller surface than stress isocontours-based surface. The difference between the two debonding initiation surfaces becomes more pronounced as the brittleness number increases, as shown in Figure VI.13b. The stress isocontours-based surface provides a tunnel between the two free surface debondings. In contrast, the energy-based surface shape is similar to that obtained with a small brittleness number, with increased surface area.

Similarly, the debonding initiation surfaces obtained using stress isocontours-based and energy-based shapes are compared for a range of interface brittleness numbers, see Figure VI.14a. The brittleness number range is selected to ensure that the CC solution is provided by the intersection of both stress and energy conditions.

For relatively small interface brittleness number, smaller than 2, the initiation sur-

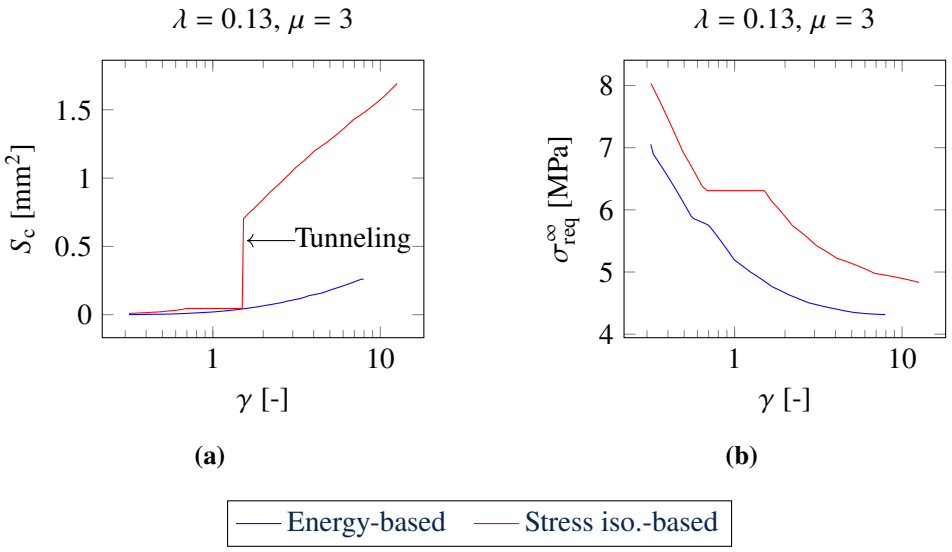

Figure VI.14 – (a) Debonding initiation surfaces and (b) corresponding loading predicted by the stress isocontours-based and energy-based shapes.

faces predicted by the two approaches are in the same order of magnitude. However, for large brittleness number, the initiation surfaces predicted by the stress isocontours approach surpass those provided by the energy-based debonding shapes. This phenomenon is caused by the tunneling effect of the stress isocontours-based shapes, which induces a sharp increase in the debonding surface for solutions triggered by the energy condition. The remote stress required to fulfill the CC is assessed in Figure VI.14b, for the similar range of brittleness number as Figure VI.14a, so that the relevancy of the stress isocontours approach in predicting the optimal CC solution can be evaluated. The stress isocontours-based shapes yield larger initiation remote stress than the energy-based ones whatever the brittleness number over the range 0.3 - 8. It is worth mentioning that in addition to the energy-based debonding shapes, the crack shape that minimizes the CC solution from the set of shapes explored with other exponents is also investigated. Regardless of the brittleness number, the energy-based shape still provides the optimum CC solution. Stress isocontours-based shapes solution exhibits a plateau for intermediate brittleness numbers explained by a CC solution driven solely by the energy condition maximum. Basing the debonding shape on stress isocontours significantly reduces computational costs, since they can be derived from a single calculation without crack. The difference induced by using stress isocontours-based surfaces compared to the optimal CC solution, *i.e.*, corresponding to that obtained with energy-based shapes, is evaluated for the same range of brittle-

ness numbers, see Figure VI.15.

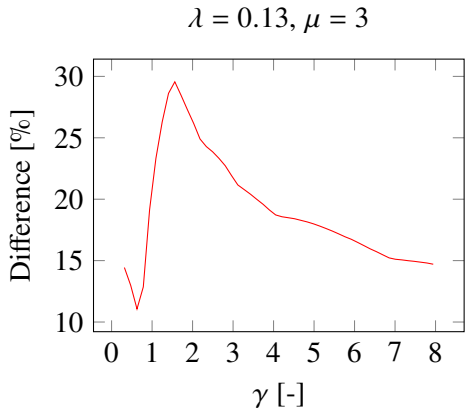

Figure VI.15 – Difference on the debonding initiation loading provided by the stress isocontours-based shapes compared to the energy-based ones.

For a relatively small interface brittleness numbers ($\gamma < 1$), limited difference of less than 15% is made by the stress isocontours-based shapes. For intermediate brittleness numbers ($1 < \gamma < 6$), the difference reaches a peak to 30% caused by energy driven solutions. The difference decreases to 15% for larger brittleness numbers ($\gamma > 6$).

Stress isocontours-based shapes therefore appear to be a relevant compromise for predicting debonding initiation remote loading using the CC for either small ($\gamma < 1$) or large brittleness numbers ($\gamma > 6$). However, for intermediate brittleness numbers, ranging from 1 to 6, difference brought by the stress isocontours-based shapes becomes more pronounced. Different results are obtained in 2D in Chapter V where the determination of possible debonding initiation shapes from stress isocontours represents a more relevant solution. Indeed, for small interface brittleness numbers, stress isocontours-based debonding shapes yield the optimal CC solution. For intermediate and large brittleness numbers, it yields differences in initiation loading of no more than 5% compared with the optimum initiation shape, difference that is never achieved with the 3D model. Stress isocontours-based shapes are able to provide debonding initiation areas similar to the optimum solution for brittleness numbers of less than 2. For larger brittleness numbers, the tunneling effect induces a larger debonding area spanning over the entire fiber pole.

The interface fracture properties identified previously in Chapter IV range from 7.2 ± 5 MPa for σ_c and from 6 ± 5 J/m^2 for G_{IC}, resulting in brittleness numbers varying from 0.4 to 11.2. There is a range of brittleness numbers between 0.4 and

1, where stress isocontours-based shapes become relevant, predicting both initiation remote stress and the corresponding area with little difference. However, the difference brought by the stress isocontours-based shapes compared to the optimal solution becomes more pronounced for the remaining range, between 1 and 8. Nevertheless, the inverse identification of the interface fracture properties is still carried out in the sequel in order to evaluate the difference induced on the identified properties.

VI.4 Inverse identification of the fiber-matrix interface fracture properties

The inverse identification of the fracture properties of the fiber-matrix interface is conducted using experimental results from samples from batch SFII. The SFII samples enable a dual observation of the front and side debonding mechanisms. In the sequel, the optimal debonding shapes correspond to the energy-based debonding shapes, following the findings in Section VI.3.

VI.4.1 Influence of the shear fracture properties

It is observed in Section IV.4 that shear fracture properties plays only a negligible role in the debonding process when the shape of the debonding is based on the normal stress isocontours. In particular, the variation of the critical tensile to shear strength ratio induces a slight difference in the equivalent stress with respect to a normal stress criterion. Similarly, Figure VI.16a shows the influence of the tensile to shear strength ratio (μ) and of the brittleness number (γ) on the loading required to fulfill the CC using the optimal debonding shapes determined in previous sections.

The loadings required to fulfill the CC appear to be slightly sensitive to the μ ratio, especially for $\mu < 2$. Consequently, determining an appropriate μ ratio, and hence shear strength, is challenging using only remote initiation loading. The initiation surfaces are slightly more influenced by the shear to tensile strengths ratio, since the surface decreases with increasing μ. This would enable an appropriate μ ratio to be determined based on the geometric parameters of the debonding observed at initiation, and consequently, restrict the range of tensile and shear strengths identified.

The influence of critical ERR in modes I and II on the initiation remote stress and debonding surface is evaluated in the sequel for different interface brittleness number. Figure VI.17 shows the influence of λ on the initiation remote loading and corresponding surface provided by the CC relying on the optimal initiation debonding shapes.

The CC solutions appear to be insensitive to the critical ERR in mode II since, whatever the λ magnitude, similar initiation remote loadings are obtained, see Fig-

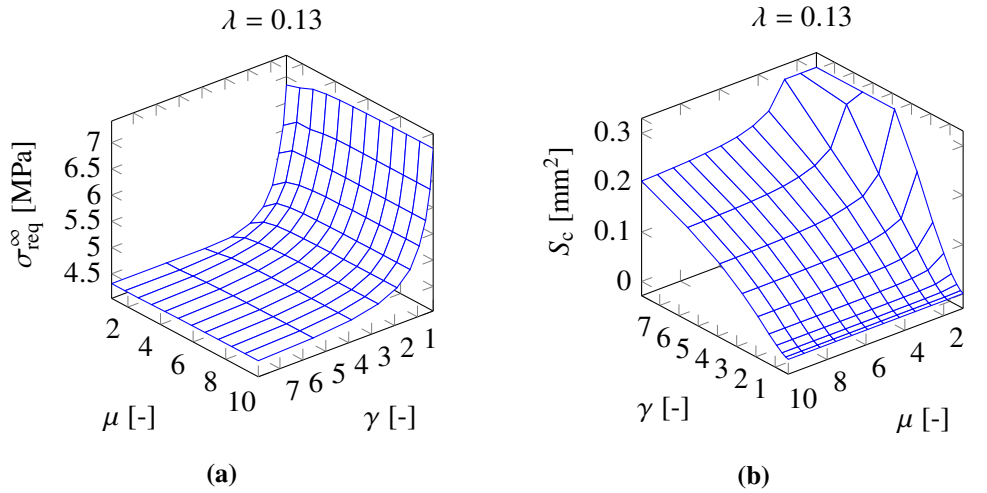

Figure VI.16 – (a) Remote stress to fulfill the CC and (b) corresponding initiation surface as a function of μ and γ based on the optimal debonding shapes.

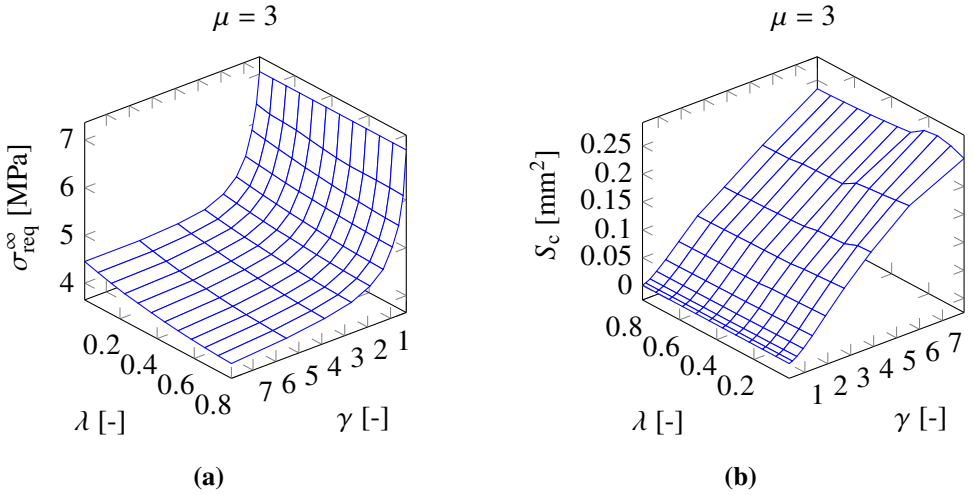

Figure VI.17 – (a) Remote stress to fulfill the CC and (b) corresponding initiation surface as a function of λ and γ.

ure VI.17a. This suggests that in average, the optimal initiation crack surface is mainly loaded under opening mode Consequently, no shear critical ERR can be identified using debonding initiation since the CC solution is independent of this parameter. The influence on the initiation debonding surface is also investigated in Figure VI.17b,

which also shows that λ has a limited influence on the initiation debonding surface.

Consequently, with this specific loading condition (tensile test on a transverse single-fiber), the inverse identification of the critical ERR in mode II does not seem feasible whereas the shear strengths can still be identified based on the debonding shapes observed experimentally. An attempt to identify the opening fracture properties and the μ ratio is proposed in the following. The inverse identification approach is divided into two steps:

1. Identification of the G_{IC} and σ_{c} couples for different μ ratio leading to a debonding initiation remote stress similar to that found experimentally;

2. Restriction of the fracture properties couples and μ ratios using the debonding geometrical parameters such as, *e.g.*, the debonding angle, length and opening.

VI.4.2 Inverse identification based on the initiation remote loading

As a reminder, the identification is carried out on three samples from batch SFII. The initiation remote stresses obtained for the three samples are summarized in Table VI.1. The three geometrical parameters describing the debonding geometry observed just after initiation are also recalled.

	SFII-2	SFII-3	SFII-4
σ^{∞} [MPa]	7.25 ± 0.04	8.03 ± 0.04	10.04 ± 0.04
$\theta_{\mathrm{d}}/2$ [deg.]	29	37	40
ℓ_{d} [mm]	0.13	0.10	0.22
δ_{nn} [µm]	1.5 ± 1.0	2.1 ± 0.8	2.1 ± 1.0

Table VI.1 – Fiber-matrix debonding geometrical parameters obtained experimentally from the SFII samples at initiation, see Chapter III for further details.

The inverse identification is performed based on the sample SFII-2 in this chapter. The results obtained for both samples SFII-3 and SFII-4 are provided in Appendix C.2. The couples of tensile strength and critical ERR in mode I leading to equivalent remote stress to the experimental one are shown as a function of the corresponding brittleness numbers and μ ratios in Figure VI.18. The identification is made on the basis of the optimal initiation debonding shapes, corresponding to the blue markers. In complement, the properties identified from the stress-isocontours based debonding shapes are also shown with the red markers.

Slightly different tensile strengths are identified using the stress isocontours-based and energy-based shapes, with an increasing difference for intermediate brittleness number, consistently with what observed in Figure VI.15. The relative difference

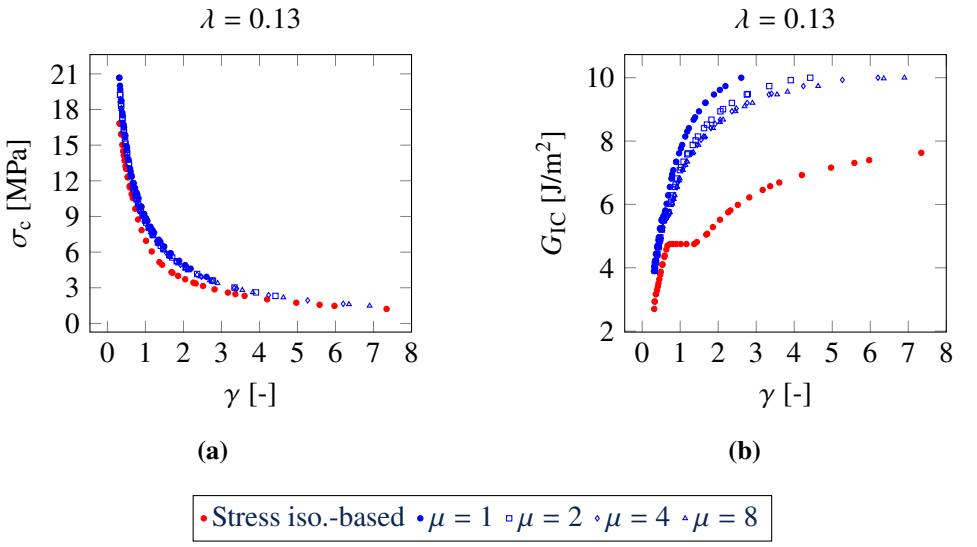

Figure VI.18 – Couples of (a) σ_c and (b) G_{IC} leading to a debonding initiation remote loading equal to the experimental one for the sample SFII-2 (7.25 MPa).

reaches 7% for $\gamma = 1.5$. Since the optimal debonding shapes induces more favorable stress and energy conditions, larger fracture properties are required to match the targeted initiation remote stress loading compared to the stress isocontours-based shapes. Given that larger differences occur on the energy criterion for intermediate and large brittleness numbers, major differences in the critical ERR identified are likely to occur, see Figure VI.18b. The debonding initiation obtained with the stress isocontours-based shapes yield a plateau where the CC solution is determined solely by the energy condition since the stress condition is already fulfilled over the entire surface range. Constant critical ERR are therefore required to match the experimental remote loading, resulting in increasing differences from optimal debonding shapes, up to a relative difference of 15%. Overall, as previously indicated, the influence of the μ ratio is negligible since the ranges of fracture properties identified remain somehow similar whatever the μ level. A slight increase in the minimum G_{IC} and decrease in the maximum σ_c identified are observed with increasing μ ratio. Similar results are also found for SFII-3 and SFII-4.

Overall, stress isocontours-based shapes appear to be relevant for determining the tensile strengths regardless of the brittleness number (Figure VI.18a). However, larger differences emanate from the critical ERR identified using the stress isocontours-based shapes, especially for brittleness numbers larger than 1 (Figure VI.18b). This difference is due to the energy condition, which differs significantly between the stress isocontours-based and energy-based shapes for intermediate and large brittle-

ness numbers.

The ranges of properties identified for the three samples are summarized in Figure VI.19 for $\mu = 1$. Slight variations are obtained over the range of properties identified by varying μ (see Figure VI.18).

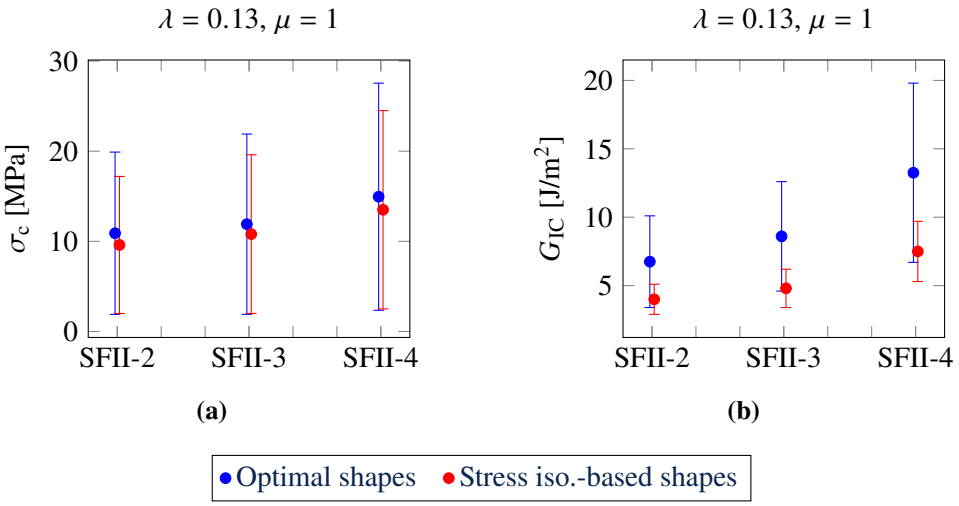

Figure VI.19 – Comparison of the interface fracture properties identified based on the remote loading at initiation.

The marker corresponds to the average value of the properties identified, while the bar corresponds to the extreme values (from Figure VI.18 and Appendix C.2). Similar properties are identified for the different samples, as the remote initiation loadings differ slightly. Increasing experimental loading at initiation result in increasing both the σ_c and G_{IC}.

VI.4.3 Properties restriction based on the debonding geometry

Additional restrictions can be applied to the range of properties identified on the basis of the geometrical parameters obtained experimentally, whose values are given in Table VI.1. The initiation surface provided by the CC can be either smaller than or equal to the arrest surface observed experimentally, as unstable debonding propagation can occur. The initiation surface reverts to the arrest surface when initiation is driven by the maximum of $G_{inc}/\overline{G_c}$. However, the optimal debonding shapes yield $G_{inc}/\overline{G_c}$ that increases monotonically so that no stable debonding can occur after initiation. Similarly, when the CC solution is given by the intersection of both stress and energy conditions, further debonding propagation takes place after initiation. Therefore, without the use of a high-speed camera, the experimentally observed debonding

surface after initiation actually corresponds to the arrest surface that has potentially already propagated. The geometrical parameters shown in Table VI.1 therefore serve as an upper limit to those obtained using the CC and therefore allow the identified couples of fracture properties and μ ratios to be restricted. It is worth recalling that, except for the debonding opening, the determination of the debonding angle and length is limited by the pixel size. The results derived from these two quantities may therefore be underestimated as sub-pixel phenomena may have occurred. Nevertheless, the comparison is made on the basis of the results presented in Chapter III because no methods have yet been established for measuring these phenomena. Consequently, the maximum uncertainties in the calculation of the debonding opening is considered as an upper bound. The debonding angle and length are considered an upper bound in this configuration.

The geometrical parameters corresponding to the identified properties obtained from the stress isocontours-based and energy-based debonding shapes are compared in Figure VI.20, for sample SFII-2.

As the experimental results are considered an upper bound, the geometrical parameters corresponding to the properties identified must remain below this limit, *i.e.*, within the hatched area. The increase in the brittleness number (γ) leads to an increase in the debonding surface area and associated geometric parameters up to a certain value where they exceed the experimental results. The restriction obtained for the debonding angle limits the γ to 0.6, 0.86 for the debonding length and 1.85 for the debonding opening. As a result, the optimal debonding shapes correctly predict the various geometric parameters for a brittleness number of between 0.3 and 0.6. Similar restrictions are applied for samples SFII-3 and SFII-4. This allows the upper and lower limits of the acceptable brittleness number range for each sample to be determined, and therefore the couples of tensile strength and critical ERR identified previously to be restricted.

The μ ratio has a significant influence on the geometry of the identified debonding, particularly for large brittleness numbers, and resulting large surfaces. For a given γ, an increase in μ results in a decrease in debonding surfaces, as the influence of shear makes debonding initiation less favorable for large surfaces. Nevertheless, the values identified for the brittleness number do not enable a μ to be determined since the results slightly vary in this range, in accordance with what is observed in Figure VI.17b. Proper identification of μ would require a larger debonding surface after initiation.

Stress isocontours-based shapes overestimate the debonding angle in all configurations since their shape directly provides a complete debonding. They provide a correct estimate of the debonding length, only before tunneling where the length increases considerably. The debonding opening is correctly estimated by the stress isocontours-based shapes over the entire range of the brittleness number while the debonding length limits the range to 0.56. The restricted properties are summarized

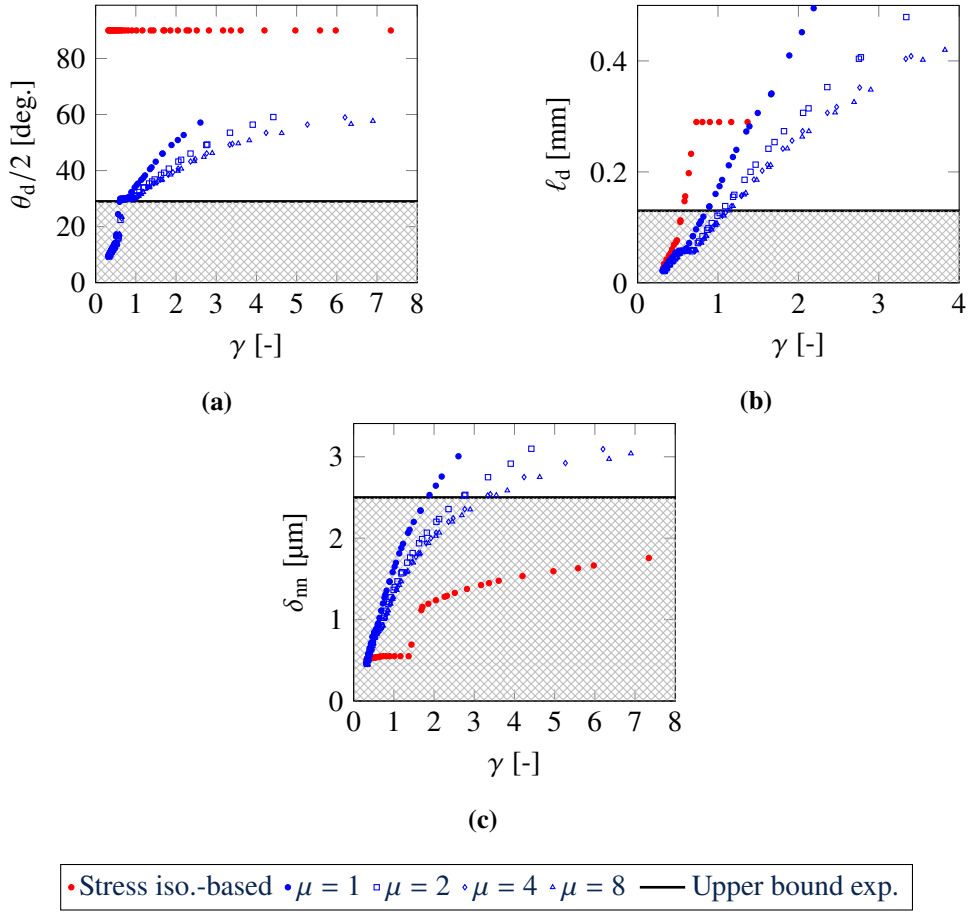

Figure VI.20 – (a) θ_d and (b) ℓ_d, and δ_{nn} (c) obtained for the different brittleness numbers and the suitable configurations for the inverse identification (Figure VI.18). The experimental validity range is indicated by the hatched zone.

in Table VI.2.

The debonding angle is not taken into account for restrictions applied to properties identified with the stress isocontours-based shapes. The fracture properties identified are in line with those identified for the SFI batch samples, although the fiber and matrix are different (see Chapter IV).

Among the range of identified properties, one couple per sample is selected and the associated geometrical parameters are compared with the side view of the debonding. The couple of tensile strength and critical ERR maximizing the brittleness number is selected. The debonding side view is shown in Figure VI.21a and Figure VI.21c

	SFII-2	
σ^∞ [MPa]	7.25 ± 0.04	
	Stress iso.	Energy iso.
λ	0.3 - 0.56	0.3 - 0.60
σ_c [MPa]	11.9 - 16.8	13.0 - 20.7
G_{IC} [J/m^2]	2.7 - 4.2	3.9 - 5.8
	SFII-3	
σ^∞	8.03 ± 0.04	
	Stress iso.	Energy iso.
λ	0.3 - 0.5	0.3 - 0.74
σ_c [MPa]	13.9 - 18.6	12.4 - 22.9
G_{IC} [J/m^2]	3.3 - 4.9	4.8 - 8.2
	SFII-4	
σ^∞	10.04	
	Stress iso.	Energy iso.
λ	0.3 - 0.65	0.3 - 1.16
σ_c [MPa]	14.8 - 23.3	11.1 - 29.8
G_{IC} [J/m^2]	5.2 - 8.9	7.6 - 15.8

Table VI.2 – Restricted interface fracture properties identified based on the geometrical parameters, for sample SFII-2, SFII-3 and SFII-4 and a μ ratio of 1.

just after initiation for sample SFII-2 and SFII-4, respectively. SFII-3 results are not presented here because the location of the debonded zone is not perfectly delineated.

The shape of the debonding obtained numerically is superimposed to assess the accuracy of the identification for sample SFII-2 in Figure VI.21b. On the one hand, energy-based shapes accurately describe the debonding angle and length at initiation, with the experimental observation encompassing the optimal debonding initiation shape. On the other hand, as pointed out previously, stress isocontours-based shapes significantly overestimate the debonding angle while accurately predicting the debonding length. Similarly for sample SFII-4 in Figure VI.21d, shape geometry provided by the optimal debonding shape is located within the side observation of the debonding. It is worth remembering that it is also possible to obtain smaller surfaces from small brittleness numbers. In particular, the debonding surface predicted by the CC corresponds to the initiation surface that is likely to propagate after initiation up to the arrest surface. The shape provided by the stress isocontours does not capture the experimentally observed debonding zone, overestimating the debonding angle. This corroborates the fact that shapes based on stress isocontours are not suitable for the configuration studied, while not providing the optimum CC solution in terms of

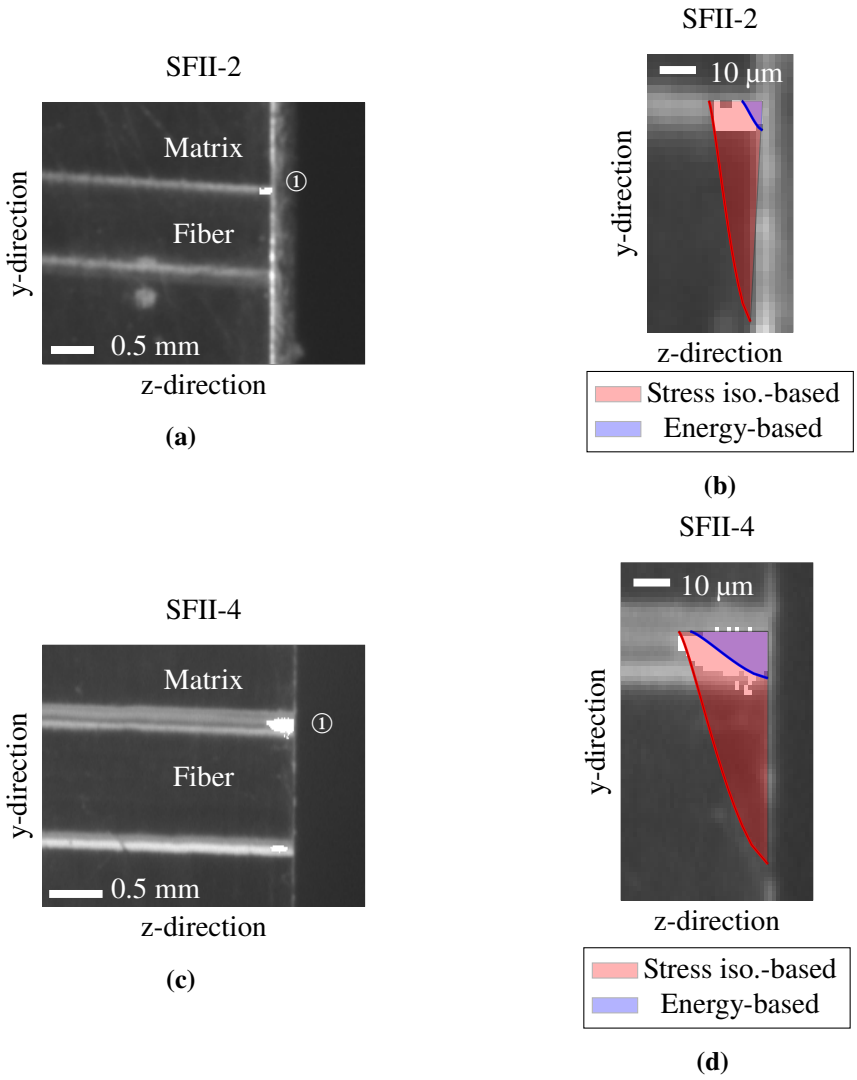

Figure VI.21 – (a) Side view of the debonding just after debonding initiation. The debonded area is highlighted using a threshold and the white pixels. (b) Debonding shapes obtained with the CC for both stress isocontours-based and energy-based shapes, corresponding to the red and blue shaded areas, superimposed on the side view.

remote loading and debonding shape.

VI.5 Conclusion

The stress isocontours-based and energy-based debonding shapes are used to assess the fiber-matrix debonding initiation shape using the CC. Energy-based shapes are difficult to determine because they require all possible shape configurations to be compared. On the basis of experimental observation, assumptions are made about the initiation location and the shape description. A power-law with an exponent of 1.5 is found to be optimal regardless of the critical ERR in mode II. Overall, the critical ERR in mode II has a negligible influence on the magnitude of the IERR to critical ERR ratio. The predicted debonding shape results in a smaller angle with larger length with increasing critical ERR in mode II, due to increased mode mixity in the vicinity of the fiber equator.

Energy-based shapes provide the optimal solution regardless of the brittleness number. The stress isocontours-based shapes overestimate the optimal CC solution by up to 15% for either small ($\gamma < 1$) or large ($\gamma > 6$) brittleness numbers. Larger differences, up to 30%, are encountered for intermediate brittleness numbers ($1 < \gamma < 6$). The energy condition causes this difference, the latter being less favorable using stress isocontours-based shapes, especially for intermediate brittleness numbers, where the energy condition triggers the CC solution. Similarly, similar surface areas are predicted by both approaches for small brittleness numbers, in contrast to large numbers where the tunnel effect significantly increases the difference.

Inverse identification is carried out on the basis of the stress isocontours-based and energy-based debonding shapes. Only the opening fracture properties are identified, since shear fracture properties slightly influence the CC solution for small surface such as the ones observed experimentally. The two approaches give similar fracture properties in terms of tensile strength, while the difference becomes more pronounced in terms of critical ERR for intermediate brittleness numbers. Stress isocontours-based shapes become relevant for either small and large brittleness numbers. Tensile strengths ranging from 11 to 30 MPa and a mode I critical ERR of 4 to 16 J/m^2 are identified with the optimum debonding shapes for the three samples.

Optimal debonding shapes provide a debonding topology consistent with the experimental observations, predicting the length, angle and the opening of the debonding compatible with those measured experimentally. Stress isocontours-based shapes are unable to provide an accurate shape with respect to experimental observation. However, the debonding surface predicted by the CC corresponds to the initiation surface that is likely to propagate after initiation to the arrest surface. Further study of debonding propagation would be required, which could be approximated using an algorithm that iteratively varies the debonding front to obtain a constant stress intensify factor at the front for different increasing debonding surfaces.

CHAPTER VIII

Conclusions and perspectives

Overall, experimental techniques were developed to characterize the debonding process on a microcomposite composed of a single glass fiber and an epoxy matrix. Monitoring of the debonding process has enabled coupled experimental-numerical approaches to be established and interface fracture properties to be identified. This final chapter describes the limitations overcome by this work and the conclusions drawn from it as well as perspectives.

- **Chapter III: Experimental characterization of fiber-matrix debonding**

  The literature review in Chapter II identified a number of problems inherent in current fiber-matrix interface experimental characterization techniques. These are summarized below:

  - Most of the characterization techniques focus on shear characterization of the fracture properties;
  - Lack of standardization of the different techniques to assess the fiber-matrix interface properties;
  - In general, there is no in-depth observation of the debonding process since fiber are often relatively small in size.

  Thus, in this work and previously at Rowan University, transverse single- and two-fiber tensile samples were fabricated using glass macro-fiber ranging from 1 to 2 mm in diameter, to ease the study of the fiber-matrix interface, and tested in uniaxial tension to subject the fiber-matrix interface to opening mode. Using one or two cameras placed parallel to the front and side surfaces of the samples,

the debonding process was monitored, enabling the debonding angle, length and opening to be extracted.

Side observations provide a correct estimate of the length and topology of the debonding for sufficiently small debonding areas at the pole of the fiber. For larger debonding areas, side observations are unable to describe the debonding angle while accurately capturing the debonding length. This is because the reflective index is similar to the bonded area due to local compressive loading. The debonding angle was extracted optically and using the DIC residual, both methods yielded similar results. It led to the identification of the remote loading at initiation and during the propagation phase. However, such an observation is limited to the pixel size as subpixel crack may occur. In this sense, the debonding opening obtained using DIC displacement fields can capture the sub-pixel phenomenon. Overall, debonding opening provides an initiation remote loadings similar to those of the debonding angle and length. However, the extraction method developed was unable to distinguish a complete crack from the process zone, raising questions about the size of the debonding extracted.

Some of the perspectives of this experimental campaign would be to use microtomography to assess the topology of the debonding in 3D for different remote loadings. In addition, it is possible to couple a numerical simulation to the experimental debonding opening and thus determine the boundaries of the angle and length measured experimentally. Samples with fiber misaligned with respect to the loading direction could also be investigated to vary the mode mixity experienced by the fiber-matrix interface. Different matrix behavior could also be studied by varying the degrees of curing, which could induce non-linearity. In particular, emerging thermoplastic matrices could also be studied as they are increasingly used to improve the recycling of composite parts. Finally, AE signals could also be used to determine the proper debonding topology in combination with numerical simulation.

- **Chapter IV: Inverse identification of the fiber-matrix interface fracture properties**

  The CC and CZM are two numerical approaches generally used to assess fiber-matrix debonding. They were used in this work on the basis of several limitations concerning their current application, summarized below:

  - The CC applications to fiber-matrix debonding are mainly limited to numerical study, no confrontation with experimental observation were previously provided to our knowledge;

- The CC and CZM are often compared based on the initiation remote loading they provide, but generally not on the debonding size and propagation phase. Additionnaly, comparison with experimental data have to be performed;
- The CC have not yet been applied to fiber-matrix debonding using a 3D model.

Inverse identification of the fiber-matrix interface fracture properties is carried out using several approaches. A comparison between 2D and 3D was carried out, as the use of a 2D model improves the efficiency of the calculations.

The CC was able to capture the observed debonding process with unstable crack initiation and propagation up to a finite debonding angle, followed by a stable propagation phase. The opening fracture properties were identified based on the initiation remote loading and restricted using the initiation debonding angle. Further restrictions on the critical energy release rates were applied based on the propagation phase. Similarly, CZM accurately predicted the debonding process. The properties identified using CZM were in the same order of magnitude as those of the CC, except G_{IIC}. Overall, CC and CZM predicted the variation of the debonding angle with the identified properties in a similar way. The CC was applied with a 3D model by basing the potential debonding shapes on the stress isocontours. Inverse identification in 3D was carried out on the basis of the debonding opening. No shear properties were identified since the debonding shapes did not experience any shear. Critical energy release rates identified in 3D were in the same order of magnitude as in 2D. Slightly smaller tensile strengths were identified in 2D because the latter model did not take into account the stress singularity at the free surface. Overall, limitations remain in this work, for example, purely linear elastic materials were considered whereas polymers can exhibit non-linear behavior. In addition, the application of a remote displacement resulting in a remote stress may not reproduce the actual loading configuration, such as the overall misalignment of the sample. The fiber orientation with respect to the loading direction was not always perfect, and this aspect was not taken into account in the model. Indeed, misalignment of the fiber may have promoted or mitigated the debonding initiation.

Debonding shapes based on stress isocontours were taken into account in the 3D model. One perspective at the time of the study was to improve this approach by considering other shapes such as those based on the energy condition, which is discussed in Chapter V. From other perspectives, based on the limitations listed above, DIC displacement fields could have been applied as boundary conditions. In addition, imperfect geometries, such as fiber misalignment should

be numerically studied. Finally, the non-linearity matrix response should be implemented, yet noting that a single calculation would be necessary for each loading level.

- **Chapter V: Influence of nearby fiber on fiber-matrix debonding**

  The CC was applied to a 2D configuration involving two fibers so that field perturbation is induced at the fiber-matrix interface. Such a configuration was considered to study the determination of the crack path inherent in the implementation of the CC. In particular, a limitation remains with regard to the current application of the CC which has only been implemented by basing the crack path on parameterized shapes or based on stress isocontours, but what is the optimal crack shape?

  All possible single debonding shapes have been investigated, including stress isocontours and energy-based shapes. Normal stress isocontours-based shapes are advantageous because no fracture properties are involved, and no cracks need to be released compared with energy-based shapes. Optimal CC solutions always lie in-between those obtained with stress isocontours-based or energy-based debonding shapes. Depending on the interface properties, *i.e.*, the interface brittleness number γ, three different configurations can be encountered:

  – Small γ: the stress-based debonding prediction provides a reasonable approximation for the possible initiation debonding shapes;

  – Intermediate γ: the possible initiation debonding shapes lie in-between the stress-based and energy-based debonding predictions;

  – Large γ: the energy-based debonding prediction provides a good approximation, as the solution tends to be energy driven.

  Basing the debonding shapes on the stress isocontours results in a difference of no larger than 5% in the initiation remote loading compared to the optimal CC solution. The CC correctly predicted the experimental initiation remote loading and the corresponding debonding angle for the different geometrical configurations studied. Larger differences are observed for the inter-center angle of 90 deg., which can be explained by the fact that the CC solution only takes into account a single initiation site, whereas the interface may have started to be damaged beforehand. In this sense, CZM are able to take into account interface damage at different locations simultaneously. As a result, they are able to more accurately encompass the experimental initiation remote loadings while overestimating the debonding angles.. In addition, the 2D model may not be representative of the actual field occurring at the free surface due to the stress

singularity. As with the limitations in the previous chapter, the idealized loading may not be representative of the actual loading configuration.

For this purpose, the determination of the optimal debonding shapes was extended in 3D since all the experimental data are extracted at the free surface, which is investigated in Chapter VI. In addition, one perspective would be to study the initiation of a debonding at one pole of the fiber with the CC in comparison with the propagation of another that has already been initiated. The loading conditions implemented in the model could also be improved by using the DIC fields observed experimentally.

- **Chapter VI: Towards the determination of optimal initiation 3D crack shapes**

  The determination of the optimal crack shape for the CC was extended to a single-fiber 3D configuration in order to verify whether shapes based on stress isocontours are a relevant possibility as in 2D. In addition, it was found in Chapter IV that stress isocontours-based shapes do not enable the identification of shear fracture properties.

  A methodology was developed to study the CC solution on the basis of several possible debonding shapes, iteratively compared. Assumptions were made about the location of debonding initiation and the debonding front shape. Energy-based debonding shapes were found to be optimal. Contrary to what was found in 2D, stress isocontours-based shapes never provided the optimal CC solution, whatever the fracture properties of the interface, *i.e.*, the brittleness number. The stress isocontours-based shapes yield correct estimate of the optimal CC solution for either small ($\gamma < 1$) or large ($\gamma > 6$) brittleness numbers. Larger differences, up to 30%, are encountered for intermediate brittleness numbers ($1 < \gamma < 6$). An inverse identification of the fiber-matrix interface fracture properties based on both approaches was also carried out. No shear properties were identified as debonding initiated for relatively small areas where shear has no influence. Both approaches identified similar tensile strength, but larger differences were found in the critical energy release rates. In addition, stress isocontours-based shapes were unable to accurately predict the experimental debonding topology, unlike optimal debonding shapes. The major limitation associated with the approach developed is that no arrest debonding surface can be derived, so the experimental results serve as an upper bound only. It is therefore difficult to determine an optimal set of interface fracture properties.

  It would therefore be interesting to assess further debonding propagation shapes to determine the arrest surface. Among the possible crack shapes, the one that maintains a constant ratio between the stress intensify factor (SIF) and the crit-

ical SIF along the front could be the most favorable. The arrest debonding surface would be that for which the ratio is no longer greater than one. The obtained arrest surface could then be compared with the experimental observation, which would enable improved identification of the interface fracture properties.

As a general conclusion, this thesis work has enabled the experimental characterization of fiber-matrix debonding using the results of transversely loaded single-fiber microcomposite samples. Those tests, coupled with a FE numerical model, can be used to identify the opening and shear fracture properties of the fiber-matrix interface. The CC and CZM were used to model the fiber-matrix interface debonding. Both approaches are capable of reproducing the debonding process observed experimentally. The use of a 2D model enables the shear fracture properties of the interface to be determined, unlike the 3D model. The 2D model does not take into account the singularity at the free surface and therefore underestimates the tensile strength compared with the 3D model. When the crack path becomes more complex, for instance in the presence of a second fiber, stress isocontours-based debonding shapes give a CC solution close to the optimum when dealing with a 2D model. However, larger discrepancies are observed when using a 3D model and the stress isocontours-based debonding shapes, leading to a difference of up to 30% with the optimum solution.

Appendices

APPENDIX A

Inverse identification of the fiber-matrix interface fracture properties

A.1 Mesh convergence study

The mesh convergence study consists of determining the appropriate mesh size that provides a solution close to a converged solution while limiting the degrees of freedom of the model. As the CC combines two conditions, the convergence analysis must be performed for both the stress energy and elastic strain fields. To this end, the variation of both fields is calculated as a function of the debonding size, *i.e.*, the angle of debonding in this case, for different mesh sizes. The variation in equivalent stress and incremental energy release rate is shown in Figure A.1. A mesh size of 10 µm is considered converged in this configuration since relative differences of less than 1% are obtained with smaller meshes. The results can be compared with the solution provided by other meshes using the relationship proposed in Equation (A.1).

$$\mathcal{F}_3 = \frac{|\sigma_{\text{eq}} - \sigma_{\text{eq}}^{\text{converged}}|}{\left(\sigma_{\text{eq}} + \sigma_{\text{eq}}^{\text{converged}}\right) \times 0.5} \times 100 \tag{A.1}$$

A similar relationship can be used to assess the converged mesh size on the IERR. The maximum relative differences obtained over the range of debonding angles for each mesh size are shown in Figure A.2. Depending on requirements, the appropriate mesh size can be selected.

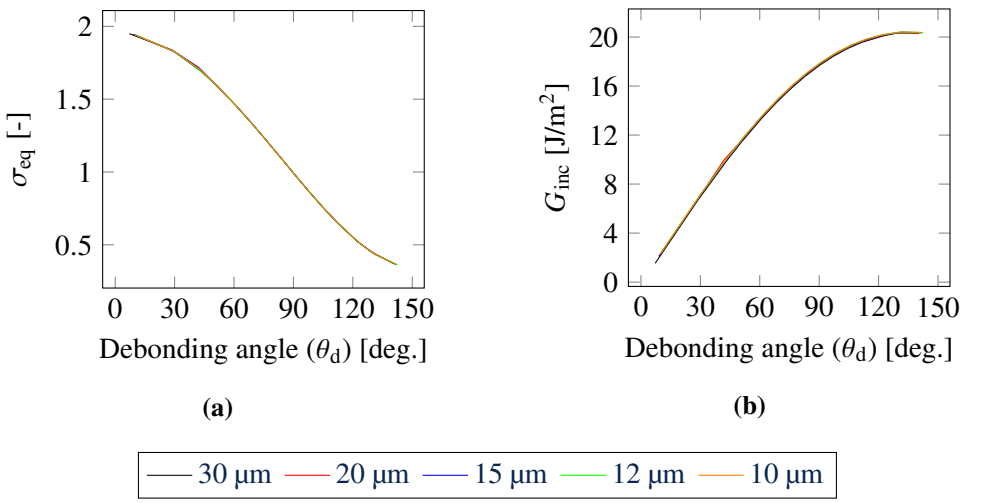

Figure A.1 – Influence of the fiber-matrix interface mesh size on (a) the equivalent stress and (b) the IERR as a function of the debonding angle.

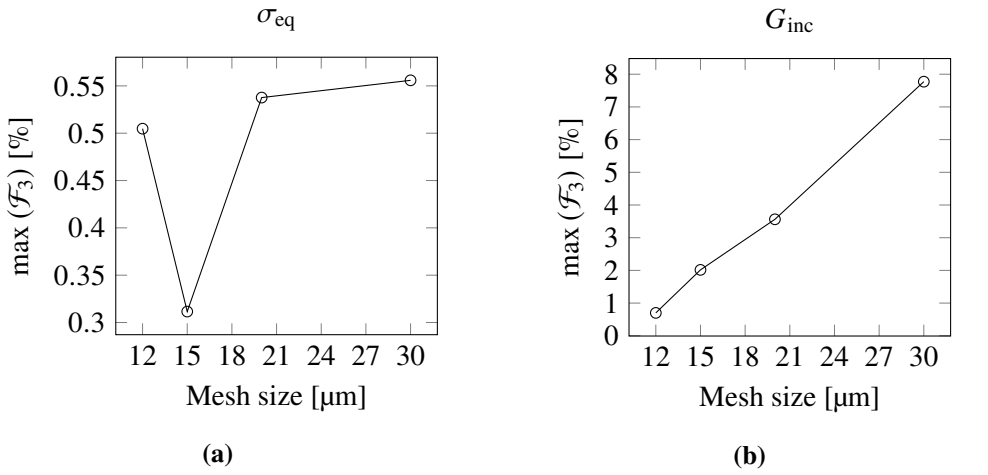

Figure A.2 – Maximum relative difference induced by the different mesh sizes compared to a converged solution regarding (a) the equivalent stress and (b) the IERR.

APPENDIX B

Influence of nearby fiber on fiber-matrix debonding

B.1 Proof of equality $G/G_c = G_{inc}/\overline{G_c}$ when $d/dS(G_{inc}/\overline{G_c}) = 0$

Recalling that G_{inc}, $\overline{G_c}$, G and G_c are depending on the debonding surface S. When, a debonding initiates for a debonding surface maximizing $G_{inc}/\overline{G_c}$:

$$\frac{d}{dS}\frac{G_{inc}}{\overline{G_c}} = 0 \tag{B.1}$$

Recalling B.1:

$$\frac{d}{dS}\frac{G_{inc}}{\overline{G_c}} = \frac{\frac{dG_{inc}}{dS}\overline{G_c} - \frac{d\overline{G_c}}{dS}G_{inc}}{\overline{G_c}^2} \tag{B.2}$$

It derives from the right part:

$$\frac{dG_{inc}}{dS}\overline{G_c} = \frac{d\overline{G_c}}{dS}G_{inc} \tag{B.3}$$

The IERR can be expressed as:

$$G_{inc} = G - S\frac{dG_{inc}}{dS} \tag{B.4}$$

Integrating B.4 into B.3:

$$\frac{\mathrm{d}G_{\mathrm{inc}}}{\mathrm{d}S}\overline{G_{\mathrm{c}}} = \frac{\mathrm{d}\overline{G_{\mathrm{c}}}}{\mathrm{d}S}\left(G - S\frac{\mathrm{d}G_{\mathrm{inc}}}{\mathrm{d}S}\right) \tag{B.5}$$

$$\frac{\mathrm{d}G_{\mathrm{inc}}}{\mathrm{d}S}\overline{G_{\mathrm{c}}} = \frac{\mathrm{d}\overline{G_{\mathrm{c}}}}{\mathrm{d}S}G - S\frac{\mathrm{d}\overline{G_{\mathrm{c}}}}{\mathrm{d}S}\frac{\mathrm{d}G_{\mathrm{inc}}}{\mathrm{d}S} \tag{B.6}$$

$$\frac{\mathrm{d}G_{\mathrm{inc}}}{\mathrm{d}S}\overline{G_{\mathrm{c}}} + S\frac{\mathrm{d}\overline{G_{\mathrm{c}}}}{\mathrm{d}S}\frac{\mathrm{d}G_{\mathrm{inc}}}{\mathrm{d}S} = \frac{\mathrm{d}\overline{G_{\mathrm{c}}}}{\mathrm{d}S}G \tag{B.7}$$

$$\frac{\mathrm{d}G_{\mathrm{inc}}}{\mathrm{d}S}\left(\overline{G_{\mathrm{c}}} + S\frac{\mathrm{d}\overline{G_{\mathrm{c}}}}{\mathrm{d}S}\right) = \frac{\mathrm{d}\overline{G_{\mathrm{c}}}}{\mathrm{d}S}G \tag{B.8}$$

The local critical ERR can be expressed as:

$$G_{\mathrm{c}} = \overline{G_{\mathrm{c}}} + S\frac{\mathrm{d}\overline{G_{\mathrm{c}}}}{\mathrm{d}S} \tag{B.9}$$

Replacing into B.8:

$$\frac{\mathrm{d}G_{\mathrm{inc}}}{\mathrm{d}S}G_{\mathrm{c}} = \frac{\mathrm{d}\overline{G_{\mathrm{c}}}}{\mathrm{d}S}G \tag{B.10}$$

$$\frac{\mathrm{d}G_{\mathrm{inc}}}{\mathrm{d}S} = \frac{\mathrm{d}\overline{G_{\mathrm{c}}}}{\mathrm{d}S}\frac{G}{G_{\mathrm{c}}} \tag{B.11}$$

Remembering that:

$$\frac{\mathrm{d}}{\mathrm{d}S}\frac{G_{\mathrm{inc}}}{\overline{G_{\mathrm{c}}}} = 0 \tag{B.12}$$

So it can be stated that:

$$\frac{\mathrm{d}G_{\mathrm{inc}}}{\mathrm{d}S} = \frac{\mathrm{d}\overline{G_{\mathrm{c}}}}{\mathrm{d}S}\frac{G_{\mathrm{inc}}}{\overline{G_{\mathrm{c}}}} \tag{B.13}$$

Finally, the following equality is obtained by replacing B.13 into B.11:

$$\frac{G_{\mathrm{inc}}}{\overline{G_{\mathrm{c}}}} = \frac{G}{G_{\mathrm{c}}} \tag{B.14}$$

B.2 Proof of inequality $\mathrm{d}/\mathrm{d}S(G/G_\mathrm{c}) < 0$ when $S = S_\mathrm{min}$

Recalling that S_min denotes the debonding surface for which $\mathrm{d}/\mathrm{d}S(G_\mathrm{inc}/\overline{G_\mathrm{c}}) = 0$.

$$\frac{\mathrm{d}}{\mathrm{d}S}\frac{G}{G_\mathrm{c}} = \frac{\frac{\mathrm{d}G}{\mathrm{d}S}G_\mathrm{c} - \frac{\mathrm{d}G_\mathrm{c}}{\mathrm{d}S}G}{{G_\mathrm{c}}^2} \tag{B.15}$$

As $G = G_\mathrm{c}$ for $S = S_\mathrm{min}$:

$$\frac{\mathrm{d}}{\mathrm{d}S}\frac{G}{G_\mathrm{c}} = \frac{\frac{\mathrm{d}G}{\mathrm{d}S}G_\mathrm{c} - \frac{\mathrm{d}G_\mathrm{c}}{\mathrm{d}S}G}{G_\mathrm{c}}\frac{1}{G_\mathrm{c}} = \left(\frac{\mathrm{d}G}{\mathrm{d}S} - \frac{\mathrm{d}G_\mathrm{c}}{\mathrm{d}S}\right)\frac{1}{G_\mathrm{c}} \tag{B.16}$$

As demonstrated by Mantič [Man09], $\frac{\mathrm{d}G}{\mathrm{d}S} < \frac{\mathrm{d}G_\mathrm{c}}{\mathrm{d}S}$ for $S = S_\mathrm{min}$, so the following equality is obtained:

$$\frac{\mathrm{d}}{\mathrm{d}S}\frac{G}{G_\mathrm{c}} = \left(\frac{\mathrm{d}G}{\mathrm{d}S} - \frac{\mathrm{d}G_\mathrm{c}}{\mathrm{d}S}\right)\frac{1}{G_\mathrm{c}} < 0 \tag{B.17}$$

APPENDIX C

Towards the determination of optimal initiation 3D crack shapes

C.1 Comparison of the critical ERR calculation

The calculation of the critical energy release rate involves the use of the mode mixity ψ , as proposed by Hutchinson and Suo [HS91]. Mode mixity is evaluated as a ratio between normal stresses and shear stresses. The latter can be calculated at each node of the interface. Different approaches have been proposed to evaluate the critical ERR, either ahead of the debonding front at a certain distance [Man09], or prior to the debonding initiation over the debonding surface [GL12]. An inherent drawback of the calculation ahead of the debonding front is the oscillatory variation of the fields in the vicinity of the front [PCM06], requiring the calculation of the mode mixity at a fixed specified distance. Both methods are thus compared to assess their difference and applied to stress isocontours-based shapes. Determination of the mode mixity ahead of the debonding front is performed at half-element size. The critical ERR are summed from the values calculated at each node and averaged with the corresponding area with respect to the other debonding shapes, and finally averaged with the total area. The critical ERR prior to debonding initiation is calculated as a sum of the local critical ERR calculated at each node averaged with the respective node area, itself averaged by the total area. Figure C.1 shows the critical ERR obtained with the two approaches as a function of the debonding surface. Overall, the trends are similar, with a minimum achieved at a slightly different debonding area. The relative difference between the two approaches does not exceed 0.3%.

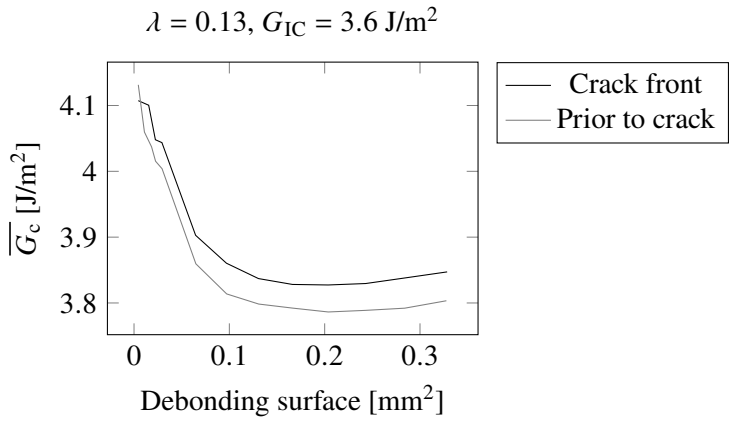

Figure C.1 – Comparison of the two approaches to determine the averaged critical ERR for fixed critical ERR.

C.2 Inverse identification for samples SFII-3 and SFII-4

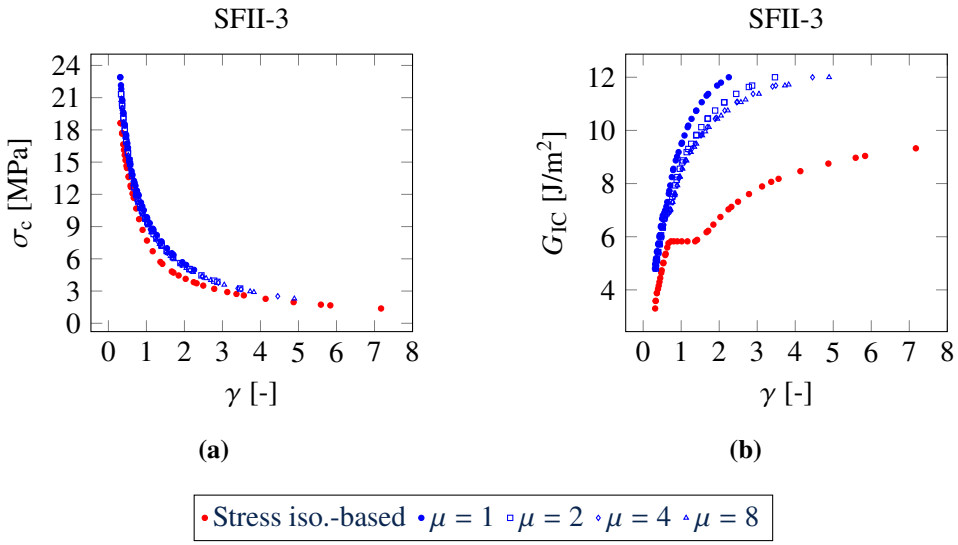

Figure C.2 – Couples of (a) σ_c and (b) G_{IC} leading to a debonding initiation remote loading equal to the experimental one for the sample SFII-3 (8 MPa).

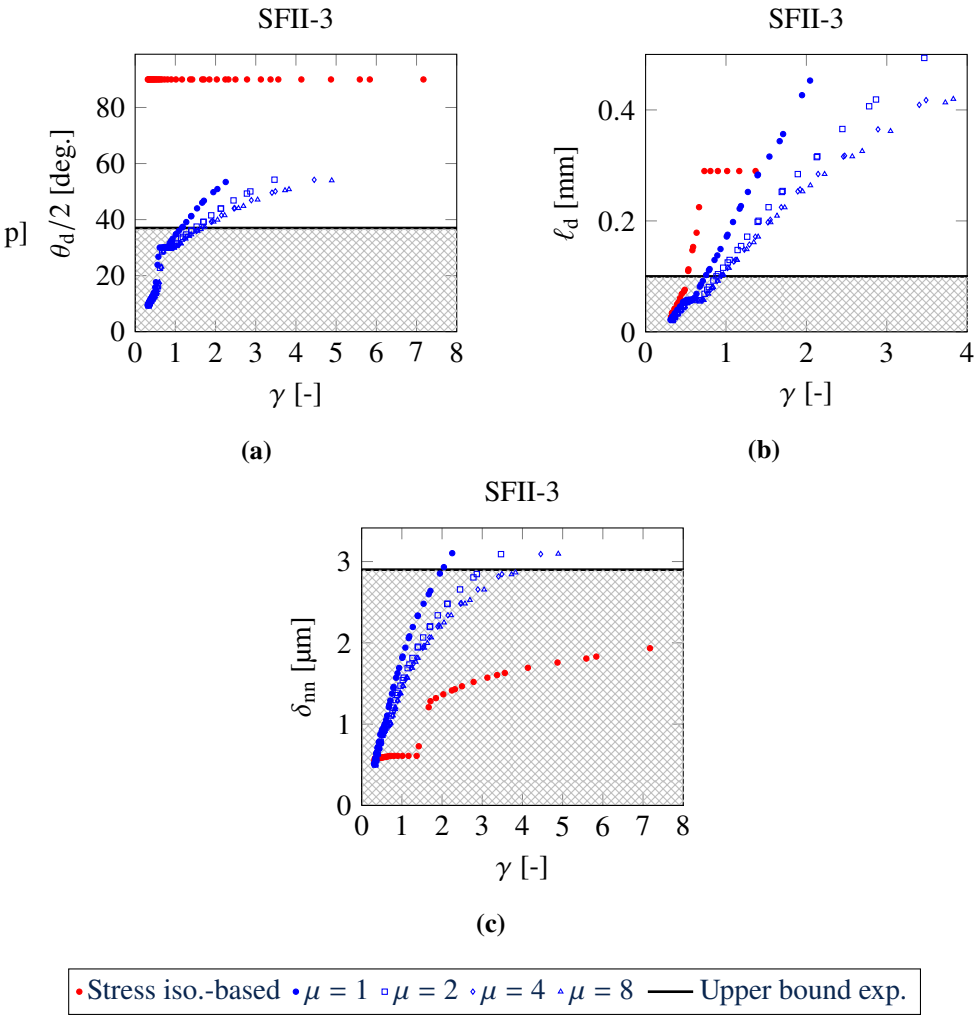

Figure C.3 – (a) θ_d and (b) ℓ_d, and δ_{nn} (c) obtained for the different brittleness numbers and the suitable configurations for the inverse identification. The experimental validity range is indicated by the hatched zone.

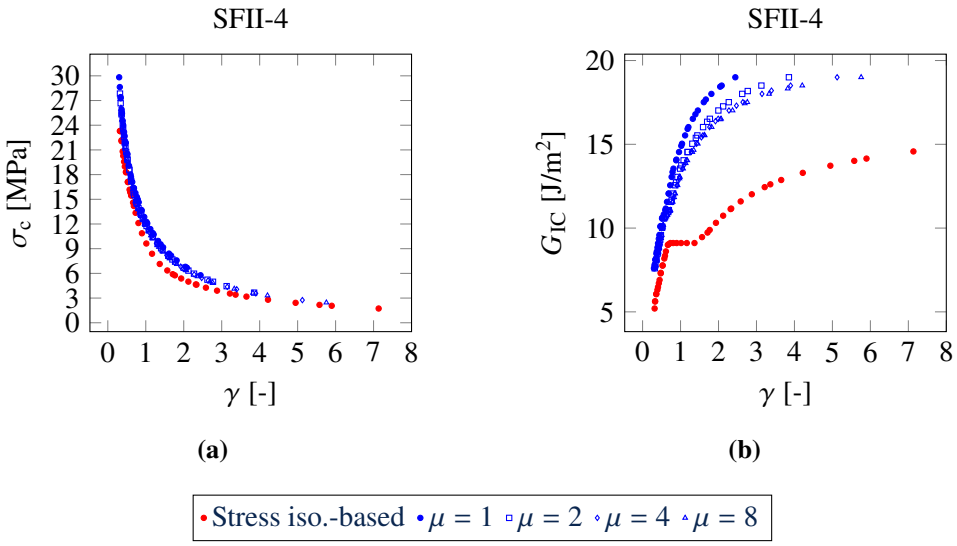

Figure C.4 – Couples of (a) σ_c and (b) G_{IC} leading to a debonding initiation remote loading equal to the experimental one for the sample SFII-4 (10 MPa).

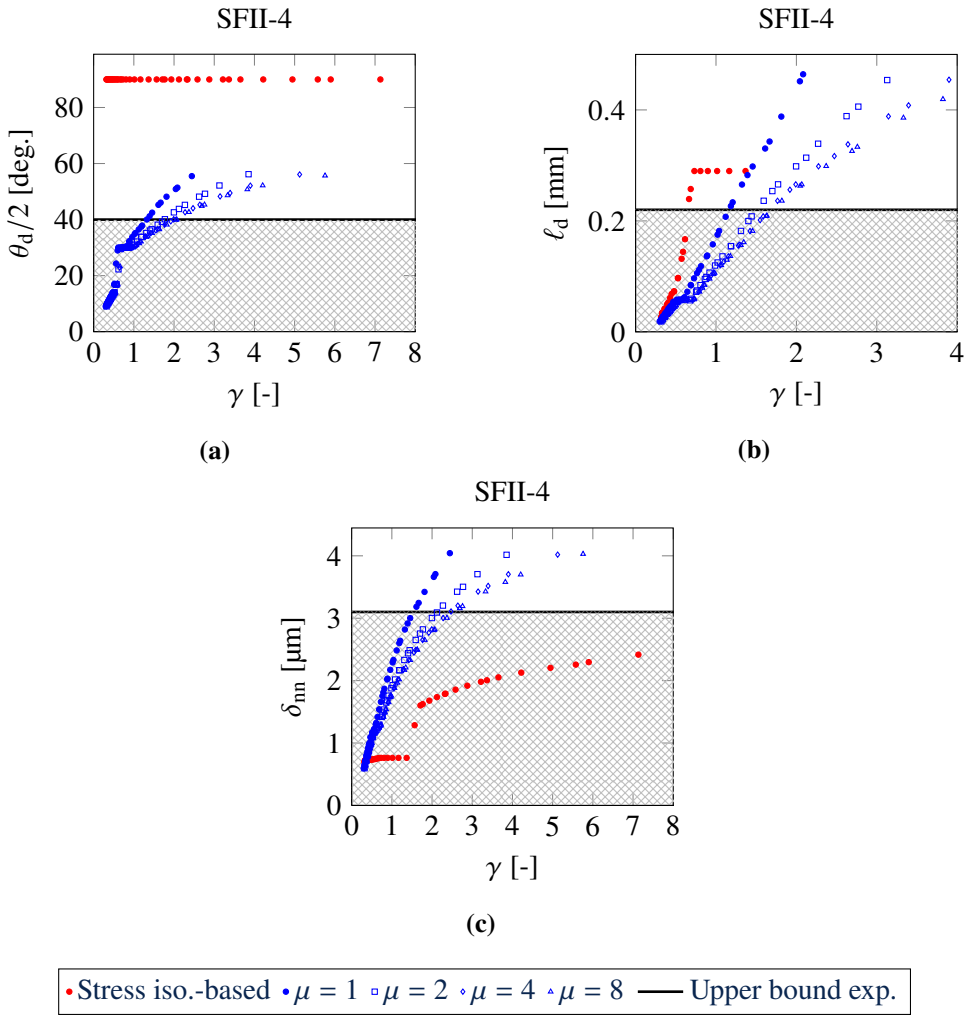

Figure C.5 – (a) θ_d and (b) ℓ_d, and δ_{nn} (c) obtained for the different brittleness numbers and the suitable configurations for the inverse identification. The experimental validity range is indicated by the hatched zone.

Bibliography

[Age+99] C Ageorges et al. "Single-fibre Broutman test: fibre–matrix interface transverse debonding". In: *Composites Part A: Applied Science and Manufacturing* 30.12 (1999), pp. 1423–1434. ISSN: 1359-835X. DOI: 10.1016/S1359-835X(99)00045-7. URL: https://www.sciencedirect.com/science/article/pii/S1359835X99000457.

[AH88] J. R. Abbott and B. G. Higgins. "Surface tension of a curing epoxy". In: *Journal of Polymer Science Part A: Polymer Chemistry* 26.7 (1988), pp. 1985–1988. ISSN: 0887-624X, 1099-0518. DOI: 10.1002/pola.1988.080260724. URL: https://onlinelibrary.wiley.com/doi/10.1002/pola.1988.080260724 (visited on 11/23/2023).

[All96] K.W. Allen. "Papyrus — some ancient problems in bonding". In: *Thirty-third Annual Conference on Adhesion and Adhesives* 16.1 (1996), pp. 47–51. ISSN: 0143-7496. DOI: 10.1016/0143-7496(96)88486-7. URL: https://www.sciencedirect.com/science/article/pii/0143749696884867.

[Ara+22] M. T. Aranda et al. "Experimental evaluation of the similarity in the interface fracture energy between PMMA/epoxy/PMMA and PMMA/epoxy joints". In: *Engineering Fracture Mechanics* 259 (Jan. 2022), p. 108076. ISSN: 00137944. DOI: 10.1016/j.engfracmech.2021.108076. URL: https://linkinghub.elsevier.com/retrieve/pii/S0013794421004884 (visited on 03/12/2024).

[Arr+23] F. Arriaga et al. "Mechanical Properties of Wood: A Review". In: *Forests* 14.6 (2023). ISSN: 1999-4907. DOI: 10.3390/f14061202.

[Ash16] M. F. Ashby. *Materials Selection in Mechanical Design*. EN. Elsevier Science & Technology, 2016. ISBN: 978-0-08-100610-8.

[Ash87] M. F. Ashby. "Technology of the 1990s: Advanced Materials and Predictive Design". In: *Philosophical Transactions of the Royal Society of London. Series A, Mathematical and Physical Sciences* 322.1567 (1987). Publisher: The Royal Society, pp. 393–407. ISSN: 2054-0272. DOI: https://doi.org/10.1098/rsta.1987.0059. URL: https://doi.org/10.1098/rsta.1987.0059 (visited on 07/25/2023).

[Bag+16] M. Baghery Borooj et al. "Optimization of plasma treatment variables for the improvement of carbon fibres/epoxy composite performance by response surface methodology". In: *Composites Science and Technology* 128 (2016), pp. 215–221. ISSN: 02663538. DOI: 10.1016/j.compscitech.2016.03.020. URL: https://linkinghub.elsevier.com/retrieve/pii/S0266353816301154 (visited on 12/01/2023).

[Bar+06] F. Barthelat et al. "Mechanical properties of nacre constituents and their impact on mechanical performance". In: *Journal of Materials Research* 21.8 (2006), pp. 1977–1986. ISSN: 2044-5326. DOI: 10.1557/jmr.2006.0239. URL: https://doi.org/10.1557/jmr.2006.0239.

[Bar59] G.I Barenblatt. "The formation of equilibrium cracks during brittle fracture. General ideas and hypotheses. Axially-symmetric cracks". In: *Journal of Applied Mathematics and Mechanics* 23.3 (1959), pp. 622–636. ISSN: 0021-8928. DOI: 10.1016/0021-8928(59)90157-1. URL: https://www.sciencedirect.com/science/article/pii/0021892859901571.

[Bau+22] F. Bausch et al. "Papyrus production revisited: differences between ancient and modern production modes". In: *Cellulose* 29.9 (2022), pp. 4931–4950. ISSN: 1572-882X. DOI: 10.1007/s10570-022-04573-y. URL: https://doi.org/10.1007/s10570-022-04573-y.

[BB02] Z. P. Bažant and E. Becq-Giraudon. "Statistical prediction of fracture parameters of concrete and implications for choice of testing standard". In: *Cement and Concrete Research* 32.4 (2002), pp. 529–556. ISSN: 00088846. DOI: 10.1016/S0008-8846(01)00723-2. URL: https://linkinghub.elsevier.com/retrieve/pii/S0008884601007232 (visited on 01/11/2024).

[BBB73] M G Bader, J E Bailey, and I Bell. "The effect of fibre-matrix interface strength on the impact and fracture properties of carbon-fibre-reinforced epoxy resin composites". In: *Journal of Physics D: Applied Physics* 6.5 (1973), pp. 572–586–4. ISSN: 00223727. DOI: 10.1088/

0022-3727/6/5/314. URL: https://iopscience.iop.org/article/10.1088/0022-3727/6/5/314 (visited on 10/23/2023).

[Ber12] J.-M. Berthelot. *Matériaux composites - Comportement mécanique et analyse des structures*. FR. TEC & DOC. Paris: Lavoisier, 2012. ISBN: 978-2-7430-1450-6.

[Bog+99] T.A. Bogetti et al. "Characterization of nanoscale property variations in polymer composite systems: 2. Numerical modeling". In: *Composites Part A: Applied Science and Manufacturing* 30.1 (1999), pp. 85–94. ISSN: 1359835X. DOI: 10.1016/S1359-835X(98)00097-9. URL: https://linkinghub.elsevier.com/retrieve/pii/S1359835X98000979 (visited on 12/05/2023).

[Bou+13] L. Bouhala et al. "Modelling of failure in long fibres reinforced composites by X-FEM and cohesive zone model". In: *Composites Part B: Engineering* 55 (2013), pp. 352–361. ISSN: 13598368. DOI: 10.1016/j.compositesb.2012.12.013. URL: https://linkinghub.elsevier.com/retrieve/pii/S1359836813003053 (visited on 01/15/2024).

[Bou+14] F. Bouville et al. "Strong, tough and stiff bioinspired ceramics from brittle constituents". In: *Nature Materials* 13.5 (2014), pp. 508–514. ISSN: 1476-4660. DOI: 10.1038/nmat3915. URL: https://doi.org/10.1038/nmat3915.

[Bra12] M. Braccini. "Adhérence interfaciale". In: M. Braccini and M. Dupeux. *Mécanique des interfaces solides*. Mécanique et Ingénierie des Matériaux. Lavoisier, 2012, pp. 109–133. ISBN: 978-2-7462-2551-0.

[Bro66] L. J. Broutman. "Glass-resin joint strength and their effect on failure mechanisms in reinforced plastics". In: *Polymer Engineering and Science* 6.3 (1966). Publisher: Wiley, pp. 263–272. DOI: 10.1002/pen.760060316. URL: https://doi.org/10.1002/pen.760060316.

[Bro69] L. J. Broutman. "Measurement of the fiber polymer matrix interfacial strength". In: *Interfaces in composites*. ASTM STP 452. American Society fro Testing and Materials, 1969, pp. 27–41.

[BT02] V. T. Bechel and G. P. Tandon. "Characterization of interfacial failure using a reflected light technique". In: *Experimental Mechanics* 42.2 (2002), pp. 200–205. ISSN: 1741-2765. DOI: 10.1007/BF02410884. URL: https://doi.org/10.1007/BF02410884.

[Car+21] N. Carrère et al. “Theoretical study based on 2D assumptions of the influence of small pores on crack initiation in adhesively bonded joints”. In: *International Journal of Adhesion and Adhesives* 111 (2021), p. 102979. ISSN: 0143-7496. DOI: 10.1016/j.ijadhadh.2021.102979. URL: https://www.sciencedirect.com/science/article/pii/S0143749621001779.

[CDD03] P. P. Camanho, C. G. Davila, and M. F. De Moura. “Numerical Simulation of Mixed-Mode Progressive Delamination in Composite Materials”. In: *Journal of Composite Materials* 37.16 (2003), pp. 1415–1438. ISSN: 0021-9983, 1530-793X. DOI: 10.1177/0021998303034505. URL: http://journals.sagepub.com/doi/10.1177/0021998303034505 (visited on 01/15/2024).

[CG64] J. Cook and J. E. Gordon. “A mechanism for the control of crack propagation in all-brittle systems”. en. In: *Proceedings of the Royal Society of London. Series A. Mathematical and Physical Sciences* 282.1391 (Dec. 1964), pp. 508–520. ISSN: 0080-4630, 2053-9169. DOI: 10.1098/rspa.1964.0248. URL: https://royalsocietypublishing.org/doi/10.1098/rspa.1964.0248 (visited on 10/12/2023).

[Cha+21] A. Chao Correas et al. “Size-effect on the apparent tensile strength of brittle materials with spherical cavities”. In: *Theoretical and Applied Fracture Mechanics* 116 (2021), p. 103120. ISSN: 01678442. DOI: 10.1016/j.tafmec.2021.103120. URL: https://linkinghub.elsevier.com/retrieve/pii/S0167844221002238 (visited on 01/24/2024).

[Cha02] N. Chandra. “Evaluation of interfacial fracture toughness using cohesive zone model”. In: *Composites Part A: Applied Science and Manufacturing* 33.10 (2002), pp. 1433–1447. ISSN: 1359-835X. DOI: 10.1016/S1359-835X(02)00173-2. URL: https://www.sciencedirect.com/science/article/pii/S1359835X02001732.

[Cid+10] M. V. Cid Alfaro et al. “Numerical homogenization of cracking processes in thin fibre-epoxy layers”. In: *European Journal of Mechanics - A/Solids* 29.2 (2010), pp. 119–131. ISSN: 09977538. DOI: 10.1016/j.euromechsol.2009.09.006. URL: https://linkinghub.elsevier.com/retrieve/pii/S099775380900117X (visited on 01/15/2024).

[CM96] R. B. Clough and W. G. McDonough. “The measurement of fiber strength parameters in fragmentation tests by using acoustic emission”. In: *Composites Science and Technology* 56.10 (1996), pp. 1119–1127. ISSN:

0266-3538. DOI: 10.1016/S0266-3538(96)00076-0. URL: https://www.sciencedirect.com/science/article/pii/S0266353896000760.

[CML15] N. Carrère, E. Martin, and D. Leguillon. "Comparison between models based on a coupled criterion for the prediction of the failure of adhesively bonded joints". In: *Engineering Fracture Mechanics* 138 (2015), pp. 185–201. ISSN: 00137944. DOI: 10.1016/j.engfracmech.2015.03.004. URL: https://linkinghub.elsevier.com/retrieve/pii/S0013794415000764 (visited on 01/03/2024).

[Cor] Correlated Solutions. *VIC-2D*. URL: https://www.correlatedsolutions.com/vic-2d.

[Cox52] H. L. Cox. "The elasticity and strength of paper and other fibrous materials". In: *British Journal of Applied Physics* 3.3 (1952), pp. 72–79. ISSN: 0508-3443. DOI: 10.1088/0508-3443/3/3/302. URL: https://iopscience.iop.org/article/10.1088/0508-3443/3/3/302 (visited on 12/20/2023).

[CPZ05] A. Carpinteri, M. Paggi, and G Zavarise. "Snap-back instability in microstructured composites and its connection with superplasticity". In: *Strength, Fracture and Complexity* 3.2 (2005). Publisher: IOS Press, pp. 61–72.

[CS19] P. Cornetti and A. Sapora. "Penny-shaped cracks by Finite Fracture Mechanics". In: *International Journal of Fracture* 219.1 (2019), pp. 153–159. ISSN: 0376-9429, 1573-2673. DOI: 10.1007/s10704-019-00383-9. URL: http://link.springer.com/10.1007/s10704-019-00383-9 (visited on 01/24/2024).

[CSC16] P. Cornetti, A. Sapora, and A. Carpinteri. "Short cracks and V-notches: Finite Fracture Mechanics vs. Cohesive Crack Model". In: *Modeling of fracture and damage in composite materials* 168 (2016), pp. 2–12. ISSN: 0013-7944. DOI: 10.1016/j.engfracmech.2015.12.016. URL: https://www.sciencedirect.com/science/article/pii/S0013794415006906.

[Cur77] J. D. Currey. "Mechanical properties of mother of pearl in tension". In: *Proceedings of the Royal Society of London. Series B. Biological Sciences* 196.1125 (Apr. 1977). Publisher: The Royal Society, pp. 443–463. DOI: 10.1098/rspb.1977.0050. URL: https://doi.org/10.1098/rspb.1977.0050.

[Dai+11] Z. Dai et al. “Effect of heat treatment on carbon fiber surface properties and fibers/epoxy interfacial adhesion”. In: *Applied Surface Science* 257.20 (2011), pp. 8457–8461. ISSN: 01694332. DOI: 10.1016/j.apsusc.2011.04.129. URL: https://linkinghub.elsevier.com/retrieve/pii/S016943321100674X (visited on 12/07/2023).

[Dil+95] N. Dilsiz et al. “Surface energy and mechanical properties of plasma-modified carbon fibers”. In: *Carbon* 33.6 (1995), pp. 853–858. ISSN: 00086223. DOI: 10.1016/0008-6223(94)00181-X. URL: https://linkinghub.elsevier.com/retrieve/pii/000862239400181X (visited on 12/07/2023).

[Dim+15] R. Dimitri et al. “Coupled cohesive zone models for mixed-mode fracture: A comparative study”. In: *Engineering Fracture Mechanics* 148 (2015), pp. 145–179. ISSN: 00137944. DOI: 10.1016/j.engfracmech.2015.09.029. URL: https://linkinghub.elsevier.com/retrieve/pii/S0013794415005457 (visited on 01/12/2024).

[Dim+17] R. Dimitri et al. “Mode-I debonding of a double cantilever beam: A comparison between cohesive crack modeling and Finite Fracture Mechanics”. In: *International Journal of Solids and Structures* 124 (2017), pp. 57–72. ISSN: 0020-7683. DOI: 10.1016/j.ijsolstr.2017.06.007. URL: https://www.sciencedirect.com/science/article/pii/S0020768317302688.

[Din75] J. M. Dinwoodie. “Timber-a review of the structure-mechanical property relationship”. In: *Journal of Microscopy* 104.1 (1975). Publisher: Wiley, pp. 3–32. DOI: 10.1111/j.1365-2818.1975.tb04002.x. URL: https://doi.org/10.1111/j.1365-2818.1975.tb04002.x.

[DL18a] A. Doitrand and D. Leguillon. “3D application of the coupled criterion to crack initiation prediction in epoxy/aluminum specimens under four point bending”. In: *International Journal of Solids and Structures* 143 (2018), pp. 175–182. ISSN: 0020-7683. DOI: 10.1016/j.ijsolstr.2018.03.005. URL: https://www.sciencedirect.com/science/article/pii/S0020768318301136.

[DL18b] A. Doitrand and D. Leguillon. “Comparison between 2D and 3D applications of the coupled criterion to crack initiation prediction in scarf adhesive joints”. In: *International Journal of Adhesion and Adhesives* 85 (2018), pp. 69–76. ISSN: 0143-7496. DOI: 10.1016/j.ijadhadh.2018.05.022. URL: https://www.sciencedirect.com/science/article/pii/S0143749618301416.

[DM93] L. T. Drzal and M. Madhukar. "Fibre-matrix adhesion and its relationship to composite mechanical properties". In: *Journal of Materials Science* 28.3 (1993), pp. 569–610. ISSN: 0022-2461, 1573-4803. DOI: 10.1007/BF01151234. URL: http://link.springer.com/10.1007/BF01151234 (visited on 10/24/2023).

[DML20] A. Doitrand, E. Martin, and D. Leguillon. "Numerical implementation of the coupled criterion: Matched asymptotic and full finite element approaches". In: *Finite Elements in Analysis and Design* 168 (2020), p. 103344. ISSN: 0168-874X. DOI: 10.1016/j.finel.2019.103344. URL: https://www.sciencedirect.com/science/article/pii/S0168874X19303002.

[Doi+17a] A. Doitrand et al. "Damage onset modeling in woven composites based on a coupled stress and energy criterion". In: *Engineering Fracture Mechanics* 169 (2017), pp. 189–200. ISSN: 0013-7944. DOI: 10.1016/j.engfracmech.2016.11.021. URL: https://www.sciencedirect.com/science/article/pii/S0013794416306348.

[Doi+17b] A. Doitrand et al. "Mesoscale analysis of damage growth in woven composites". In: *Composites Part A: Applied Science and Manufacturing* 96 (2017), pp. 77–88. ISSN: 1359-835X. DOI: 10.1016/j.compositesa.2017.02.018. URL: https://www.sciencedirect.com/science/article/pii/S1359835X17300660.

[Doi+20] A. Doitrand et al. "Determination of interface fracture properties by micro- and macro-scale experiments in nacre-like alumina". In: *Journal of the Mechanics and Physics of Solids* 145 (2020), p. 104143. ISSN: 0022-5096. DOI: 10.1016/j.jmps.2020.104143. URL: https://www.sciencedirect.com/science/article/pii/S002250962030377X.

[Doi+23] A. Doitrand et al. "A review of the coupled criterion". In: (2023). DOI: hal-04023438.

[Dow+00] T. D. Downing et al. "Determining the interphase thickness and properties in polymer matrix composites using phase imaging atomic force microscopy and nanoindentation". In: *Journal of Adhesion Science and Technology* 14.14 (2000), pp. 1801–1812. ISSN: 0169-4243, 1568-5616. DOI: 10.1163/156856100743248. URL: http://www.tandfonline.com/doi/abs/10.1163/156856100743248 (visited on 12/05/2023).

[DS67] B. V. Derjaguin and V. P. Smilga. "Electronic Theory of Adhesion". In: *Journal of Applied Physics* 38.12 (1967), pp. 4609–4616. ISSN: 0021-8979, 1089-7550. DOI: 10.1063/1.1709192. URL: https://pubs.

aip.org/jap/article/38/12/4609/3047/Electronic-Theory-of-Adhesion (visited on 12/04/2023).

[DSH96] L.T. Drzal, N. Sugiura, and D. Hook. "The role of chemical bonding and surface topography in adhesion between carbon fibers and epoxy matrices". In: *Composite Interfaces* 4.5 (1996), pp. 337–354. ISSN: 0927-6440, 1568-5543. DOI: 10.1163/156855497X00073. URL: https://www.tandfonline.com/doi/full/10.1163/156855497X00073 (visited on 12/05/2023).

[Dug60] D.S. Dugdale. "Yielding of steel sheets containing slits". In: *Journal of the Mechanics and Physics of Solids* 8.2 (1960), pp. 100–104. ISSN: 0022-5096. DOI: 10.1016/0022-5096(60)90013-2. URL: https://www.sciencedirect.com/science/article/pii/0022509660900132.

[Dum+23] T. Duminy et al. "Anisotropic fracture in nacre-like alumina". In: *Theoretical and Applied Fracture Mechanics* 123 (2023), p. 103710. ISSN: 01678442. DOI: 10.1016/j.tafmec.2022.103710. URL: https://linkinghub.elsevier.com/retrieve/pii/S0167844222004591 (visited on 11/07/2023).

[Dun69] J. Dundurs. "Edge-Bonded Dissimilar Orthogonal Elastic Wedges Under Normal and Shear Loading". In: *Journal of Applied Mechanics* 36.3 (1969), pp. 650–652. ISSN: 0021-8936, 1528-9036. DOI: 10.1115/1.3564739. URL: https://asmedigitalcollection.asme.org/appliedmechanics/article/36/3/650/385409/Discussion-EdgeBonded-Dissimilar-Orthogonal (visited on 01/03/2024).

[DV93] M. Desaeger and I. Verpoest. "On the use of the micro-indentation test technique to measure the interfacial shear strength of fibre-reinforced polymer composites". In: *Composites Science and Technology* 48.1 (1993), pp. 215–226. ISSN: 02663538. DOI: 10.1016/0266-3538(93)90139-8. URL: https://linkinghub.elsevier.com/retrieve/pii/0266353893901398 (visited on 01/25/2024).

[DWC96] C. DiFrancia, T. C. Ward, and R. O. Claus. "The single-fibre pull-out test. 1: Review and interpretation". In: *Composites Part A: Applied Science and Manufacturing* 27.8 (1996), pp. 597–612. ISSN: 1359835X. DOI: 10.1016/1359-835X(95)00069-E. URL: https://linkinghub.elsevier.com/retrieve/pii/1359835X9500069E (visited on 12/21/2023).

[DY99] S. Deng and L. Ye. "Influence of Fiber-Matrix Adhesion on Mechanical Properties of Graphite/Epoxy Composites: I. Tensile, Flexure, and Fatigue Properties". In: *Journal of Reinforced Plastics and Composites* 18.11 (1999), pp. 1021–1040. ISSN: 0731-6844, 1530-7964. DOI: 10.1177/073168449901801105. URL: http://journals.sagepub.com/doi/10.1177/073168449901801105 (visited on 10/31/2023).

[EF84] A.G. Evans and K.T. Faber. "Crack-Growth Resistance of Microcracking Brittle Materials". In: *Journal of the American Ceramic Society* 67.4 (1984), pp. 255–260. ISSN: 0002-7820, 1551-2916. DOI: 10.1111/j.1151-2916.1984.tb18842.x. URL: https://ceramics.onlinelibrary.wiley.com/doi/10.1111/j.1151-2916.1984.tb18842.x (visited on 12/08/2023).

[Esq+16] D. Esqué-de Los Ojos et al. "Understanding the mechanical behavior of fiber/matrix interfaces during push-in tests by means of finite element simulations and a cohesive zone model". In: *Computational Materials Science* 117 (2016), pp. 330–337. ISSN: 09270256. DOI: 10.1016/j.commatsci.2016.02.009. URL: https://linkinghub.elsevier.com/retrieve/pii/S0927025616300362 (visited on 01/15/2024).

[Fer+23] F. Ferrian et al. "Size effects on spheroidal voids by Finite Fracture Mechanics and application to corrosion pits". In: *Fatigue & Fracture of Engineering Materials & Structures* 46.3 (2023), pp. 875–885. ISSN: 8756-758X, 1460-2695. DOI: 10.1111/ffe.13902. URL: https://onlinelibrary.wiley.com/doi/10.1111/ffe.13902 (visited on 01/24/2024).

[Foi84] R. T. Foister. "Dynamic surface properties due to amine migration and chemical reaction in primary amine/epoxide systems". In: *Journal of Colloid and Interface Science* 99.2 (1984), pp. 568–585. ISSN: 00219797. DOI: 10.1016/0021-9797(84)90145-0. URL: https://linkinghub.elsevier.com/retrieve/pii/0021979784901450 (visited on 11/23/2023).

[Gal93] C. Galiotis. "A study of mechanisms of stress transfer in continuous- and discontinuous-fibre model composites by laser Raman spectroscopy". In: *Composites Science and Technology* 48.1 (1993), pp. 15–28. ISSN: 02663538. DOI: 10.1016/0266-3538(93)90116-X. URL: https://linkinghub.elsevier.com/retrieve/pii/026635389390116X (visited on 12/19/2023).

[Gar+16] I.G. García et al. “A numerical study of transverse cracking in cross-ply laminates by 3D finite fracture mechanics”. In: *Composites Part B: Engineering* 95 (2016), pp. 475–487. ISSN: 1359-8368. DOI: 10.1016/j.compositesb.2016.03.023. URL: https://www.sciencedirect.com/science/article/pii/S1359836816300476.

[Gar+21] W. Garat et al. “Surface energy determination of fibres for Liquid Composite Moulding processes: Method to estimate equilibrium contact angles from static and quasi-static data”. In: *Colloids and Surfaces A: Physicochemical and Engineering Aspects* 611 (2021), p. 125787. ISSN: 09277757. DOI: 10.1016/j.colsurfa.2020.125787. URL: https://linkinghub.elsevier.com/retrieve/pii/S0927775720313807 (visited on 11/23/2023).

[Gen+19] T. Gentieu et al. “Size effect in particle debonding: Comparisons between finite fracture mechanics and cohesive zone model”. In: *Journal of Composite Materials* 53.14 (2019). Publisher: SAGE Publications Ltd STM, pp. 1941–1954. ISSN: 0021-9983. DOI: 10.1177/0021998318816471. URL: https://doi.org/10.1177/0021998318816471 (visited on 11/17/2021).

[GGM90] A.H Gilbert, B Goldstein, and G Marom. “A liquid droplet measurement technique as a means of assessing the interlaminar shear strength of fibre-reinforced composites”. In: *Composites* 21.5 (1990), pp. 408–414. ISSN: 00104361. DOI: 10.1016/0010-4361(90)90439-4. URL: https://linkinghub.elsevier.com/retrieve/pii/0010436190904394 (visited on 12/07/2023).

[Gir+23a] H. Girard et al. “Experimental characterization of in-plane debonding at fiber-matrix interface using single glass macro fiber samples”. In: *Composites Part A: Applied Science and Manufacturing* 171 (2023), p. 107573. ISSN: 1359-835X. DOI: 10.1016/j.compositesa.2023.107573. URL: https://www.sciencedirect.com/science/article/pii/S1359835X23001495.

[Gir+23b] H. Girard et al. “Numerical simulation of fiber–matrix debonding: Inverse identification of interface properties”. In: *Engineering Fracture Mechanics* (2023), p. 109254. ISSN: 0013-7944. DOI: 10.1016/j.engfracmech.2023.109254. URL: https://www.sciencedirect.com/science/article/pii/S0013794423002126.

[Gir+24] H. Girard et al. “Influence of nearby fiber on fiber–matrix debonding: Coupled Criterion prediction and debonding shape determination”. In: *Journal of the Mechanics and Physics of Solids* 183 (2024), p. 105498.

ISSN: 00225096. DOI: 10.1016/j.jmps.2023.105498. URL: https://linkinghub.elsevier.com/retrieve/pii/S0022509623003022 (visited on 12/21/2023).

[GL12] I. G. García and D. Leguillon. "Mixed-mode crack initiation at a v-notch in presence of an adhesive joint". In: *International Journal of Solids and Structures* 49.15 (2012), pp. 2138–2149. ISSN: 00207683. DOI: 10.1016/j.ijsolstr.2012.04.018. URL: https://linkinghub.elsevier.com/retrieve/pii/S0020768312001655 (visited on 01/03/2024).

[GMG15] I.G. García, V. Mantič, and E. Graciani. "Debonding at the fibre–matrix interface under remote transverse tension. One debond or two symmetric debonds?" In: *European Journal of Mechanics - A/Solids* 53 (2015), pp. 75–88. ISSN: 0997-7538. DOI: 10.1016/j.euromechsol.2015.02.007. URL: https://www.sciencedirect.com/science/article/pii/S0997753815000200.

[Goo33] J. N. Goodier. "Concentration of Stress Around Spherical and Cylindrical Inclusions and Flaws". In: *Journal of Applied Mechanics* 1.2 (1933), pp. 39–44. ISSN: 0021-8936. DOI: 10.1115/1.4012173. URL: https://doi.org/10.1115/1.4012173 (visited on 11/10/2023).

[Goo52] R. J. Good. "A Thermodynamic Derivation of Wenzel's Modification of Young's Equation for Contact Angles; Together with a Theory of Hysteresis". In: *Journal of the American Chemical Society* 74.20 (1952), pp. 5041–5042. ISSN: 0002-7863, 1520-5126. DOI: 10.1021/ja01140a014. URL: https://pubs.acs.org/doi/abs/10.1021/ja01140a014 (visited on 11/23/2023).

[GPM14] I.G. García, M. Paggi, and V. Mantič. "Fiber-size effects on the onset of fiber–matrix debonding under transverse tension: A comparison between cohesive zone and finite fracture mechanics models". In: *Engineering Fracture Mechanics* 115 (2014), pp. 96–110. ISSN: 0013-7944. DOI: 10.1016/j.engfracmech.2013.10.014. URL: https://www.sciencedirect.com/science/article/pii/S0013794413003408.

[Gri21] A. A. Griffith. "VI. The phenomena of rupture and flow in solids". In: *Philosophical Transactions of the Royal Society of London. Series A, Containing Papers of a Mathematical or Physical Character* 221.582 (1921). Publisher: The Royal Society, pp. 163–198. DOI: 10.1098/rsta.1921.0006. URL: https://doi.org/10.1098/rsta.1921.0006.

[GS99] E.K Gamstedt and B.A Sjögren. "Micromechanisms in tension-compression fatigue of composite laminates containing transverse plies". In: *Composites Science and Technology* 59.2 (1999), pp. 167–178. ISSN: 0266-3538. DOI: 10.1016/S0266-3538(98)00061-X. URL: https://www.sciencedirect.com/science/article/pii/S026635389800061X.

[Ham+19] Z. Hamam et al. "Modelling of Acoustic Emission Signals Due to Fiber Break in a Model Composite Carbon/Epoxy: Experimental Validation and Parametric Study". In: *Applied Sciences* 9.23 (2019), p. 5124. ISSN: 2076-3417. DOI: 10.3390/app9235124. URL: https://www.mdpi.com/2076-3417/9/23/5124 (visited on 03/14/2024).

[Ham+21] Z. Hamam et al. "Acoustic Emission Signal Due to Fiber Break and Fiber Matrix Debonding in Model Composite: A Computational Study". In: *Applied Sciences* 11.18 (2021), p. 8406. ISSN: 2076-3417. DOI: 10.3390/app11188406. URL: https://www.mdpi.com/2076-3417/11/18/8406 (visited on 03/14/2024).

[HD80] G.E. Hammer and L.T. Drzal. "Graphite fiber surface analysis by X-ray photoelectron spectroscopy and polar/dispersive free energy analysis". In: *Applications of Surface Science* 4.3 (1980), pp. 340–355. ISSN: 03785963. DOI: 10.1016/0378-5963(80)90083-5. URL: https://linkinghub.elsevier.com/retrieve/pii/0378596380900835 (visited on 11/23/2023).

[HD92] P.J. Herrera-Franco and L.T. Drzal. "Comparison of methods for the measurement of fibre/matrix adhesion in composites". In: *Composites* 23.1 (1992), pp. 2–27. ISSN: 0010-4361. DOI: 10.1016/0010-4361(92)90282-Y. URL: https://www.sciencedirect.com/science/article/pii/001043619290282Y.

[HHM76] K. Horie, M. Hiromichi, and I. Mita. "Bonding of epoxy resin to graphite fibres". In: *Fibre Science and Technology* 9.4 (1976), pp. 253–264. ISSN: 00150568. DOI: 10.1016/0015-0568(76)90008-7. URL: https://linkinghub.elsevier.com/retrieve/pii/0015056876900087 (visited on 12/05/2023).

[HJ90] J. W. Hutchinson and H. M. Jensen. "Models of fiber debonding and pullout in brittle composites with friction". In: *Mechanics of Materials* 9.2 (1990), pp. 139–163. ISSN: 01676636. DOI: 10.1016/0167-6636(90)90037-G. URL: https://linkinghub.elsevier.com/retrieve/pii/016766369090037G (visited on 01/03/2024).

[HMP76] A. Hillerborg, M. Modéer, and P.-E. Petersson. "Analysis of crack formation and crack growth in concrete by means of fracture mechanics and finite elements". In: *Cement and Concrete Research* 6.6 (1976), pp. 773–781. ISSN: 00088846. DOI: 10.1016/0008-8846(76)90007-7. URL: https://linkinghub.elsevier.com/retrieve/pii/0008884676900077 (visited on 01/11/2024).

[Hna20] K. H. Hnaihen. "The Appearance of Bricks in Ancient Mesopotamia". In: *Athens Journal of History* 6.1 (2020), pp. 73–96. ISSN: 2407-9677. DOI: 10.30958/ajhis.6-1-4. URL: https://doi.org/10.30958/ajhis.6-1-4.

[Hög06] J. L. Högberg. "Mixed mode cohesive law". In: *International Journal of Fracture* 141.3 (2006), pp. 549–559. ISSN: 0376-9429, 1573-2673. DOI: 10.1007/s10704-006-9014-9. URL: http://link.springer.com/10.1007/s10704-006-9014-9 (visited on 01/15/2024).

[Hog90] P.J. Hogg. "A model for stress corrosion crack growth in glass reinforced plastics". In: *Composites Science and Technology* 38.1 (1990), pp. 23–42. ISSN: 02663538. DOI: 10.1016/0266-3538(90)90069-H. URL: https://linkinghub.elsevier.com/retrieve/pii/026635389090069H (visited on 10/23/2023).

[HS91] J.W. Hutchinson and Z. Suo. "Mixed Mode Cracking in Layered Materials". In: *Advances in Applied Mechanics*. Ed. by J. W. Hutchinson and T. Y. Wu. Vol. 29. Elsevier, 1991, pp. 63–191. ISBN: 0065-2156. DOI: 10.1016/S0065-2156(08)70164-9. URL: https://www.sciencedirect.com/science/article/pii/S0065215608701649.

[HW92] X. -Z. Hu and F. H. Wittmann. "Fracture energy and fracture process zone". In: *Materials and Structures* 25.6 (1992), pp. 319–326. ISSN: 0025-5432, 1871-6873. DOI: 10.1007/BF02472590. URL: http://link.springer.com/10.1007/BF02472590 (visited on 12/08/2023).

[Igl+02] J.G. Iglesias et al. "Effect of Glass Fiber Surface Treatments on Mechanical Strength of Epoxy Based Composite Materials". In: *Journal of Colloid and Interface Science* 250.1 (2002), pp. 251–260. ISSN: 00219797. DOI: 10.1006/jcis.2002.8332. URL: https://linkinghub.elsevier.com/retrieve/pii/S0021979702983323 (visited on 10/24/2023).

[Irw57] G. R. Irwin. "Analysis of Stresses and Strains Near the End of a Crack Traversing a Plate". In: *Journal of Applied Mechanics* 24.3 (1957), pp. 361–364. ISSN: 0021-8936, 1528-9036. DOI: 10.1115/1.4011547.

URL: https://asmedigitalcollection.asme.org/appliedmechanics/article/24/3/361/1111028/Analysis-of-Stresses-and-Strains-Near-the-End-of-a (visited on 12/06/2023).

[Jan92] B. Z. Jang. "Control of interfacial adhesion in continuous carbon and kevlar fiber reinforced polymer composites". In: *Composites Science and Technology* 44.4 (1992), pp. 333–349. ISSN: 02663538. DOI: 10.1016/0266-3538(92)90070-J. URL: https://linkinghub.elsevier.com/retrieve/pii/026635389290070J (visited on 10/31/2023).

[JHJ09] A. C. Johnson, S. A. Hayes, and F. R. Jones. "Data reduction methodologies for single fibre fragmentation test: Role of the interface and interphase". In: *Composites Part A: Applied Science and Manufacturing* 40.4 (2009), pp. 449–454. ISSN: 1359835X. DOI: 10.1016/j.compositesa.2009.01.008. URL: https://linkinghub.elsevier.com/retrieve/pii/S1359835X09000141 (visited on 12/19/2023).

[JHJ12] A. C. Johnson, S. A. Hayes, and F. R. Jones. "The role of matrix cracks and fibre/matrix debonding on the stress transfer between fibre and matrix in a single fibre fragmentation test". In: *Composites Part A: Applied Science and Manufacturing* 43.1 (2012), pp. 65–72. ISSN: 1359-835X. DOI: 10.1016/j.compositesa.2011.09.005. URL: https://www.sciencedirect.com/science/article/pii/S1359835X11002892.

[JK73] J. R. Jenness and D. E. Kline. "Dynamic mechanical properties of some epoxy matrix composites". In: *Journal of Applied Polymer Science* 17.11 (1973), pp. 3391–3422. ISSN: 0021-8995, 1097-4628. DOI: 10.1002/app.1973.070171113. URL: https://onlinelibrary.wiley.com/doi/10.1002/app.1973.070171113 (visited on 03/11/2024).

[JPL13] T. Jollivet, C. Peyrac, and F. Lefebvre. "Damage of Composite Materials". In: *Procedia Engineering* 66 (2013), pp. 746–758. ISSN: 18777058. DOI: 10.1016/j.proeng.2013.12.128. URL: https://linkinghub.elsevier.com/retrieve/pii/S1877705813019619 (visited on 10/20/2023).

[Kal+92] M. N. Kallas et al. "Interfacial stress state present in a "thin-slice" fibre push-out test". In: *Journal of Materials Science* 27.14 (1992), pp. 3821–3826. ISSN: 0022-2461, 1573-4803. DOI: 10.1007/BF00545464. URL: http://link.springer.com/10.1007/BF00545464 (visited on 01/25/2024).

[KBM92] J.-K. Kim, C. Baillie, and Y.-W. Mai. "Interfacial debonding and fibre pull-out stresses: Part I Critical comparison of existing theories with experiments". In: *Journal of Materials Science* 27.12 (1992), pp. 3143–3154. ISSN: 0022-2461, 1573-4803. DOI: 10.1007/BF01116004. URL: http://link.springer.com/10.1007/BF01116004 (visited on 12/22/2023).

[KDM74] D. H. Kaelble, P. J. Dynes, and L. Maus. "Surface Energy Analysis of Treated Graphite Fibers". In: *The Journal of Adhesion* 6.3 (1974), pp. 239–258. ISSN: 0021-8464, 1545-5823. DOI: 10.1080/00218467408075029. URL: http://www.tandfonline.com/doi/abs/10.1080/00218467408075029 (visited on 11/23/2023).

[Kha19] Rafiullah Khan. "Fiber bridging in composite laminates: A literature review". In: *Composite Structures* 229 (2019), p. 111418. ISSN: 02638223. DOI: 10.1016/j.compstruct.2019.111418. URL: https://linkinghub.elsevier.com/retrieve/pii/S0263822318346051 (visited on 12/13/2023).

[KMM98] J.-K. Kim, Y.-W. Mai, and Y.-W. Mai. *Engineered Interfaces in Fiber Reinforced Composites*. Elsevier, 1998. ISBN: 978-0-08-042695-2. DOI: 10.1016/B978-0-08-042695-2.X5000-3. URL: https://linkinghub.elsevier.com/retrieve/pii/B9780080426952X50003 (visited on 11/23/2023).

[KN02] B. W. Kim and J. A. Nairn. "Observations of Fiber Fracture and Interfacial Debonding Phenomena Using the Fragmentation Test in Single Fiber Composites". In: *Journal of Composite Materials* 36.15 (2002), pp. 1825–1858. ISSN: 0021-9983, 1530-793X. DOI: 10.1177/0021998302036015243. URL: http://journals.sagepub.com/doi/10.1177/0021998302036015243 (visited on 12/19/2023).

[Koy+09] J. Koyanagi et al. "Mixed-mode interfacial debonding simulation in single-fiber composite under a transverse load". In: *Journal of Solid Mechanics and Materials Engineering* 3.5 (2009), pp. 796–806. DOI: 10.1299/jmmp.3.796.

[KSW01] J.-K. Kim, M.-L. Sham, and J. Wu. "Nanoscale characterisation of interphase in silane treated glass fibre composites". In: *Composites Part A: Applied Science and Manufacturing* 32.5 (2001), pp. 607–618. ISSN: 1359835X. DOI: 10.1016/S1359-835X(00)00163-9. URL: https://linkinghub.elsevier.com/retrieve/pii/S1359835X00001639 (visited on 12/04/2023).

[KT65] A. Kelly and W. R. Tyson. "Tensile properties of fibre-reinforced metals: Copper/tungsten and copper/molybdenum". In: *Journal of the Mechanics and Physics of Solids* 13.6 (1965), pp. 329–350. ISSN: 00225096. DOI: 10.1016/0022-5096(65)90035-9. URL: https://linkinghub.elsevier.com/retrieve/pii/0022509665900359 (visited on 12/18/2023).

[Kus+11] V.I. Kushch et al. "Numerical simulation of progressive debonding in fiber reinforced composite under transverse loading". In: *Recent Advances in Micromechanics of Materials* 49.1 (2011), pp. 17–29. ISSN: 0020-7225. DOI: 10.1016/j.ijengsci.2010.06.020. URL: https://www.sciencedirect.com/science/article/pii/S0020722510001278.

[KZM95] J.-K. Kim, L.-M. Zhou, and Y.-W. Mai. "Techniques for Studying Composite Interfaces". In: *Handbook of Advanced Materials Testing*. New York, 1995, pp. 327–366. ISBN: 978-0-429-07679-4.

[LC92] K. M. Liechti and Y. S. Chai. "Asymmetric Shielding in Interfacial Fracture Under In-Plane Shear". In: *Journal of Applied Mechanics* 59.2 (1992), pp. 295–304. ISSN: 0021-8936, 1528-9036. DOI: 10.1115/1.2899520. URL: https://asmedigitalcollection.asme.org/appliedmechanics/article/59/2/295/422891/Asymmetric-Shielding-in-Interfacial-Fracture-Under (visited on 12/07/2023).

[Leg02] D. Leguillon. "Strength or toughness? A criterion for crack onset at a notch". In: *European Journal of Mechanics - A/Solids* 21.1 (2002), pp. 61–72. ISSN: 0997-7538. DOI: https://doi.org/10.1016/S0997-7538(01)01184-6. URL: https://www.sciencedirect.com/science/article/pii/S0997753801011846.

[Leg14] D. Leguillon. "An attempt to extend the 2D coupled criterion for crack nucleation in brittle materials to the 3D case". In: *Theoretical and Applied Fracture Mechanics* 74 (2014), pp. 7–17. ISSN: 0167-8442. DOI: 10.1016/j.tafmec.2014.05.004. URL: https://www.sciencedirect.com/science/article/pii/S0167844214000731.

[Li+06] S. Li et al. "Mixed-mode cohesive-zone models for fracture of an adhesively bonded polymer–matrix composite". In: *Engineering Fracture Mechanics* 73.1 (2006), pp. 64–78. ISSN: 00137944. DOI: 10.1016/j.engfracmech.2005.07.004. URL: https://linkinghub.elsevier.com/retrieve/pii/S0013794405001694 (visited on 01/12/2024).

[LK22] R. Livingston and B. Koohbor. "Characterizing fiber-matrix debond and fiber interaction mechanisms by full-field measurements". In: *Composites Part C: Open Access* 7 (2022), p. 100229. ISSN: 2666-6820. DOI: 10.1016/j.jcomc.2022.100229. URL: https://www.sciencedirect.com/science/article/pii/S2666682022000020.

[LSB88] W. J. Lee, J. C. Seferis, and J. C. Berg. "Characterizing high performance composite processability with dynamic fiber wettability measurements". In: *Polymer Composites* 9.1 (Feb. 1988), pp. 36–41. ISSN: 0272-8397, 1548-0569. DOI: 10.1002/pc.750090106. URL: https://4spepublications.onlinelibrary.wiley.com/doi/10.1002/pc.750090106 (visited on 11/23/2023).

[Lut+18] V. Lutz et al. "Ex-PAN carbon fibers vs carbon nanotubes fibers: From conventional epoxy based composites to multiscale composites". In: *European Polymer Journal* 106 (2018), pp. 9–18. ISSN: 00143057. DOI: 10.1016/j.eurpolymj.2018.06.023. URL: https://linkinghub.elsevier.com/retrieve/pii/S0014305718308061 (visited on 05/17/2024).

[Man+15] V. Mantič et al. "A linear elastic-brittle interface model: application for the onset and propagation of a fibre-matrix interface crack under biaxial transverse loads". In: *International Journal of Fracture* 195.1 (2015), pp. 15–38. ISSN: 1573-2673. DOI: 10.1007/s10704-015-0043-0. URL: https://doi.org/10.1007/s10704-015-0043-0.

[Man09] V. Mantič. "Interface crack onset at a circular cylindrical inclusion under a remote transverse tension. Application of a coupled stress and energy criterion". In: *International Journal of Solids and Structures* 46.6 (2009), pp. 1287–1304. ISSN: 0020-7683. DOI: 10.1016/j.ijsolstr.2008.10.036. URL: https://www.sciencedirect.com/science/article/pii/S0020768308004630.

[Mar+08] E. Martin et al. "Competition between deflection and penetration at an interface in the vicinity of a main crack". In: *International Journal of Fracture* 151.2 (2008), pp. 247–268. ISSN: 1573-2673. DOI: 10.1007/s10704-008-9228-0. URL: https://doi.org/10.1007/s10704-008-9228-0.

[Mar+13] K. Martyniuk et al. "3D in situ observations of glass fibre/matrix interfacial debonding". In: *Composites Part A: Applied Science and Manufacturing* 55 (2013), pp. 63–73. ISSN: 1359-835X. DOI: 10.1016/j.compositesa.2013.07.012. URL: https://www.sciencedirect.com/science/article/pii/S1359835X13001966.

[Mar+16] E. Martin et al. “Initiation of edge debonding: coupled criterion versus cohesive zone model”. In: *International Journal of Fracture* 199.2 (2016), pp. 157–168. ISSN: 0376-9429, 1573-2673. DOI: 10.1007/s10704-016-0101-2. URL: http://link.springer.com/10.1007/s10704-016-0101-2 (visited on 01/24/2024).

[Mar+18] E. Martin et al. “Understanding the tensile strength of ceramics in the presence of small critical flaws”. In: *Engineering Fracture Mechanics* 201 (2018), pp. 167–175. ISSN: 0013-7944. DOI: 10.1016/j.engfracmech.2018.06.021. URL: https://www.sciencedirect.com/science/article/pii/S0013794418303837.

[Mar+20] E. Martin et al. “Prediction of interfacial debonding between stiff spherical particles and a soft matrix with the coupled criterion”. In: *Theoretical and Applied Fracture Mechanics* 109 (2020), p. 102749. ISSN: 0167-8442. DOI: 10.1016/j.tafmec.2020.102749. URL: https://www.sciencedirect.com/science/article/pii/S0167844220303256.

[Mar12] E. Martin. “Interaction fissure-interface”. In: M. Braccini and M. Dupeux. *Mécanique des interfaces solides*. Mécanique et Ingénierie des Matériaux. Lavoisier, 2012, pp. 179–196. ISBN: 978-2-7462-2551-0.

[Mar22] E. Martin. “Modélisation des interfaces fibre/matrice dans les composites : une perspective bibliographique”. INSA Lyon, 2022. URL: http://www.mecamat.org/.

[McC89] L. N. McCartney. “New theoretical model of stress transfer between fibre and matrix in a uniaxially fibre-reinforced composite”. In: *Proceedings of the Royal Society of London. A. Mathematical and Physical Sciences* 425.1868 (1989), pp. 215–244. ISSN: 0080-4630. DOI: 10.1098/rspa.1989.0104. URL: https://royalsocietypublishing.org/doi/10.1098/rspa.1989.0104 (visited on 01/03/2024).

[MCM80] J. F. Mandell, J. H. Chen, and F. J. McGarry. “A microdebonding test for in situ assessment of fibre/matrix bond strength in composite materials”. In: *International Journal of Adhesion and Adhesives* 1.1 (1980), pp. 40–44. ISSN: 01437496. DOI: 10.1016/0143-7496(80)90033-0. URL: https://linkinghub.elsevier.com/retrieve/pii/0143749680900330 (visited on 01/25/2024).

[MD91] M. S. Madhukar and L. T. Drzal. “Fiber-Matrix Adhesion and Its Effect on Composite Mechanical Properties: II. Longitudinal (0°) and Transverse (90°) Tensile and Flexure Behavior of Graphite/Epoxy Composites”. In: *Journal of Composite Materials* 25.8 (1991). Publisher: SAGE

Publications Ltd STM, pp. 958–991. ISSN: 0021-9983. DOI: 10.1177/002199839102500802. URL: https://doi.org/10.1177/002199839102500802 (visited on 10/20/2023).

[MD92] M. S. Madhukar and L. T. Drzal. "Fiber-Matrix Adhesion and Its Effect on Composite Mechanical Properties. III. Longitudinal (0°) Compressive Properties of Graphite/Epoxy Composites". In: *Journal of Composite Materials* 26.3 (1992), pp. 310–333. ISSN: 0021-9983, 1530-793X. DOI: 10.1177/002199839202600301. URL: http://journals.sagepub.com/doi/10.1177/002199839202600301 (visited on 10/24/2023).

[Meu+98] P.F.M Meurs et al. "Determination of the interfacial normal strength using single fibre model composites". In: *Composites Part A: Applied Science and Manufacturing* 29.9 (1998), pp. 1027–1034. ISSN: 1359-835X. DOI: 10.1016/S1359-835X(97)00130-9. URL: https://www.sciencedirect.com/science/article/pii/S1359835X97001309.

[MJ99] S. I. Moon and J. Jang. "The mechanical interlocking and wetting at the interface between argon plasma treated UHMPE fiber and vinylester resin". In: *Journal of Materials Science* 34.17 (1999), pp. 4219–4224. ISSN: 00222461. DOI: 10.1023/A:1004642500738. URL: http://link.springer.com/10.1023/A:1004642500738 (visited on 12/01/2023).

[MKS19] C. B. Montgomery, B. Koohbor, and N. R. Sottos. "A Robust Patterning Technique for Electron Microscopy-Based Digital Image Correlation at Sub-Micron Resolutions". In: *Experimental Mechanics* 59.7 (2019), pp. 1063–1073. ISSN: 0014-4851, 1741-2765. DOI: 10.1007/s11340-019-00487-2. URL: http://link.springer.com/10.1007/s11340-019-00487-2 (visited on 05/18/2024).

[MMR87] B. Miller, P. Muri, and L. Rebenfeld. "A microbond method for determination of the shear strength of a fiber/resin interface". In: *Composites Science and Technology* 28.1 (1987), pp. 17–32. ISSN: 02663538. DOI: 10.1016/0266-3538(87)90059-5. URL: https://linkinghub.elsevier.com/retrieve/pii/0266353887900595 (visited on 12/26/2023).

[MS11] J. Mosler and I. Scheider. "A thermodynamically and variationally consistent class of damage-type cohesive models". In: *Journal of the Mechanics and Physics of Solids* 59.8 (2011), pp. 1647–1668. ISSN: 00225096. DOI: 10.1016/j.jmps.2011.04.012. URL: https://linkinghub.

elsevier.com/retrieve/pii/S0022509611000743 (visited on 01/12/2024).

[Muñ+16a] M. Muñoz-Reja et al. "Crack onset and propagation at fibre–matrix elastic interfaces under biaxial loading using finite fracture mechanics". In: *Composites Part A: Applied Science and Manufacturing* 82 (2016), pp. 267–278. ISSN: 1359-835X. DOI: 10.1016/j.compositesa.2015.09.023. URL: https://www.sciencedirect.com/science/article/pii/S1359835X15003449.

[Muñ+16b] M. Muñoz-Reja et al. "Influence of a neighbour fibre on the onset and growth of a fibre-matrix debond under biaxial loading. A study by Finite Fracture Mechanics at linear elastic interfaces". In: *21st European Conference on Fracture, ECF21, 20-24 June 2016, Catania, Italy* 2 (2016), pp. 2022–2029. ISSN: 2452-3216. DOI: 10.1016/j.prostr.2016.06.254. URL: https://www.sciencedirect.com/science/article/pii/S2452321616302657.

[Nay+19] R. Naylor et al. "Mechanically Regularized FE DIC for Heterogeneous Materials". In: *Experimental Mechanics* 59.8 (2019), pp. 1159–1170. ISSN: 0014-4851, 1741-2765. DOI: 10.1007/s11340-019-00529-9. URL: http://link.springer.com/10.1007/s11340-019-00529-9 (visited on 05/29/2024).

[Nee87] A. Needleman. "A Continuum Model for Void Nucleation by Inclusion Debonding". In: *Journal of Applied Mechanics* 54.3 (1987), pp. 525–531. ISSN: 0021-8936, 1528-9036. DOI: 10.1115/1.3173064. URL: https://asmedigitalcollection.asme.org/appliedmechanics/article/54/3/525/423262/A-Continuum-Model-for-Void-Nucleation-by-Inclusion (visited on 01/11/2024).

[Nee90] A. Needleman. "An analysis of tensile decohesion along an interface". In: *Journal of the Mechanics and Physics of Solids* 38.3 (1990), pp. 289–324. ISSN: 00225096. DOI: 10.1016/0022-5096(90)90001-K. URL: https://linkinghub.elsevier.com/retrieve/pii/002250969090001K (visited on 01/11/2024).

[Net+89] A.N. Netravali et al. "An acoustic emission technique for measuring fiber fragment length distributions in the single-fiber- composite test". In: *Composites Science and Technology* 35.1 (1989), pp. 13–29. ISSN: 02663538. DOI: 10.1016/0266-3538(89)90068-7. URL: https://linkinghub.elsevier.com/retrieve/pii/0266353889900687 (visited on 12/15/2023).

[NG79] A. W. Neumann and R. J. Good. "Techniques of Measuring Contact Angles". In: *Surface and Colloid Science*. Ed. by R. J. Good and R. R. Stromberg. Boston, MA: Springer US, 1979, pp. 31–91. ISBN: 978-1-4615-7971-7 978-1-4615-7969-4. DOI: 10.1007/978-1-4615-7969-4_2. URL: http://link.springer.com/10.1007/978-1-4615-7969-4_2 (visited on 11/23/2023).

[NL97] J. A. Nairn and Y. C. Liu. "Stress transfer into a fragmented, anisotropic fiber through an imperfect interface". In: *International Journal of Solids and Structures* 34.10 (1997), pp. 1255–1281. ISSN: 00207683. DOI: 10.1016/S0020-7683(96)00065-0. URL: https://linkinghub.elsevier.com/retrieve/pii/S0020768396000650 (visited on 12/19/2023).

[NOT08] M. Nishikawa, T. Okabe, and N. Takeda. "Determination of interface properties from experiments on the fragmentation process in single-fiber composites". In: *Materials Science and Engineering: A* 480.1 (2008), pp. 549–557. ISSN: 0921-5093. DOI: 10.1016/j.msea.2007.07.067. URL: https://www.sciencedirect.com/science/article/pii/S0921509307014797.

[NR12] T. Nilsson and R. Rowell. "Historical wood – structure and properties". In: *Wood Science for Conservation* 13.3, Supplement (2012), S5–S9. ISSN: 1296-2074. DOI: 10.1016/j.culher.2012.03.016. URL: https://www.sciencedirect.com/science/article/pii/S1296207412000659.

[Ohs+78] T. Ohsawa et al. "Temperature dependence of critical fiber length for glass fiber-reinforced thermosetting resins". In: *Journal of Applied Polymer Science* 22.11 (1978), pp. 3203–3212. ISSN: 0021-8995, 1097-4628. DOI: 10.1002/app.1978.070221115. URL: https://onlinelibrary.wiley.com/doi/10.1002/app.1978.070221115 (visited on 12/18/2023).

[OSK09] S. Ogihara, Y. Sakamoto, and J. Koyanagi. "Evaluation of Interfacial Tensile Strength in Glass Fiber/Epoxy Resin Interface using the Cruciform Specimen Method". In: *Journal of Solid Mechanics and Materials Engineering* 3.9 (2009), pp. 1071–1080. DOI: 10.1299/jmmp.3.1071.

[OW69] D. K. Owens and R. C. Wendt. "Estimation of the surface free energy of polymers". In: *Journal of Applied Polymer Science* 13.8 (1969), pp. 1741–1747. ISSN: 0021-8995, 1097-4628. DOI: 10.1002/app.1969.070130815. URL: https://onlinelibrary.wiley.com/doi/10.1002/app.1969.070130815 (visited on 11/23/2023).

[PBM01] S. A. Page, J. C. Berg, and J.-A. E. Månson. "Characterization of epoxy resin surface energetics". In: *Journal of Adhesion Science and Technology* 15.2 (2001), pp. 153–170. ISSN: 0169-4243, 1568-5616. DOI: 10.1163/156856101743382. URL: http://www.tandfonline.com/doi/abs/10.1163/156856101743382 (visited on 11/23/2023).

[PCM06] F. París, E. Correa, and V. Mantič. "Kinking of Transversal Interface Cracks Between Fiber and Matrix". In: *Journal of Applied Mechanics* 74.4 (2006), pp. 703–716. ISSN: 0021-8936. DOI: 10.1115/1.2711220. URL: https://doi.org/10.1115/1.2711220 (visited on 04/04/2022).

[PCV96] F. París, J. C. Caño, and J. Varna. "The fiber-matrix interface crack — A numerical analysis using Boundary Elements". In: *International Journal of Fracture* 82.1 (1996), pp. 11–29. ISSN: 0376-9429, 1573-2673. DOI: 10.1007/BF00017861. URL: http://link.springer.com/10.1007/BF00017861 (visited on 01/15/2024).

[PD90] M. J. Pitkethly and J. B. Doble. "Characterizing the fibre/matrix interface of carbon fibre-reinforced composites using a single fibre pull-out test". In: *Composites* 21.5 (1990), pp. 389–395. ISSN: 00104361. DOI: 10.1016/0010-4361(90)90436-Z. URL: https://linkinghub.elsevier.com/retrieve/pii/001043619090436Z (visited on 12/22/2023).

[Pig87] M. R. Piggott. "Debonding and friction at fibre-polymer interfaces. I: Criteria for failure and sliding". In: *Composites Science and Technology* 30.4 (1987), pp. 295–306. ISSN: 02663538. DOI: 10.1016/0266-3538(87)90017-0. URL: https://linkinghub.elsevier.com/retrieve/pii/0266353887900170 (visited on 12/22/2023).

[Pit+93] M. J. Pitkethly et al. "A round-robin programme on interfacial test methods". In: *Composites Science and Technology* 48.1 (1993), pp. 205–214. ISSN: 02663538. DOI: 10.1016/0266-3538(93)90138-7. URL: https://linkinghub.elsevier.com/retrieve/pii/0266353893901387 (visited on 12/27/2023).

[PJL00] Soo-Jin Park, Joong-Seong Jin, and Jae-Rock Lee. "Influence of silane coupling agents on the surface energetics of glass fibers and mechanical interfacial properties of glass fiber-reinforced composites". In: *Journal of Adhesion Science and Technology* 14.13 (Jan. 2000), pp. 1677–1689. ISSN: 0169-4243, 1568-5616. DOI: 10.1163/156856100742483. URL: http://www.tandfonline.com/doi/abs/10.1163/156856100742483 (visited on 11/23/2023).

[PM00] E. Pisanova and E. Mäder. "Acid–base interactions and covalent bonding at a fiber–matrix interface: contribution to the work of adhesion and measured adhesion strength". In: *Journal of Adhesion Science and Technology* 14.3 (2000), pp. 415–436. ISSN: 0169-4243, 1568-5616. DOI: 10.1163/156856100742681. URL: http://www.tandfonline.com/doi/abs/10.1163/156856100742681 (visited on 12/05/2023).

[PMQ95] P. W. M. Peters, E. Martin, and J. M. Quenisset. "Slip and Frictional Shear Stresses in Ceramic Matrix Composites". In: *Journal of Composite Materials* 29.5 (1995), pp. 550–572. ISSN: 0021-9983, 1530-793X. DOI: 10.1177/002199839502900501. URL: http://journals.sagepub.com/doi/10.1177/002199839502900501 (visited on 01/03/2024).

[PP11] K. Park and G. H. Paulino. "Cohesive Zone Models: A Critical Review of Traction-Separation Relationships Across Fracture Surfaces". In: *Applied Mechanics Reviews* 64.6 (2011), p. 060802. ISSN: 0003-6900, 2379-0407. DOI: 10.1115/1.4023110. URL: https://asmedigitalcollection.asme.org/appliedmechanicsreviews/article/doi/10.1115/1.4023110/370063/Cohesive-Zone-Models-A-Critical-Review-of (visited on 01/11/2024).

[PSL06] S.-J. Park, M.-K. Seo, and J.-R. Lee. "Roles of interfaces between carbon fibers and epoxy matrix on interlaminar fracture toughness of composites". In: *Composite Interfaces* 13.2 (2006). Publisher: Taylor & Francis, pp. 249–267. ISSN: 0927-6440. DOI: 10.1163/156855406775997079. URL: https://doi.org/10.1163/156855406775997079.

[PTZ88] L. S. Penn, G. C. Tesoro, and H. X. Zhou. "Some effects of surface-controlled reactions of Kevlar 29 on the interface in epoxy composites". In: *Polymer Composites* 9.3 (1988), pp. 184–191. ISSN: 0272-8397, 1548-0569. DOI: 10.1002/pc.750090304. URL: https://4spepublications.onlinelibrary.wiley.com/doi/10.1002/pc.750090304 (visited on 12/26/2023).

[PWL87] T. V. Parry, J. M. Wilson, and D. C. Leck. "Pull-out steel fasteners from a laminated composite subjected to external pressure". In: *Composites Science and Technology* 28.4 (1987), pp. 279–290. ISSN: 02663538. DOI: 10.1016/0266-3538(87)90026-1. URL: https://linkinghub.elsevier.com/retrieve/pii/0266353887900261 (visited on 12/22/2023).

[QS91] Y. Qiu and P. Schwartz. “A new method for study of the fiber-matrix interface in composites: single fiber pull-out from a microcomposite”. In: *Journal of Adhesion Science and Technology* 5.9 (1991), pp. 741–756. ISSN: 0169-4243, 1568-5616. DOI: 10.1163/156856191X00675. URL: http://www.tandfonline.com/doi/abs/10.1163/156856191X00675 (visited on 12/26/2023).

[RCA09] F.A. Ramirez, L.A. Carlsson, and B.A. Acha. “A method to measure fracture toughness of the fiber/matrix interface using the single-fiber fragmentation test”. In: *Composites Part A: Applied Science and Manufacturing* 40.6 (2009), pp. 679–686. ISSN: 1359835X. DOI: 10.1016/j.compositesa.2009.04.011. URL: https://linkinghub.elsevier.com/retrieve/pii/S1359835X09001092 (visited on 12/15/2023).

[Ret18] J. Rethoré. *UFreckles*. Version v 2.0. Language: en. Oct. 1, 2018. DOI: 10.5281/ZENODO.1433775. URL: https://zenodo.org/record/1433775 (visited on 11/03/2023).

[Reu29] A. Reuss. “Berechnung der Fließgrenze von Mischkristallen auf Grund der Plastizitätsbedingung für Einkristalle .” In: *ZAMM - Journal of Applied Mathematics and Mechanics / Zeitschrift für Angewandte Mathematik und Mechanik* 9.1 (1929), pp. 49–58. ISSN: 0044-2267, 1521-4001. DOI: 10.1002/zamm.19290090104. URL: https://onlinelibrary.wiley.com/doi/10.1002/zamm.19290090104 (visited on 11/22/2023).

[Sap+18] A. Sapora et al. “Finite Fracture Mechanics crack initiation from a circular hole”. In: *Fatigue & Fracture of Engineering Materials & Structures* 41.7 (2018), pp. 1627–1636. ISSN: 8756-758X, 1460-2695. DOI: 10.1111/ffe.12801. URL: https://onlinelibrary.wiley.com/doi/10.1111/ffe.12801 (visited on 01/24/2024).

[Sch+12] J. Schindelin et al. “Fiji: an open-source platform for biological-image analysis”. In: *Nature Methods* 9.7 (2012), pp. 676–682. ISSN: 1548-7091, 1548-7105. DOI: 10.1038/nmeth.2019. URL: https://www.nature.com/articles/nmeth.2019 (visited on 02/14/2024).

[Sco74] D. A. Scola. “High-modulus fibers and the fiber-resine interface in resin composite”. In: *Interfaces in Polymer Matrix Composites: Composite Materials*. Ed. by E. P. Plueddemann. Vol. 6. New York: Academic press, 1974, pp. 217–284. ISBN: 0-12-136506-9.

[SCP16] C. Sandino, E. Correa, and F. París. "Numerical analysis of the influence of a nearby fibre on the interface crack growth in composites under transverse tensile load". In: *Modeling of fracture and damage in composite materials* 168 (2016), pp. 58–75. ISSN: 0013-7944. DOI: 10.1016/j.engfracmech.2016.01.022. URL: https://www.sciencedirect.com/science/article/pii/S0013794416000503.

[SLL02] J.G. Swadener, K.M. Liechti, and Y-M. Liang. "Shear induced toughening in bonded joints: experiments and analysis". In: *International Journal of Fracture* 114.2 (2002), pp. 113–132. ISSN: 03769429. DOI: 10.1023/A:1015013618976. URL: http://link.springer.com/10.1023/A:1015013618976 (visited on 12/07/2023).

[SM66] G. K. Schmitz and A. G. Metcalfe. "Stress Corrosion of E-Glass Fibers". In: *I&EC Product Research and Development* 5.1 (1966), pp. 1–8. ISSN: 0536-1079, 1943-2976. DOI: 10.1021/i360017a001. URL: https://pubs.acs.org/doi/abs/10.1021/i360017a001 (visited on 10/23/2023).

[SN03] J. Schultz and M. Nardin. "Theories and Mechanisms of Adhesion". In: *Handbook of Adhesive Technology*. Ed. by A. Pizzi and K. L. Mittal. 2nd Edition. CRC Press, 2003. ISBN: 0-8247-0986-1.

[SNN20] K. Shirasu, C. Nagai, and K. Naito. "Mechanical anisotropy of PAN-based and pitch-based carbon fibers". In: *Mechanical Engineering Journal* 7.4 (2020), pp. 19–00599–19–00599. ISSN: 2187-9745. DOI: 10.1299/mej.19-00599. URL: https://www.jstage.jst.go.jp/article/mej/7/4/7_19-00599/_article (visited on 03/11/2024).

[SPS93] A. M. Sastry, S. L. Phoenix, and P. Schwartz. "Analysis of interfacial failure in a composite microbundle pull-out experiment". In: *Composites Science and Technology* 48.1 (1993), pp. 237–251. ISSN: 02663538. DOI: 10.1016/0266-3538(93)90141-3. URL: https://linkinghub.elsevier.com/retrieve/pii/0266353893901413 (visited on 12/26/2023).

[ST12] C. V. Singh and R. Talreja. "Damage in composite materials". In: *Damage and Failure of Composite Materials*. Cambridge: Cambridge University Press, 2012, pp. 36–56. ISBN: 978-0-521-81942-8. DOI: 10.1017/CBO9781139016063.004. URL: https://www.cambridge.org/core/books/damage-and-failure-of-composite-materials/damage-in-composite-materials/79913CFC3E07B24C0A9CBBECC0B96510.

[SZG17] M.M. Shokrieh, A. Zeinedini, and S.M. Ghoreishi. "On the mixed mode I/II delamination R-curve of E-glass/epoxy laminated composites". In: *Composite Structures* 171 (2017), pp. 19–31. ISSN: 02638223. DOI: 10.1016/j.compstruct.2017.03.017. URL: https://linkinghub.elsevier.com/retrieve/pii/S0263822317303318 (visited on 12/13/2023).

[TA12] N. G. Tsouvalis and K. N. Anyfantis. "Determination of the fracture process zone under Mode I fracture in glass fiber composites". In: *Journal of Composite Materials* 46.1 (2012), pp. 27–41. ISSN: 0021-9983, 1530-793X. DOI: 10.1177/0021998311401934. URL: http://journals.sagepub.com/doi/10.1177/0021998311401934 (visited on 12/13/2023).

[Táv+11] L. Távara et al. "BEM analysis of crack onset and propagation along fiber–matrix interface under transverse tension using a linear elastic–brittle interface model". In: *Engineering Analysis with Boundary Elements* 35.2 (2011), pp. 207–222. ISSN: 09557997. DOI: 10.1016/j.enganabound.2010.08.006. URL: https://linkinghub.elsevier.com/retrieve/pii/S0955799710002031 (visited on 01/15/2024).

[TCJ96] D. Tripathi, F. Chen, and F. R. Jones. "The effect of matrix plasticity on the stress fields in a single filament composite and the value of interfacial shear strength obtained from the fragmentation test". In: *Proceedings of the Royal Society of London. Series A: Mathematical, Physical and Engineering Sciences* 452.1946 (1996), pp. 621–653. ISSN: 1364-5021, 1471-2946. DOI: 10.1098/rspa.1996.0032. URL: https://royalsocietypublishing.org/doi/10.1098/rspa.1996.0032 (visited on 12/19/2023).

[TJ97] D. Tripathi and F. R. Jones. "Measurement of the load-bearing capability of the fibre/matrix interface by single-fibre fragmentation". In: *Composites Science and Technology* 57.8 (1997), pp. 925–935. ISSN: 02663538. DOI: 10.1016/S0266-3538(97)00016-X. URL: https://linkinghub.elsevier.com/retrieve/pii/S026635389700016X (visited on 12/19/2023).

[TJ98] D Tripathi and F. R Jones. "Single fibre fragmentation test for assessing adhesion in fibre reinforced composites". In: *Journal of Materials Science* 33.1 (1998), pp. 1–16. ISSN: 00222461. DOI: 10.1023/A:1004351606897. URL: http://link.springer.com/10.1023/A:1004351606897 (visited on 12/19/2023).

[TKB00] G.P Tandon, R.Y Kim, and V.T Bechel. "Evaluation of interfacial normal strength in a SCS-0/epoxy composite with cruciform specimens". In: *Composites Science and Technology* 60.12 (2000), pp. 2281–2295. ISSN: 0266-3538. DOI: 10.1016/S0266-3538(00)00020-8. URL: https://www.sciencedirect.com/science/article/pii/S0266353800000208.

[TKB02] G. P. Tandon, R. Y. Kim, and V. T. Bechel. "Fiber–Matrix Interfacial Failure Characterization Using a Cruciform-Shaped Specimen". In: *Journal of Composite Materials* 36.23 (2002). Publisher: SAGE Publications Ltd STM, pp. 2667–2691. ISSN: 0021-9983. DOI: 10.1177/002199802761675575. URL: https://doi.org/10.1177/002199802761675575 (visited on 08/24/2023).

[TKC16] K. R. Totten, B. Kutub, and L. A. Carlsson. "In situ determination of the fiber–matrix interface tensile strength". In: *Journal of Composite Materials* 50.5 (2016). Publisher: SAGE Publications Ltd STM, pp. 589–599. ISSN: 0021-9983. DOI: 10.1177/0021998315579926. URL: https://doi.org/10.1177/0021998315579926 (visited on 09/27/2022).

[Toy74] M. Toya. "A crack along the interface of a circular inclusion embedded in an infinite solid". In: *Journal of the Mechanics and Physics of Solids* 22.5 (1974), pp. 325–348. ISSN: 00225096. DOI: 10.1016/0022-5096(74)90002-7. URL: https://linkinghub.elsevier.com/retrieve/pii/0022509674900027 (visited on 01/03/2024).

[TPW05] J. H. Tsai, A. Patra, and R. Wetherhold. "Finite element simulation of shaped ductile fiber pullout using a mixed cohesive zone/friction interface model". In: *Composites Part A: Applied Science and Manufacturing* 36.6 (2005), pp. 827–838. ISSN: 1359835X. DOI: 10.1016/j.compositesa.2004.10.025. URL: https://linkinghub.elsevier.com/retrieve/pii/S1359835X04002660 (visited on 01/15/2024).

[TRH16] Z. Tomičević, S. Roux, and F. Hild. "Evaluation of fatigue crack network growth in cast iron for different biaxial loading paths via full-field measurements". In: *International Journal of Fatigue* 92 (2016), pp. 281–303. ISSN: 0142-1123. DOI: 10.1016/j.ijfatigue.2016.07.013. URL: https://www.sciencedirect.com/science/article/pii/S0142112316302171.

[TSV01] M.G.A. Tijssens, L. J. Sluys, and E. Van Der Giessen. "Simulation of fracture of cementitious composites with explicit modeling of microstructural features". In: *Engineering Fracture Mechanics* 68.11 (2001),

pp. 1245–1263. ISSN: 00137944. DOI: 10.1016/S0013-7944(01)00017-0. URL: https://linkinghub.elsevier.com/retrieve/pii/S0013794401000170 (visited on 01/12/2024).

[TTK00] N. Taniguchi, K. Toge, and H. Kawada. "Evaluation of the mechanical properties of PMC interface using slice compression test — Analysis of transfer mechanism of interfacial shear stress". In: *Composite Interfaces* 7.5 (2000). Publisher: Taylor & Francis, pp. 349–361. ISSN: 0927-6440. DOI: 10.1163/156855400750262879. URL: https://doi.org/10.1163/156855400750262879.

[TTV01] V. Tamuzs, S. Tarasovs, and U. Vilks. "Progressive delamination and fiber bridging modeling in double cantilever beam composite specimens". In: *Engineering Fracture Mechanics* 68.5 (2001), pp. 513–525. ISSN: 00137944. DOI: 10.1016/S0013-7944(00)00131-4. URL: https://linkinghub.elsevier.com/retrieve/pii/S0013794400001314 (visited on 12/13/2023).

[Tve90] V. Tvergaard. "Effect of fibre debonding in a whisker-reinforced metal". In: *Materials Science and Engineering: A* 125.2 (1990), pp. 203–213. ISSN: 09215093. DOI: 10.1016/0921-5093(90)90170-8. URL: https://linkinghub.elsevier.com/retrieve/pii/0921509390901708 (visited on 01/12/2024).

[Uem+23] H. Uematsu et al. "Enhancement of interfacial adhesion to carbon fibers via electrostatic interaction using polyvinyl chloride as a model matrix". In: *Surfaces and Interfaces* 42 (Nov. 2023), p. 103287. ISSN: 24680230. DOI: 10.1016/j.surfin.2023.103287. URL: https://linkinghub.elsevier.com/retrieve/pii/S2468023023006570 (visited on 12/04/2023).

[VBE97] J. Varna, L.A. Berglund, and M.L. Ericson. "Transverse single-fibre test for interfacial debonding in composites: 2. Modelling". In: *Composites Part A: Applied Science and Manufacturing* 28.4 (1997), pp. 317–326. ISSN: 1359-835X. DOI: 10.1016/S1359-835X(96)00125-X. URL: https://www.sciencedirect.com/science/article/pii/S1359835X9600125X.

[VCP20] M.L. Velasco, E. Correa, and F. París. "Interaction between fibres in the transverse damage in composites". In: *Engineering Fracture Mechanics* 239 (2020), p. 107273. ISSN: 0013-7944. DOI: 10.1016/j.engfracmech.2020.107273. URL: https://www.sciencedirect.com/science/article/pii/S0013794420308560.

[VJB96] J. Varna, R. Joffe, and L.A. Berglund. "Interfacial toughness evaluation from the single-fiber fragmentation test". In: *Composites Science and Technology* 56.9 (1996), pp. 1105–1109. ISSN: 02663538. DOI: 10.1016/0266-3538(96)00096-6. URL: https://linkinghub.elsevier.com/retrieve/pii/0266353896000966 (visited on 12/15/2023).

[Vod23] R. Vodička. "A mixed-mode dependent interface and phase-field damage model for solids with inhomogeneities". In: *Theoretical and Applied Fracture Mechanics* 127 (2023), p. 104009. ISSN: 01678442. DOI: 10.1016/j.tafmec.2023.104009. URL: https://linkinghub.elsevier.com/retrieve/pii/S0167844223002720 (visited on 05/16/2024).

[Voi89] W. Voigt. "Ueber die Beziehung zwischen den beiden Elasticitätsconstanten isotroper Körper". In: *Annalen der Physik* 274.12 (1889), pp. 573–587. ISSN: 0003-3804, 1521-3889. DOI: 10.1002/andp.18892741206. URL: https://onlinelibrary.wiley.com/doi/10.1002/andp.18892741206 (visited on 11/22/2023).

[Wan97] C. Wang. "Fracture mechanics of single-fibre pull-out test". In: *Journal of Materials Science* 32.2 (1997), pp. 483–490. ISSN: 00222461. DOI: 10.1023/A:1018534323464. URL: http://link.springer.com/10.1023/A:1018534323464 (visited on 12/20/2023).

[Wen+22] K. Wen et al. "Electrostatic incitation on fiber surface for enhancing mechanical properties of fiber-reinforced composite". In: *Composites Science and Technology* 228 (2022), p. 109627. ISSN: 02663538. DOI: 10.1016/j.compscitech.2022.109627. URL: https://linkinghub.elsevier.com/retrieve/pii/S0266353822003694 (visited on 12/04/2023).

[Wil+90] J.G. Williams et al. "Properties of the interphase in organic matrix composites". In: *Materials Science and Engineering: A* 126.1 (1990), pp. 305–312. ISSN: 09215093. DOI: 10.1016/0921-5093(90)90137-R. URL: https://linkinghub.elsevier.com/retrieve/pii/092150939090137R (visited on 12/04/2023).

[Wil57] M. L. Williams. "On the Stress Distribution at the Base of a Stationary Crack". In: *Journal of Applied Mechanics* 24.1 (1957), pp. 109–114. ISSN: 0021-8936, 1528-9036. DOI: 10.1115/1.4011454. URL: https://asmedigitalcollection.asme.org/appliedmechanics/article/24/1/109/1110895/On-the-Stress-Distribution-at-the-Base-of-a (visited on 01/24/2024).

[WJT20] H. Wang, K. Jin, and J. Tao. "Improving the interfacial shear strength of carbon fibre and epoxy via mechanical interlocking effect". In: *Composites Science and Technology* 200 (2020), p. 108423. ISSN: 02663538. DOI: 10.1016/j.compscitech.2020.108423. URL: https://linkinghub.elsevier.com/retrieve/pii/S0266353820322132 (visited on 12/01/2023).

[WS90] J.-S. Wang and Z. Suo. "Experimental determination of interfacial toughness curves using Brazil-nut-sandwiches". In: *Acta Metallurgica et Materialia* 38.7 (July 1990), pp. 1279–1290. ISSN: 09567151. DOI: 10.1016/0956-7151(90)90200-Z. URL: https://linkinghub.elsevier.com/retrieve/pii/095671519090200Z (visited on 12/07/2023).

[You05] T. Young. "III. An essay on the cohesion of fluids". In: *Philosophical Transactions of the Royal Society of London* 95 (Dec. 31, 1805), pp. 65–87. ISSN: 0261-0523, 2053-9223. DOI: 10.1098/rstl.1805.0005. URL: https://royalsocietypublishing.org/doi/10.1098/rstl.1805.0005 (visited on 11/23/2023).

[YT10] L. Yang and J.L. Thomason. "Interface strength in glass fibre–polypropylene measured using the fibre pull-out and microbond methods". In: *Special Issue on 10th Deformation & Fracture of Composites Conference: Interfacial interactions in composites and other applications* 41.9 (2010), pp. 1077–1083. ISSN: 1359-835X. DOI: 10.1016/j.compositesa.2009.10.005. URL: https://www.sciencedirect.com/science/article/pii/S1359835X09003157.

[Zha+97] H. Zhang et al. "Transverse single-fibre test for interfacial debonding in composites: 1. Experimental observations". In: *Composites Part A: Applied Science and Manufacturing* 28.4 (1997), pp. 309–315. ISSN: 1359835X. DOI: 10.1016/S1359-835X(96)00123-6. URL: https://linkinghub.elsevier.com/retrieve/pii/S1359835X96001236 (visited on 12/14/2023).

[ZLG97] P. Zinck, V. Lacrampe, and J.-F. Gérard. "Microcomposites et composites multifilamentaires à matrice polymère thermodurcissable et fibres de verre". In: P. Reynaud and J.-F. Gérard. *Interfaces dans les composites à fibres longues*. Hermes. Vol. 7. Revue des composites et des matériaux avancés. 1997, pp. 31–58. ISBN: 978-2-86601-653-1.

[ZM05] S. Zhandarov and E. Mäder. "Characterization of fiber/matrix interface strength: applicability of different tests, approaches and parameters". In: *Composites Science and Technology* 65.1 (2005), pp. 149–160. ISSN:

0266-3538. DOI: 10.1016/j.compscitech.2004.07.003. URL: https://www.sciencedirect.com/science/article/pii/S026635380400171X.

[ZTV18] L. Zhuang, R. Talreja, and J. Varna. "Transverse crack formation in unidirectional composites by linking of fibre/matrix debond cracks". In: *Composites Part A: Applied Science and Manufacturing* 107 (2018), pp. 294–303. ISSN: 1359-835X. DOI: 10.1016/j.compositesa.2018.01.013. URL: https://www.sciencedirect.com/science/article/pii/S1359835X18300137.

FOLIO ADMINISTRATIF

THESE DE L'INSA LYON, MEMBRE DE L'UNIVERSITE DE LYON

NOM : **GIRARD** DATE de SOUTENANCE : **10/09/2024**

Prénoms : **Hugo**

TITRE : **Characterization of the fiber-matrix interface fracture properties in long fiber composites**

NATURE : **Doctorat** Numéro d'ordre : **2024ISAL0072**

École Doctorale : **Matériaux de Lyon**

Spécialité : **Matériaux**

RÉSUMÉ :
Fiber-matrix interface in long fiber composite is a key aspect of global composite mechanical properties since it drives damage initiation and load transfer. Fiber-matrix interface debonding is usually the first type of damage that occurs when the composite is subjected to transverse loading. After initiation, the interface debonding propagates and often kinks into the matrix, leading to further critical defects for the structure. As a result, it is crucial to accurately characterize the fiber-matrix interface in order to prevent or control damage in composites. Going beyond existing experimental methods currently focused on interface shear fracture properties, single-fiber microcomposite tensile sample loaded transversely are developed to simultaneously characterize opening and shear fracture properties. An accurate experimental characterization of the fiber-matrix debonding process allowed the identification of the interface fracture properties using adequate 2D and 3D numerical approaches and related fracture models such as the Coupled Criterion (CC) and Cohesive Zone Models (CZM). Both the CC and the CZM are able to reproduce the experimentally observed debonding process in 2D, the 3D model being able to describe the free surface singularity. In 3D, the fracture property identification yields tensile strengths and critical energy release rates respectively slightly higher and in the same order of magnitude than those identified in 2D. The 3D model does not enable identifying the shear fracture properties, unlike in 2D. In 2D the optimal initiation crack shapes correspond to i) the stress isocontours for small brittleness numbers, ii) the energy-based shapes for large brittleness numbers and iii) neither of them for intermediate brittleness numbers. The 2D stress isocontours-based debonding shapes provide an accurate estimate of the initiation loading. In 3D, the optimum initiation crack always corresponds to energy-based debonding shapes and the 3D stress isocontours-based debonding shapes may thus overestimate the initiation loading by up to 30%.

MOTS-CLÉS : **Décohésion, fibre-matrice, critère couplé, matériau composite**

Laboratoire(s) de recherche : **MatéIS**

Directeur de thèse : **GODIN Nathalie**

Président du Jury : **CARRERE Nicolas**

Composition du Jury :
Estevez Rafael, Laurin Frédéric, Carrère Nicolas, Drapier Sylvain, Long Didier, Muñoz-Reja Mar, Godin Nathalie, Doitrand Aurélien, Rinaldi Renaud, Bikard Jérôme